UNIVERSITY OF SOUTHAMPTON

Faculty of Science, Engineering and Maths

School of Ocean and Earth Sciences

Derivation of Acoustic and Physical Properties from High-Resolution Seismic Reflection Data

by

Luke John William PINSON

MGEOPHYS

Thesis for the degree of DOCTOR OF PHILOSOPHY

November 2009

University of Southampton

Abstract

Faculty of Engineering, Science and Mathematics

School of Ocean and Earth Science

Doctor of Philosophy

Derivation of Acoustic and Physical Properties from High-Resolution Seismic Reflection Data

by Luke J. W. Pinson

Acoustic measurements in sediments can remotely provide information about their physical properties. This thesis develops methods using high-resolution marine seismic reflection data to generate accurate, precise, and repeatable estimations of the *in situ* seismic quality factor (Q) and velocity, within the uppermost 100 m of unconsolidated marine sediments. This was achieved using a single channel Chirp sonar (1.5–13.0 kHz) and a Boomer sonar (0.2–4.0 kHz) towed with a multi-channel streamer that provides offsets up to 80 m. These methods were applied in the Solent (Southampton, U.K.) to test empirical models that predict sediment physical properties from these acoustic properties, and in lake Windermere (Cumbria, U.K.) where the new quantitative information helps distinguish between, and identify, previously unknown glacial and lacustrine deposits.

The spectral-ratio technique was used to reliably estimate Q from seismic reflection data, without assumptions on how attenuation varies with frequency. Based on empirical observations, it is demonstrated here that Q can characterise the dominant fabric of the sediment that is supporting wave-propagation—whether it is clay dominated and has a Q over 75, or coarse-grain dominated and has a Q less than 75. The Chirp source is the most effective single sonar to estimate Q, however, improved results were obtained by combining Boomer and Chirp data to examine attenuation over four octaves (0.5–8.0 kHz). Frequency-independent Q (with 95% confidence intervals) of 135 ($+12$; -10) was obtained for silty-clay, 63 ($+10$; -7) for fine-sand, and 33 ($+6$; -4) for gyttja.

Boomer multi-channel seismic data were acquired in the Solent over a 30 m core and a sampled sand deposit, and in lake Windermere where over 150 km of survey lines were required to cover most of the lake. An optimal processing methodology was developed for high-resolution seismic data using iterative Kirchhoff prestack depth migration, Burg deconvolution and F-K filtering; velocities were derived using migration velocity analysis. Additionally, a method was developed to obtain the streamer depth profile from the surface ghost. The Solent study proved that measurements of velocity and Q together can identify unconsolidated coarse-grain sediment and distinguish between gravel, sand and silt, and differentiate between unconsolidated and over-consolidated clay sediments. In Windermere, five seismic stratigraphic sequences were identified from the depth migrated data: I—till (c. 2000–3000 m/s); II—glacio-fluvial (c. 1750 m/s); III—glacio-lacustrine/lacustrine (1500 m/s + 6 s^{-1}); IV—disturbed/slumped (c. 1500 m/s); V—lacustrine (c. 1490 m/s). A new deglacial history for lake Windermere is proposed, which has important implications on the overall character of the ice-sheet retreat in Britain after the last glacial maximum.

Dedication

To Nan and Gog who passed away during my PhD; thank you for all your love, support, and encouragement you gave to me along my way.

Contents

List of Figures

List of Tables

Declaration of Authorship

I, **Luke J. W. Pinson**, declare that this thesis and the work presented in it are my own and has been generated by me as the result of my own original research.

Derivation of Acoustic and Physical Properties from High-Resolution Seismic Reflection Data

I confirm that:

1. This work was done wholly or mainly while in candidature for a research degree at this University;
2. Where any part of this thesis has previously been submitted for a degree or any other qualification at this University or any other institution, this has been clearly stated;
3. Where I have consulted the published work of others, this is always clearly attributed;
4. Where I have quoted from the work of others, the source is always given. With the exception of such quotations, this thesis is entirely my own work;
5. I have acknowledged all main sources of help;
6. Where the thesis is based on work done by myself jointly with others, I have made clear exactly what was done by others and what I have contributed myself;
7. Either none of this work has been published before submission, or parts of this work have been published as:

   Estimating quality factor and mean grain size of sediments from high-resolution marine seismic data, Luke J. W. Pinson, Timothy J. Henstock, Justin K. Dix, Jonathan M. Bull, Geophysics, 73(4), G19–G28, 2008.

Signed:

Dated:

Acknowledgements

First I would like to express my extreme gratitude to my supervisors, Timothy Henstock, Justin Dix, and Jonathan Bull, for their all round support and encouragement since I began my studies of geophysics at the turn of the millennium. In addition to this, I would like to thank my primary supervisor Tim Henstock for his expert guidance and advice, and invaluable feedback whilst he patiently waited for me to complete my PhD; Justin Dix for his relentless enthusiasm, scientific insight, and advice on thesis content; and Jonathan Bull for his much-appreciated encouragement and advice, and for the opportunities he created that allowed me to apply my research to Windermere and outside of academia.

During my occasionally interdisciplinary project I have been privileged to work with several experts in their fields of study. I am very grateful to Angus Best and Jeremy Sothcott for their help with processing the very awkward 30 m core from the Solent, and for their insight and advice on wave propagation in sediments. Similarly, I am grateful to Veerle Huvenne for her advice, and for teaching me how to use the Mastersizer 2000. I am very grateful to John Davis for providing his expertise and some of his own time to the field excursions. I would like to also thank him for his enthusiasm towards our research and for acquiring a seabed grab at the specified co-ordinates. Thanks to Charlotte Thompson and Alice Lefebrve for showing me how to analyse the sediments in the seabed grab. Thanks to Gary Robb for donating to me his research literature that proved invaluable. Special thanks to Mark Vardy whom I shared so much useful scientific discussion with throughout my PhD, in the office, in the pub, on Windermere, and on the Russian border in the Arctic Circle. I look forward to working with you again one day. Thanks to Elizabeth Haworth for help and advice on the study of Windermere, and her hospitality. Thanks to Pierre Cazenave for that touch of computer wizardry when all else had failed.

I would also like to thank the crew of the Bill Conway during the Solent surveys, Ben James during the Windermere Survey, the Freshwater Biology Association for the use of their premises and their library, BOSCORF for providing the core storage and logging facilities, and Peter Martin and the staff of The National Oceanographic Library for helping me with my researches.

Finally, I thank my parents Brian and Janet Pinson, and my Grandparents, for their everlasting support and encouragement in all I do.

This project has been supported by a Natural Environmental Research Council studentship NER/S/A/2005/13978, and the Joint Research Equipment Initiative.

Glossary of Terms

Accurate	Close to the true value.
ATP	Attenuation trend plot.
Amelioration	Climatic improvement: warming from stadial to interstadial conditions.
BIIS	British and Irish Ice Sheet.
Boomer	Seismic source comprising an insulated metal plate that is explosively repelled by a magnetic field.
BOSCORF	British Ocean Sediment Core Research Facility.
BP	Before present.
cal	Calender years.
CDP	Common Depth-Point between source and receiver.
Chirp	Digital frequency modulated marine seismic source with output determined by source sweep.
Clay dominated	Sediment with a clay fabric that supports wave wave-propagation.
Clayey-sand	Sand dominated sediment with some clay.
Clayey-silt	Silt dominated sediment with some clay.
Coarse-grain dominated	Sediment with a silt/sand/gravel fabric that supports wave-propagation.
CRP	Common Reflection Point.
DGPS	Differential GPS.

FBA	Freshwater Biological Association.
FFID	Field file identification number.
G-S	Grain-sliding (theory).
Gyttja	Organic detritus silt.
Late-glacial	During and after the retreat of the BIIS, before the Holocene.
LGM	Last Glacial Maximum.
MCS	Multi-channel seismic.
MVA	Migration Velocity Analysis.
Over-consolidated	In shallow unconsolidated sediment environments this term is used to refer to previously unconsolidated fine-grained–clay sediments that have become drained probably through burial, and have significantly increased elastic moduli (e.g. Richardson and Briggs, 1993). Such sediments are difficult to deform by hand as opposed to unconsolidated sediment.
Overdeepening	Eroded below asymptotic fluvial erosion.
Phi (ϕ)	Logarithmic grain size scale representing grain diameter. Each unit is equal to one Udden-Wentworth grade (Wentworth, 1922).
Post-glacial	Holocene.
Precise	Measurements/estimations with an acceptable degree of spread (e.g. with a small 95% confidence interval).
PSDM	Prestack depth migration.
Q	Quality factor.
Q$_{SR}$	Quality factor produced by the spectral ratio technique.
Reliable	Capable of yielding the same or compatible results in

	different experiments. Can be depended upon with confident certainty.
RMO	Residual move-out.
RTK–GPS	Real Time Kinematic GPS.
SAX99 data	Data from the Sediment Acoustics Experiment 09 (Thorsos et al., 2001).
Sandy-clay	Clay dominated sediment with some sand.
Sandy-silt	Silt dominated sediment with some sand.
Shallow sediments	Sediments no deeper than 50 m below the seabed.
Silty-clay	Clay dominated sediment with some silt.
Silty-sand	Sand dominated sediment with some silt.
S/N	Signal–to–Noise ratio.
SSP	Spectral signature plot.
SSS	Seismic Sequence Stratigraphy (following Eyles and Mullins (1997)).
Sub-horizontal	A reflection nearly horizontal in time.
TY data	Data from Turgut and Yamamoto (1990) .
Unconsolidated	Sediment with little or negligible shear modulus. Easily deformed by hand.
W13	32.77 ms long Chirp sweep (1.5–13 kHz).
W32	16.38 ms Chirp sweep (1.5–13 kHz).
YD	Younger Dryas period of ice re-advance (11.55 – 12.80 ka cal BP).

Chapter 1

Introduction

1.1 Rationale

If compressional-wave properties within the shallowest 100 m of unconsolidated marine sediment could be obtained remotely using high-resolution seismic reflection data, these properties could be obtained over large areas relatively quickly and cheaply in comparison to coring the sediments or placing instruments in-situ. There would be near-perfect coupling at the seawater interface, and the observations are repeatable because they are non-destructive to the sediments and their *in situ* properties. This is in contrast to intrusive methods that suffer from random coupling losses, high variability due to scattering from local inclusions at spot locations (e.g. anomalous shells and pebbles), and possible fluctuations in arrival amplitudes after repeated observations at the same location, due to the slow evolution of the microscopic arrangements of the sediment grains (Buckingham, 2000).

Much effort has been expended on laboratory studies of unconsolidated marine sediments, but aside from the use in theoretical studies, the only utility in knowing their acoustic and physical properties in the laboratory is if these can be used to predict the same properties for the *in situ* conditions (Hamilton and Bachman, 1982). Ultimately, predictive capability will depend on establishing what *in situ* properties are significant and then to measure those properties to the necessary accuracy (Kibblewhite, 1989).

If remote acoustic properties such as compressional-wave attenuation (inversely proportional to quality factor) and seismic velocity can be accurately and precisely estimated from high-resolution seismic reflection data, and then related to sediment physical properties (such as mean grain size, density, porosity, and vertical extent), they would provide another dimension to aid high-resolution seismic inter-

pretation and derive cost-effectively valuable information for offshore industries in construction, drilling, aggregate dredging, etc.

The objectives of this thesis are primarily to develop methods for accurately and precisely measuring quality factor and seismic velocity within shallow sediments, using high-resolution seismic sources and towed multi-channel receivers. The secondary objectives are to test the inversion of these acoustic properties into physical sediment properties that can be used to differentiate between sediment types in the Solent, and to use the quantitative information to improve characterisation of unknown sediments and deposits in a structurally complex environment in order to enhance interpretation. The structurally complex environment is provided by the preserved glacial paleo-landscape buried beneath sedimentation in lake Windermere. The removal of the British and Irish Ice sheet after the last glacial maximum is currently a highly debated topic (e.g. Bradwell et al., 2008), hence, superior seismic interpretation of glacial deposits is of great importance here, to help justify their proposed genesis and character of ice-removal at the time.

1.2 Synopsis

This section summarises the contents of each chapter, and the appendices in brief:

Chapter 2 introduces the relationship between quality factor and velocity dispersion, and reviews the results from experiments that have intrusively measured compressional-wave velocity and attenuation within *in situ* unconsolidated marine sediments, and the current wave propagation theories that have attempted to fit them. Due to the lack of a single conclusive wave propagation model and their limited use in a range of sediments, empirical models from the literature are summarised and discussed for the use in this thesis.

Chapter 3 describes the spectral-ratio technique used to determine sediment quality factor remotely, using high-resolution seismic reflection data. The effectiveness within different types of sediment is examined by demonstrating the technique over three sediment packages of known grain size in the Solent. The usefulness of

quality factor as a tool to predict dominant sediment fabric is discussed. This chapter appears in its published form with a shortened introduction to avoid unnecessary repetition of wave-propagation theory in the previous chapters of this thesis.

Chapter 4 details the collection of multi-channel seismic data over two locations in the Solent, where a core and seabed grab were obtained to ground-truth the experiment. The depth migration methodology is explained, which uses iterative Kirchhoff prestack depth migration to determine the seismic velocity within the sediments. The sediment seismic velocities are used to predict saturated bulk density, porosity, and grain size using empirical models from the literature. The predictions are compared to the results from laboratory analyses on the sediments. These predictions are combined with remote estimations of quality factor to determine unconsolidated coarse-grain dominated sediment from over-consolidated clay dominated sediment, before the seismic velocity predictions refine the sediment types.

Chapter 5 introduces lake Windermere and the aims of the Windermere investigation. Previous sediment and geophysical investigations are summarised and the acquisition of our single channel and multi-channel high-resolution seismic data are detailed. Problems relating to the complex depth profile of the multi-channel streamer in fresh water are resolved by using the lake-surface ghost recorded at each channel. This was required for correct depth migration of the multi-channel seismic data. The processing steps required to clean the migrated data are demonstrated and the kriging method used to produce surface maps of sequence horizons is explained.

Chapter 6 presents depth migrations of six high-resolution seismic reflection profiles over Windermere and identifies five distinct seismic stratigraphic sequences based upon seismic velocity, geomorphology, and seismic character. The sizes and shapes of complex glacial retreat structures can be resolved from the data, and signify active glacial ice-retreat from Windermere, which is contrary to the previous held theory of rapid downwasting of the British and Irish Ice sheet in the region

after the last glacial maximum.

Chapter 7 reviews the effectiveness of high-resolution seismic reflection data for determining sediment acoustic and physical properties, and summarises the important outcomes of this work. Recommendations for further work are made that include the development of empirical models and a method for measuring velocity dispersion.

There are four appendices that accompany some of the content in these chapters: **Appendix A** describes the implementation of iterative reweighted robust least-squares regression used for determining quality factor from spectral ratios; **Appendix B** discusses the importance of using the correct method to derive a mean grain size of a sediment when it is the 3D size that is important to the research; **Appendix C** contains photos of the core sections and grain size analysis results from the core studied in Chapter 4; **Appendix D** discusses the thermocline within Windermere that was present during the survey and the expected fresh water seismic velocity.

Chapter 2

Sediment Acoustic Models

2.1 Attenuation and Velocity Dispersion

As seismic waves propagate they are attenuated in ways that are characteristic of the media, with energy being lost through intrinsic attenuation and scattering. The main wave-propagation theories within unconsolidated marine sediments dispute the dissipation mechanisms that generate intrinsic attenuation and often hold scattering accountable for deviations from model estimations in the field. They often investigate velocity dispersion because this is an indicator of how attenuation is dependent upon frequency, and what dissipation mechanisms are in effect.

The relationship between attenuation and velocity can be demonstrated by assuming that we have attenuation data over a range of frequencies and a velocity measurement at a reference frequency. Integrating the attenuation data will lead to a theoretical estimate of the corresponding velocity at chosen frequencies using an approximate form of the Kramers-Kronig relations (a real application of this is shown in Turgut and Yamamoto, 1990):

$$\frac{dV(f)}{V(f)} = \frac{Q^{-1}(f)}{f}\, df. \tag{2.1}$$

Here V is velocity and Q^{-1} represents the attenuation as the reciprocal of the quality factor (Q) at a particular frequency f. Integrating from a reference frequency f_0 to f, where the velocity V_0 at the reference frequency is known, we obtain

$$V(f) = V_0\, exp\,(\frac{1}{\pi} \int_{f_0}^{f} \frac{Q^{-1}(f)}{f}\, df) \quad . \tag{2.2}$$

By integrating Equation (2.1) without limits, and in terms of $Q(f)$ (where k and C are constants),

$$ln\,V + k = \frac{1}{Q(f)}\,ln\,f, \tag{2.3}$$

$$ln\,CV = ln\,f^{\frac{1}{Q(f)}}, \tag{2.4}$$

it can be shown that $Q(f)$ and V have the following relationship:

$$Q(f) \longrightarrow \infty \quad \Rightarrow \quad \frac{dV(f)}{V(f)} \longrightarrow 0 \tag{2.5}$$

Therefore, within sediments that exhibit near-linear scaling of attenuation with frequency there will be near-logarithmic velocity dispersion, and as the Q of sediments increase velocity dispersion will become less pronounced. Consequently, velocity dispersion is difficult to detect if present, and has lead to investigators such as Hamilton (1972) to claim that velocity dispersion is very weak or absent in water saturated sediments. However, velocity measurements from two recent and comprehensive studies within sandy homogeneous sediments, the Sediment Acoustics Experiment of 1999 (SAX99— Thorsos et al., 2001) and the crosshole tomography experiments of Turgut and Yamamoto (TY— Turgut and Yamamoto, 1990), both suggest that there are low and high frequency asymptotic values in velocity dispersion and a transition region between 1 kHz and 10 kHz (Figure 2.1a and Figure 2.1c). Within the measured data from SAX99, velocity increases from c. 1620 m/s at 0.2 kHz to c. 1750 m/s at 10 kHz, and the attenuation data at 4 kHz corresponds to a Q of c. 30 for the sandy sediment. Within the TY data velocity dispersion is even more significant in sandy sediment over a shorter frequency range: velocity increases from c. 1580 m/s at 2 kHz to c. 1740 m/s at 10 kHz. This greater velocity dispersion is associated with higher, significantly non-linear attenuation, which corresponds to a Q of c. 10 at 4 kHz.

This transition region for velocity dispersion and attenuation is essentially the experimental frequency range of our high-resolution sonar systems (c. 0.2–8.0 kHz). Therefore, good precision in velocity estimation could be made difficult in sediments that have a low Q, and *having* to assume any particular type of attenuation dependence upon frequency when estimating Q is clearly not appropriate.

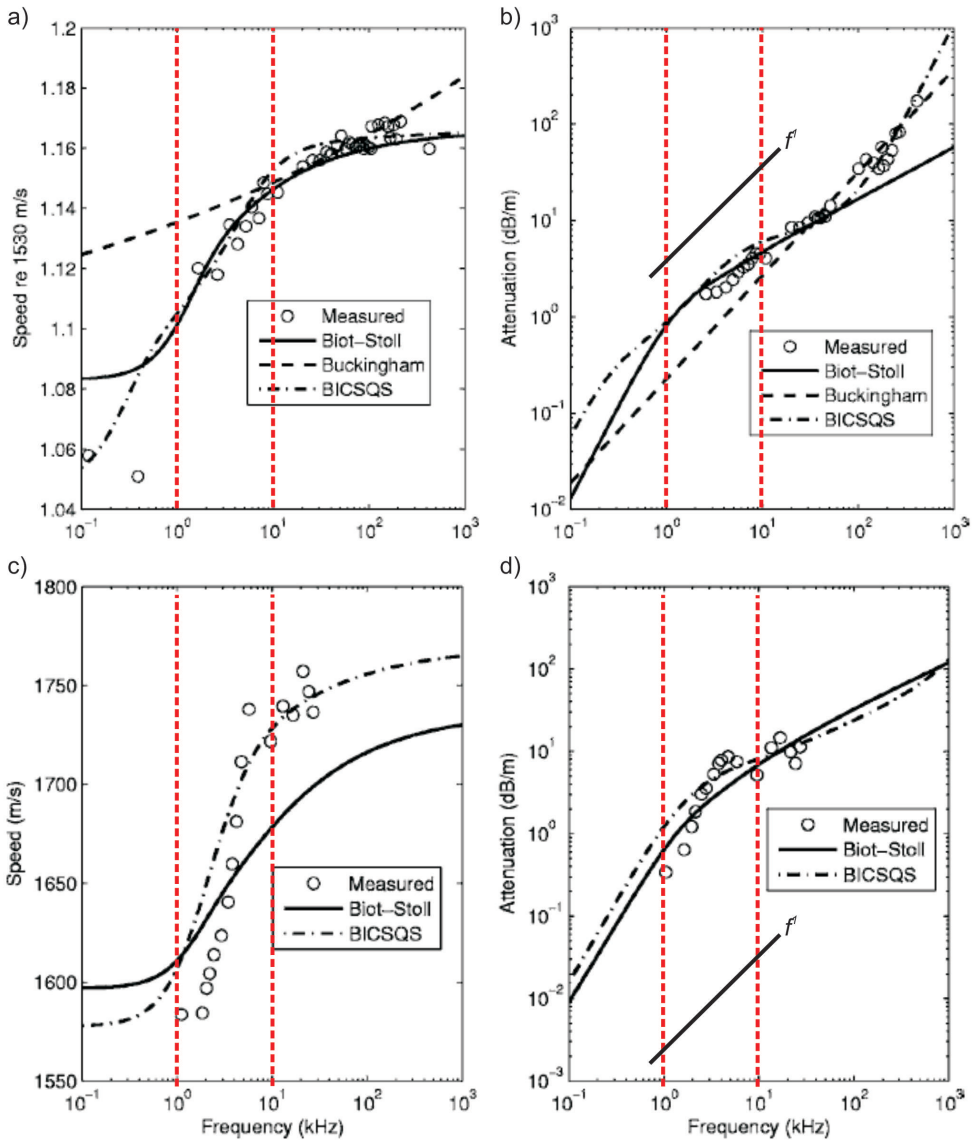

Figure 2.1: Vertical red dotted lines contain the region from 1 kHz to 10 kHz and is essentially the experimental frequency range of our high-resolution seismic sources. Diagrams are adapted from Buchanan (2006): a) SAX99 compressional-wave speed relative to 1530 m/s vs. frequency; b) SAX99 compressional-wave attenuation vs. frequency; c) TY compressional-wave speed vs. frequency; d) TY compressional-wave attenuation vs. frequency. Various models attempt to fit the data.

2.2 Theoretical Sediment Models

Acoustic wave-propagation theory in porous media was presented by Biot more than 50 years ago (Biot, 1956a,b). Today Biot theory still provides the basis for one of the two main competing wave-propagation theories in saturated, unconsolidated marine sediments. Biot-Stoll theory (Biot, 1956a,b; Stoll, 1974) considers unconsolidated sediment as a poro-elastic medium with an elastic frame (allowing it to support a shear wave) and interstitial pore fluid, asserting that the elastic moduli of an uncemented sediment are effectively zero at zero effective stress (e.g. at the surface) and that attenuation is controlled by fluid flow. It predicts that two dissipation mechanisms occur simultaneously: the primary through viscous losses associated with the relative movement of the pore fluid through the mineral frame, and the secondary through frictional losses at grain-to-grain contacts. The Biot-Stoll model exhibits a marked velocity dispersion and a non-linear scaling of attenuation with frequency that has a transition from low to high asymptotic values between 50 Hz to 10 kHz—i.e., it predicts that Q varies strongly with frequency (Equation (3.1)) in this frequency range. This is where the effects of fluid motion relative to the mineral frame would be most pronounced, particularly in coarser granular sediment (Stoll, 2002). The observations from the SAX99 and the TY datasets are generally in agreement with the Biot-Stoll model (see Buchanan, 2006), however, it is unable to match the observed frequency dependence of sound speed and attenuation above 10 kHz from SAX99, and underestimates the magnitude of the observed sound speed dispersion in the TY data (Figure 2.1).

The "Biot model with grain contact squirt flow and shear drag" (BICSQS) (Chotiros and Isakson, 2004) is the foremost extension to Biot-Stoll theory. It incorporates a developed form of squirt flow theory (Dvorkin and Nur, 1993), which replaces the dry frame assumption and takes into account the movement of fluid between the grain-to-grain surfaces. The BICSQS produces the most superior fits for compressional-wave speed and attenuation to the SAX99 and TY sediment observations: it provides a better fit to the lower frequency observations in wave speed, and the greater attenuation at higher frequencies in the SAX99 data; and can attain the degree of velocity dispersion exhibited by the TY data (Figure 2.1).

Alternatively, there is grain-sliding (G-S) theory (Buckingham, 2000) that assumes the grains in an unconsolidated sediment are unbounded and do not form a macroscopic elastic frame. The primary forces arise from grain-to-grain interactions, which provides the rigidity to support a shear wave, and attenuation is derived from microscopic frictional losses. The absence of viscous flow means that predicted wave properties are independent of permeability and tortuosity. The macroscopic governing physical properties are instead grain size, porosity and overburden pressure. Energy is lost when a velocity gradient across grain contacts forces micro-asperities separated by a very thin film of interstitial fluid to slip past each other, until the viscosity of the lubricating fluid film increases enough for the system to come to rest (strain hardening). The G-S model predicts a near-linear scaling of compressional-wave attenuation with frequency in granular unconsolidated sediments (i.e., Q is approximately constant), and a wave speed that is only logarithmically dispersive with respect to frequency. This fits observations from the SAX99 data very well above 10 kHz (Figure 2.1a and 2.1b), and is in accord with other observations in a range of sediments, from both low-frequency seismic surveys and high-frequency laboratory studies (e.g., Hamilton, 1972; Bowles, 1997; Simpson and Houston, 2000; Williams et al., 2002; Simpson et al., 2003). Figures 2.2a and 2.2b demonstrate this near-linear dependence of attenuation on frequency observed when attenuation measurements are compiled from a range of studies, for sands and fine-grained sediments respectively. Note the lack of observations within our experimental frequency range (c. 0.2–8.0 kHz).

During Acoustics'08 Paris conference the BICSQS model was presented with a correction that accounted for viscous drag within the grain-contact fluids at higher frequencies (Chotiros and Isakson, 2008), and the G-S model was updated to become the VGS model that takes account of the effective viscosity of the thin layer of pore fluid between grains, which limits the degree of strain hardening that can occur below 10 kHz (Buckingham, 2008). The resulting sound speed and attenuation curves from both these models now virtually match the observations from SAX99.

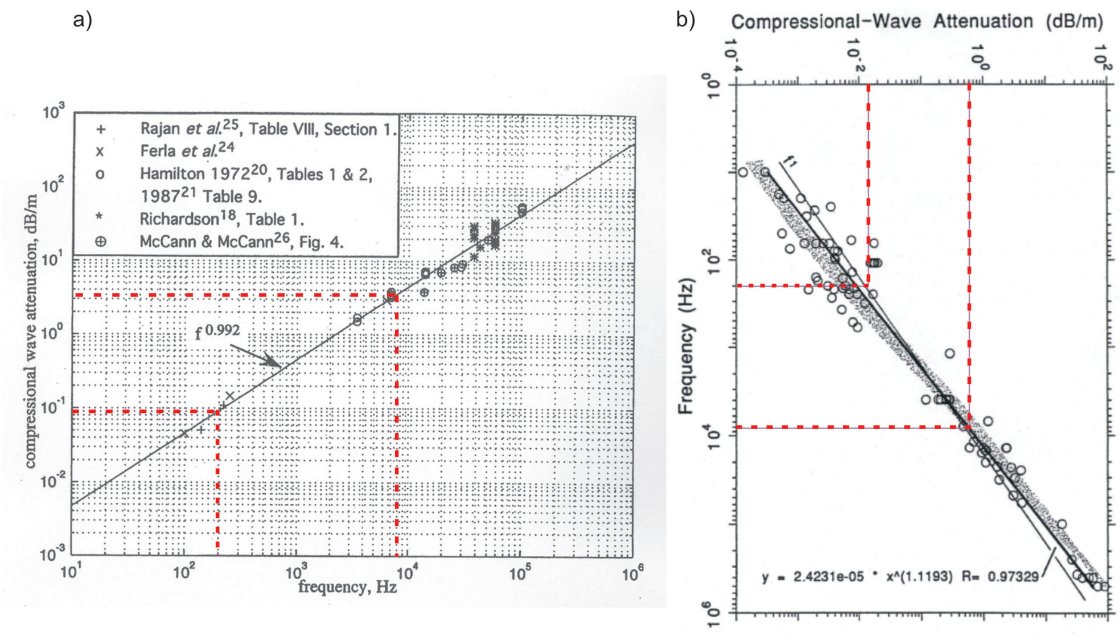

Figure 2.2: Diagrams showing compressional-wave attenuation against frequency: a) In unconsolidated sands (Buckingham, 2000); b) In unconsolidated fine-grained sediments (Bowles, 1997). The red dashed lines show the experimental frequency range of the high-resolution seismic sources used in this thesis.

2.3 Empirical Sediment Models

Empirical models have significant advantages over theoretical models: there are no difficult–impossible to measure parameters (e.g. pore size, tortuosity, grain roughness, frame modulus), and they are constructed from naturally occurring sediments (Jackson and Richardson, 2007).

Numerous investigations have produced regressions between the acoustic and physical properties of unconsolidated marine sediments for specific environments (e.g. Buchan et al., 1972). This limits their applicability. I have chosen to use the regression models from Hamilton and Bachman (1982) and Richardson and Briggs (1993) in this thesis because they are based on large compilations of data from a range of environments, and use relatively strict collection and measurement methods.

Hamilton and Bachman (1982) produced empirical regression equations for three general environments: continental terrace (shelf and slope), abyssal hill, and abyssal plain. By separating the measured properties into the environments the sediments were deposited in, they eliminated the issues of different sedimentation regimes, sediment composition, and sediment compaction. Richardson and Briggs (1993) produced regressions whereby the regression coefficients are multiplied by the seismic velocity of the water in the particular environment of interest.

Historically, the regressions from Hamilton and Bachman (1982) are the most widely used, however, it has been reported that these yield consistently higher sound speeds; the cause is unclear, but it follows that the regressions from Richardson and Briggs (1993) are now preferred, especially when using remote classification systems (Jackson and Richardson, 2007).

Figure 2.3 compares the regressions of velocity on saturated bulk density and porosity for the continental shelf environment from Hamilton and Bachman (1982), and for a water seismic velocity of 1500 m/s from Richardson and Briggs (1993). The relationship between saturated bulk density and velocity is similar to porosity and velocity, because of the linear relationship between saturated bulk density and porosity (Hamilton and Bachman, 1982). Generally, velocity increases as porosity reduces because the sediment fabrics change from being predominantly clay

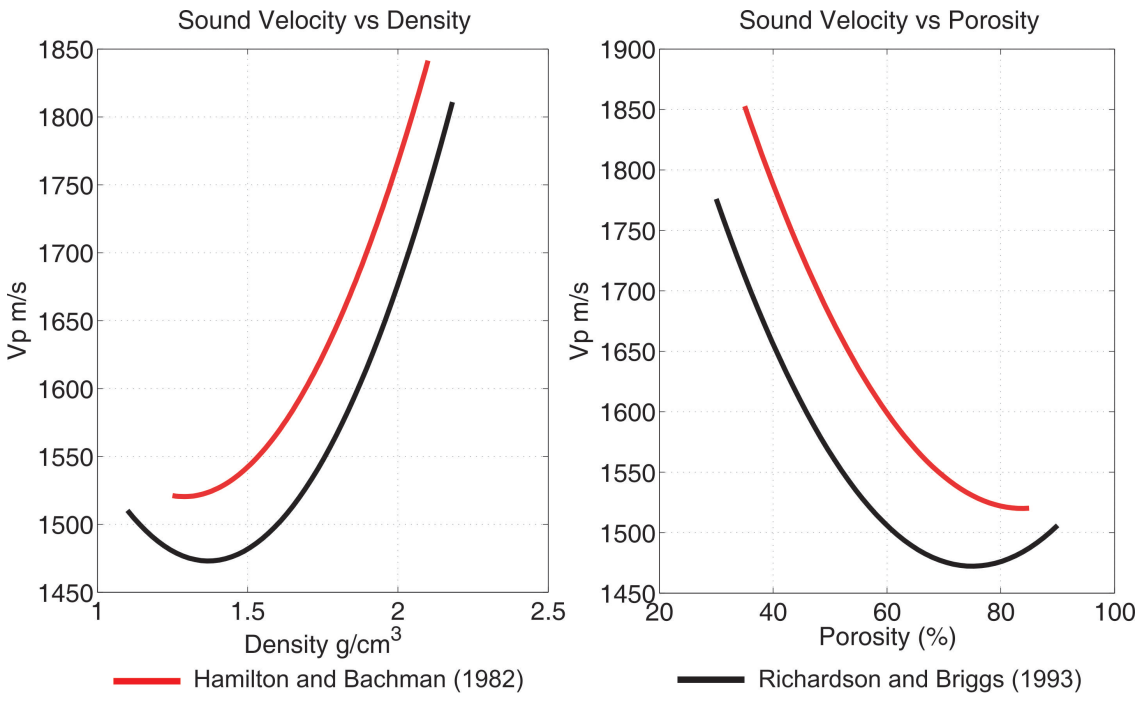

Figure 2.3: Empirical regression models of velocity vs. saturated bulk density and porosity.

dominated to coarse-grain dominated; the increasing amounts of coarse-grain (i.e., silt-size and sand-size) particles relative to clay particles produces an increasing contribution to the elastic moduli (McCann and McCann, 1990). However, this does not hold true near the velocity minima, which are lower than the assumed water velocities within the models. This is known as the "low-velocity effect" and occurs in muddy sediments at high porosities. The increase in sediment density and reduction in porosity, produced from the introduction of more coarse-grained sediment, is not immediately met with corresponding increases in the frame elastic moduli, which is still dominated by the clay-fabric (Hamilton and Bachman, 1982; McCann and McCann, 1990; Jackson and Richardson, 2007).

The relationship between compressional-wave attenuation data and sediment mean grain size is often found in the literature, even-though most workers conclude that there is very little predictive value in this relationship or none at all (e.g. Buchan et al., 1972; Akal, 1972; Jackson and Richardson, 2007). Stevenson et al. (2002) represented attenuation as Q and produced a model of this against mean grain size to help show that sediments with very low Q are indicative of highly

attenuating poorly sorted gravel deposits.

Figure 2.4 shows the relationship between Q and sediment mean grain size, based on the classic experimental data from Shumway (1960) and Hamilton (1972), where careful measurements were carried out on a range of sediments from the San Diego area. The primary function of this new model is to locate regions where changes in the dominant attenuating mechanism take place. The advantage of representing attenuation as Q here, is that it enhances the resolution about the sediment mean grain size of 6 ϕ (where $\phi = -\log_2(\text{mm})$). Here, sediment changes from having a coarse-grain dominated fabric to a clay dominated fabric that suspends coarser grains within its matrix (McCann and McCann, 1969). This evidently results in a significant increase in the Q for grain sizes between 6 ϕ and 9+ ϕ, which is most-likely a result of the active attenuation mechanisms being suppressed. Applying G-S theory to the scenario would suggest that the reduced attenuation is caused by insufficient grain-to-grain interaction. Applying Biot theory suggests that the

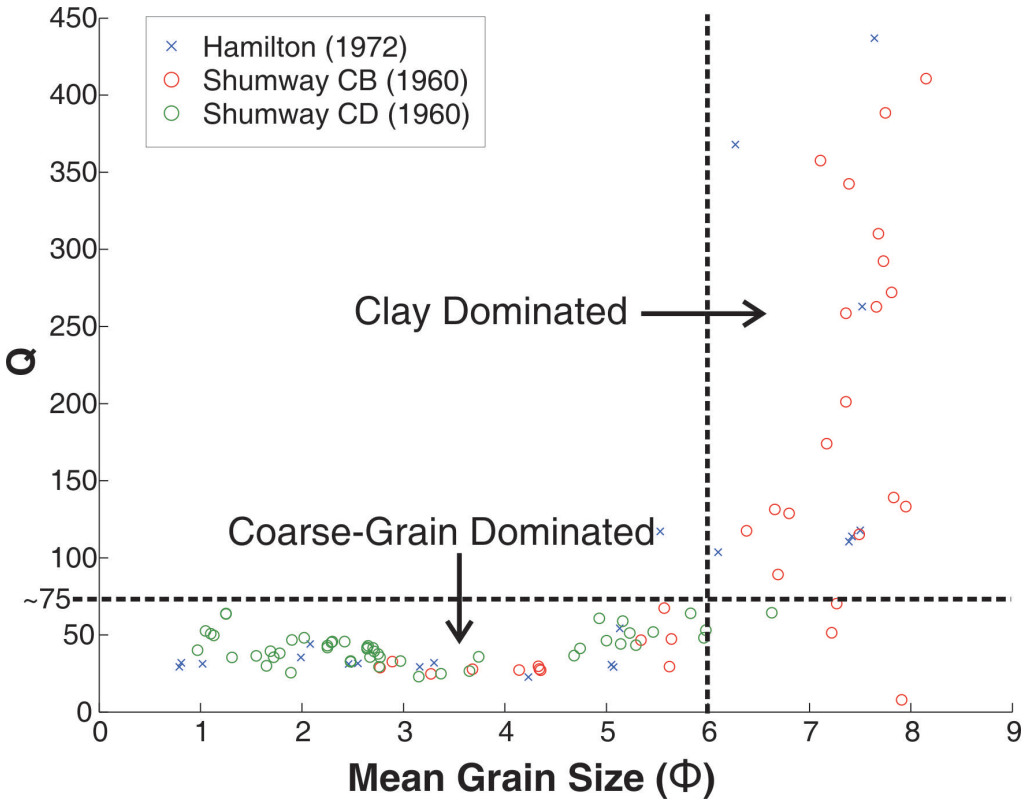

Figure 2.4: Q vs. mean grain size (ϕ) of sediments from the San Diego area (from Tables 1 and 2 in Hamilton, 1972; Shumway, 1960). Dashed lines divide the figure into a coarse-grain dominated zone and a clay dominated zone.

velocity of the propagating wave is dominated by the bulk moduli of the mineral and fluid components, and is hardly affected by the small shear and frame bulk modulus of the clay fabric. These small moduli though, will ensure that the clay framework and the fluid move almost in phase as the wave propagates, meaning that there would be very little differential velocity to cause viscous dissipation.

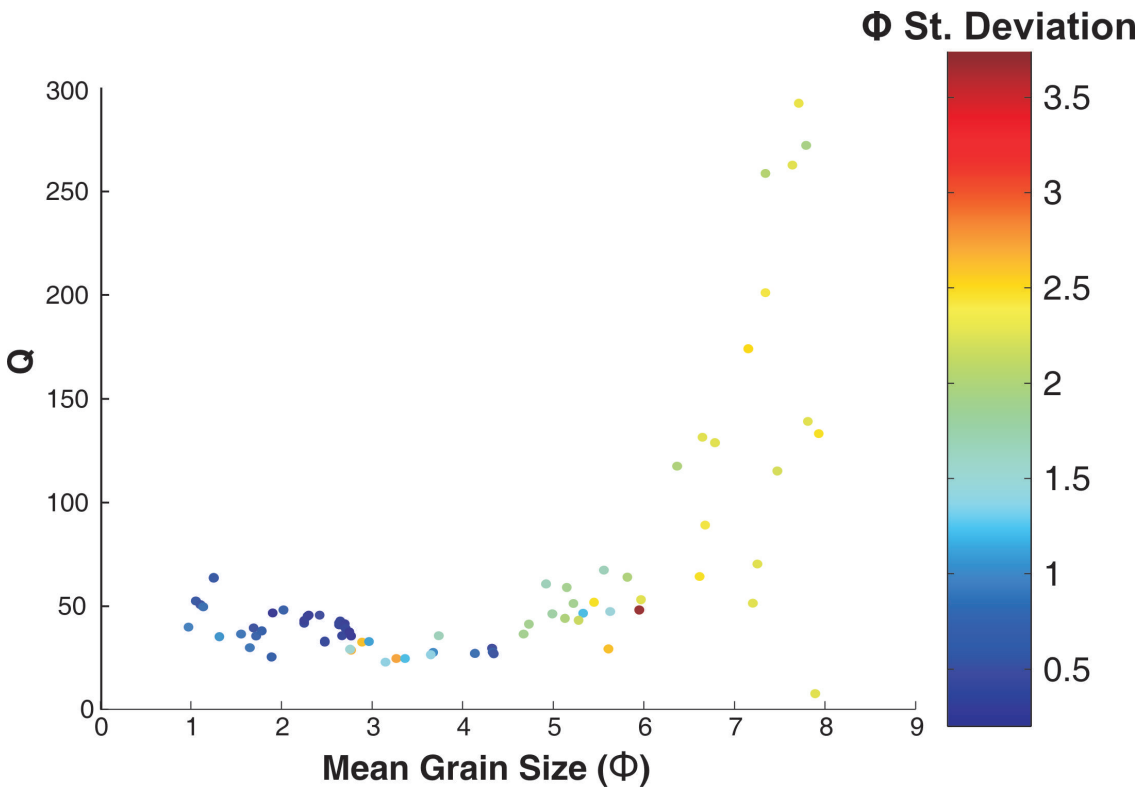

Figure 2.5: Q vs. mean grain size (ϕ) with ϕ standard deviation colour scale, from sediments in the San Diego area (data from Shumway, 1960).

Another observation is that the lowest Q values are consistently present between a mean grain size of 3 ϕ and 4 ϕ. This reduction in Q could be associated with the poorer sorting of the sediments compared with the mean grain sizes of 1–2 ϕ (Figure 2.5). Attenuation in poorly sorted sediments has not been as thoroughly studied as more homogeneous sediments, however, they have recently become important to authors investigating the effects of squirt flow attenuation (e.g. Best et al., 2001).

Applying Biot theory to this scenario fails because poorer sorted sediment should have reduced permeability, which would suppress viscous flow attenuation, and hence increase Q. However, in poorly sorted sediments there should be an abundance

of compliance heterogeneities (at the contacts of compliant irregularly shaped clay flocs and non-compliant stiff silt/sand grains), which would provide the compliant, water saturated pores necessary for squirt flow to become a significant mechanism of attenuation. Best et al. (2001) conclude that squirt flow attenuation is at its greatest when the mass ratio of compliant to non-compliant minerals is close to unity; this is generally in agreement with the location of the lowest Q values between 3 ϕ and 4 ϕ on Figure 2.5, hence squirt flow is most-likely the dominant attenuation mechanism at this point.

2.4 Conclusions

Measurements of velocity dispersion and attenuation from the literature, for a wide range of unconsolidated marine sediment types, often reveal that velocity dispersion is small (logarithmic) and that attenuation scales with the first power of frequency (e.g. Hamilton, 1972). Biot based wave-propagation theories claim that there must be more complex dependencies with frequency, and draw upon recent comprehensive studies within sandy sediments, where a transition zone between 1 kHz and 10 kHz exhibits substantial velocity dispersion and a non-linear dependence of attenuation on frequency. This frequency range encompasses the range of our high-resolution seismic sonar, hence a method of estimating attenuation must be developed that does not first require assumptions on how attenuation scales with frequency.

We are fortunate to have two very different theories that fit these same comprehensive experiments in sandy sediments; we are unfortunate that the governing parameters of wave-propagation in unconsolidated marine sediments are still ambiguous. There is no doubt that Biot based theory works in fused structures (Berryman, 1980). However, that unconsolidated sediment does not have a perfect elastic frame is an elementary observation at high strain levels (Figure 2.6). Because of this assumption and the independence from permeability and tortuosity, I favour the representation of unconsolidated sediment in grain-sliding theory (Buckingham, 2000), where its governing parameters imply that wave-properties are sensitive to grain size and depth (overburden pressure). These do not explicitly occur in Biot-Stoll theory and makes grain-sliding theory more readily applicable to *in situ* acoustic measurements, from a larger range of sediment types and depths in the field. Nevertheless, it seems preferable to avoid predicting sediment physical properties from acoustic measurements using wave-propagation theories, especially as homogeneous sand deposits will not be under investigation.

Acoustic measurements in this thesis shall be related to physical properties using the discussed empirical models from the literature. These are useful prediction tools (Buckingham, 2005) and contain some degree of flexibility to better represent the environment in which the acoustic measurements were acquired. It is important to have an understanding of the wave-propagation theories though, so that the

dominant fabrics that support wave propagation in the sediments can be discussed.

The observations of quality factor (Q) as a function of mean grain size suggests potential uses for discriminating between dominant sediment fabrics via attributing high Q values to sediments with a clay dominated fabric (6–9+ ϕ), low Q values to sediments with a coarse-grain dominated fabrics (0–6 ϕ), and the lowest Q values to highly compliant, poorly sorted sediments. Hence, where it is possible, a representation of the sorting will be shown for the sediments in this thesis.

Figure 2.6: Biot theory: "developed for the propagation of stress waves in a porous *elastic* solid..." — M. A. Biot, 1956.

Chapter 3

Estimating the Q of Solent Sediments

---

[1] *In this chapter I present the published work on how to estimate Q from high-resolution seismic data, and the results from comparing Q with mean grain size for sediments in the Solent (U.K.).* ***This paper received honourable mention for Best Paper in Geophysics in 2008.***

3.1 Introduction

Previous studies have used high-resolution Chirp sources to estimate compressional-wave attenuation in near-surface sediments remotely (LeBlanc et al., 1992; Stevenson et al., 2002; Schock, 2004a,b). LeBlanc et al. (1992) developed an attenuation-based classification model that relates the relaxation time of sediments to the shift in instantaneous frequency of the seismic signal. Stevenson et al. (2002) developed this method by estimating the instantaneous frequency shift only from maximum amplitudes (i.e., from interpolating between seabed and sub-bottom interface reflections). Their analyses assume a linear scaling of compressional-wave attenuation with frequency and require a specific chirped pulse that will remain zero phase before and after dispersion and attenuation (LeBlanc et al., 1992). Williams et al.

[1] Chapter published as (author list reflective of relative contributions): Estimating quality factor and mean grain size of sediments from high-resolution marine seismic data, Luke J. W. Pinson, Timothy J. Henstock, Justin K. Dix, Jonathan M. Bull, Geophysics, 73(4), G19–G28, 2008.

(2002) and Schock (2004a) use a spectral-ratio method on maximum amplitudes to approximate the compressional-wave attenuation for an input of the first iteration of an inversion based on the Biot model (Biot, 1956a,b). The scaling of compressional-wave attenuation is near-linear with frequency between 4 kHz and 8 kHz (Schock, 2004a). The data of Williams et al. (2002), who use a range of additional methods from SAX99, arguably show the same relationship between 2 kHz and 400 kHz. Schock (2004a) speculates that an increasing scattering attenuation counters the decreasing intrinsic attenuation predicted by the Biot model, whereas Williams et al. (2002) additionally suggest that a combination of Biot and G-S theory is possible.

Scattering produces frequency-dependent attenuation (O'Doherty and Anstey, 1971; Hosken et al., 1992; Muller and Shapiro, 2004). Multiple backscattering is a function of the vertical correlation between scatterers relative to the seismic wavelength (Shapiro and Hubral, 1999). Random diffraction and refraction effects are functions of the finite horizontal extent of inhomogeneities relative to the Fresnel zone of the incident wave (Muller and Shapiro, 2004). Scattering sedimentary layers can be identified within high-resolution seismic data and rejected for further quantitative examination (e.g. Schock, 2004a). We use this approach because our interest lies in determining the sediment physical properties that relate to intrinsic attenuation, rather than the sediment package structures that cause scattering attenuation.

We accept that the relationship between frequency and compressional-wave attenuation is still ambiguous, and we will not constrain ourselves with assumptions required for a full sediment-model inversion. Instead, we evaluate how attenuation varies with frequency within unconsolidated marine sediments using our high-resolution (broadband) seismic reflection sonar systems (c. 0.5–8.0 kHz). We use an adaptation of the spectral-ratio method (Båth, 1974) and do not require assumptions on how compressional-wave attenuation varies with frequency. We identify trends in attenuation with frequency within the spectral-ratios, and assign a quality factor (Q_{SR}) to them by fitting a curve using iteratively reweighted robust least-squares regression. In this study, we demonstrate repeatable significant Q_{SR}

fits with 95% confidence intervals of approximately ±10 within known unconsolidated sediments from the Solent (U.K.). We also combine data from separate Boomer and Chirp high-resolution sources over the same location to observe Q_{SR} over more than an order of magnitude variation in frequency, or more than four octaves. We have chosen three unconsolidated sediment packages to demonstrate that fewer observations are required to achieve our desired level of confidence in Q_{SR} for higher-attenuating coarse-grain dominated sediments, than for lower-attenuating clays. We assess our results by relating the Q_{SR} of our Solent sediments to their known mean grain sizes using an existing empirical model.

3.2 Spectral-Ratio Calculation

The spectral-ratio method (Båth, 1974; Jannsen et al., 1985) has been adapted here for the application to seismic reflection data so that compressional-wave attenuation is measured explicitly as a function of two-way time, as opposed to distance and velocity. Within the seismic reflection data, we require a sub-bottom sub-horizontal reflection that forms the lower boundary of a laterally consistent sediment package beneath the seabed. We assume that within our experimental frequency range (c. 0.2–8.0 kHz), spherical divergence and reflection coefficients are independent of frequency.

Allowing both the compressional-wave attenuation coefficient $\alpha(f)$ and the quality factor $Q(f)$ to be functions of frequency f, their relationship is defined as

$$\alpha(f) = \frac{\pi \cdot f}{c(f) \cdot Q(f)} = \frac{\pi \cdot f \cdot \Delta t(f)}{X \cdot Q(f)} \quad , \tag{3.1}$$

where $c(f)$ is the phase velocity, $\Delta t(f)$ the two-way time and X the distance travelled within the attenuating medium. By attenuating the unknown amplitude $A_0(f)$, emitted from a seismic source at distance and time zero, the amplitude of the seabed reflection $A_S(f)$ for some frequency, at sonar–seabed depth X_S, and seawater attenuation $\alpha_S(f)$, is given as

$$|A_S(f)| = |A_0(f) \cdot G_S \cdot R_S| \cdot exp\,(-2 \cdot \alpha_S(f) \cdot X_S) \quad , \tag{3.2}$$

assuming that R_S, the unknown seabed reflection coefficient, and G_S, the unknown spherical divergence within the water column, are independent of frequency.

Similarly, where R_R, the unknown reflection coefficient from a sub-bottom interface, and G_R, the unknown spherical divergence beneath the seabed, are independent of frequency, the amplitude of the reflection from the sub-bottom interface $A_R(f)$ for some frequency at sub-bottom depth X_R, and sediment attenuation $\alpha_R(f)$, is given as

$$|A_R(f)| = |A_0(f) \cdot G_S \cdot G_R \cdot (1 - R_S^2) \cdot R_R| \cdot exp\,(-2 \cdot \alpha_S(f) \cdot X_S) \cdot exp\,(-2 \cdot \alpha_R(f) \cdot X_R). \tag{3.3}$$

By assuming normal incidence, the two-way transmission coefficient across the seabed interface in Equation (3.3) is represented as $(1 - R_S^2)$. The unknown components $A_0(f)$, G_S, and all the unknown responses from the source and the receiver that have not been shown, can be eliminated by taking the ratio of $A_R(f)$ and $A_S(f)$:

$$\left|\frac{A_R(f)}{A_S(f)}\right| = \left|\frac{G_R \cdot (1 - R_S^2) \cdot R_R}{R_S}\right| \cdot exp\left(-2 \cdot \alpha_R(f) \cdot X_R\right) \quad . \tag{3.4}$$

By substituting for $\alpha_R(f)$ in Equation (3.4) using Equation (3.1) where $\Delta t_R(f)$ is the two-way time within the sediment, we obtain

$$\left|\frac{A_R(f)}{A_S(f)}\right| = \left|\frac{G_R \cdot (1 - R_S^2) \cdot R_R}{R_S}\right| \cdot exp\frac{-\pi \cdot f \cdot \Delta t_R(f)}{Q(f)} \quad . \tag{3.5}$$

Taking the natural log of Equation (3.5) gives

$$ln\left|\frac{A_R(f)}{A_S(f)}\right| = ln\left|\frac{G_R \cdot (1 - R_S^2) \cdot R_R}{R_S}\right| - \frac{\pi \cdot f \cdot \Delta t_R(f)}{Q(f)} \quad , \tag{3.6}$$

where all the unknown components have become separated from the measurable components and $Q(f)$. Unknown components G_R, R_S, and R_R can be assumed constant from trace to trace if the interfaces are sub-horizontal, seismic energy is normally incident upon them, and sediment properties are laterally consistent.

These conditions minimize energy losses through transmission losses (refraction and critical angles) and mode conversion, and preserve amplitudes generated by the two interfaces and the amount of spherical divergence that occurs between them. If we measure amplitudes reflected from isolated single planar interfaces, possible focusing effects from irregular interfaces and tuning effects with reflections from neighboring interfaces are removed, and we can assume that the unknown components are independent of frequency.

However, by causality, velocity dispersion occurs if attenuation is present in the propagation, which could cause the reflection coefficients to vary with frequency. According to the Kramers-Kronig relation, for a constant Q velocity dispersion is only logarithmic, and as long as Q remains greater than 20 there will be a change of

less than 5% in the seabed reflection coefficient, which we consider negligible. The lowest Q commonly encountered is that of coarse sands, which tends to be about 30 (Hamilton, 1972; Guigné et al., 1989; Stevenson et al., 2002). Considering a frequency-dependent Q_{SR}, the Biot model predicts a variation in R_S with frequency of no more than 5% within our experimental frequency range (Schock, 2004a), which we also consider negligible. Thus, by plotting the natural log of $|A_R(f)/A_S(f)|$ as a function of $\pi \cdot f \cdot \Delta t_R(f)$ and fitting an appropriate curve using least-squares regression, the relationship of $1/Q(f)$ with frequency can be assessed.

It is inconsequential whether $1/Q(f)$ is independent or dependent upon frequency as it is found by simply differentiating the curve. Equally, a straight line fit implies that a frequency-independent Q_{SR} is appropriate for the dataset. The precision in curve fitting can be improved by plotting the results from many traces taken over the same interfaces. Any linear variation in attenuation from small changes in sediment thickness between the sub-horizontal interfaces is accounted for by considering $\Delta t_R(f)$. Small changes in $\Delta t_R(f)$ also will incur equivalent changes in G_R, which combines with the other unknown frequency-independent constants to form the intercept of the curve. Variations in G_R are frequency independent; they produce only small changes in the value of the intercept that average out during the regression and do not affect gradients of the fitted curve.

3.3 High-Resolution Seismic Sources

The logarithmic dependence of attenuation with frequency requires a large frequency range in order to assess the relationship between the two. Hence, we use high-resolution seismic reflection data, and where possible, we combine data from Boomer and Chirp sources over the same location to produce an extended frequency range. Boomer sources consist of an insulated metal plate that is repelled explosively by a magnetic field. This motion generates a broadband pulse that peaks near 1 kHz and is repeatable (e.g. Simpkin and Davis, 1993). The effective power spectrum above −30 dB spans approximately 0.2–4.0 kHz (Figure 3.1a). Chirp profilers produce a digital, highly repeatable, broadband pulse, making such profilers ideal for qualitative and quantitative examination of the sub-seabed down to approximately 30 m (e.g., Schock and LeBlanc, 1990; Bull et al., 1998; Stevenson et al., 2002).

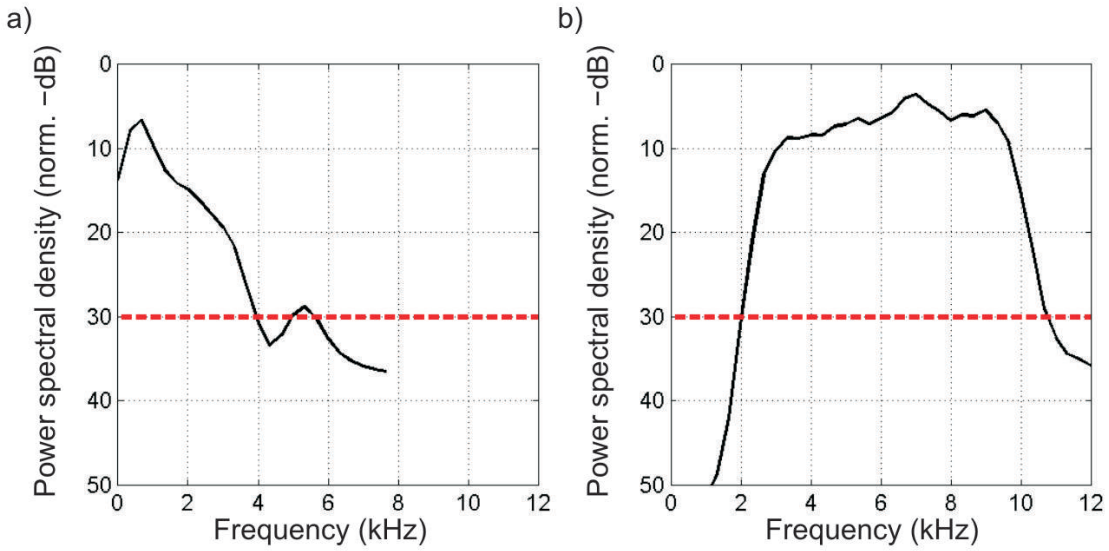

Figure 3.1: Source power spectra recovered from the seabed reflection at location A in this study, (a) Boomer and (b) Chirp. The power spectra are normalized and then smoothed over a 100-Hz window.

In this study, we calibrate our Chirp sonar to produce a linear sweep with a sine-squared taper function covering 1/8th of the time duration (Gutowski et al., 2002). The wide effective power spectrum exhibited by the Chirp source spans 2–11 kHz (Figure 3.1b) and facilitates improved vertical and spectral resolution over the

Boomer source. Therefore, by combining Boomer and Chirp data, attenuation can be measured over 4 octaves of frequency (e.g. 0.5–8.0 kHz) or more. Streamers are towed directly behind the sources. The streamer used with the Boomer source comprises seven hydrophone elements spaced across 1 m, and the streamer used with the Chirp source comprises eight hydrophone elements spaced across 1 m.

3.4 Spectral-Ratio Technique

3.4.1 Sediment Package Selection

We must adhere to the criteria established for Equation (3.6) when selecting suitable sediment packages to analyze. We require a consistent sub-horizontal sub-bottom reflector and a consistent sub-horizontal seabed reflection, both without any neighboring reflections within 1 to 2 ms, to avoid tuning effects. The target reflection must be shallower than the first seabed multiple, reducing the possibility of delayed energy affecting the spectra. Using multiple traces that sample the reflectors can improve curve fitting by averaging out noise and the effects of local inhomogeneities, provided that there is no lateral variation in the sediments. Including lateral variations will decrease the precision in the Q_{SR} assigned to a sediment package because attenuation, spherical divergence, and reflection coefficients may vary from trace to trace.

In this study, we examine three different sediment packages from the Solent, shown in Figure 3.2. The seabed and sub-bottom lithology is determined from a combination of core samples and investigations by West (1980) and Velegrakis (2000). The mean grain size is reported as ϕ, which is a logarithmic scale representing grain diameter (mm) ($\phi = -\log_2(\text{mm})$). The sorting is represented as the range from the mean ϕ to the 16^{th} and 84^{th} percentile of the grain size distribution.

The sediment package at location A (Figure 3.3a and 3.3b) consists of a thin layer of gravel dunes approximately 1–2 m thick, overlying the Bembridge Marls formation (silty-clays), which have a mean grain size and sorting of 7.7 ϕ ($+1.3$; -3.1), determined from standard nomenclature analysis of a 17-m core (Dean, 1995). Three surveys were carried out over the sediment package at location A: southwest–northeast Chirp survey in tidal flow direction (750 traces); northeast–southwest Chirp survey against tidal flow direction (1250 traces); and a single Boomer survey (125 traces).

The sediment package at location B (Figure 3.3c) consists of a veneer of sand overlying some of the Headon Beds, which include shelly clays with some sands. Based on data from an adjacent borehole, this portion of the Headon Beds has a

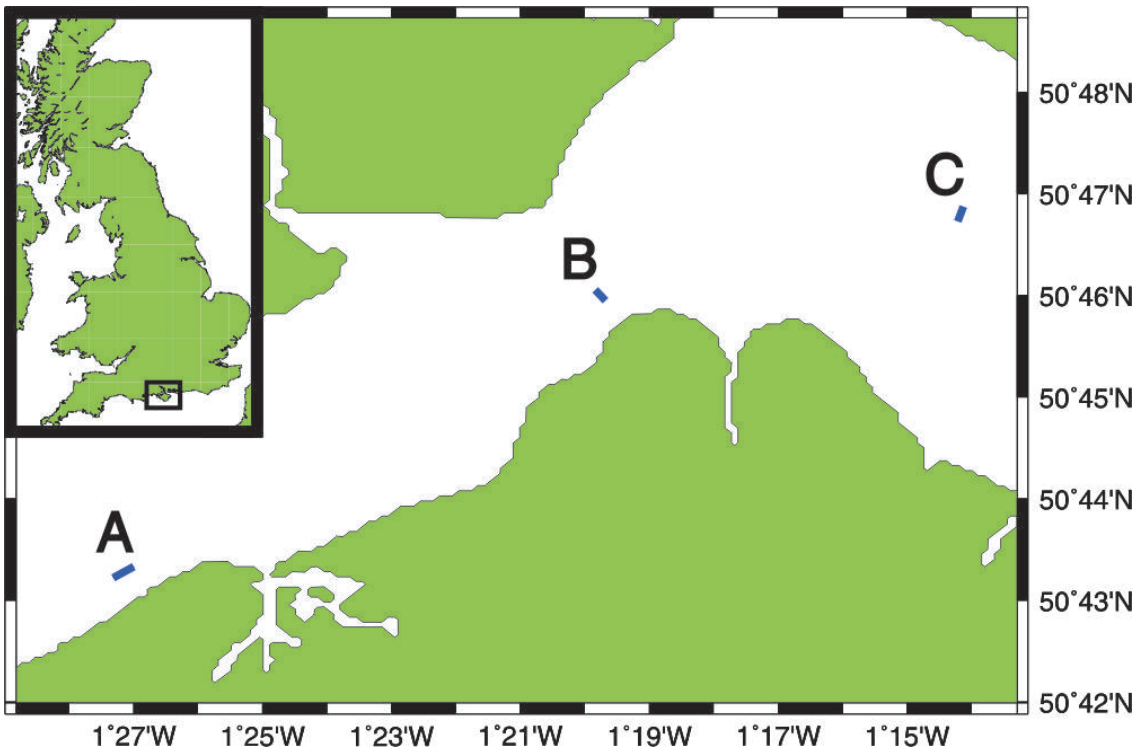

Figure 3.2: Map locating the survey lines over the sediment packages at locations A, B, and C within the Solent U.K.

mean grain size and sorting of 6.9 ϕ (+2.1; −1.5). The sediment package at location C (Figure 3.3d) is known as Brambles Bank and consists of unconsolidated sands with a mean grain size and sorting of 2.5 ϕ (+0.3; −0.3), as determined by a seabed grab. The Brambles Bank sands overlay the more consolidated Barton Sand beds, which form the sub-bottom interface. Single Chirp surveys were carried out over the sediment packages at locations B and C, and the analyses use 400 traces and 45 traces, respectively.

3.4.2 Data Processing

We correlate the Chirp seismic data with the original source sweep to correctly collapse the waveform (not required with Boomer data). Further processing to improve interpretability such as filtering, divergence corrections, instantaneous amplitude calculations and trace mixing, is used only to identify the seabed and sub-bottom reflections and is not applied to the analyzed data. Such processing would modify the spectral content of the data and would be detrimental to the accuracy of the

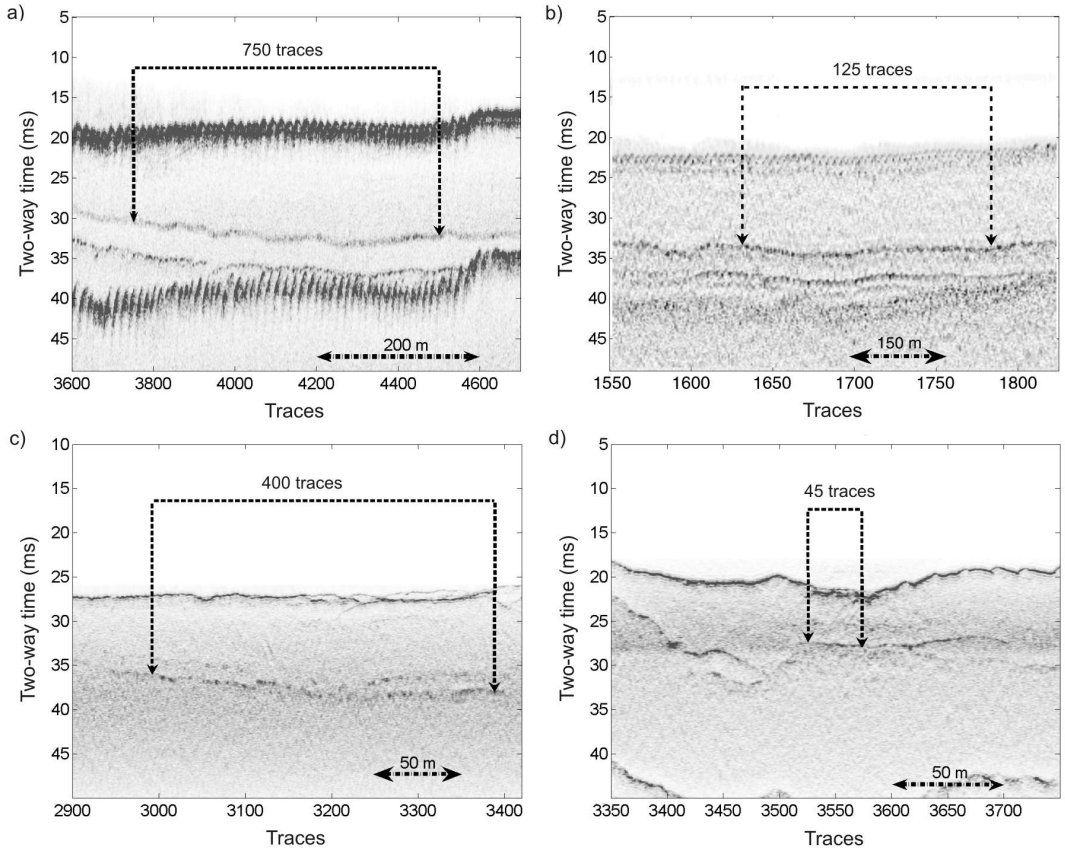

Figure 3.3: a) Chirp profile over location A (Bembridge Marls), with attenuation examined between the seabed and a sub-bottom reflection 11 ms beneath (two-way time); b) Boomer profile over location A (Bembridge Marls), with attenuation examined between the seabed and a sub-bottom reflection 11 ms beneath (two-way time); c) Chirp profile over location B (Headon Beds), with attenuation examined between the seabed and a sub-bottom reflection 10 ms beneath (two-way time); d) Chirp profile over location C (sands), with attenuation examined between the seabed and a sub-bottom reflection 7 ms beneath (two-way time).

spectral-ratio calculations.

After traces containing suitable reflections are identified, they are windowed within the raw/correlated data and passed through 1-kHz wide zero-phase Ormsby band-pass filters (with additional 0.5-kHz tapers) that increase in steps of 0.25 kHz. The strongest amplitudes from the seabed and sub-bottom reflections on each trace are extracted from the band-passed time-domain data. The two-way time between the two maximum amplitudes taken from each trace also is calculated, and an amplitude window is passed over a transparent part of the water column to retrieve the background noise floor and assess the signal-to-noise content of the

measurements.

If no coherent reflections are present close to the sub-bottom reflector, it might be possible to estimate levels of scattered noise there and use that to assess the signal-to-noise content instead. We found that using frequency bands smaller than 1 kHz generated instability because of poorer the signal-to-noise ratio (S/N), whereas larger frequency bands reduce resolution across our frequency range. Zero-phase band-pass filters ensure that the energy remains centered upon the picked interface, generating the strongest and most precise reflection in the time domain.

3.4.3 Interpretation of Spectral-Ratio Plots

After the spectral-ratio calculation is applied to the traces over a sediment package, two plots are produced. The spectral signature plot (SSP) is a plot of $-ln(A_R/A_S)$ versus f for the mean, median and standard deviation of all the traces within successive 1-kHz frequency bands incrementing by 0.25 kHz. The attenuation trend plot (ATP) is a plot of $-ln(A_R/A_S)$ versus $\pi \cdot f \cdot \Delta t_R(f)$ for each trace within select frequency bands chosen from the SSP. The ATP shows the best-fitting Q_{SR} model derived using iteratively reweighted robust least-squares regression.

The SSP is used to identify the frequency bands that contain an attenuation trend. A small number of outliers can strongly affect the mean data points. However, the median data points are robust to such contamination and it is an indication of good S/N when mean and median are similar. Comparing these with the ratio of amplitudes from the water column and seabed reflection ($-ln(Noise/A_S)$) gives an indication of the frequency range at the target reflector that still contains signal above any background noise. Because of the negative y-axis, when the background noise curve is above the mean and median data points, it is weaker than the signal. We select independent uncontaminated frequency bands for plotting on the ATP using the following empirically derived criteria: the background noise is weaker than two-thirds of the standard deviation range within the frequency band and within the two previous and following frequency bands; the lowest selected uncontaminated frequency band has a central frequency with a power greater than -30 dB returned from the seabed; and finally, median frequency band measurements do not follow

changes in the background noise curve, confirming that noise is not stronger in the temporal location of the target reflector. Each frequency band on the SSP is 1 kHz wide with central frequencies 0.25 kHz apart. Therefore, the two previous and following frequency bands of the frequency band being considered also are assessed. At least two uncontaminated frequency bands must be selected from the SSP for plotting in the ATP. To be considered independent measurements for statistical purposes, the 1-kHz frequency ranges may not overlap (ignoring tapers), and to avoid throwing away information, they must define at least the beginning and end of the observed attenuation trend. Any additional uncontaminated frequency bands that lie between, which can be included without producing any overlap in frequency content, should be spaced equally about the center of the attenuation trend.

In the ATP, Q_{SR} is estimated using two statistical fits. First, ordinary least-squares regression is used to fit the data in which all data points are given equal weighting. This is shown on the ATP with its 95% confidence interval and the intercept value. We also show the correlation coefficient, which is a measure of the accuracy of fit, and the t-statistic, which shows the significance of the correlation by calculating the probability of the correlation coefficient occuring by chance, if the true correlation is zero.

Least-squares estimates are optimal given independent normally distributed errors with constant variance but can behave badly when the error distribution is not normal (Fox, 1997). In our case, responses of the data at different frequencies are not of equal quality and do not exhibit constant variance. The variance in errors might increase when frequency is relatively low and little measurable attenuation occurs, and/or when frequency is relatively high and the S/N is reduced. Therefore, we make a robust estimate of Q_{SR} using an iteratively reweighted robust least-squares regression (see Appendix A). The robust fitting method uses weights to reflect confidence within frequency bands with low variance and to counter error structure within the data during the fitting process. Thus, the robust Q_{SR} remains stable in the presence of high-leverage outliers near the extremities of the fitted curve and should be the most accurate and unbiased result.

3.5 Experiment Results

3.5.1 Solent Location A

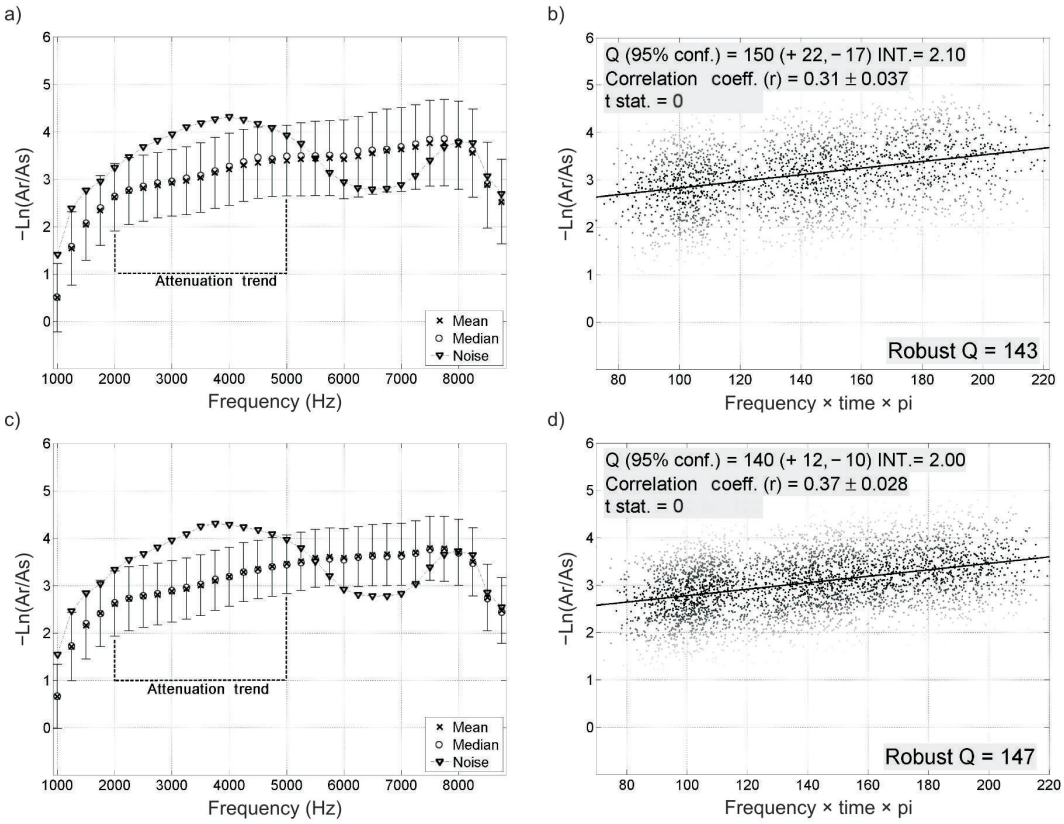

Figure 3.4: Results from location A (Bembridge Marls): a) Chirp SW–NE SSP (750 traces) showing attenuation trend 2.00–5.00 kHz; b) Chirp SW–NE ATP using frequency bands 2.50, 3.50 and 4.50 kHz; c) Chirp NE–SW SSP (1250 traces) showing attenuation trend 2.00–5.00 kHz; d) Chirp NE–SW ATP using frequency bands 2.50, 3.50 and 4.50 kHz.

From location A, we estimate the Q_{SR} of a sediment package that extends 11 ms (two-way time) beneath the seabed (Figure 3.3a and 3.3b). SSPs from the two Chirp surveys (Figures 3.4a and 3.4c) show the same trends and the same uncontaminated frequency range between 2.00 and 5.00 kHz. Below 2.00 kHz, the mean and median residuals follow the shape of the background noise curve. Above 5.00 kHz, the background noise becomes stronger than the signal from the sub-bottom reflector. From these attenuation trends, the 1-kHz uncontaminated frequency bands centered upon 2.50, 3.50 and 4.50 kHz are selected for use in the

ATPs. Thus, over a frequency range of 2.00–5.00 kHz, a linear regression line fits the data within the ATPs (Figures 3.4b and 3.4d) with frequency-independent robust Q_{SR} values of 143 and 147. Both robust Q_{SR} values fall within the predicted 95% confidence intervals of 150 (+22; −17) and 140 (+12; −10) respectively. However, the Chirp northeast–southwest survey has better precision and a higher correlation of 0.37 because of the greater number of traces over the same distance resulting from the tidal flow direction.

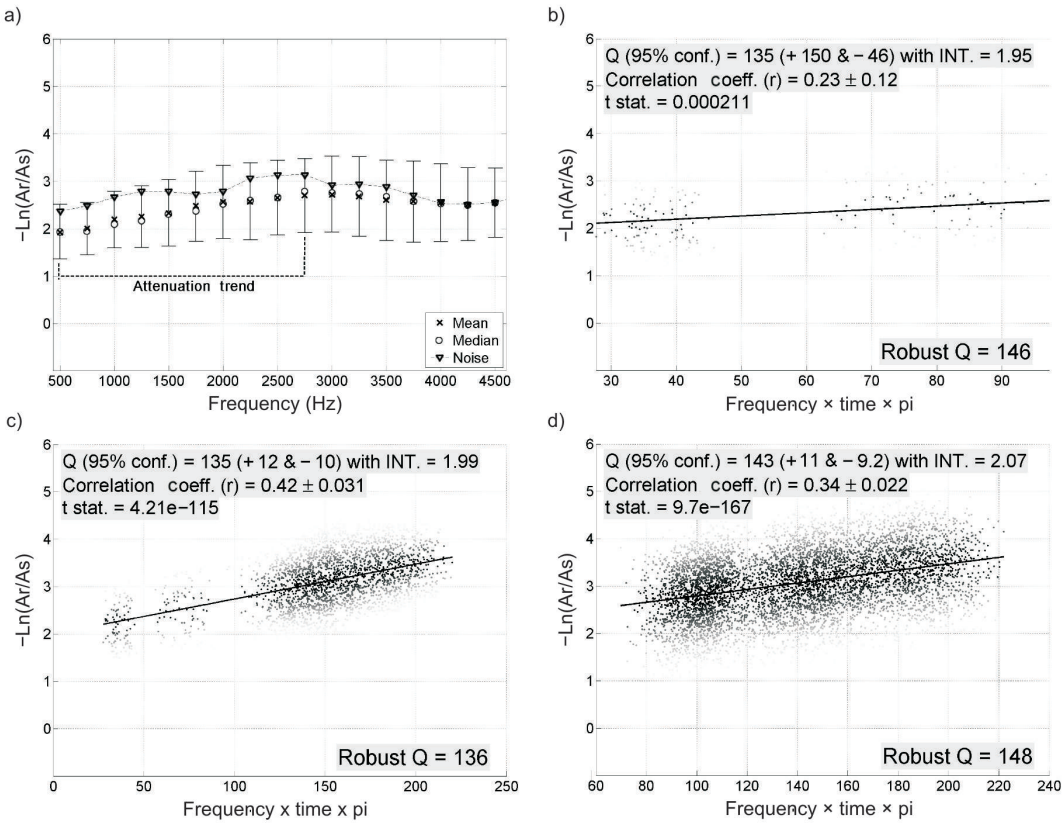

Figure 3.5: Results from location A (Bembridge Marls): a) Boomer SSP showing attenuation trend 0.50–2.75 kHz; b) Boomer ATP using 1.00- and 2.25- kHz frequency bands; c) Combined Chirp NE–SW (1250 traces) and Boomer ATP using frequency bands 1.00, 2.00, 3.50 and 4.50 kHz; d) Combined Chirp NE–SW (1250 traces) and Chirp SW–NE (750 traces) ATP.

Figures 3.5a and 3.5b show the results from applying this spectral-ratio technique to the Boomer data over the same sediment package. The SSP in Figure 3.5a shows that the S/N within the Boomer data is inferior to the Chirp data, but an uncontaminated frequency range is observed between 0.50 kHz and 2.75 kHz. Above

2.75 kHz, noise contaminates the ratios, and at 4.00 kHz, the Boomer power spectrum falls below −30 dB, allowing the background noise to become stronger than the signal, and the two converge. Therefore, from this attenuation trend, the 1-kHz uncontaminated frequency bands centered on 1.00 kHz and 2.25 kHz are selected for use in the ATP. Over the frequency range of 0.50–2.75 kHz, we use a linear regression line to fit the data within the ATP (Figure 3.5b) and find a frequency-independent robust Q_{SR} of 146. The robust Q_{SR} falls within the 95% confidence interval of 135 (+150; −46) and has a correlation of 0.23. This is consistent with the Chirp results, but the 95% confidence interval is poor because there are fewer traces over the sediment package resulting from the slower firing rate of the Boomer source, and because of a reduced frequency range relative to the Chirp data.

Combining the 1- and 2-kHz frequency bands from the Boomer and the 3.5- and 4.5-kHz frequency bands from the northeast–southwest Chirp enables Q_{SR} to be examined from 0.5 to 5.0 kHz and produces the ATP in Figure 3.5c. The addition of the Boomer data derives a superior result, with a frequency-independent robust Q_{SR} of 136 that lies within a precise 95% confidence interval of 135 (+12; −10) and has a correlation coefficient of 0.42. Combining the southwest–northeast and northeast–southwest Chirp datasets (Figure 3.5d) gives a 95% confidence interval of (+11; −9), which is an improvement over that achieved by the northeast–southwest Chirp data alone, but the correlation coefficient of 0.34 lies between the correlations achieved by the two datasets individually. Therefore, the more accurate result is from the combination of the Boomer data with the northeast–southwest survey, which provided the extended frequency range. The zero values of the t-statistic show that all the correlations are statistically significant and that a linear fit is appropriate over this frequency range.

3.5.2 Solent Location B

From location B, we estimate the Q_{SR} of a sediment package that extends 10 ms (two-way time) beneath the seabed (Figure 3.3c). The SSP in Figure 3.6a shows an uncontaminated frequency range between 1.75kHz and 7.25 kHz. Below 1.75 kHz and above 7.25 kHz, the background noise becomes stronger than the signal from

the sub-bottom reflector. From this attenuation trend, 1-kHz uncontaminated frequency bands centered upon 2.25, 3.25, 4.50, 5.75, and 6.75 kHz are selected for use in the ATP. Over the frequency range of 1.75–7.25 kHz, we find that a linear regression line fits the data within the ATP (Figure 3.6b) with a frequency-independent robust Q_{SR} of 106. The robust Q_{SR} falls within the precise 95% confidence interval of 107 (+6; −5). The t-statistic is zero, confirming the linear fit and implying that the correlation coefficient of 0.64 is significant.

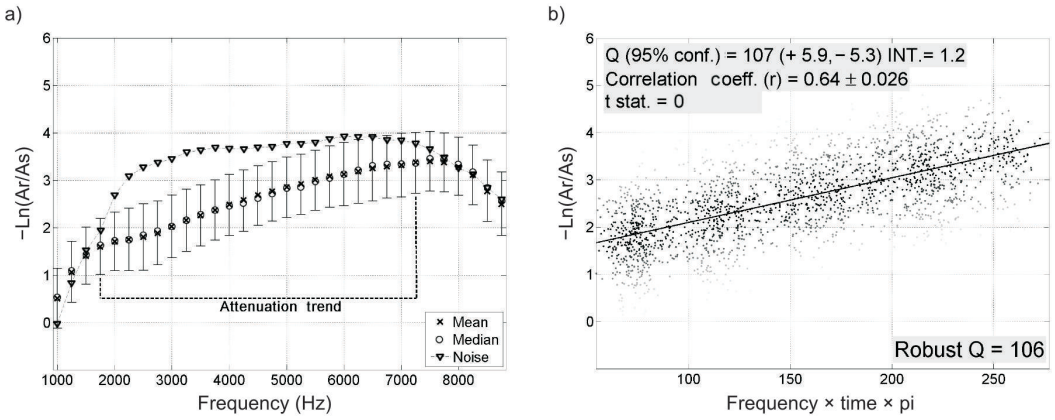

Figure 3.6: Results from location B (Headon Beds): a) Chirp SSP exhibiting an uncontaminated attenuation trend 1.75–7.25 kHz; b) ATP using frequency bands 2.25, 3.25, 4.50, 5.75, and 6.75 kHz and showing the robust Q_{SR} for these sediments.

3.5.3 Solent Location C

From location C, we estimate the Q_{SR} of a sediment package that extends 7 ms (two-way time) below the seabed (Figure 3.3d). The SSP in Figure 3.7a shows an uncontaminated frequency range between 1.75 kHz and 7.25 kHz. Below 1.75 kHz, the effective Chirp power spectrum falls towards −50 dB, and we observe increased standard deviation about the mean ratio. Above 7.25 kHz, the background noise becomes stronger than the signal from the sub-bottom reflector. From this attenuation trend, 1-kHz uncontaminated frequency bands centered upon 2.25, 3.25, 4.50, 5.75, and 6.75 kHz are selected for use in the ATP. Over the frequency range of 1.75–7.25 kHz, we find that a linear regression line fits the data within the ATP (Figure 3.7b) with a frequency-independent robust Q_{SR} of 66. The robust

Q_{SR} falls within the 95% confidence interval of 63 (+10; −7). The t-statistic is zero, confirming the linear fit and implying that the correlation coefficient of 0.7 is significant.

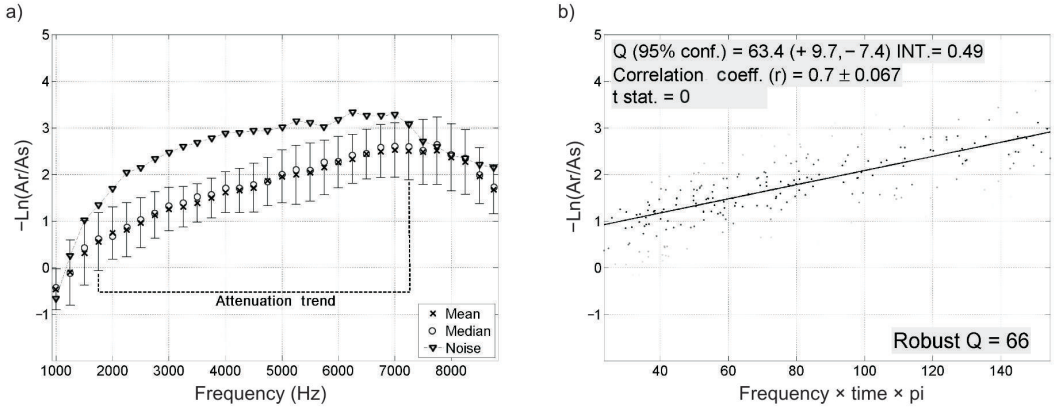

Figure 3.7: Results from location C (sands): a) Chirp SSP exhibiting an uncontaminated attenuation trend 1.75–7.25 kHz; b) ATP using frequency bands 2.25, 3.25, 4.50, 5.75, and 6.75 kHz and showing the robust Q_{SR} for these sediments.

3.6 Discussion

Robust estimates of Q_{SR} all converge within the 95% confidence intervals about the ordinary least-squares Q_{SR}, implying a Gaussian error structure is reasonable and that the 95% confidence limits produced are meaningful. The t-statistics indicate that all the Q_{SR} fits are appropriate and the correlations, which range from 0.23 to 0.70, are significant. The SSPs makes full use of the power spectrum information, so that any variation of Q_{SR} with frequency above the background noise levels are identified and evaluated robustly. We showed that it is simple to combine high-resolution seismic data from alternative sources, allowing us to observe Q_{SR} variation over a broader frequency range. The successful combination of Boomer and Chirp data also confirms that all the source/receiver responses (which would be different between the Chirp and Boomer surveys) are eliminated from the measurements when the ratios are taken. Figure 3.8 reviews the application of our spectral-ratio technique.

We have tested how the number of observations (traces multiplied by independent frequency bands) affects the ordinary least-squares regression estimate of Q_{SR} and the corresponding 95% confidence interval, using the Chirp northeast–southwest survey data from location A. By keeping the same three independent frequency bands used previously (measuring attenuation between 2.0–5.0 kHz) and selecting successively longer sections about a common centerpoint, we show that precision and correlation increase with the number of traces (Figure 3.9). Adding the Q_{SR} derived from the combination of the Chirp northeast–southwest data with the Boomer survey data (measuring attenuation between 0.5–5.0 kHz), we see that fewer observations are required to achieve an equivalent 95% confidence interval of $+12; -10$, and a more accurate fit with a correlation of 0.42 is produced.

The result from combining the southwest–northeast and northeast–southwest Chirp survey data looks slightly anomalous because of the reduction in correlation; this is because it is unlikely that the lines are exactly coincident. Therefore, the accuracy in the Q_{SR} fit is dependent on bandwidth and slightly dependent on precision (Figure 3.9). Precision is dependent on the variation in observed attenuation, which depends on $\Delta t_R(f)$ and $Q(f)$.

It follows that in sediments in which attenuation is weaker and more observations are used, such as the Bembridge Marls (7.7 ϕ) in location A, greater benefit is obtained from using iteratively reweighted robust least-squares regression to subdue the effects of outliers. The two independent Chirp surveys and the Boomer survey found the robust Q_{SR} to be 143, 147 and 146 respectively, although the respective Q_{SR} and 95% confidence intervals from the ordinary least-squares regression were 150 ($+22$; -17), 140 ($+12$; -10), and 135 ($+150$; -46).

Comparison of Chirp SSPs from the three locations shows that the standard deviation in each frequency band reduces as Q_{SR} reduces. Therefore, more traces were required over the sediment packages at locations A and B relative to C to achieve a desirable 95% confidence interval. Location A shows the greatest standard deviation in the frequency bands, possibly also because of the poorer sorting of the sediment and the seawater-gravel interface. Precision diminishes as Q_{SR} increases because $1/Q(f)$ (the gradient of the fitted curve) becomes smaller and the

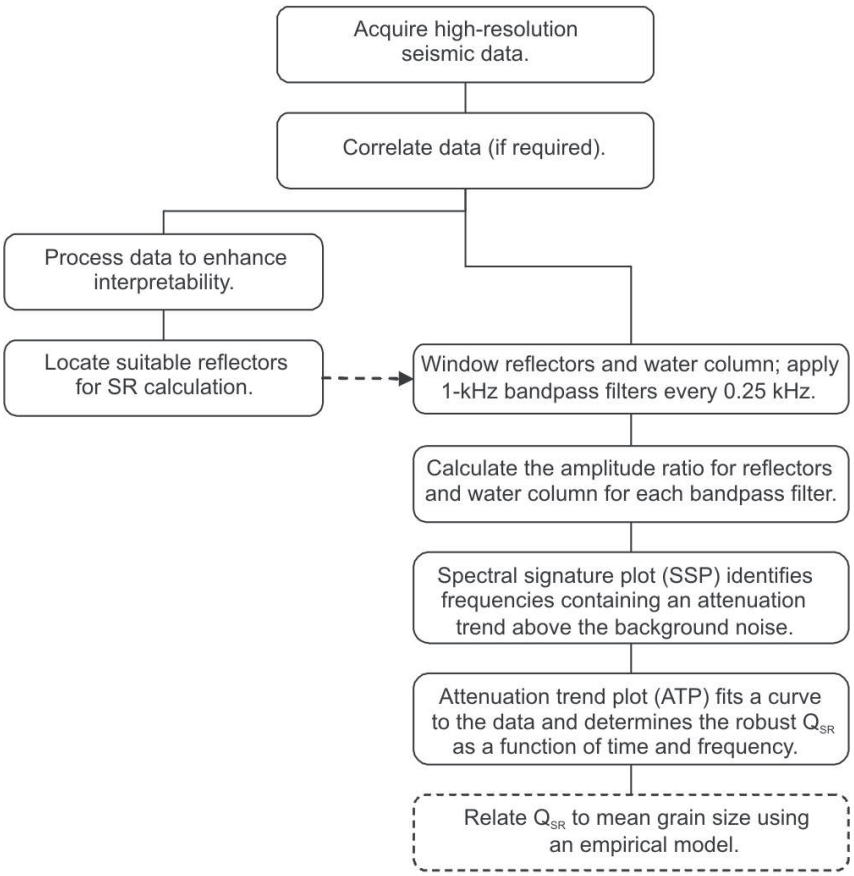

Figure 3.8: Flow diagram for the spectral-ratio technique presented in this chapter.

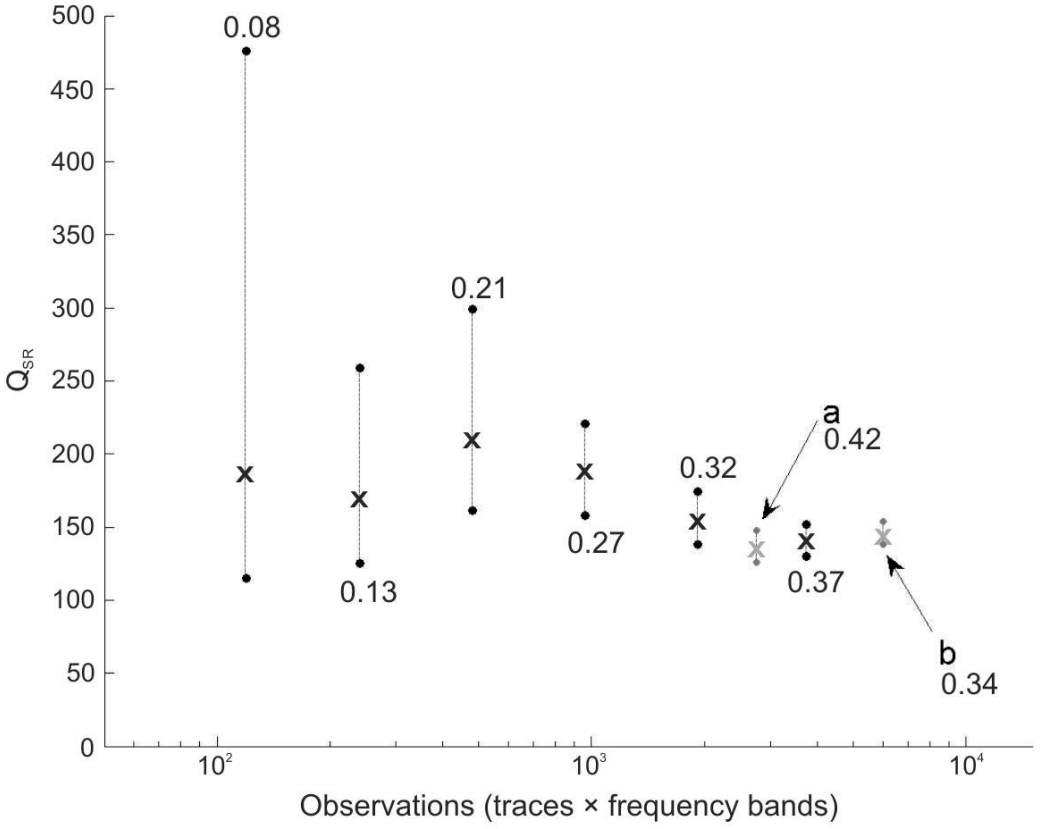

Figure 3.9: Graph showing 95% confidence (black dots) and predicted Q_{SR} (crosses) calculated using linear ordinary least-squares regression against the number of observations over the sediment at location A about a common midpoint, from the NE–SW Chirp data: a) locates the result from the addition of the Boomer data; b) locates the result from the addition of the SW–NE Chirp data.

fit becomes more ambiguous. White (1992) confirms that Q is estimated most easily when the effect of attenuation is large. Consequently, to achieve a desirable 95% confidence interval of about ±10 for the Q_{SR} of the Bembridge Marls (7.7 ϕ), at least 1250 traces using only Chirp data are required. This equates to the complete 400-m section examined over the Bembridge Marls, much greater than the 200-m and 25-m sections necessary over the better sorted lower Q_{SR} sediments at locations B and C. Thus, the length scales over which lateral homogeneity is required are relatively short.

Examining how noise affects the frequency ranges at the three locations, we see that above 8.00 kHz within all Chirp SSPs, the signal from the sub-bottom

reflector has become attenuated completely and begins to follow the background noise curve. This noise contamination at the higher frequencies causes attenuation trends to effectively flatten out, which is also observed in synthetic examples by Matheney and Nowack (1995). Chirp SSPs from location A (Figures 3.4a and 3.4c) show that the ratios with the sub-bottom reflector could be contaminated with an increase in background noise at 5 kHz. Although the background noise measured from the water column is stronger at 5–8 kHz, the amplitudes from the sub-bottom reflector are being taken from a different temporal location where this noise has a reduced effect. The lower Q_{SR} of the sediment packages from locations B and C allow a measurable amount of attenuation to take place at 1.75 kHz, as opposed to location A, where the higher Q_{SR} causes less significant attenuation below 2 kHz and the measurements become sensitive to background noise.

The constant Q_{SR} fits for the three different substrates suggest that intrinsic attenuation, similar to that explained by G-S theory (Buckingham, 2000) for unconsolidated sediments, is dominant over scattering attenuation within our frequency range. Near-linear scaling of compressional-wave attenuation with frequency has been identified by other researchers. Hamilton (1972) combined his results with others and observed compressional-wave attenuation to scale with frequency to a power close to unity between 5 Hz and 1000 kHz within unconsolidated sands, clays and mixed sediments. Bowles (1997) compiled experiments in unconsolidated fine-grained sediments spanning 10 Hz to 500 kHz (although without observations in the interval 0.6–4.0 kHz) and found a similar scaling with frequency to the power of 1.12. Williams et al. (2002) report a linear scaling of compressional-wave attenuation with frequency in sandy sediment from the SAX99 site from 1.7 to 400 kHz. Our results in fine-grained sediment between 0.50 kHz and 5.00 kHz support Bowles' (1997) conclusion; our results in sandy sediments between 1.75–7.25 kHz suggest that a near-linear scaling of attenuation with frequency can be extended to coarse-grain dominated sediments. Furthermore, this argues for the validity of using empirical models generated from higher-frequency laboratory attenuation studies, to relate lower-frequency remote attenuation measurements to sediment physical properties.

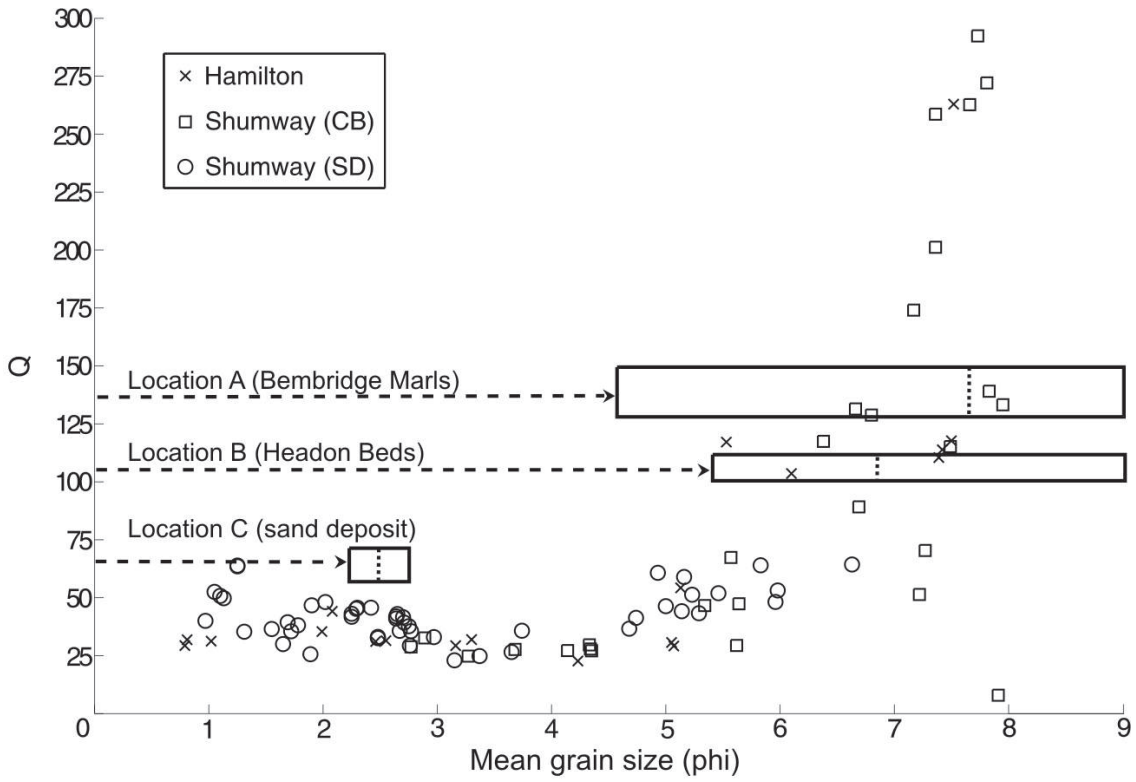

Figure 3.10: Q vs. mean grain size (ϕ) of sediments from the San Diego area (from Tables 1 and 2 in Hamilton, 1972; Shumway, 1960). Dashed lines locate the Solent robust Q_{SR} fits. Solid boxes represent the 95% confidence interval in the ordinary least-squares regession of Q_{SR} and the sorting of the sediment. The vertical dashed lines represent the mean grain size of the sediments.

Figure 3.10 compares our observations to a compilation of attenuation studies over a wide range of sediments from the San Diego, California, area (Shumway, 1960; Hamilton, 1972). The most accurate robust Q_{SR} of 136 from location A for the Bembridge Marls (7.7 ϕ) is consistent with the higher Q observations in the model. The relatively thin layer of gravel above the Bembridge Marls had little effect upon the overall attenuation. The robust Q_{SR} of 106 for the Headon Beds (6.4 ϕ) from location B conforms with the curve defined by the San Diego observations, and the lowest robust Q_{SR} of 66 from the Bramble Bank sands (2.5 ϕ) from location C is generally consistent with the lower Q observations in the model. It is apparent that Q is not diagnostic below 6 ϕ and a Q of 75, although other properties such as compressional-wave velocity may help resolve these coarse-grain dominated sediments (e.g. Hamilton, 1972). Our results and the majority of

observations from San Diego suggest that Q becomes greater than 75 after 6 ϕ, the point where larger grains become suspended in a clay matrix (McCann and McCann, 1969).

3.7 Conclusions

The spectral-ratio technique presented here for seismic reflection data shows that a frequency-independent Q_{SR} is the most appropriate fit to both unconsolidated sand and clay matrix dominated sediments in the Solent over the frequency range 0.5–8.0 kHz. The linearity of compressional-wave attenuation with frequency leads us to conclude that intrinsic attenuation is dominant over scattering attenuation within this frequency range, for these sediment packages.

For sediment packages that have the prerequisite conditions of lateral homogeneity and isolated sub-horizontal reflections above the first seabed multiple, high-resolution seismic sources can estimate the Q_{SR} with a 95% confidence interval of about ± 10, with a significant correlation coefficient. Estimating Q_{SR} in clay dominated sediment packages, where attenuation is weaker and the Q_{SR} fit more ambiguous, requires more observations to improve the 95% confidence interval and benefits from the use of iteratively reweighted robust least-squares regression to subdue outliers. If possible, data acquired using two seismic sources, such as a Chirp and Boomer sonar, can be combined to extend the frequency range over which attenuation is analysed and to improve the confidence and correlation of the Q_{SR} fit.

Q values provide a limited ability to differentiate mean grain sizes. For a Q less than 75, the sediment is likely to be coarse-grain dominated with a mean grain size ranging from 1 to 6 ϕ. For a Q over 75, the sediment is likely to be clay dominated with a mean grain size greater than 6 ϕ.

Chapter 4

Velocity Determination for Solent Sediments

4.1 Introduction

In Chapter 3, techniques were developed to derive Q from single channel seismic reflection data. These techniques were applied successfully to a case study for the Solent. In this chapter, I analyse high-resolution multi-channel seismic (MCS) reflection data from two locations in the Solent. One is location C from Chapter 3, over a Holocene sand deposit, the other over the location of a c. 30 m sediment core, which will be designated Solent location D (Figure 4.1a). The aim of this chapter is to test methods of predicting sediment physical properties and sediment types from remote measurements of velocity and Q.

Interval compressional-wave velocity (hereafter also called velocity) can be derived using migration velocity analysis during prestack depth migration of MCS data. This should be equivalent to the *in situ* sediment velocity, and can be used with a range of empirical regression models from the literature to predict sediment physical properties. Here, I will test empirical regressions of velocity on sediment saturated bulk density (hereafter, bulk density) and porosity from Hamilton and Bachman (1982) and Richardson and Briggs (1993), and the dominant grain fabric as predicted by the Q, with laboratory measurements of these properties performed upon the recovered sediments.

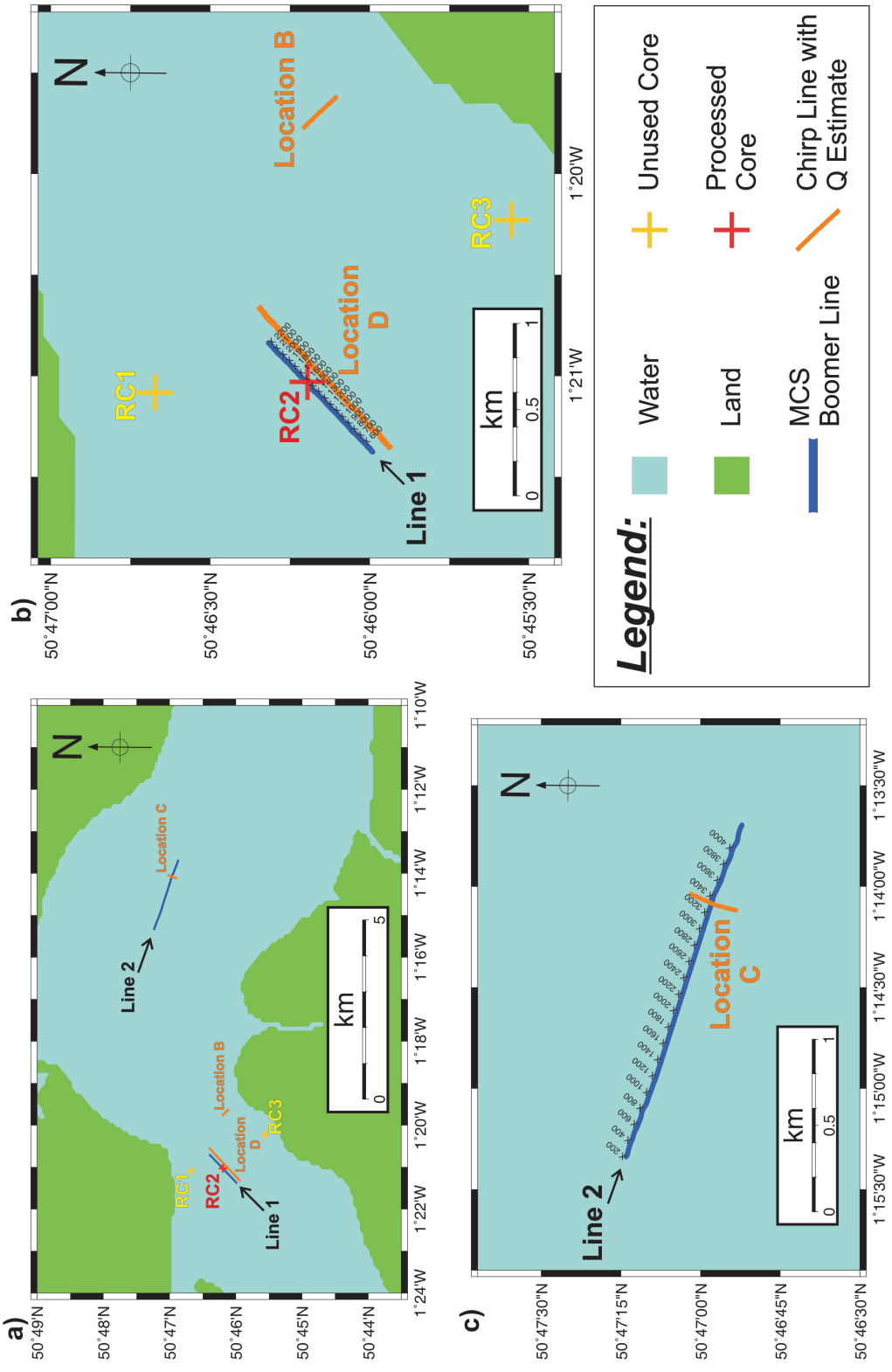

Figure 4.1: a) Map locating the rotary cores and survey lines over the sediment packages at locations C and D in the Solent; b) Location of RC2 between CDPs 1520 and 1600 along the Boomer MCS line, and adjacent Chirp profile over location D; c) Location of the Boomer MCS line through the Chirp profile at CDPS 3200–3400 over location C.

4.2 Acquisition

The rotary core RC2 (Figure 4.1b) collected by Fugro, was located close to an existing Chirp profile that contained good sub-bottom reflectors from which an estimate of Q_{SR} could be made. Hence, RC2 was chosen over RC1 and RC3 for this investigation. The analysis of RC2 is detailed in Section 4.3.

A Boomer MCS survey was carried out over RC2 parallel with the Chirp profile for stratigraphic consistency (Figure 4.1b). The survey was continued over the Holocene sand deposit at location C (Figure 4.1c) where the mean grain size and Q_{SR} have been previously reported in Chapter 3. The catamaran mounted Boomer (Applied Acoustic Engineering AA200) operated at 300 J with a shot trigger every 750 ms. A DGPS antenna was mounted on the Boomer catamaran providing sub-metre shot positioning. The first channel of the multi-channel streamer had an x and y offset from the source of +7.1 m and +5.8 m respectively (Figure 4.2). The survey was conducted with a survey speed of c. 3 knots (1.5 m/s), providing an along track sampling of c. 1 m for all channels.

Data was recorded with a sample interval of 0.125 ms and a record length of 150 ms on two DDS-4 tapes in SEGD format using a Geometrics Strataview R60 networked to a personal computer. The custom-built multi-channel streamer comprises sixty 1-m spaced groups of seven hydrophone elements, which provided a minimum and maximum source-receiver offset of c. 7 m and 67 m. Table 4.1 contains the start and end field file identification numbers (FFIDs) for the two MCS lines, with their source and receiver laybacks from the antenna and headings.

The previous Chirp surveys over locations C and D used a Chirp sonar calibrated to produce a linear sweep with a sine-squared taper function covering 1/8th of the time duration (Gutowski et al., 2002). The wide effective power spectrum exhibited by this sweep spans 1.5–13.0 kHz and is useful for Q_{SR} estimation. The Chirp streamer, which comprises eight hydrophone elements spaced across 1 m, was towed directly behind.

Basin-d/y-label	FFIDs	Source Offset (m)	Receiver Offset (m)	Heading (°)
Tape 1 (location D)				
Line 1	452–2643	0	7.1	45
Tape 2 (location C)				
Line 2	1698–5115	0	7.1	107

Table 4.1: MCS Boomer data contained on tapes 1 and 2, collected on the 09/11/07 in the Solent.

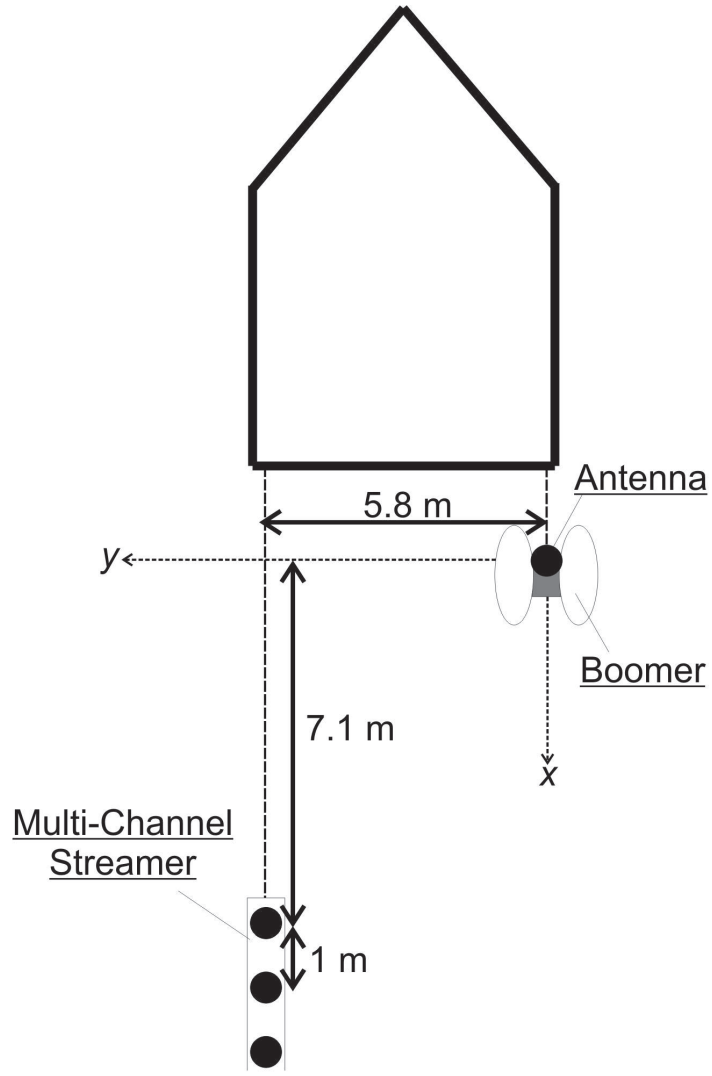

Figure 4.2: Towed Boomer and multi-channel streamer geometry. Measurements are relative to x and y about the antenna as required by ProMAX®.

4.3 Core Analysis

Cable percussion boring was used to initiate RC2 by penetrating the gravel seabed. From 3.20 m beneath the seabed, rotary coring was used to extend the borehole to 30.70 m beneath the seabed. Some samples were taken by Fugro and recorded and some parts were lost. However, it was possible to position the donated core sections at the correct depths using the borehole records, and the marked locations of the Fugro samples within the core sections.

The BOSCORF GEOTEK Multi-Sensor core logger (Rothwell and Rack, 2006) was used to measure the compressional-wave amplitudes and velocities, wet bulk densities, and fractional porosities (hereafter, porosity) for every 2 cm of the sediments within the core sections from RC2. Unfortunately, because of the drained nature of the sediments, coupling of the p-wave transducer was very poor and reliable velocities could not be produced.

Grain-size analysis of RC2 was undertaken using a Malvern Mastersizer 2000 particle size analyser. Samples were taken every 25 cm along RC2, with additional samples taken from discrete units considered a significant change in composition, or simply interesting for comparison.

The Mastersizer 2000 measures particles from 0.02 μm to 2000 μm in size (the finest clay to very coarse sand) using laser diffraction. Laser diffraction will provide similar results to sieving when characterising spherical or semi-spherical particles. Significant differences might be observed for non-spherical particles though, because sieving classifies particles by their smallest diameter and laser diffraction reports a spherical equivalent size, which relates to the volume of the particle. Therefore, laser diffraction is the more reliable measure of particle size, but the results can still be readily compared with sieving results, for example, with those already produced from location C.

Laser diffraction fundamentally generates volume moment mean diameters and distributions of grain size (avoiding the need to count the number of particles), which should be ideal descriptors of sediments when relating to their Q (Stevenson et al., 2002).

I use a volume weighted geometric mean (Zhang and Zhang, 1989; Merkus, 2009)

because sediments often exhibit log-normal distributions (Krumbein and Pettijohn, 1938). This will produce comparable results to the "graphic method" on a logarithmic ϕ scale (Folk and Ward, 1957; Pierce and Graus, 1981), which was used to characterise the sand at location C for Chapter 3.

Care should be taken when comparing the mean grain sizes of sediments from the literature because some investigations use the volume weighted arithmetic mean. Appendix B demonstrates the considerable differences produced between these two means using two samples from RC2 (a similar experiment can be found in Pierce and Graus, 1981), and explains why geometric type means are more representative of 3D mean grain size, which is important to Q.

The grain size distributions from RC2 are equivalent to log-normal distributions, hence the volume weighted geometric mean is used to describe the mean grain size, with the distances from the 16th and 84th percentiles used as a representation of the sorting (these would occur one standard deviation from the volume weighted geometric mean given log-normal distribution). Appendix C contains photos and the grain size results from the RC2 core sections positioned relative to depth.

4.4 Multi-Channel Seismic Data Processing

To measure seismic velocity in sediments it is necessary to record the reflected signal simultaneously at multiple horizontal distances from the source. MCS data provides a wave-field containing multiple energy travel paths that can be used to determine the velocity structure of the sub-surface at common depth points (CDPs). This can be used to migrate the reflected and diffracted energy back to its original location in space, to produce a detailed image in depth. This is termed depth migration. In iterative pre-stack depth migration (PSDM) the velocity model used by the migration is improved upon by using migration velocity analysis (MVA), and used for the next PSDM. This process is iterated until a satisfactory velocity model and migration have been achieved.

The wave-field is dependent upon the source-receiver geometry being correct. The horizontal positioning of the streamer relative to the antenna/Boomer is determined by using the velocity of the direct arrival. This is determined by applying linear move-out to the channels and identifying the velocity that causes the reduced direct arrival to arrive simultaneously at all channels. The layback to the streamer can then be calculated. The MCS is designed to be neutrally buoyant in seawater and the channels should tow at a constant depth c. 0.5 m beneath the sea-surface (c. 0.4 m beneath the Boomer plate).

Here I use the Kirchhoff migration algorithm in ProMAX® (*Prestack Kirchhoff Depth Migration*) in the common offset domain. This computes travel-times as a function of the velocity model using maximum amplitude ray-tracing or by solving the eikonal equation. Travel-time maps relate the time from each CDP to a region of points in the sub-surface; the amplitudes of all the times sharing the same image point are summed. The migration quality depends on the velocity model being relatively close to the actual velocity field. The output of the PSDM can be imaged as common reflection point (CRP) gathers (a collection of depth migrated traces that sample the CDP at increasing offsets) and/or offset sections (depth migrated sections each containing traces produced by a specific source-receiver offset). These are cleaned and then stacked to produce a migrated depth section.

The velocity model can be divided into interval velocities that represent veloc-

ity packages for the seawater or different sediment types. If interval velocities are correct the reflections in the CRP gathers or offset sections will align at constant depth and stack constructively. MVA evaluates how well energy is focused at reflection events in the stacked migrated depth section by examining their associated pre-stack CRP gathers. If reflection arrivals in the CRP gathers dip upwards with greater offset there is negative residual move-out (RMO) indicating a velocity underestimate; if reflection arrivals dip downwards with greater offset there is a positive RMO indicating a velocity overestimate (Figure 4.3). The objective of MVA is to use the RMO to update the velocity model, so that after the next migration the reflections will be better focused onto their correct locations in the sub-surface.

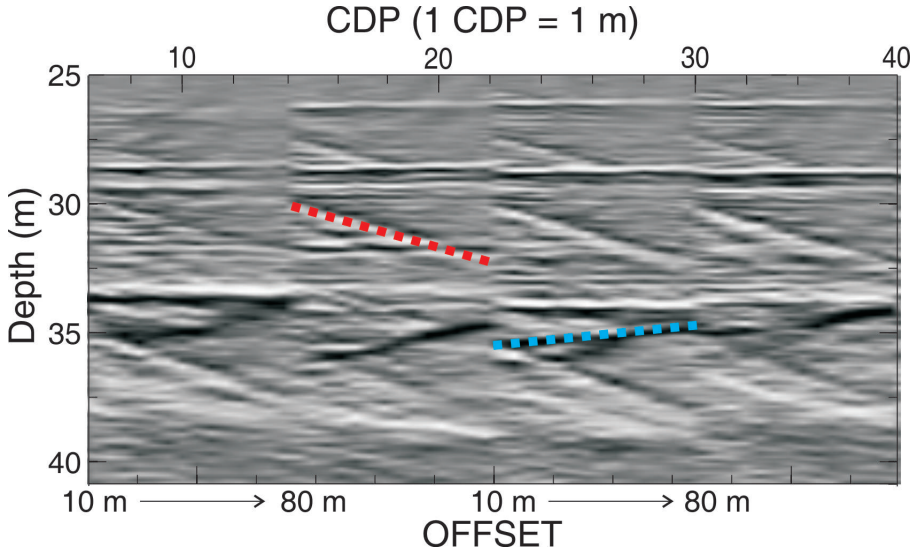

Figure 4.3: CRP gathers centred upon CDPs 10, 18, 26 and 32. Each gather increases with offset from 10–80 m. The red dots highlight reflection arrivals exhibiting positive RMO (this is in fact a multiple of the focused reflection above). The blue dots highlight reflection arrivals exhibiting negative RMO.

ProMAX® provides horizon-based velocity analysis with the *Interactive Horizon Residual Move-Out Analysis* package. Horizons can be picked from the migrated depth section, which is shown beneath the (semi-transparent) current velocity model, and linked with their pre-stack CRP gathers. The coherence of stacking the reflections in the gathers is measured in a semblance panel that shows the semblance along the picked horizon. The interpreter picks the appropriate semblances to remove the RMO in the CRP gathers along the selected horizon. New velocity

functions with depth are generated immediately, and applied to the CRP gathers so the interpreter can gauge the effects. If satisfactory, the corrections can be applied to the working velocity model, which updates the velocity interval above the picked horizon. This is then saved and used with the next migration. If the horizon has become well focused, the correction was successful and deeper horizons can be examined until the interpreter is satisfied that the optimal velocity model down to the required depth has been achieved.

This is known as a layer stripping approach and is applied to the MCS data here, after migration with Kirchhoff PSDM using eikonal equation travel-times. Initially a uniform velocity model is used that has the same velocity as the direct arrival between source and receiver. The interval velocity between the seabed and the sea-surface is determined first by picking the seabed horizon, and then subsequent deeper reflections are used to determine deeper interval velocities.

In location C only the seabed and the basal reflection of the unconsolidated sand deposit needed to be migrated accurately. In location D, the seabed and sub-bottom reflections c. 2–3 m apart down to the seabed multiple were focused using MVA so that the velocity model about the location of RC2 would have as much detail as possible.

The post-migration processing steps used here to clean the data before stacking were originally developed for the more complex Windermere Boomer MCS data, and are fully described in Section 5.4.2. The steps are applied here because they also produce the best results for the MCS data in the Solent: the stacked migrated section (Figure 4.4a) benefits from applying Burg adaptive deconvolution to the migrated offset sections before stacking (Figure 4.4b) because this compresses the wavelets and removes reverberation; and F-K filtering of the subsequent CRP gathers after deconvolution removes most delayed energy to produce a relatively clean image, with good detail just beneath the seabed and of weaker interfaces (Figure 4.4c).

Figure 4.5 compares the Boomer depth migration over location D with processed time-domain data. The single channel Chirp data is noisier and less effective at penetrating the seabed (Figure 4.5a). The strength of reflections observed in a single

channel of MCS data are improved following a brute stack of five channels (Figures 4.5b and 4.5c respectively), but little additional benefit is derived. The depth migrated Boomer data (Figure 4.5d) is evidently the best image of the sub-surface. The optimised stacking of all 60 channels up to an offset c. 70 m significantly improves the S/N and sampling of the sub-bottom reflections, and the ability to filter out delayed energy with offset before stacking, produces a more detailed and reliable image of the sub-surface.

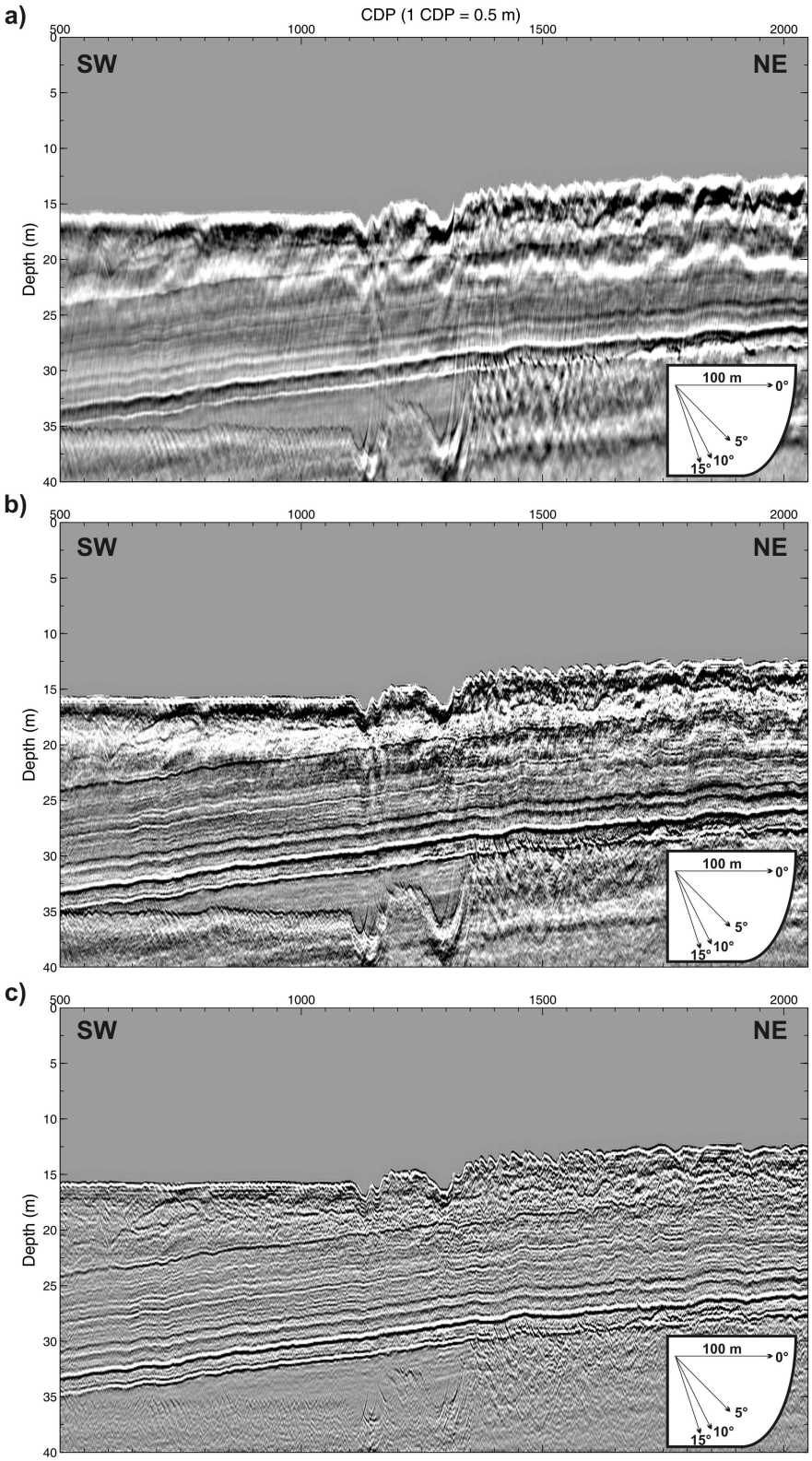

Figure 4.4: Kirchhoff prestack depth migration of Boomer MCS data over location D: a) Stacked migrated section; b) Burg adaptive deconvolution applied to offset sections before stacking; c) Burg adaptive deconvolution applied to offset sections and F-K filtering applied to the subsequent CRP gathers before stacking.

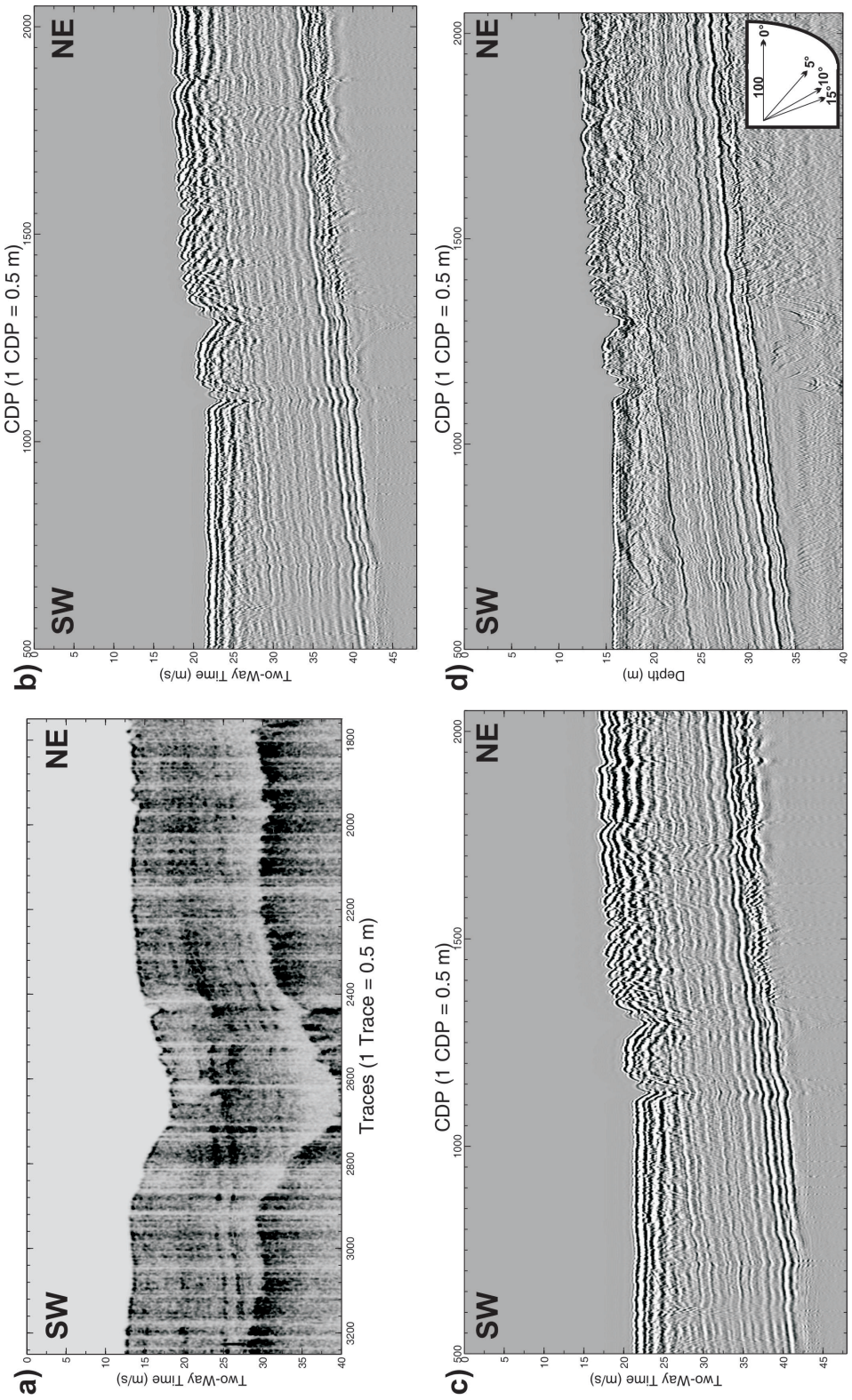

Figure 4.5: Seismic data over location D: a) Processed Chirp data; b) Processed single channel of Boomer MCS data; c) Processed five channel brute stack of Boomer MCS data; d) Processed depth migration of Boomer MCS data.

4.5 Velocity and Physical Property Results

4.5.1 Solent location C

The sand deposit at location C is up to c. 6 m thick (Figure 4.6). An arbitrary velocity gradient that does not interfere with the migration of the sand deposit was used for the data beneath the basal reflection. MVA determined an average velocity of 1610 ± 20 m/s for the sand deposit (Figure 4.6a). Direct observations on the sand in the laboratory measured the bulk density and porosity to be 1.86 ± 0.05 g/cm^3 and 47 ± 3% respectively.

4.5.2 Solent location D

Data from location D were migrated using MVA to a depth of 16 m beneath the seabed in the location of RC2 (Figure 4.7). Beneath this it was not possible to completely remove the seabed multiple, and an arbitrary velocity was used that did not interfere with the focusing of reflections above. RC2 is at CDP 1560, so I compare the section for CDPs 1520–1600 with the stratigraphy, bulk density, and porosity measurements from the core analyses (Figure 4.8). The mean core values of physical properties are calculated from the top 16 m of core.

Figure 4.7a shows that the top c. 3 m of sediment at location D has a relatively high-velocity, and is c. 1860 ± 30 m/s in the location of RC2. This velocity package has been labelled A on Figures 4.7a and 4.8, and corresponds with the top 3.20 m of sandy-gravel logged at RC2 (Figure 4.8). Package B has a lower velocity of 1630 ± 20 m/s, and is c. 1.5 m thick in the location of RC2. This corresponds with the top 1.10 m of clay beneath the gravel (Figure A.5 in Appendix C), which is noted as being not as stiff as the sediment in the rest of the core (but becoming stiffer with depth), and exhibits an increase in porosity and a decrease in bulk density away from the mean values at the top of the package (Figure 4.8).

The sediments in package C have a velocity of 1710 ± 20 m/s in the location of RC2, which is slightly less than those in package D that have a velocity of 1740 ± 20 m/s (Figure 4.8). The boundary between the packages marks the beginning of a transition in porosity from above the mean to below, and in the bulk density

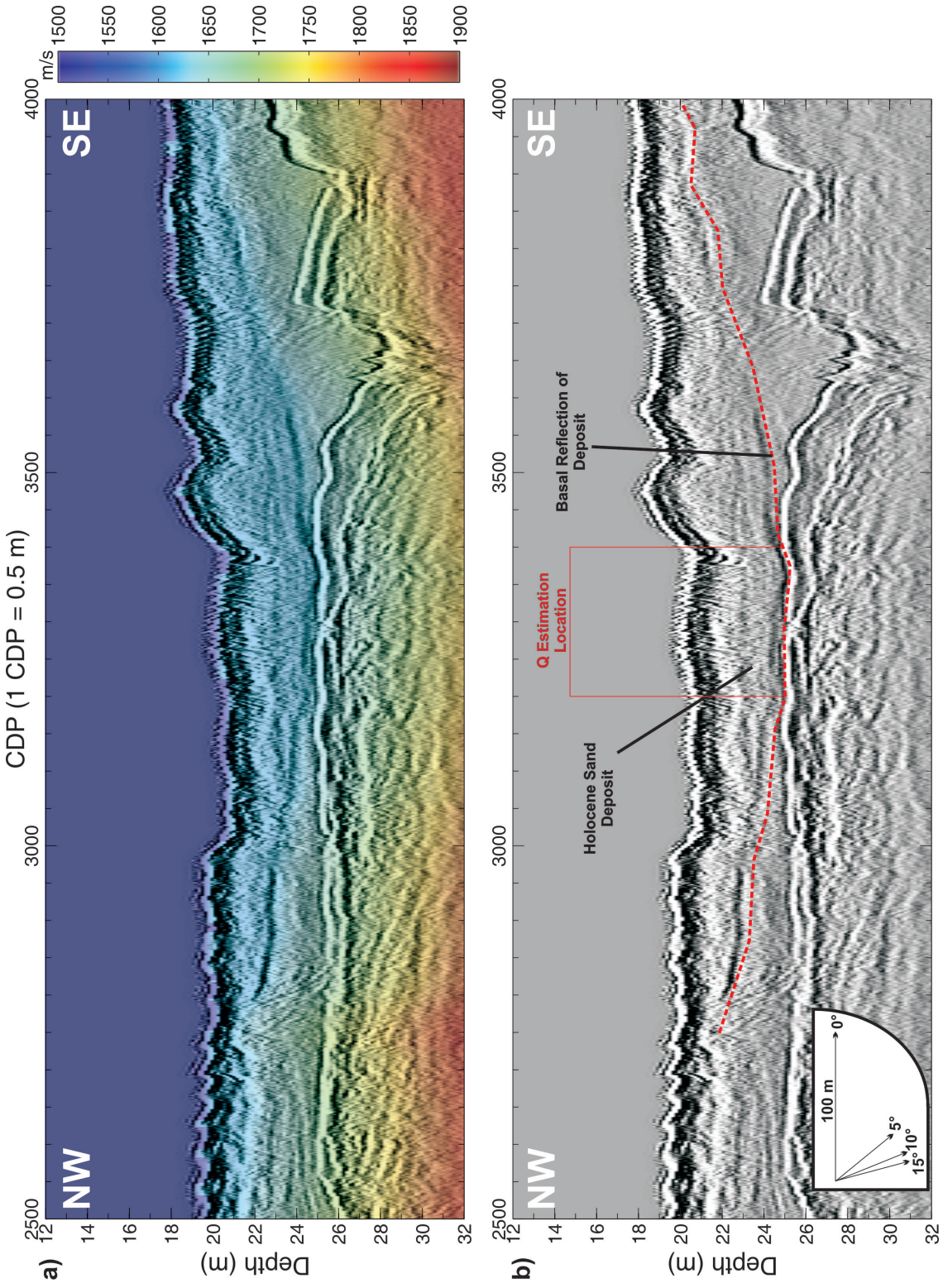

Figure 4.6: Boomer MCS data over location C: a) Velocity model and migrated depth section; b) Migrated depth section showing approximate location of Q estimation with Chirp data.

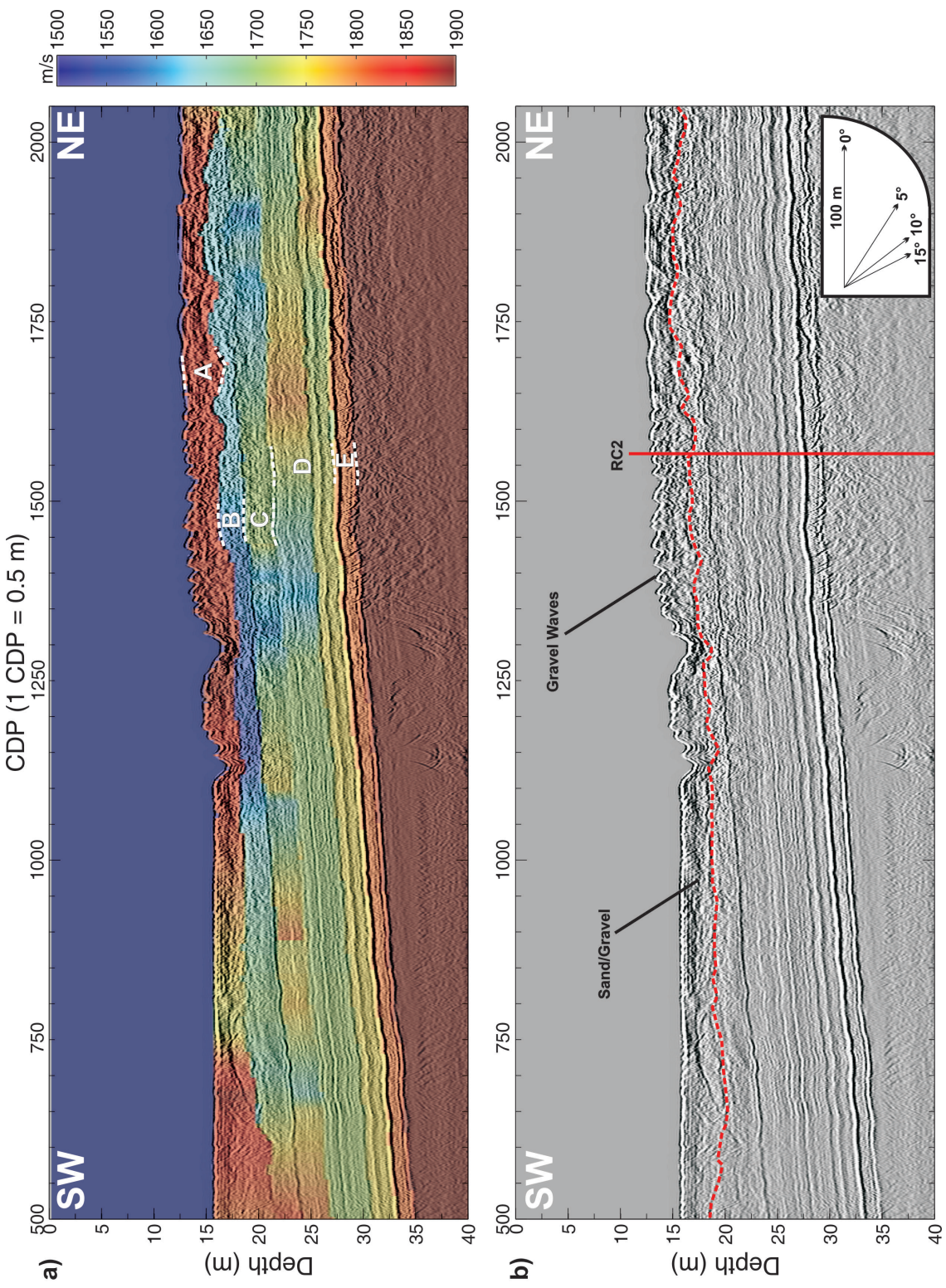

Figure 4.7: Boomer MCS data over location D : a) Velocity model and migrated depth section with velocity packages labelled; b) Migrated depth section showing location of RC2.

from below the mean to above, implying greater consolidation. A higher velocity of 1800 ± 30 m/s distinguishes package E, and corresponds with strong bounding reflections, and relatively consistent low porosity of c. 20 % and high bulk density of 2.4 g/cm^3. Between 15.1 m and 15.4 m depth is a layer of consolidated sediment that causes this (Figure A.11 identifies this as siltstone in Appendix C).

Most of the stronger reflections within the MCS data can be correlated with 20–50 cm thick silty sediments within the clay dominated sediments, some shelly layers, and the two very strong reflections between 15.0 m and 16.5 m with two siltstone layers.

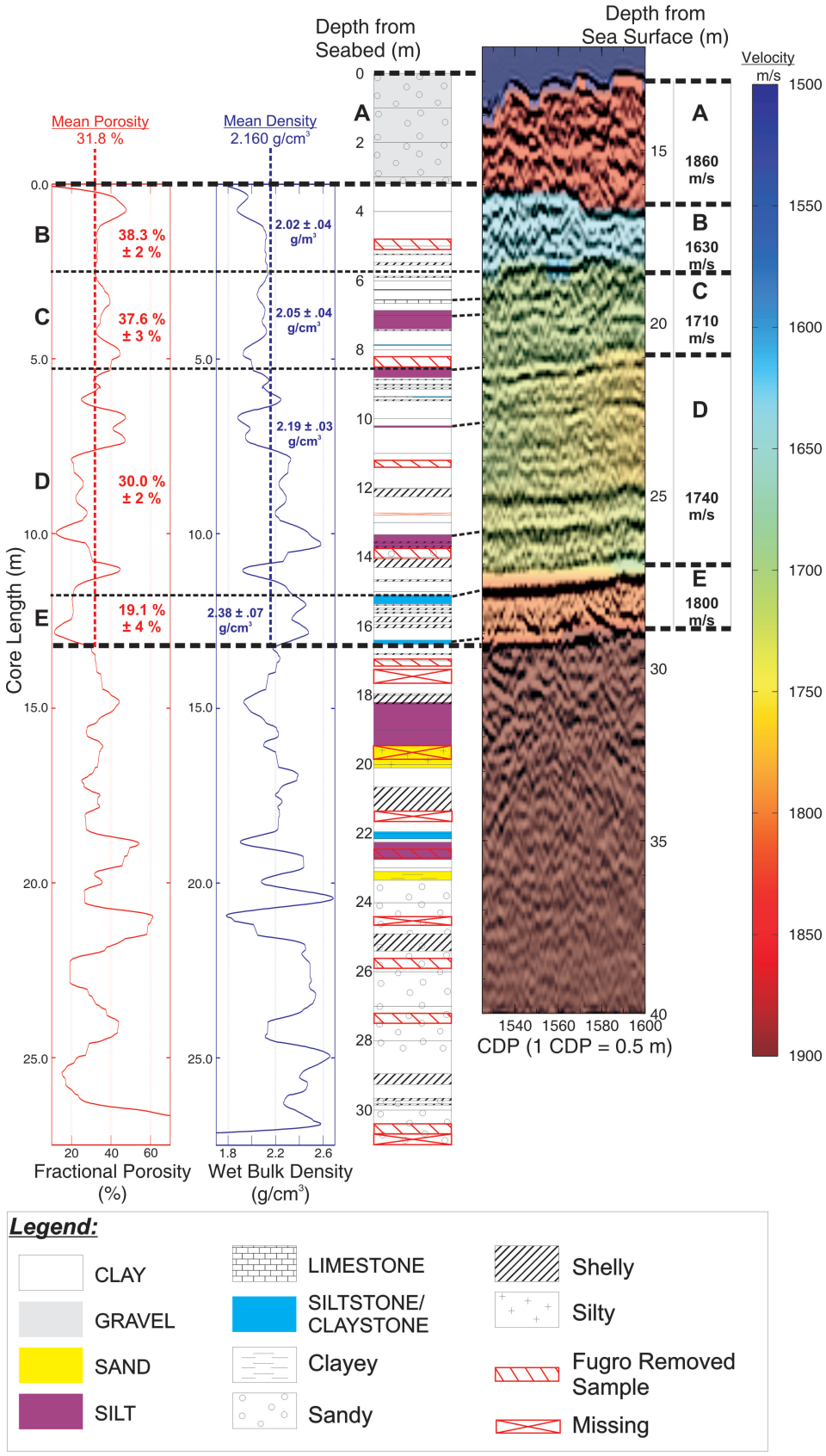

Figure 4.8: Comparison of RC2 laboratory analysis with depth migrated Boomer MCS data. Packages A–E located, with corresponding average velocities, bulk densities and porosities shown.

4.6 Quality Factor Estimates and Grain Size

In Chapter 3, the Holocene sand deposit in location C, which has a mean grain size of 2.5 ϕ (+0.3; −0.3), was found to have a robust Q_{SR} of 66 with a 95% confidence interval of 63 (+10; −7). Applying the same methodology, the Q_{SR} in location D is estimated for the sediment package between the seabed and a strong sub-bottom reflector c. 11 ms (two-way time) beneath, using 640 traces of correlated Chirp data (Figure 4.9a). This spans c. 300 m of sediment across the location of RC2. This strong reflection has been correlated with the consolidated sediment beginning at 15.10 m beneath the seabed within the depth migration data. The mean grain size calculated for the sediment in RC2 above this depth is 6.7 ϕ (+0.3; −0.3) (Appendix C).

The SSP in Figure 4.9b shows an uncontaminated frequency range between 1.5 kHz and 5.25 kHz. From this attenuation trend, 1-kHz uncontaminated frequency bands centred upon 1.75, 2.75, 3.75, and 4.75 kHz are selected for use in the ATP. A linear regression line fits the data within the ATP (Figure 4.9c) with a frequency-independent robust Q_{SR} of 147. The robust Q_{SR} falls within the 95% confidence interval of 154 (+14; −12). The t-statistic is zero, confirming the linear fit and implying that the correlation coefficient of 0.43 is significant.

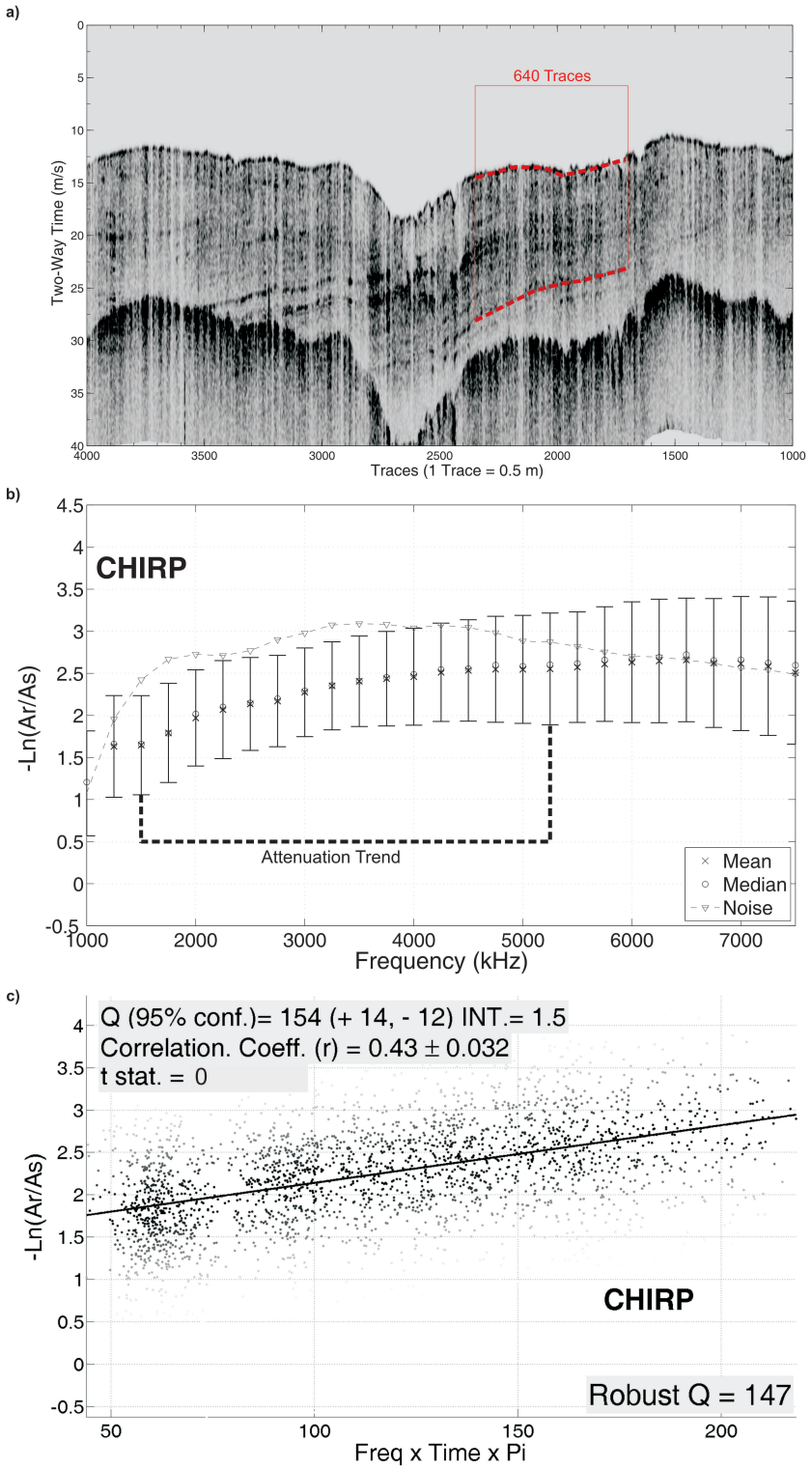

Figure 4.9: a) Chirp profile over location D, with attenuation examined between the seabed and a sub-bottom reflection c. 11 ms beneath (two-way time); b) Chirp SSP exhibiting an uncontaminated attenuation trend 1.5–5.25 kHz; b) ATP using frequency bands 1.75, 2.75, 3.75, and 4.75 kHz and showing the robust Q_{SR} for these sediments.

4.7 Discussion

Figures 4.10 and 4.11 relate compressional-wave velocity to bulk density and porosity respectively, within unconsolidated marine sediments using two empirical regression equations: the continental shelf equations of Hamilton and Bachman (1982) and the equations of Richardson and Briggs (1993) that adapt to the local environment by using the local water velocity to scale the regression coefficients (1490 m/s here—as derived from the depth migrations). The models are divided into sediment type zones using the average bulk densities and porosities of sediment types from Hamilton (1980).

The Richardson and Briggs (1993) model is extrapolated from the coarse sand zone into the gravel zone; this is reasonable because sound velocity increases with increasing mean grain size and decreasing amounts of clay-size sediment (Hamilton and Bachman, 1982). Other velocities, bulk densities and porosities of gravel from the literature agree with this extrapolation (e.g., velocity >1700 m/s, bulk density 2.0–2.5 g/cm^3, and porosity c. 30%: Kim, 2009; Dann et al., 2009).

Considering that the pore-water volume within an unconsolidated sediment can strongly influence the compressional-wave velocity (Akal, 1972; Hamilton and Bachman, 1982), the Richardson and Briggs (1993) regressions are the superior models, and so will be the primary choice for predictions.

The sediment velocity of 1610 ± 20 m/s at location C predicts that the sediment here has a bulk density of 1.91 (+3 ; −4) g/cm^3 (Figure 4.10) and a porosity of 43.5 ± 2% (Figure 4.11), which correlates with a coarse–fine sand (0–3 ϕ). These predictions are in reasonable agreement with the measured bulk density and porosity of the laboratory sample (1.86 ± 0.05 g/cm^3 and 47 ± 3% respectively), and has correctly refined the unconsolidated coarse-grain dominated fabric predicted by the robust Q_{SR} of 66, to sand size grains. The grain size correlation using the average bulk density values from Hamilton (1980) gave the more precise result of fine sand (2–3 ϕ), which matches the sieving result of 2.5 ϕ (+0.3; −0.3). In this case, the velocity determined from MVA is sufficient to accurately predict the physical properties of the unconsolidated sediment using the empirical regressions from Richardson and Briggs (1993).

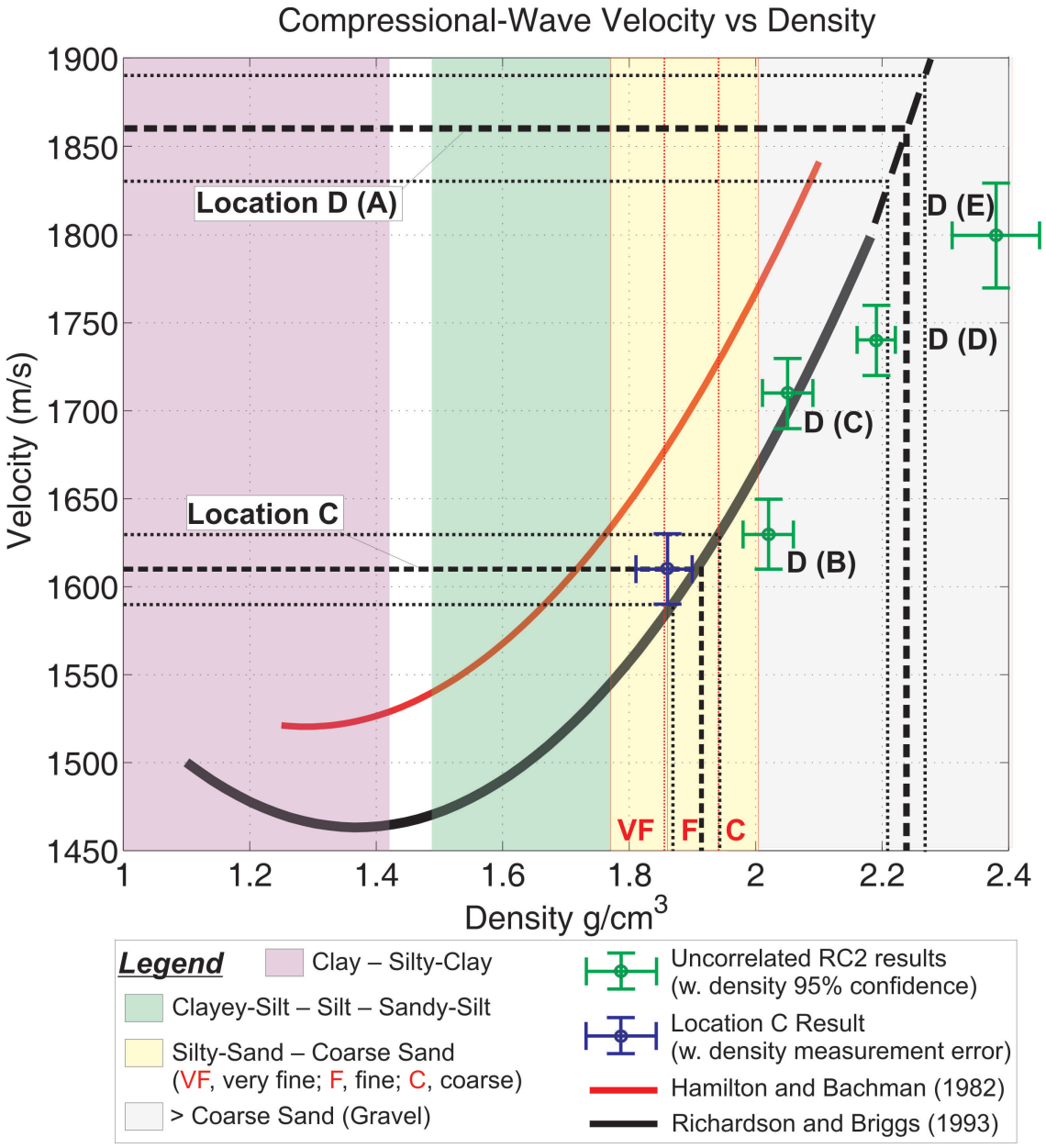

Figure 4.10: Empirical regression models relating compressional-wave velocity with bulk density from Hamilton and Bachman (1982) for continental shelf sediments, and Richardson and Briggs (1993) using the local water velocity of 1490 m/s. Predictions of bulk densities for the sediments from location C, and package A from location D are marked with black dashed lines (the fine dashed lines represent the velocity uncertainty). Green circles locate packages B–E from location D with their measured velocities and bulk densities. The graph is divided into sediment zones defined by the average bulk density values of sediment types from Hamilton (1980). The gravel zone and dashed part of the Richardson and Briggs (1993) model are extrapolated.

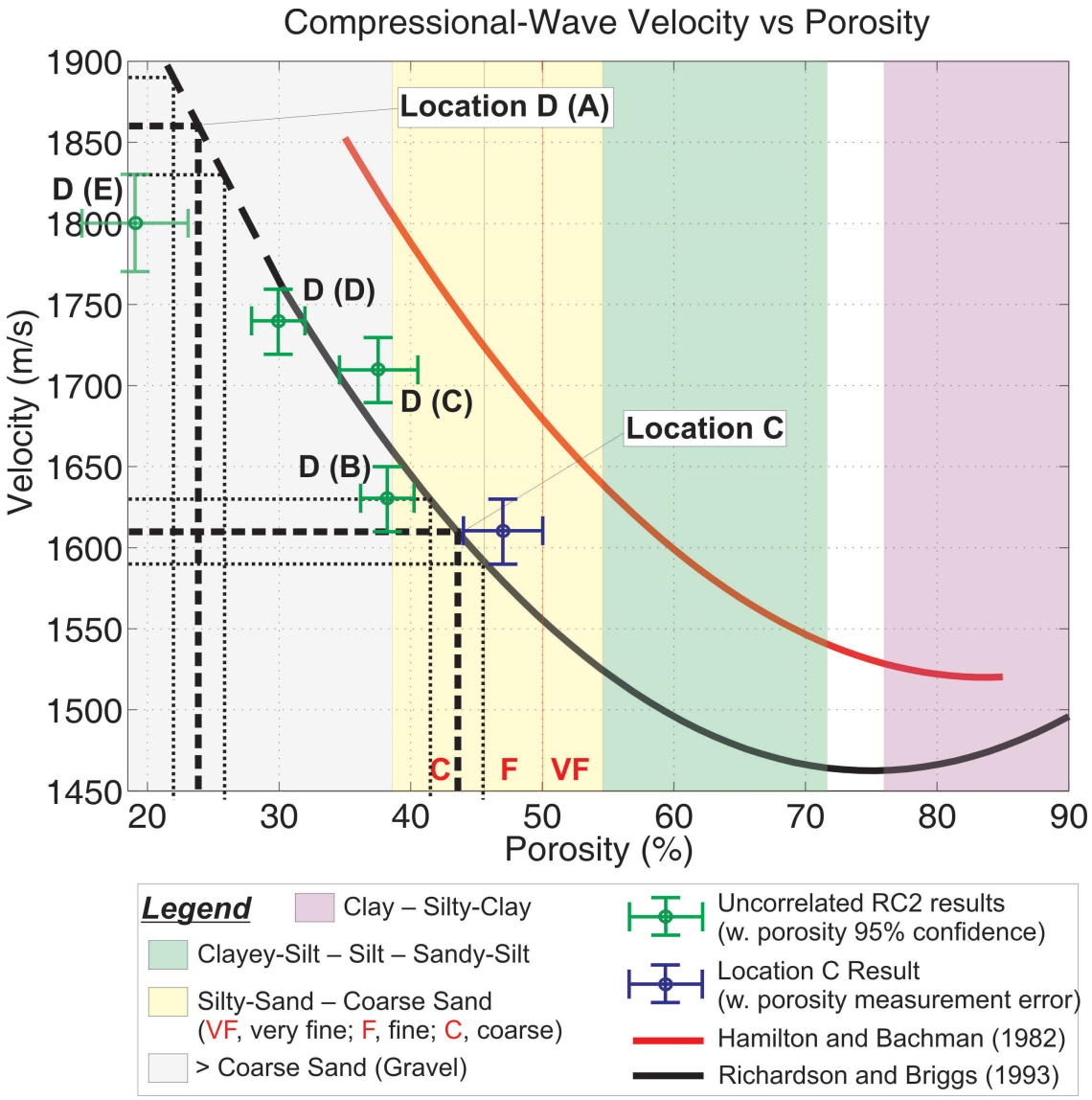

Figure 4.11: Empirical regression models relating compressional-wave velocity with porosity from Hamilton and Bachman (1982) for continental shelf sediments, and Richardson and Briggs (1993) using the local water velocity of 1490 m/s. Predictions of porosities for the sediments from location C, and package A from location D are marked with black dashed lines (the fine dashed lines represent the velocity uncertainty). Green circles locate packages B–E from location D with their measured velocities and porosities. The graph is divided into sediment zones defined by the average porosity values of sediment types from Hamilton (1980). The gravel zone and dashed part of the Richardson and Briggs (1993) model are extrapolated.

In location D, the velocity of 1860 ± 30 m/s for sediment package A that forms the seabed predicts a bulk density of 2.24 ± 0.03 g/cm^3 (Figure 4.10) and a porosity of 24.0 ± 2% (Figure 4.11). These values are consistent with those found within gravel. Unfortunately, a Q_{SR} could not be produced for package A (the gravel layer—Figure 4.8) because its lower-bounding reflection was not coherent in the Chirp data. Other qualitative indicators though, such as its irregular thickness and the presence of waves at the seabed, clearly visible in the depth migrated Boomer data (Figure 4.7), indirectly indicate that this is an unconsolidated, relatively dynamic deposit.

The measured velocities and core bulk densities and porosities for packages B–E at location D, are located on Figures 4.10 and 4.11 with green circles and cross-hairs. The measured porosities and densities for packages B–D obtained from the core are also in reasonable agreement with predictions from the observed seismic velocities, although, generally the measured bulk density tends to be slightly higher and the porosity slightly lower. This is typical of over-consolidated fine-grained sediments (Richardson and Briggs, 1993), which is the case here, as observed from the stiffness of the core material (Appendix C). Package E, which is the most consolidated, falls furthest from the curve. It may have similar bulk density and porosity as the coarse-sand/gravel that the curve is derived from, but does not have a similar bulk and shear moduli.

Hence, the sediment type correlations with predicted density and porosity indicate that the fine-grained sediments within the top 16 m of RC2, which has a mean grain size of 6.7 ϕ ($+0.3$; -0.3), is coarse sand and gravel. However, the robust Q_{SR} of 147 from location D is *not* indicative of unconsolidated coarse-grain dominated sediment (Figure 4.12). Such a high Q_{SR} occurs in sediments with a clay dominated fabric (6–9+ ϕ). Therefore, the high Q_{SR}, and the high velocities of the sediments within RC2, together indicate that location D contains over-consolidated sediments (i.e., with reduced porosity and increased elastic moduli) with a mean grain size of 6–9+ ϕ. This is a key demonstration of the usefulness in cross-plotting velocity and attenuation results for sediment classification.

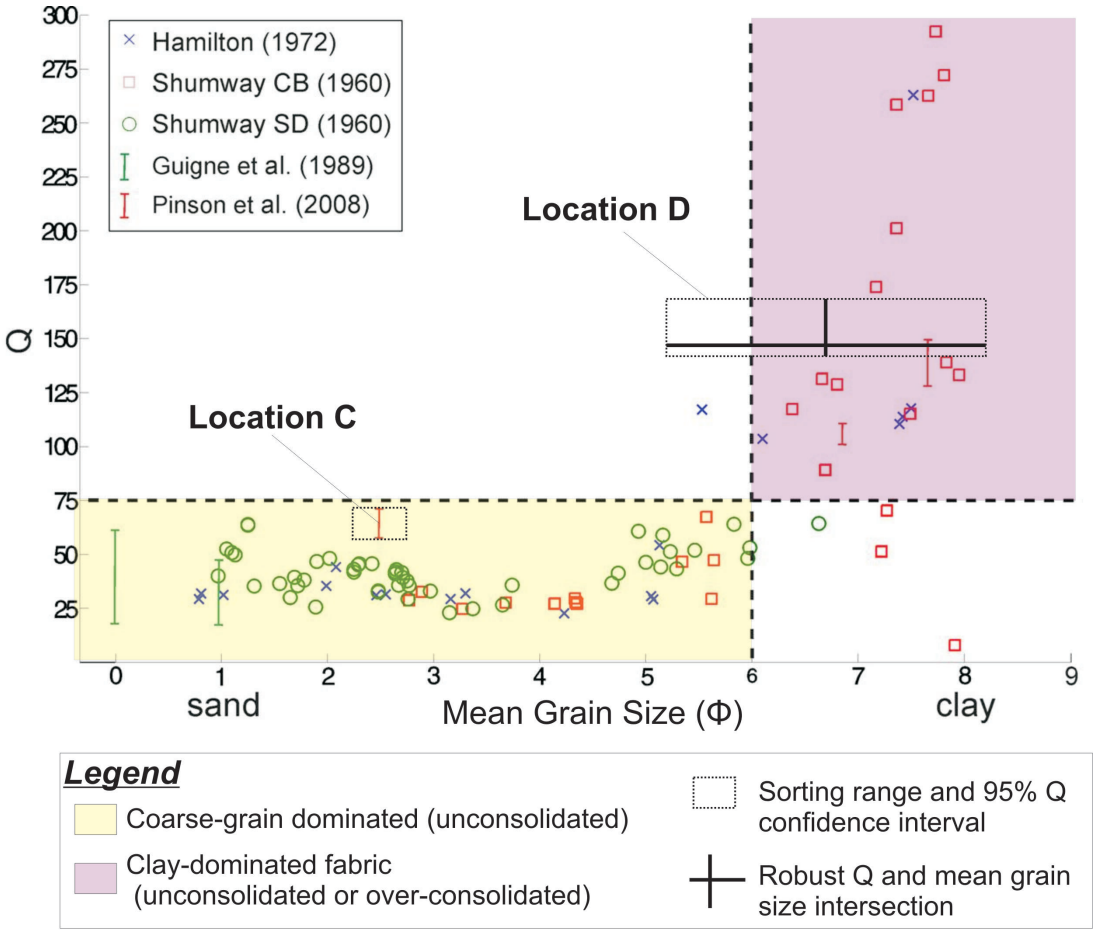

Figure 4.12: Q vs. mean grain size (ϕ) model of empirical data, divided into coarse-grain dominated and clay dominated fabric zones. Results from locations C and D are indicated.

4.8 Conclusions

The migration of Boomer multi-channel seismic data over location C (fine sand) identified a sediment deposit up to 6 m thick with a velocity of 1610 ± 20 m/s. The robust Q_{SR} of 66 obtained from the previous Chirp sonar survey indicated that this deposit was unconsolidated coarse-grained sediment. Subsequent comparison of the velocity to bulk density and porosity using the empirical models for unconsolidated marine sediments from Richardson and Briggs (1993), generated good predictions of the bulk density (1.91 (+3 ; −4) g/cm^3) and porosity (43.5 ± 2%) that were within the measurement error limits for the sample. These values reduced the ambiguity in the coarse-grain sediment prediction and indicate coarse–fine sand (0–3 ϕ).

The sediments contained within a core from location D were correctly predicted as having a clay dominated fabric (6–9+ ϕ) from the robust Q_{SR} of 147, and the seismic velocities made reasonable predictions of the bulk densities and porosities of the sediment packages, despite them being over-consolidated silty-clays. However, this did make the (unconsolidated) sediment type correlation incorrect.

The environment based empirical models from Hamilton and Bachman (1982) are in essence a good idea because different environments contain different sediment types. However, they always predicted velocities that were too high for the sediment here. The insensitivity to local water velocity make them inferior to the Richardson and Briggs (1993) global models.

In summary, the techniques developed for determination of quality factor (Chapter 3) and velocity (this chapter) can be applied to high-resolution seismic reflection data to identify unconsolidated sediments with coarse-grain or clay dominated fabrics, and then determine layer thicknesses, bulk density and porosity, which in turn can refine their grain size. The combination of quality factor observations with sediment type correlations based on predicted bulk density and porosity, can also identify a clay dominated sediment that is over-consolidated. The predictions of bulk density and porosity for over-consolidated clays should be used judiciously because these empirical models were derived from unconsolidated sediments, however, the results here show that the Richardson and Briggs (1993) models are quite robust until velocities greater than 1800 m/s are reached.

Additionally, having estimates of quality factor, velocity, bulk density and porosity allows for more accurate determinations of seabed and sub-bottom reflection coefficients (e.g. Bull et al., 1998), which are important for elucidating sub-seabed geology.

Chapter 5

Windermere Survey

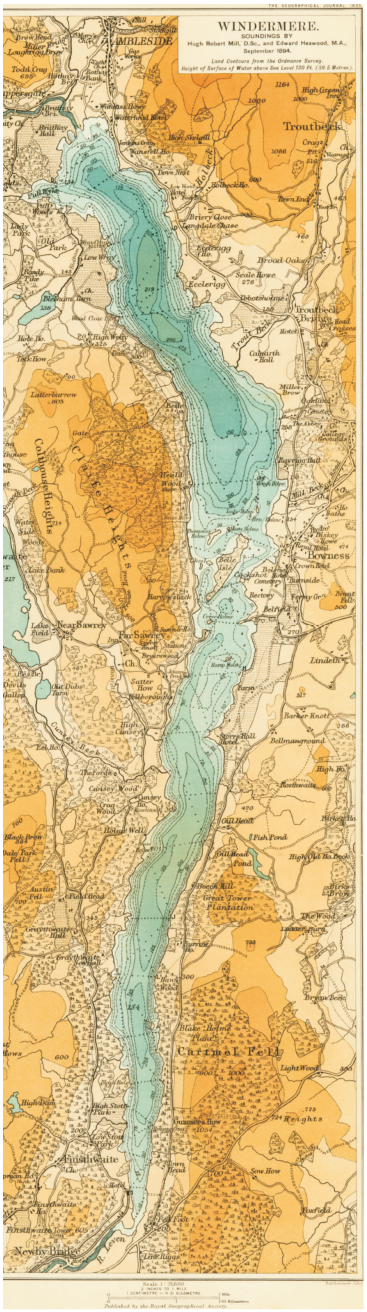

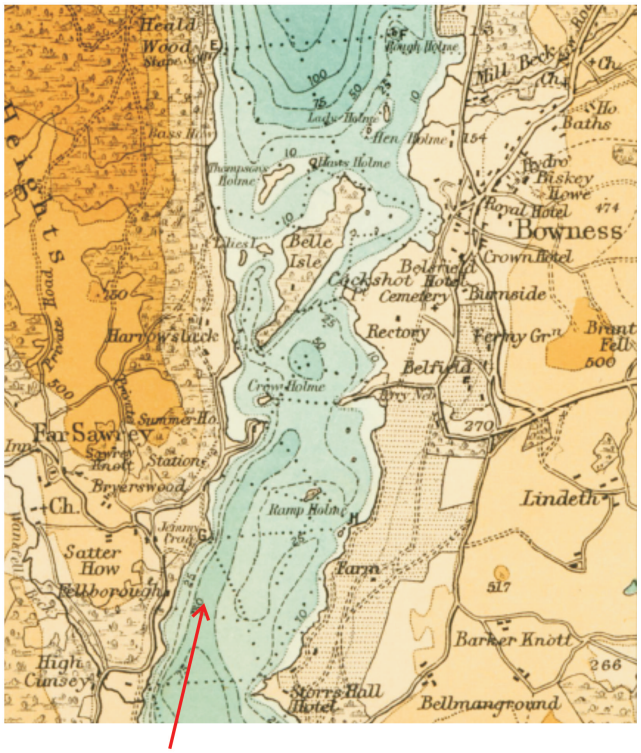

"Remnant of an old river valley..."

Dr. H. R. Mill, 1895, Bathymetrical Survey of the English Lakes, Geography Journal, vol. 6, no. 2, p. 135--166.

"The object of our survey was to lay down on maps the isobaths or contour-lines of depth, and so compare the scenery of the subaqueous with that of the sub-aerial region of the Lake District. I fear that this comparison, however completely it may be made, cannot throw much light on the origin of the lake-basins, for the original hollow, whether it were the result of cracking, or crumpling, or scooping, must be by this time effectually covered by the blankets of ever-thickening sediment, through which no distinct evidence of primitive form can be felt."

Dr. H. R. Mill, 1895, Bathymetrical Survey of the English Lakes, Geography Journal, vol. 6, no. 1, p. 46--73.

Figure 5.1: First depth sounding of Windermere (Mill, 1895).

5.1 Introduction

Windermere is a glacial ribbon lake located in the southeast of the Lake District, UK, and is the largest, and most thoroughly researched natural lake in England (Brodie et al., 2007). The results from the first bathymetric survey by Mill (1895) are shown in Figure 5.1. It has evolved to be 17.7 km long, 1.6 km at the widest point (Holmes, 1964), 0.87 km wide on average (Jenkin, 1942), and has an area of 14.82 km^2 (Mortimer and Worthington, 1942; Pennington, 1991). Windermere is divided into a "North Basin" and "South Basin" (Figure 5.2): the greatest depth is 67 m in the North Basin and 44 m in the South Basin; they have an average depth of 22.3 m; and they have a mean lake-level 39.3 m above sea-level, which fluctuates by 1.8 m (Mortimer and Worthington, 1942).

Glacial lakes make interesting seismic reflection targets because of the high preservation potential of the late-glacial and post-glacial sediment record, and glacial recession structures beneath (e.g. Heim and Finckh, 1984; Eyles and Mullins, 1997; Eyles and J. I. Boyce, 2000). Lakes also provide calmer waters, without tides, making them advantageous to experimental high-resolution geophysics. The study of Windermere was based at the Freshwater Biology Association (FBA) facility situated on the lake (Figure 5.2), and used the Centre for Ecology and Hydrology's survey vessel "The John Lund", to tow the 60 m multi-channel streamer. A previous seismic survey provided evidence that Windermere contained thick sediment packages not obscured by gas (Howell, 1971), hence, Windermere was considered a prime candidate for the following objectives:

1. Measure velocity and attenuation within glacial, glacio-lacustrine, and lacustrine deposits and sediments, and assess the use of empirical models derived from marine sediments for relating acoustic properties to physical properties of lacustrine sediments.

2. Quantify sediment thicknesses and depth to the last glacial retreat surface.

3. Interpret how ice from the British and Irish Ice-Sheet (BIIS) was removed after the Last Glacial Maximum (LGM). Did it actively retreat from the valley

leaving behind morainic retreat structures preserved beneath the sediments, or did it stagnate and melt *in situ*?

4. Identify changes in sedimentation or discrete sediment deposits that may be associated with climatic events.

5. Investigate how methods such as PSDM can improve images and interpretation in this environment.

6. Locate areas of structural interest for a 3D Chirp survey.

Over 150 km of high-resolution MCS data was obtained using the Boomer, with additional single channel Boomer and Chirp data. This chapter details the collection and processing of the data, and Chapter 6 discusses the results and interpretation.

This chapter briefly summarises previous sediment sampling investigations and geophysics surveys in Section 5.2, before Section 5.3 details our own data acquisition in Windermere. Section 5.4 describes: how analysis of the lake-surface ghost notch frequency was used to determine the depth profile of the multi-channel streamer that sagged in fresh water; the processing required to clean the migrated data; and the Kriging method used for producing surfaces of sequence horizons using all the acquired data. Section 5.5 is then a summary.

The results presented here are the first from a lacustrine environment to combine qualitative stratigraphic interpretation with quantitative acoustic attributes on such a high-resolution scale. Additionally, our study is the most comprehensive seismic investigation of a British lake.

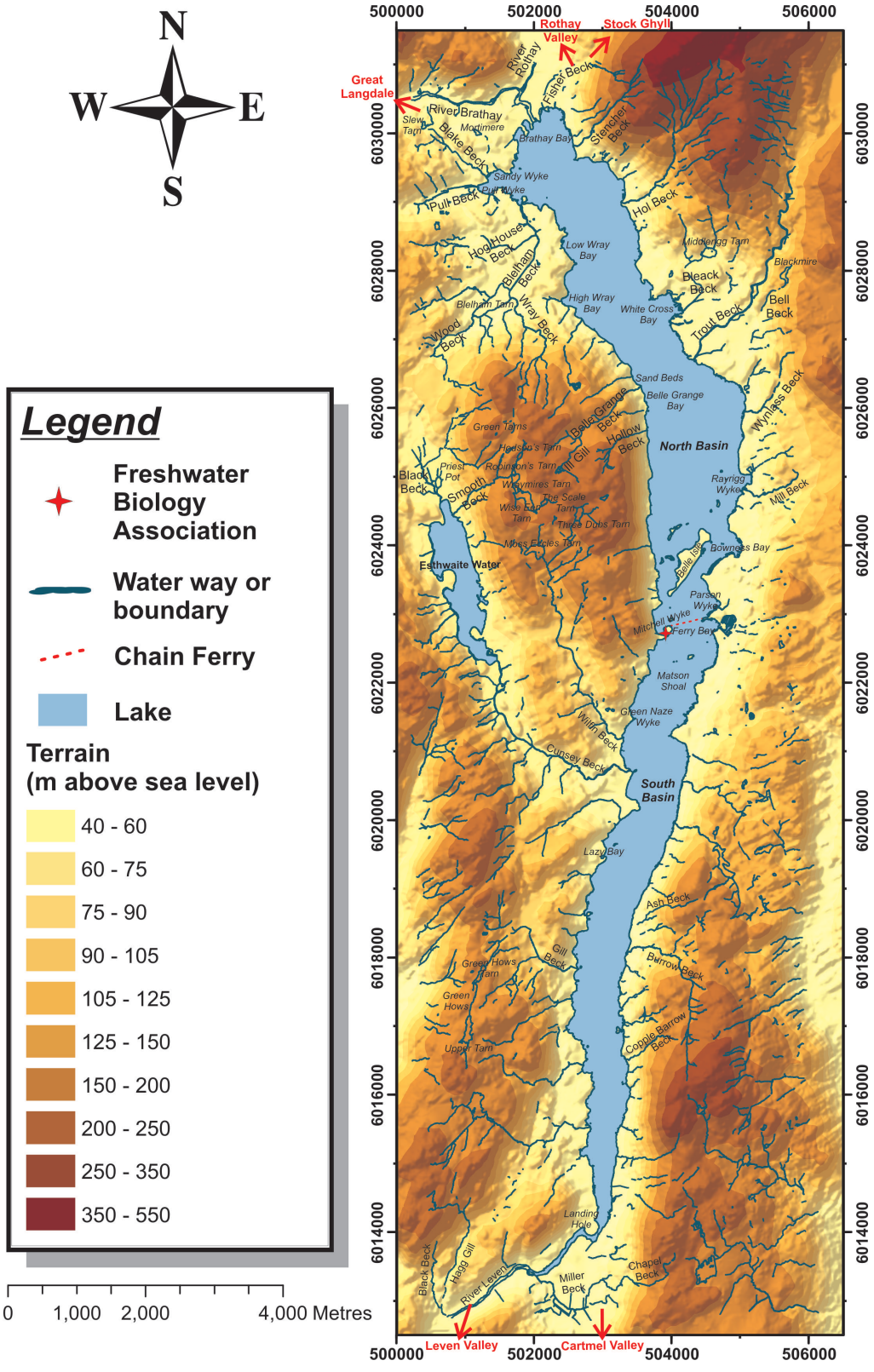

Figure 5.2: Map of Windermere identifying: the North Basin and South Basin; Belle Isle; the FBA; chain ferry crossing; inflows from the surrounding terrain; and the outflow into the Leven Valley. Co-ordinates are UTM zone 30. Terrain is an interpolated surface of OS Land-Form Profile DTM 1:10000 data from Edina Digimap.

5.2 Previous Surveys and Windermere Sediments

5.2.1 Core Investigations

Cores from the basins have revealed a detailed history of the biological and climatic conditions within the Windermere catchment since deglaciation, and have been fundamental to palaeolimnology research in Britain since the first 6 m core was taken almost 70 years ago using a Jenkin core-sampler (Jenkin et al., 1941). The most detailed representations of the 6 m FBA cores taken from Windermere are found in Holmes (1964), and are used where possible to relate to the seismic data in this study.

Dredging Investigations Ltd prospected for aggregate in Windermere in 1971. They used a shell and auger which bored down to 16 m. Their results complement the FBA cores well because they were targeting coarser sediment beneath the lacustrine fines, and reported sediments based upon their grain size using terms from The British Soil Classification System for Engineering Purposes: G (gravel) and S (sand) for coarse components; F (fine soil), M (silt) and C (clay) for fine components (Somerville, 1983). Again, where possible these results are related to the seismic data.

5.2.2 Geophysics

Two land seismic refraction surveys identified a rock bar between the southern end of Windermere and the Cartmel Valley, beneath a veneer of morainic material (Coster and Gerrard, 1947; Wilson, 1987). This indicated that the valley was never truly dammed by a moraine as originally claimed by Marr (1896, 1916). Both investigations question how the lower outlet into the adjacent Leven valley formed: was it water or ice eroded? Wilson (1987) concluded that both valleys were formed before the Devensian glaciation by diffluent action at this juncture, and that the overflow into the Leven Valley has over-time been enhanced fluvially by the outflow from Windermere. However, neither study commented on the deserted glacial drainage channel on the west side of the lower reach of Windermere, which was formed in the final retreat stages of the BIIS by melt-waters emanating from the glacier in

the South Basin, and draining through the Levin Valley (Hollingworth, 1951). Perhaps melt-water produced by the retreating BIIS is the main agent of erosion that created the outflow into the Leven Valley?

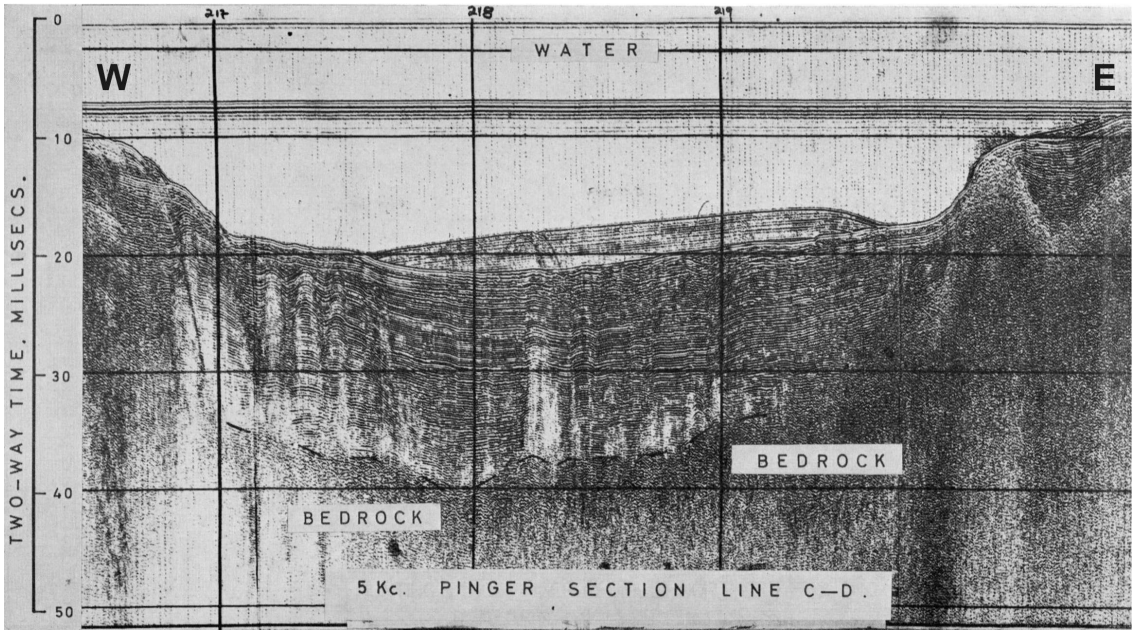

Figure 5.3: Pinger profile along chain ferry route (Howell, 1971).

Howell (1971) published Pinger and Sparker profiles of Windermere showing that the sediment deposits in the central areas of the lake were vastly thicker than historic coring could have predicted. He assumed a fresh water velocity of 1483 m/s (Kaye and Laby, 1966), and 1540 m/s for the unconsolidated sediments of the lakebed for depth estimation. He identified "bedrock" (possibly a till surface) at a maximum of 73 m beneath lake-level in the North Basin and 75 m in the South Basin, and sediment thicknesses up to 21 m in the North Basin and 40 m in the South Basin. He separated the sediment into two types, which can be seen in Figure 5.3: a lower layer exhibiting closely spaced acoustic reflectors draped over irregular hollows, containing contortions due to consolidation and slumping; an upper layer rarely exceeding 3 m in thickness, which contains fewer internal acoustic reflectors and no contortions, with incomplete coverage of the lake. The incomplete coverage of the upper layer is demonstrated in his figure (Figure 5.3) showing a transect following the chain ferry route (then serviced by the steam-powered "Drake"). This area was too hazardous for us to survey due to the shallow water, and the diesel

powered "Mallard" making a return crossing every 20 minutes.

Windermere has also been previously surveyed using an analogue Boomer by Gerald Sergeant, a now retired professor of geology from Queensland University. He built his own Boomer system (McCarthy, 2007), and ran lines across Windermere in the 1983 and 1987. Paper sections are held at the FBA but the navigation is poor.

5.3 Survey Methodology

5.3.1 Boomer MCS Data Acquisition

A Boomer survey employing the 60 m multi-channel streamer was carried out over the 26th–28th of September 2007 on "The John Lund" captained by Ben James (Figure 5.4). Over 150 km of data was collected within 57 lines (where the streamer was towing straight) and recorded onto five DDS-4 tapes. The custom-built multi-channel streamer comprises sixty 1-metre spaced groups of seven hydrophone elements, and was towed 10–20 m behind the source. The catamaran mounted Boomer (Applied Acoustic Engineering AA200) operated at 300 J with a shot trigger every

Figure 5.4: Aboard "The John Lund": a) Inside the cabin; b) 60 m multi-channel streamer; c) Deployed Boomer towed alongside MCS and yellow warning buoys. Photos by Mark Vardy and Luke Pinson.

750 ms, and had a layback of 9 m or 13 m behind the boat. The data was recorded with a sample interval of 0.125 ms and a record length of 150 ms on the customised Geometrics Strataview R60, which was networked to a computer recording the data real-time to tapes in SEGD format. An on-board DGPS receiver provided sub-metre boat positioning. Figure 5.5 shows the acquisition geometry in measurements relative to the on-board DGPS antenna, as required by the *2D marine geometry spreadsheet* in ProMAX®. The layback of the 1st channel behind the boat ($Z_{Layback}$) is derived from calculating the distance between it and the source utilising the direct velocity arrival (v_{da}), and added to the known layback of the source. The survey was conducted with a survey speed of c. 3 knots (1.5 m/s), giving an along track sampling of approximately 1 m for all channels. Figure 5.6 shows the straight MCS Boomer lines over the lake with their corresponding day/year-line tag; the MCS lines used in this thesis for PSDM appear in red. Tables 5.1–5.3 at the end of this section contain the start and end FFIDs of each MCS line, with the source and receiver laybacks from the antenna and the heading of the survey line.

The survey strategy produced many diagonal cross-lines from one side of the lake to the other in order to cover as much of the lake as possible. MCS lines 2807-line2, 2807-line3 and 2807-line4, follow the same axis line of the North Basin as an axial section derived from cores in Pennington (1943) and Holmes (1964).

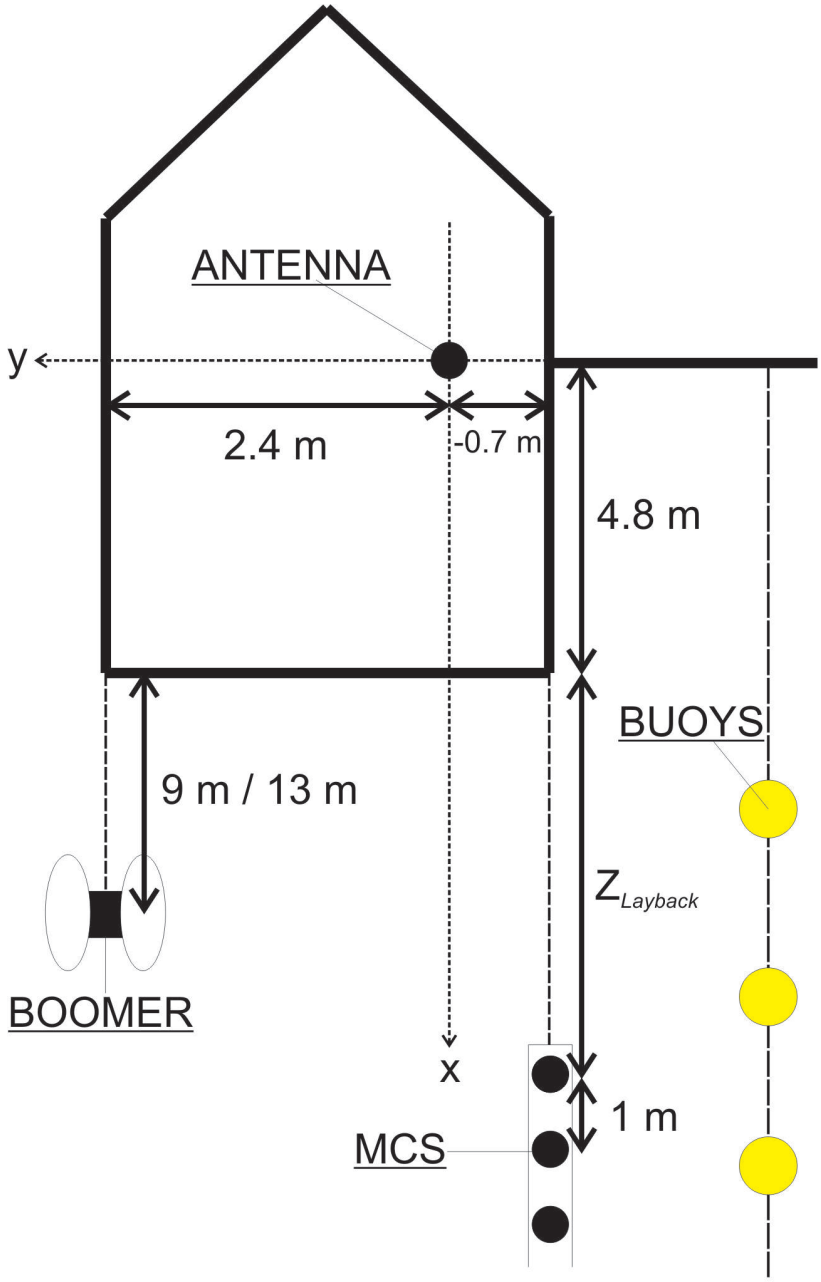

Figure 5.5: Boomer and multi-channel streamer geometry on board "The John Lund". Measurements are relative to x and y about the antenna, as required by ProMAX®.

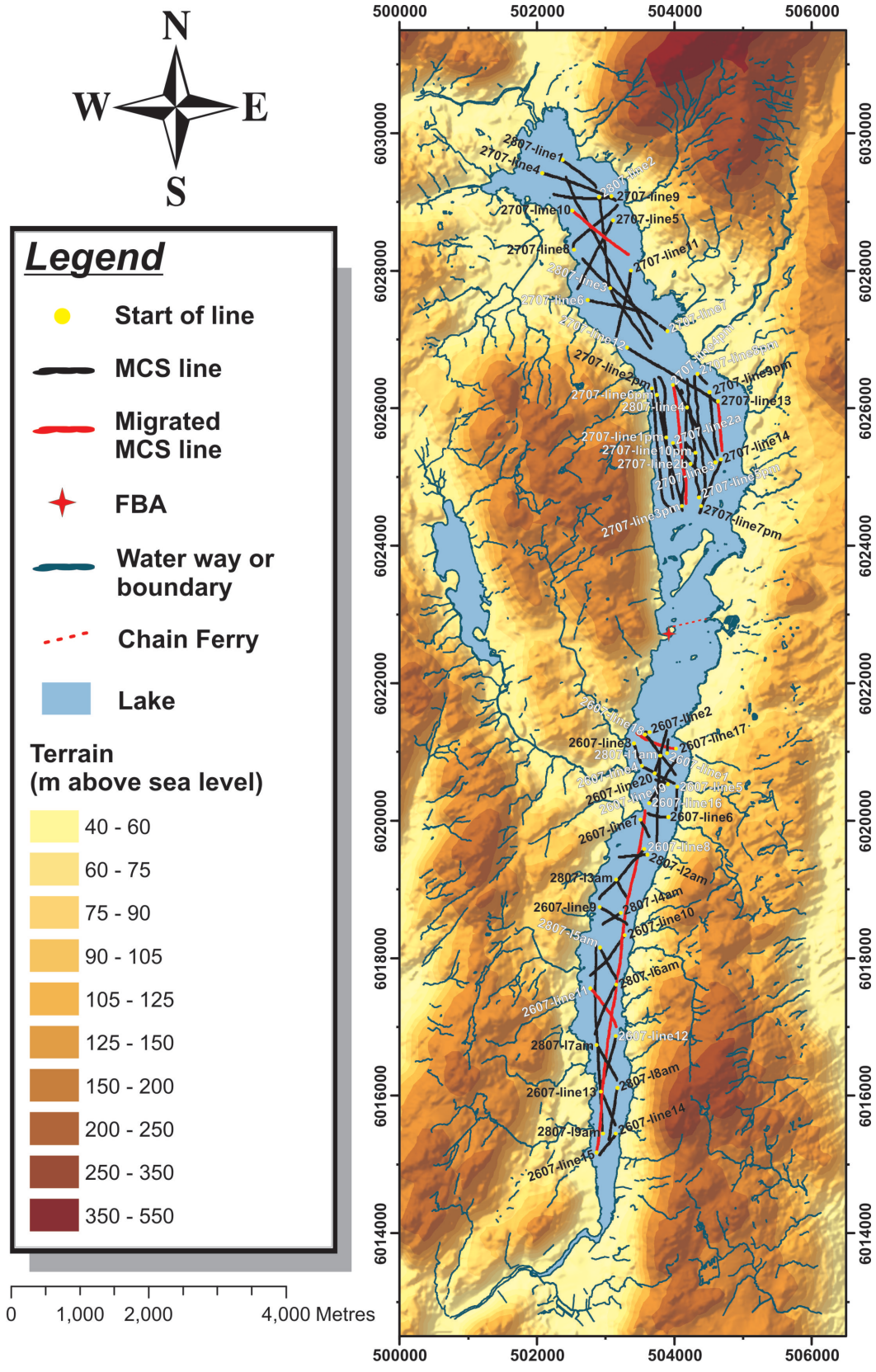

Figure 5.6: Map locating the 57 straight Boomer MCS lines over Windermere. The lines have their day/year-line labels (black or white) located at the start of each line. The 6 lines migrated for this thesis are red. Co-ordinates are UTM zone 30.

5.3.2 Boomer Single Channel Seismic Data Acquisition

The MCS dataset was augmented with single channel Boomer profiles where anthropogenic factors, and/or proximity to the lake shore, prevented safe use of the 60 m multi-channel streamer. On the 26th of September single channel Boomer data was collected in the North Basin by "The John Lund". A 7 m streamer, with seven hydrophone elements forming a single hydrophone group, was towed directly behind the source. The survey was conducted at c. 4 knots (2 m/s) and the DGPS antenna was located on "The John Lund", as in Figure 5.5, providing sub-metre boat positioning. The Boomer operated at 300 J with a shot trigger every 500 ms, and the data was recorded on a CODA system with a sample interval of 0.05 ms and a record length of 256 ms. Figure 5.7 shows the single channel Boomer data collected in the North Basin, with the MCS data and the core site locations.

5.3.3 Chirp Seismic Data Acquisition

Single channel Chirp data was collected from an electric tourist launch (Figure 5.8) hired from Shepherds (Windermere) Ltd. The DGPS antenna was mounted on the Chirp catamaran providing sub-metre shot positioning, and the Chirp mini-streamer was towed directly behind. Data was recorded on the CODA system. On the 24th of September sweep W32 was used (16.38 ms long), triggering every 250 ms, and recorded with a sample rate of 0.026 ms, and a 133 ms record length. On the 25th of September sweep W13 was used (32.77 ms long), triggering every 250 ms, and recorded with a 0.026 ms sample rate, and a 137 ms record length. Using the higher energy sweep W13 produced better images, but the effective 105 ms trace after correlation was not long enough to see to the bottom of thick sediment deposits, which were usually beneath c. 40 m of water (equivalent to 55 ms two-way time). A longer record length of at least 163 ms would have given, a more adequate, 130 ms of effective correlated trace. Both W13 and W32 are linear sweeps with a sine-squared taper function covering 1/8th of the time duration (Gutowski et al., 2002), and have the same wide effective power spectrum of 1.5–13.0 kHz.

The aims of the single channel Chirp survey were: to pass over the known shell and auger sites taken by Dredging Investigations Ltd (1970); to explore briefly the

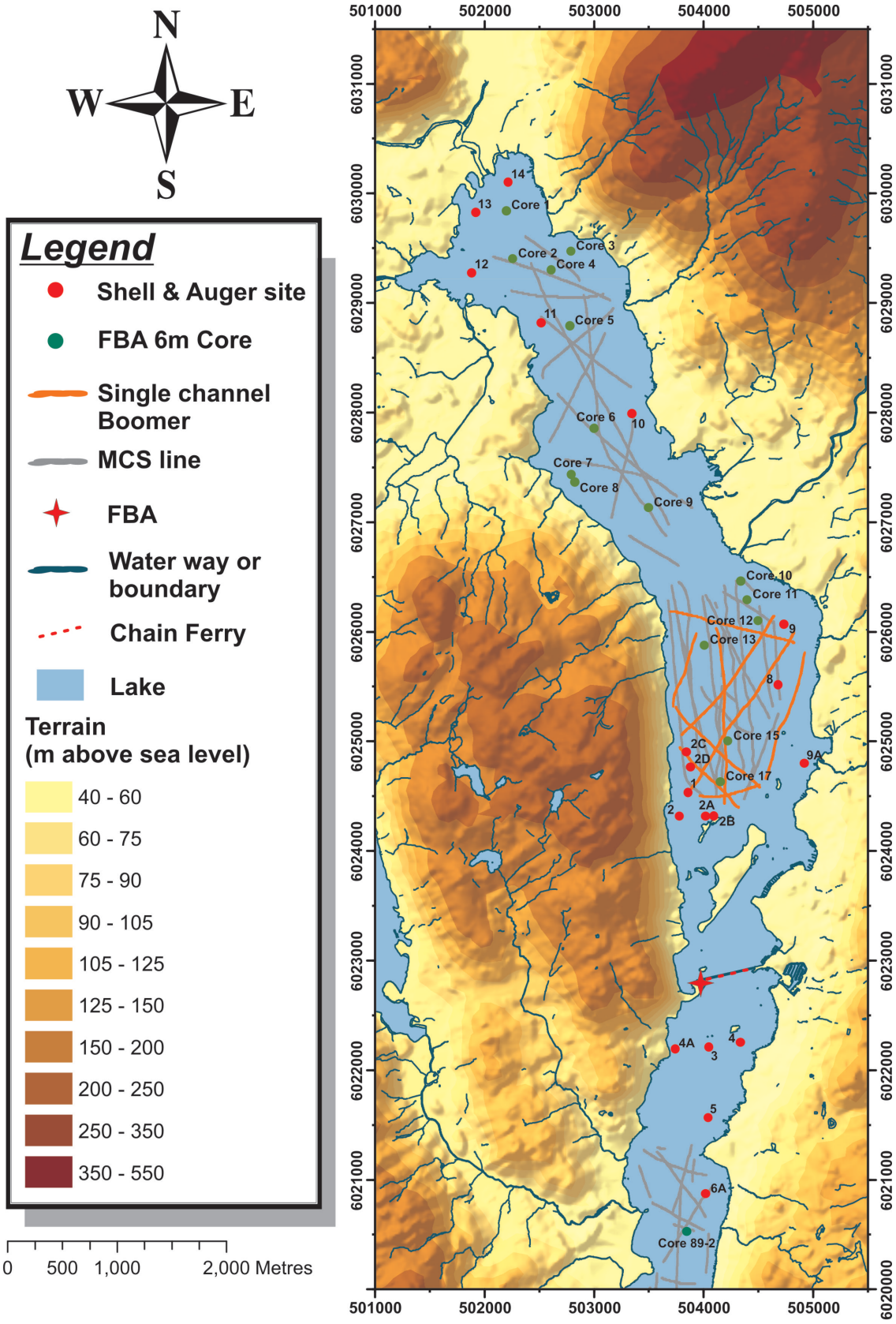

Figure 5.7: Map locating the single channel Boomer data in the North Basin, with the MCS data in grey behind, and the core locations. Co-ordinates are UTM zone 30.

South basin; to take cross-sections over the North Basin; and to obtain data using a greater bandwidth for estimations of sediment Q. Figure 5.9 shows the single channel Chirp data collected and the locations of the core sites.

A 3D Chirp survey was carried out in February 2008 over two areas that contained complex slump deposits. Details of this survey can be found in Vardy (2009) and Vardy et al. (2010). The single channel and 3D Chirp data are shown in Figure 5.9, along with the core site locations.

Figure 5.8: Aboard a Shepherds Ltd electric tourist launch: a) DGPS, CODA system, and Geoacoustics Chirp box; b) Canvas hood protecting operators and equipment from rain; ear defenders protecting operators from generator noise; c) Launch towing the Chirp sonar with mounted antenna.

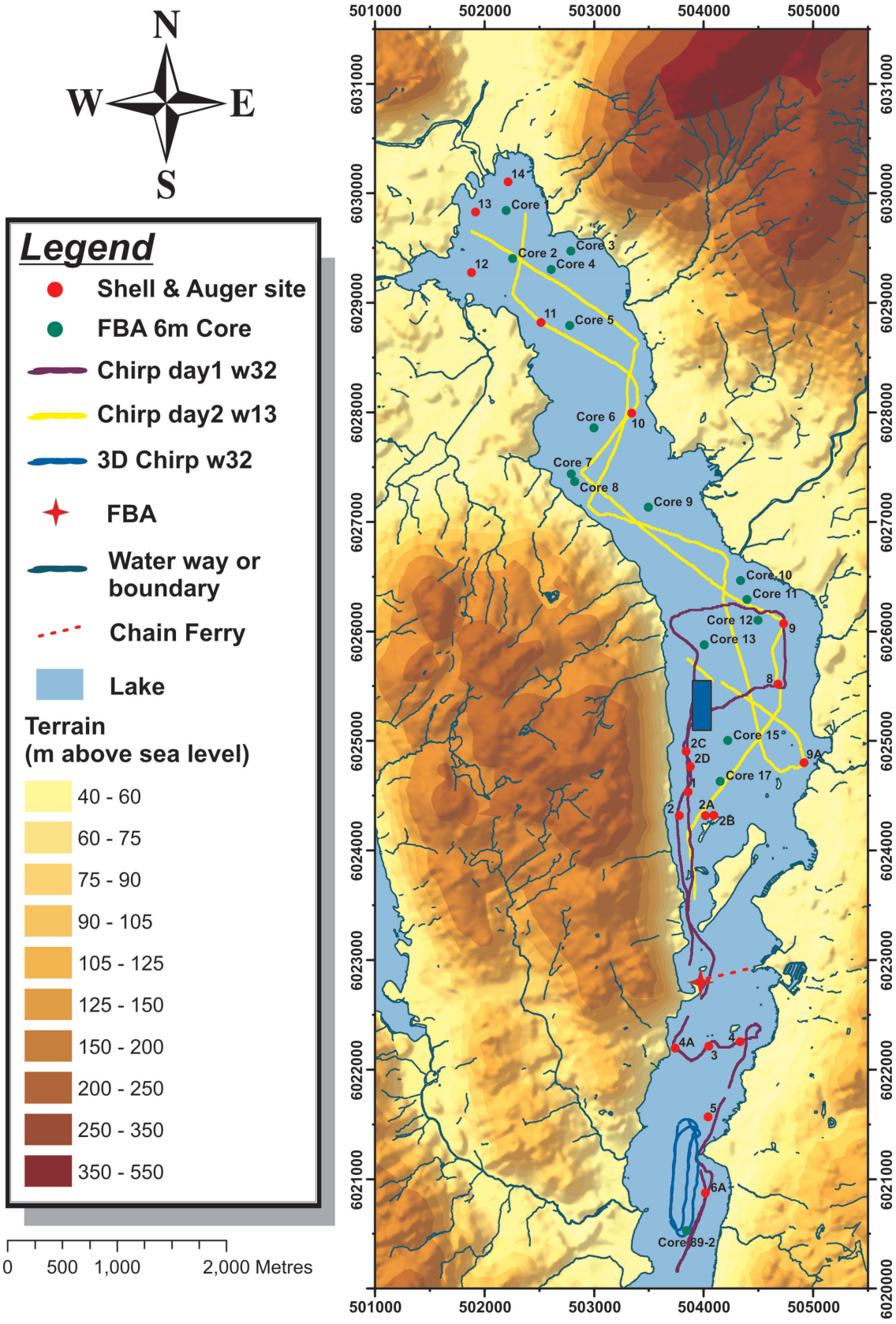

Figure 5.9: Map locating the Chirp data over Windermere, with the core locations. The blue box is the location of the 3D chirp volume described in Vardy (2009) and Vardy et al. (2010). Co-ordinates are UTM zone 30.

Basin-d/y-label	FFIDs	V_{da} (m/s)	Source Offset (m)	Receiver Offset (m)	Heading (°)
(South Basin)					
SB-2607-line1	113–250	1470	13.8	22.2	4.0
SB-2607-line2	454–510	1470	13.8	22.0	272.7
SB-2607-line3	660–830	1470	13.8	22.5	160.3
SB-2607-line4	860–1170	1470	13.8	27.7	118.3
SB-2607-line5	1200–1390	1470	13.8	28.4	183.6
SB-2607-line6	1480–1670	1470	13.8	28.7	278.5
SB-2607-line7	1760–1915	1470	13.8	28.0	152.4
SB-2607-line8	2030–2580	1470	13.8	28.2	222.5
SB-2607-line9	2650–2920	1470	13.8	27.7	122.0
SB-2607-line10	3030–3460	1470	13.8	28.4	220.2
SB-2607-line11	3580–4000	1470	13.8	28.0	145.1
SB-2607-line12	4070–4508	1470	13.8	28.2	197.0
SB-2607-line13	4575–4901	1470	13.8	28.0	157.0
SB-2607-line14	4975–5210	1470	13.8	28.4	218.0
SB-2607-line15	5561–8839	1470	13.8	28.0	8.2
SB-2607-line16	8910–9380	1470	13.8	28.0	32.3
SB-2607-line17	9460–9820	1470	13.8	28.9	291.7
SB-2607-line18	9950–10370	1470	13.8	28.1	142.9
SB-2607-line19	10520–10630	1470	13.8	28.7	286.6
SB-2607-line20	10700–11116	1470	13.8	28.0	15.5

Table 5.1: MCS Boomer data contained on tapes 1 and 2, collected on the 26/09/07 in the South Basin.

Basin-d/y-label	FFIDs	V_{da} (m/s)	Source Offset (m)	Receiver Offset (m)	Heading (°)
(North Basin)					
NB-2707-line2a	690–905	1465	13.8	31.3	134.0
NB-2707-line2b	905–1019	1465	13.8	28.0	134.0
NB-2707-line3	1242–4130	1465	13.8	29.0	332.0
NB-2707-line4	4550–5196	1465	13.8	29.5	110.3
NB-2707-line5	5300–5970	1465	13.8	28.8	207.1
NB-2707-line6	6118–6750	1465	13.8	29.4	104.1
NB-2707-line7	7148–8150	1465	13.8	28.6	309.7
NB-2707-line8	8250–8814	1465	13.8	29.4	48.8
NB-2707-line9	8947–9420	1465	13.8	28.7	272.2
NB-2707-line10	9720–10595	1465	13.8	29.2	128.9
NB-2707-line11	10735–11268	1465	13.8	29.0	193.2
NB-2707-line12	11400–12240	1465	13.8	29.2	120.8
NB-2707-line13	12604–13000	1465	13.8	29.1	175.5
NB-2707-line14	13070–13520	1465	13.8	28.9	202.2
NB-2707-line1pm	13600–14150	1465	13.8	28.9	353.1
NB-2707-line2pm	14290–15367	1465	13.8/17.8 (14790)	29.0	172.2
NB-2707-line3pm	15570–16912	1465	17.8	28.8	347.5
NB-2707-line4pm	17235–18384	1465	17.8	28.8	173.4
NB-2707-line5pm	18750–20406	1465	17.8	28.7	354.1
NB-2707-line6pm	20950–22076	1465	17.8	28.8	171.3
NB-2707-line7pm	22611–24436	1465	17.8	28.5	354.4
NB-2707-line8pm	24899–25184	1465	17.8	28.8	135.5
NB-2707-line9pm	25288–26015	1465	17.8	28.7	173.1
NB-2707-line10pm	26430–26595	1465	17.8	28.2	313.9

Table 5.2: MCS Boomer data contained on tapes 3 and 4, collected on the 27/09/07 in the North Basin. On NB-2707-line2pm the Boomer layback was increased at FFID 14790.

Basin-d/y-label	FFIDs	V_{da} (m/s)	Source Offset (m)	Receiver Offset (m)	Heading (°)
(South Basin)					
SB-2807-line1am	136–1029	1470	17.8	29.5	182.3
SB-2807-line2am	1160–1427	1470	17.8	28.7	264.9
SB-2807-line3am	1692–1930	1470	17.8	29.5	149.4
SB-2807-line4am	2102–2300	1470	17.8	29.2	239.2
SB-2807-line5am	2558–2910	1470	17.8	29.5	152.5
SB-2807-line6am	2971–3490	1470	17.8	29.4	203.1
SB-2807-line7am	3600–4000	1470	17.8	29.5	149.5
SB-2807-line8am	4060–4570	1470	17.8	29.3	189.1
SB-2807-line9am	4825–6851	1470	17.8	28.8	357.3
(North Basin)					
NB-2807-line1	10200–10670	1465	18.8	29.7	127.5
NB-2807-line2	10770–11700	1465	18.8	29.7	173.7
NB-2807-line3	11700–13035	1465	18.8	30.0	144.2
NB-2807-line4	13180–14233	1465	18.8	29.8	182.8

Table 5.3: MCS Boomer data contained on tape 5, collected on the 28/09/07 in the South and North Basins.

5.4 Processing Methodology

5.4.1 Geometry Correction

A problem inherent to surveying a fresh water lake was sagging of the 60 m multi-channel streamer. Assuming a simple constant streamer depth for prestack depth migration (PSDM) in this situation produces bowed common reflection point (CRP) gathers—or complex residual move-out (RMO)—and leads to inaccuracies in velocity estimation, which produces inaccurate depths and a poor migration.

If the source-receiver geometry is correct, the primary reflections in the CRP gathers should exhibit linearity when the correct interval velocities are used. Figure 5.10 and Figure 5.11 demonstrate the problem of using CRP gathers with an incorrect streamer depth profile, by using a constant streamer depth of 0.5 m with MCS line 2607-line11 in the South Basin. Figures 5.10a and 5.11a, have a water velocity of 1490 m/s above an evident thermocline (c. 20 m) and 1550 m/s beneath, and a sediment velocity gradient increasing from 1460 m/s to 1950 m/s at the sediment bottom. This velocity model brings the furthest offset in line with the nearest offset within the CRP gathers. The arrivals are bowed, but are near-linear for the offsets 0–45 m, and then again for offsets 45–80 m, with different RMOs. Using a velocity model to best image offsets of 0–45 m produces a depth of 105 m to the bottom of the sediment, and requires a water velocity of 1510 m/s above the thermocline, 1610 m/s below, and a sediment velocity gradient that increases to 2600 m/s at the sediment bottom (Figure 5.10b and Figure 5.11b). Using a velocity model that best images offsets of 45–80 m produces a shallower depth of 85 m to the bottom of sediment, and requires a water velocity of 1490 m/s, and a sediment velocity gradient that increases to 1850 m/s at the sediment bottom (Figure 5.10c and Figure 5.11c).

Using a constant streamer depth of 0.5 m for prestack migration produces bowed CRP gathers of almost uniform shape throughout the MCS sections, regardless of reflector geometries, depth, line orientation, the basin being surveyed, or which day the survey took place. The fresh water velocity also appears anomalously high on all MCS lines (see Appendix D for appropriate fresh water velocities here and historical

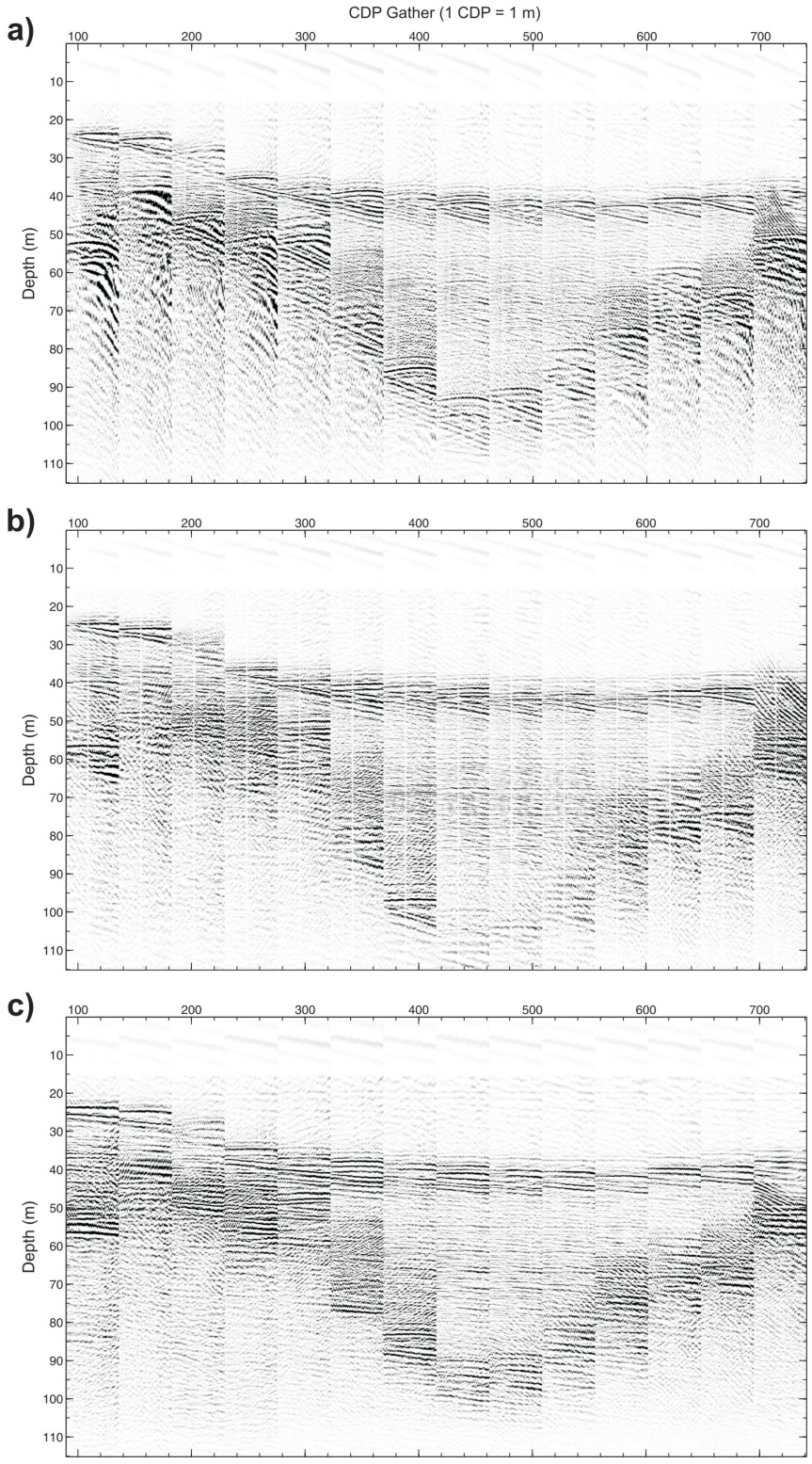

Figure 5.10: Depth migrated CRP gathers from MCS line 2607-line11 in the South Basin: a) Full offset range (0–80), using a velocity model that aligns the nearest and furthest offset within the CRP gathers; b) Near offset gathers (0–45 m) flattened using a faster velocity model to remove RMO; c) Far offset gathers (45–80 m) flattened using a slower velocity model to remove RMO.

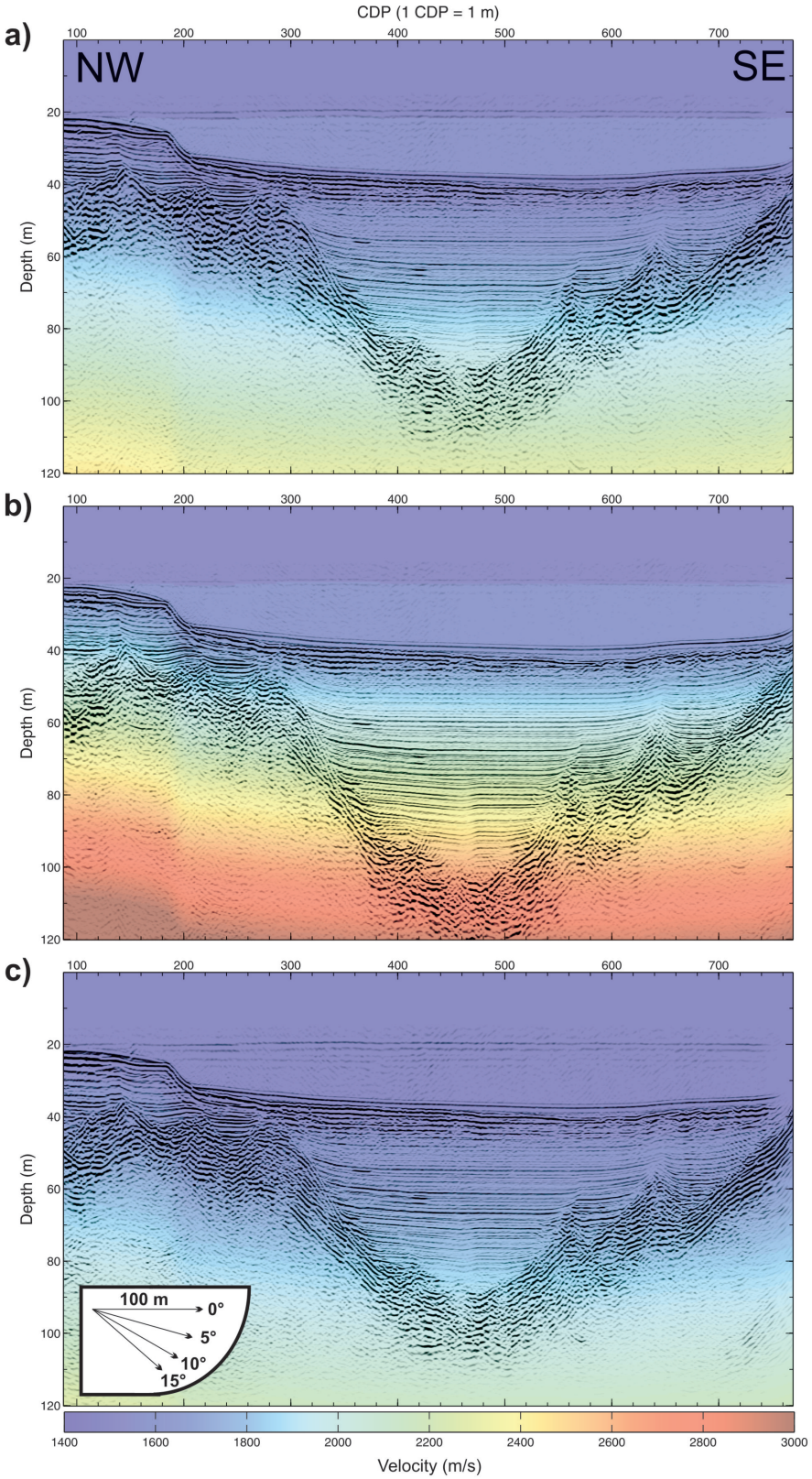

Figure 5.11: PSDM images of MCS line 2607-line11 from the South Basin, with velocity models designed to remove RMO from the CRP gathers: a) the full offset range (0–80 m); b) the near offsets (0–45 m); c) the far offsets (45–80 m).

measurements of the thermocline), in both near and far offsets, as demonstrated above. The shape of the CRPs indicates that energy is arriving sooner at the middle channels relative to the other channels than expected. Such a scenario is conceivable if the streamer is sagging in the fresh water. The streamer is filled with oil that makes it neutrally buoyant in seawater (density c. 1025 kg/m^3). When in fresh water (density c. 1000 kg/m^3), travelling at survey speed (1.5 m/s), the more distal channels are likely to tow deeper than the front channels, which are being pulled towards the surface by the boat. The tow buoy attached to the end may also drag the last channels towards the surface, allowing the streamer to sag towards the centre.

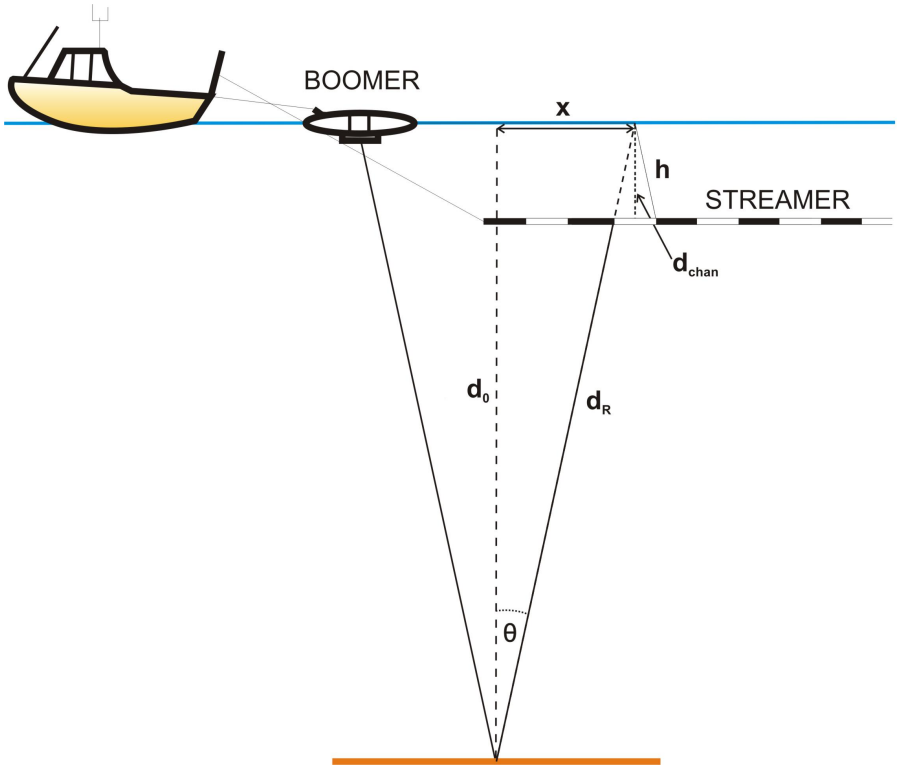

Figure 5.12: Ghost notch frequency analysis: Boomer and streamer geometry above a deep lakebed reflection in Windermere. The depth of the streamer beneath the lake surface is exaggerated.

The depth to each channel in the steamer, during a straight line at nominal survey speed, can be determined from the ghost notch frequencies. Figure 5.12 shows how up-going seismic energy is reflected at the water-air interface (where the phase is reversed) and recorded by the hydrophone channel again. This will produce

a notch in the power spectrum at frequency f_{notch} through destructive interference, where half the wavelength (λ) associated with f_{notch} is equal to h, the distance travelled from the surface to the channel, at surface water velocity v_{vda} (obtained from the direct arrival):

$$2h = \lambda = \frac{v_{vda}}{f_{notch}}. \tag{5.1}$$

A similar technique has been implemented by Kragh and Combee (2000) where the streamer depth profile is deduced from the reflections recorded at each channel from a horizontal saline-brine interface, and ghost notch frequency analysis is used to determine the instantaneous sea surface elevation above each receiver. During the Windermere survey fluctuations in height of the lake surface were negligible and will average over shots to determine the streamer depth profile. From Figure 5.12, distances d_0, d_R and d_{chan} can be redefined as:

$$d_0 = \frac{t_0 \times v_{ave}}{2}; \tag{5.2}$$

$$d_R = \frac{twt \times v_{ave}}{2}; \tag{5.3}$$

$$d_{chan} = \frac{t_h \times v_{vda}}{2}. \tag{5.4}$$

Here t_0 is the two-way time at normal incidence, twt is the two-way time between the source and a receiving channel, and v_{ave} is the constant velocity field assumed to be encountered by energy propagating from near to far offsets. For the ghost reflection from the lake surface, t_h is the two-way time directly between the streamer and the surface, at the surface velocity (v_{vda}). Using equivalent angles, h can be redefined as:

$$h = \frac{t_h \times v_{vda}}{2cos\theta}. \tag{5.5}$$

Assuming the chosen reflection is deep enough relative to the distance between the source and the near offset, t_0 can be approximated with the *twt* recorded at the nearest channel (twt_{chan1}), and any small error in θ incurred by assuming a symmetrical travel path between the source and the receiving channel (which is not at the surface), will be negligible. This allows $cos\ \theta$ to be expressed in terms of time, which is readily available from the seismic trace:

$$cos\ \theta = \frac{2t_0 \times v_{ave}}{2twt \times v_{ave}} = \frac{t_0}{twt} \approx \frac{twt_{chan1}}{twt}. \tag{5.6}$$

Substituting into (5.5),

$$h = \frac{t_h \times v_{vda} \times twt}{2twt_{chan1}}. \tag{5.7}$$

Multiplying by 2 and substituting back into (5.1) gives:

$$\lambda = \frac{v_{vda}}{f_{notch}} = \frac{t_h \times v_{vda} \times twt}{twt_{chan1}}, \tag{5.8}$$

hence,

$$t_h = \frac{twt_{chan1}}{f_{notch} \times twt}. \tag{5.9}$$

Thus, t_h for each channel can be found by identifying f_{notch} and using the *twt* of the original reflection. The depth of each channel, d_{chan}, can then be calculated using Equation (5.4).

Two locations from the North Basin are chosen for ghost notch frequency analysis: traces in CDPs 3265–3365 from MCS line 2707-line3 (Figure 5.13a), and traces in CDPs 1355–1415 from MCS line 2707-line10 (Figure 5.13b). These lines survey in different orientations and pass over the deepest parts of Windermere (c. 65 m). The large *twt* to the lakebed minimises the angle of incidence upon the lakebed and the lake surface, thus, minimising errors introduced by the assumptions. To check the depth is satisfactory for our approximation in Equation (5.6), $d_{R(chan1)}$ is calculated

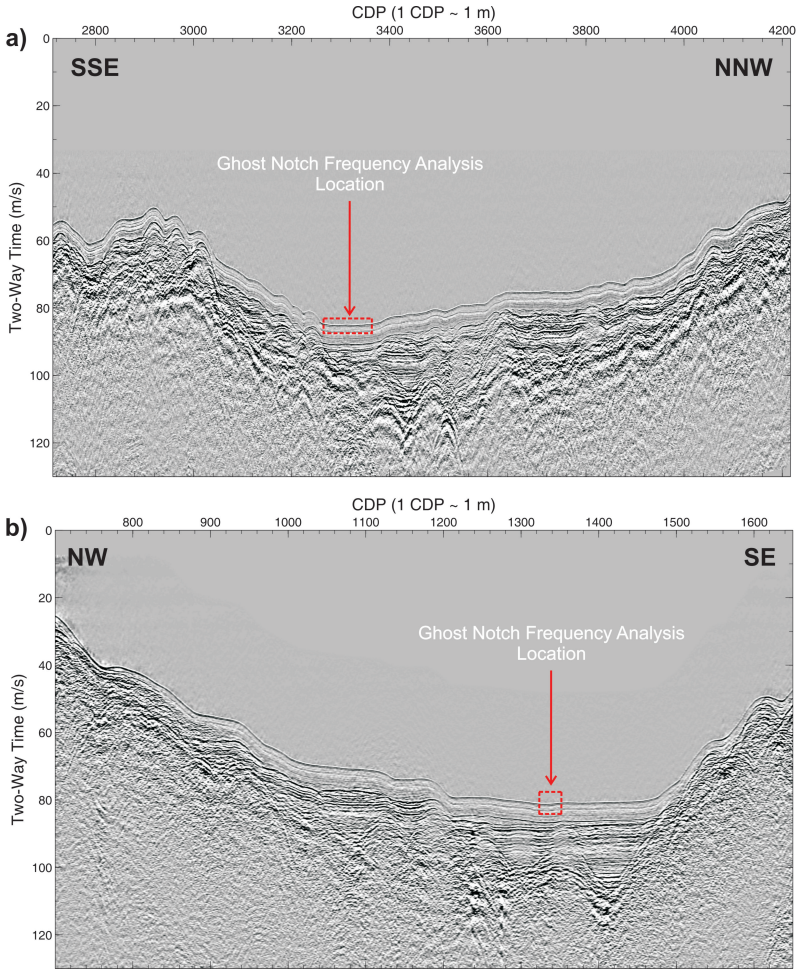

Figure 5.13: North Basin lines used for ghost notch frequency analysis: a) MCS line 2707-line3 traces 3265–3365; b) MCS line 2707-line10 traces 1355–1415.

and compared to d_0. From Figure 5.12, θ can be found by:

$$tan\theta = \frac{x}{d_0}. \tag{5.10}$$

Assuming d_0 is 65 m, and using the source-receiver offset (x_{chan1}) calculated for those lines, c. 15 m,

$$\theta = 6.6°. \tag{5.11}$$

Hence, the distance travelled to the nearest channel is,

$$d_{R(chan1)} = \frac{d_0}{cos\theta}, \tag{5.12}$$

$$d_{R(chan1)} = 65.4\ m. \tag{5.13}$$

The difference between d_0 and $d_{R(chan1)}$ is less than 1%. Comparing θ produced by using $d_{R(chan1)}$ instead of d_0 for offsets 16 m (channel 2) and 75 m (channel 60), gives 3.2° instead of 7.0°, and 29.4° instead of 30.0° respectively.

As expected, the approximation for theta at the near offsets is less precise, however, given the cosines of 3.2° and 7.0° are 0.998 and 0.993 respectively, the error incurred on the calculation of t_h from Equation (5.9) is negligible. Thus, the approximations using the geometry from these lines are sufficient.

The ghost notch frequency is determined on each channel using *Interactive Spectral Analysis* in ProMAX®. The traces from the CDPs contain reflections from a near horizontal lakebed that are all windowed together, obtaining an average power spectrum for each channel. The first notch to appear in the power spectrum is identified as the receiver ghost notch, as demonstrated in Figure 5.14 with its associated harmonics. As the Boomer is towed c. 10 cm below the surface, the source ghost notch would be of higher frequency than the receiver notch. Figure 5.15 shows the depth profiles derived from MCS lines 2707-line3 and 2707-line10 using the v_{vda} of 1465 m/s from the North Basin, and the resulting 3rd degree polynomial fit that is shown in Equation (5.14) below:

$$d_{chan}(v_{1465}) = -0.0000087 \times chan^3 - 0.000084 \times chan^2 + 0.065 \times chan... + 1.37. \tag{5.14}$$

Both lines show similar profiles and the difference in the number of traces used (100 for MCS line 2707-line3 and 60 for MCS line 2707-line10) evidently has little effect. Figure 5.15 shows that the first channel is 1.4 m below the surface, where the streamer descends at a steady rate until channel 30, 3 m below the surface. From

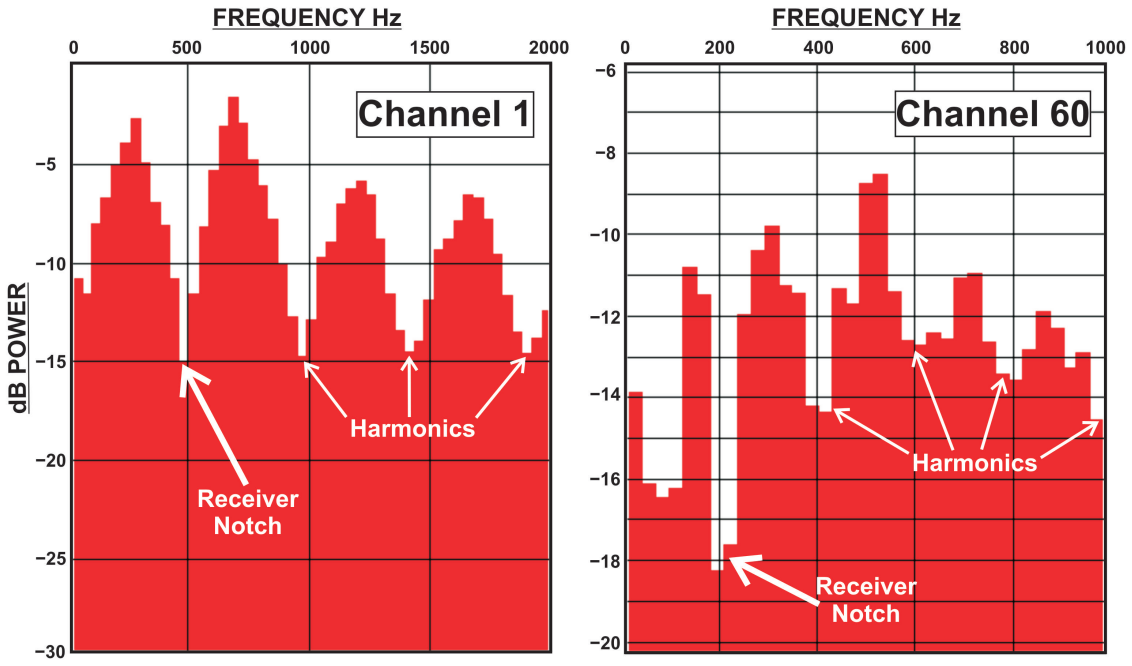

Figure 5.14: Receiver ghost notch frequency identification on channels 1 and 60, from the lakebed on MCS line 2707-line10.

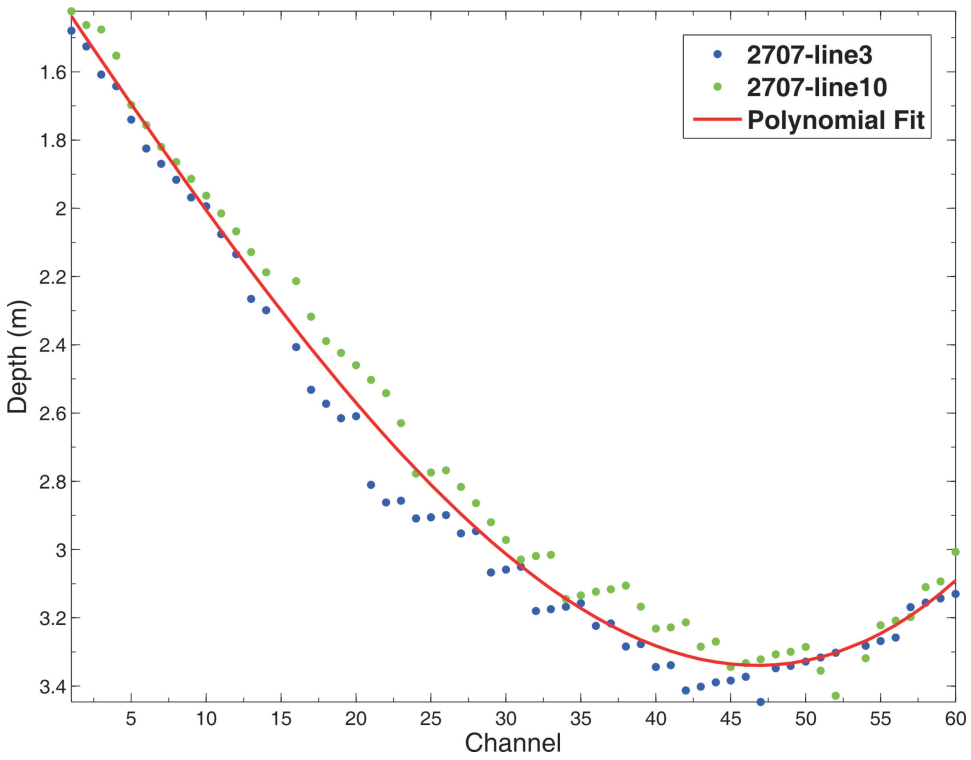

Figure 5.15: Streamer depth profiles from two lines in the North Basin, obtained using ghost notch frequency analysis.

here the rate of descent reduces and the streamer reaches a maximum depth of 3.3 m at channel 45. The last 15 channels then rise towards the surface again, with channel 60 at a depth of 3 m. The depth profile is consistent with the shape of the bowed CRP gathers, with the sag reaching a maximum between the near and far offsets.

To correct for the streamer sag, new receiver depths are calculated using Equation (5.14) in *Trace Header Math*(ProMAX®), and then applied to the geometry database using *Database/Header Transfer*(ProMAX®), so each channel has a true depth assigned to it for migration. Figure 5.16 shows the migrated data from MCS line 2607-line11 following depth corrections. The CRP gathers in Figure 5.16a are no longer bowed, and RMO is removed at the lakebed using a reasonable velocity for fresh water of 1450 m/s (Appendix D).

Accounting for the streamer sag immediately enhances the prestack depth migration of MCS line 2607-line11 (Figure 5.16b) and all other MCS lines, regardless of velocity model complexity. This is further demonstrated here by migrating another line from the South Basin using a simple uniform velocity model of 1470 m/s (the local v_{vda}). Figures 5.17a and 5.17b show MCS line 2607-line17 migrated using a simple streamer geometry of 0.5 m below the surface, and Figures 5.17c and 5.17d show the migration with the sag corrected geometry applied. The lakebed CRP gathers in Figure 5.17a exhibit an apparent negative RMO, normally indicating a higher fresh water velocity is required. Figure 5.17c shows that with the corrected geometry the lakebed CRP gathers exhibit linearity, and the stack in Figure 5.17d shows improved focussing of energy beneath deposits, and unsurprisingly, a sharper lakebed reflection than Figure 5.17b.

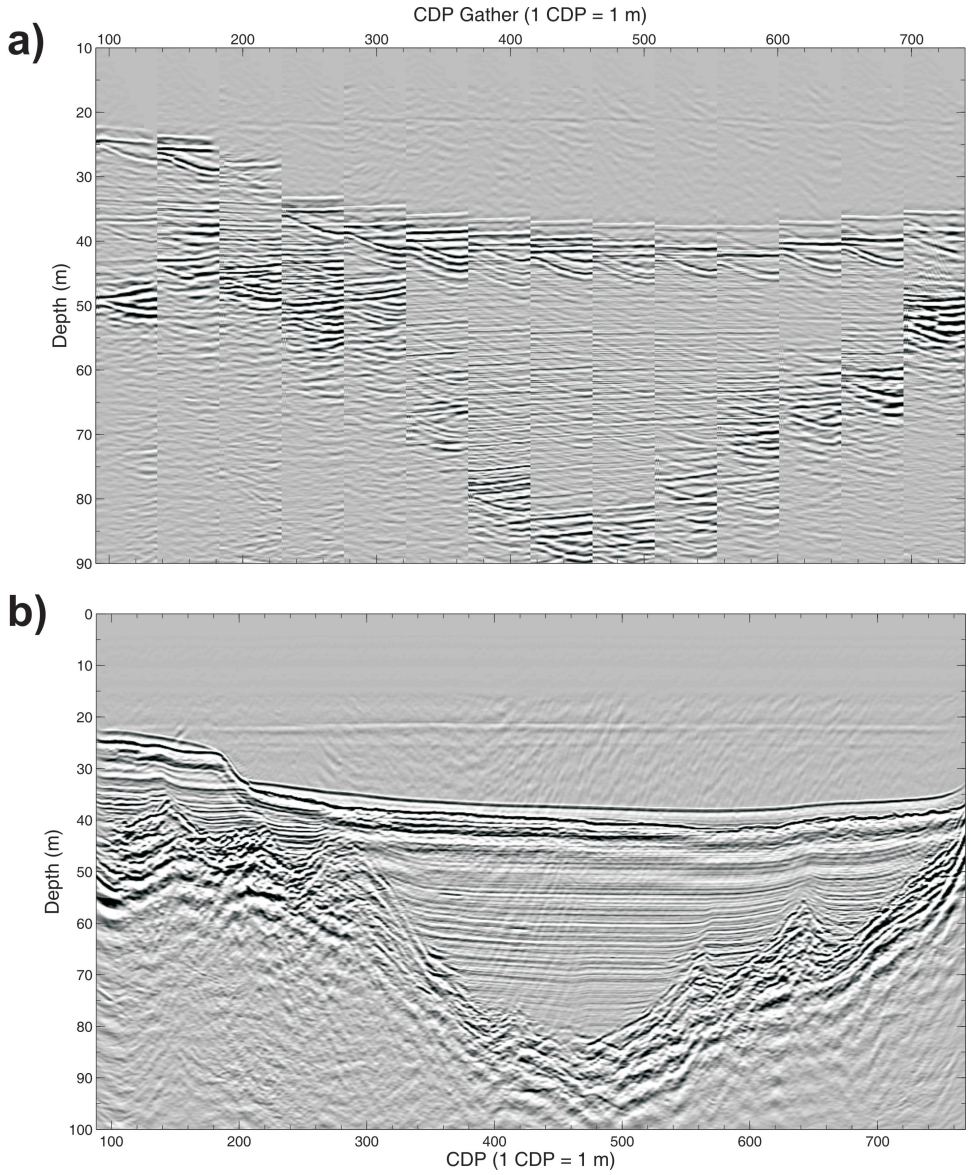

Figure 5.16: Migration of MCS line 2607-line11 using streamer sag corrected geometry, with a constant 1450 m/s velocity model: a) CRP gathers; b) Migrated depth section.

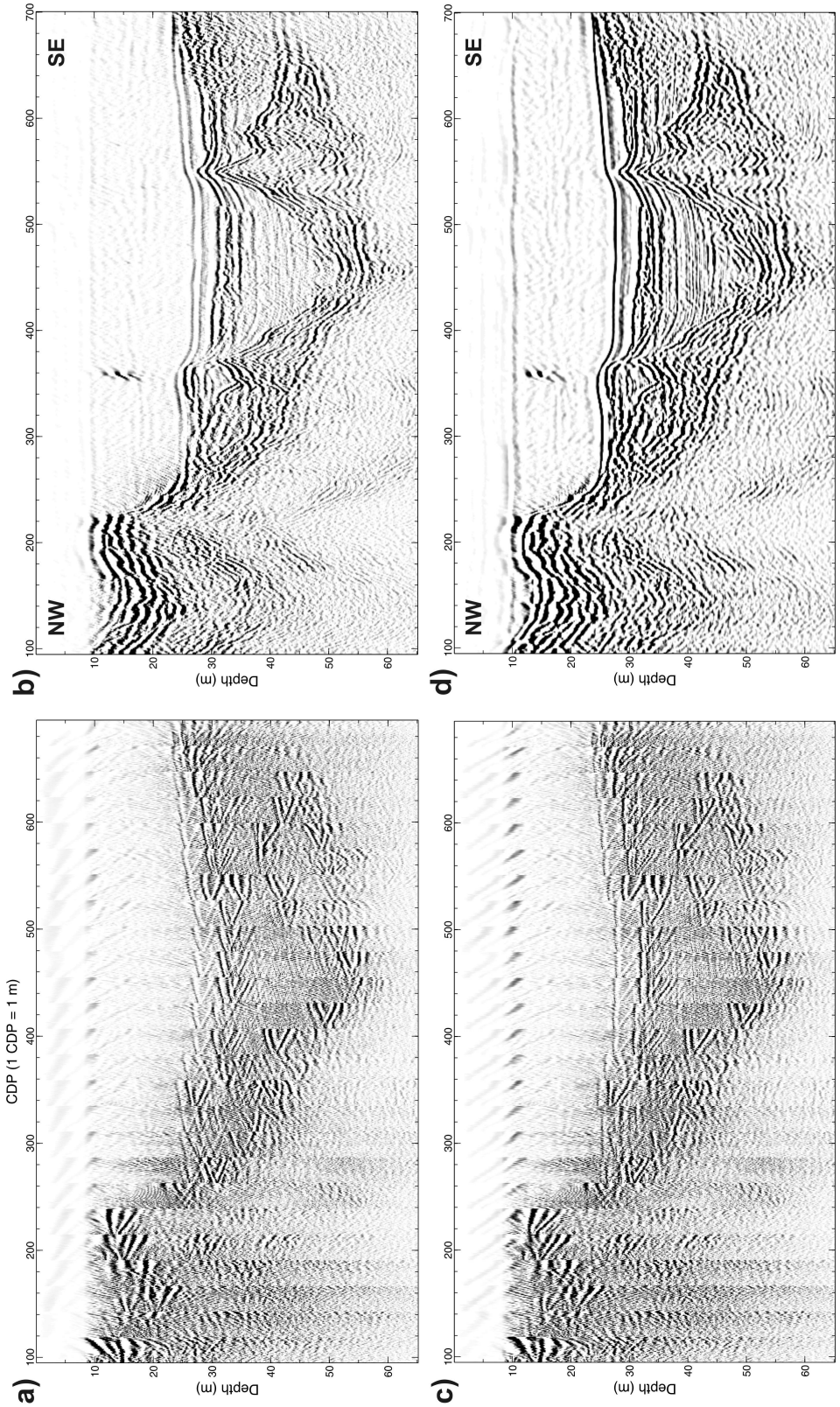

Figure 5.17: Migration of MCS line 2607-line17: with simple streamer geometry and a constant 1470 m/s velocity model—a) CRP gathers and b) migrated depth section; with sag corrected geometry applied and a constant 1470 m/s velocity model—c) CRP gathers and d) migrated depth section.

5.4.2 Processing and Migration of Boomer MCS Data

There are two aims of the processing and prestack depth migration of MCS lines over Windermere:

1. Accurately estimate the velocity within different types of deposits.
2. Image the nature of the bedrock and till deposits to aid facies identification and ice retreat interpretation.

The two aims complement each other: the focusing of the reflections determines when the velocities used for the sediment/deposit packages are correct. However, occasionally adjacent facies create large velocity contrasts in the velocity model and produce unwanted noise.

To demonstrate this, as well as the processing steps applied to all the migrated lines in Chapter 6, I use the example of MCS line 2707-line13 in the North Basin. This line runs along the eastern flank of the basin, between the shore and the deeper axial part. It passes near two shell and auger core sites and an FBA core, and so is of great interest. Three factors make this line difficult to process: three sediment/deposit packages and lake water, with velocities ranging from c. 1450–4000 m/s, are within a depth range of 15 m; a lateral change in deposit; and receiver ghost reflections.

Kirchhoff PDSM (Section 4.4) is appropriate for these datasets because it can handle data with complex substructures containing steep dips and reasonably high velocity contrasts. Despite its assumptions about smoothly-varying velocity fields, Kirchoff PSDM is remarkably robust and is the historical PSDM of choice (Long, 2004). A layer stripping approach is followed, with Kirchoff PSDM using maximum amplitude ray-tracing to compute travel-times unless otherwise stated. The initial velocity model is a uniform 1450 m/s (c. the velocity of the lake water).

Figure 5.18a shows MCS line 2707-line13 migrated using a 2 package velocity model (a velocity model attempting to resolve the lakebed, and the bottom reflections of two packages beneath). The lakebed lies beneath 25–30 m of water with an average velocity 1440 m/s. The two targeted packages here are characterised as follows:

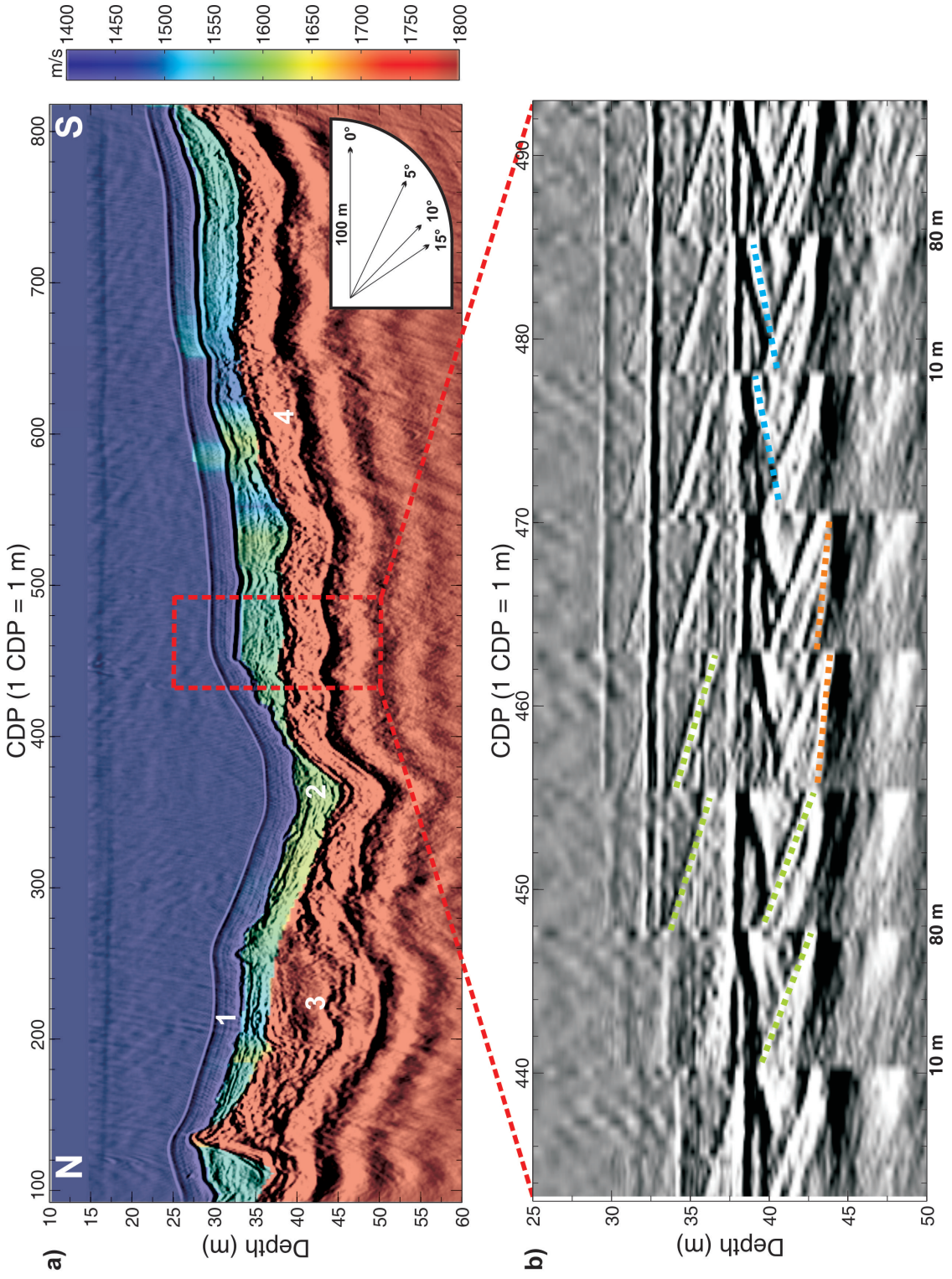

Figure 5.18: North Basin MCS line 2707-line13: a) Migrated data using the 2 package velocity model (the four target sediment/deposit packages are numbered) with 1800 m/s used beneath; b) CRP super gathers combining every 9 CDPs between 430 and 490, highlighting examples of receiver ghosts of the focused reflections (green dots), interbed multiples (orange dots), and primary reflections from the unfocused deepest reflector (blue dots).

1. Sediment drape 3–4 m thick, containing 2 faint horizontal reflections. This has an average velocity c. 1450 m/s, which is the same as, or less than the water velocity used to focus the lakebed in some locations.

2. Sediment layer 3–5 m thick, with some coarse internal reflections that dip in the general direction of the underlying surface. There is perhaps an erosive surface to this package about CDP 400. This has an average velocity c. 1550 m/s.

The CRP gathers (Figure 5.18b) show the three focused reflections at 30 m, 33 m and 38 m, which define the bounding reflections of the two sediment packages targeted by the velocity model. However, three additional types of energy are not properly focused: receiver ghosts (green dots), interbed multiples (orange dots), and reflections from a faster layer beneath (blue dots). Since the streamer deepens with offset, the receiver ghost takes longer to arrive with offset, and has an apparent positive RMO. After application of the geometry corrections that sought to correct the apparent negative RMO in the primary reflection, the receiver ghost has an increased positive RMO and appears as steeply dipping discrete events in the CRP gathers.

The primary reflection of the package underlying package 2 has a negative RMO in Figure 5.18b. This primary reflection has an associated interbed multiple that can be seen on Figure 5.18a 40–45 m deep in the red dashed box. Judging by the offset of the multiple to the position of the primary reflection, the delay occurs within package 1, the sediment drape. The velocity of 1800 m/s used beneath the two targeted packages has actually focused this multiple, which, owing to the regular thickness of the sediment drape, exhibits a similar shape to the associated primary reflection when that becomes focused. Figure 5.18b shows that this interbed multiple is clearly distinguished from the associated receiver ghost in the CRP gathers, because it is offset from the original reflection, and has a smaller positive RMO.

Removing unwanted energy from the CRP gathers helps resolve the primary reflections that have yet to be focused. Firstly, Burg adaptive deconvolution (Jurkevics and Wiggins, 1984; Burrascano and Lucci, 1989) is applied to all the migrated offsets before stacking. This removes reverberation, noise from delayed energy, and

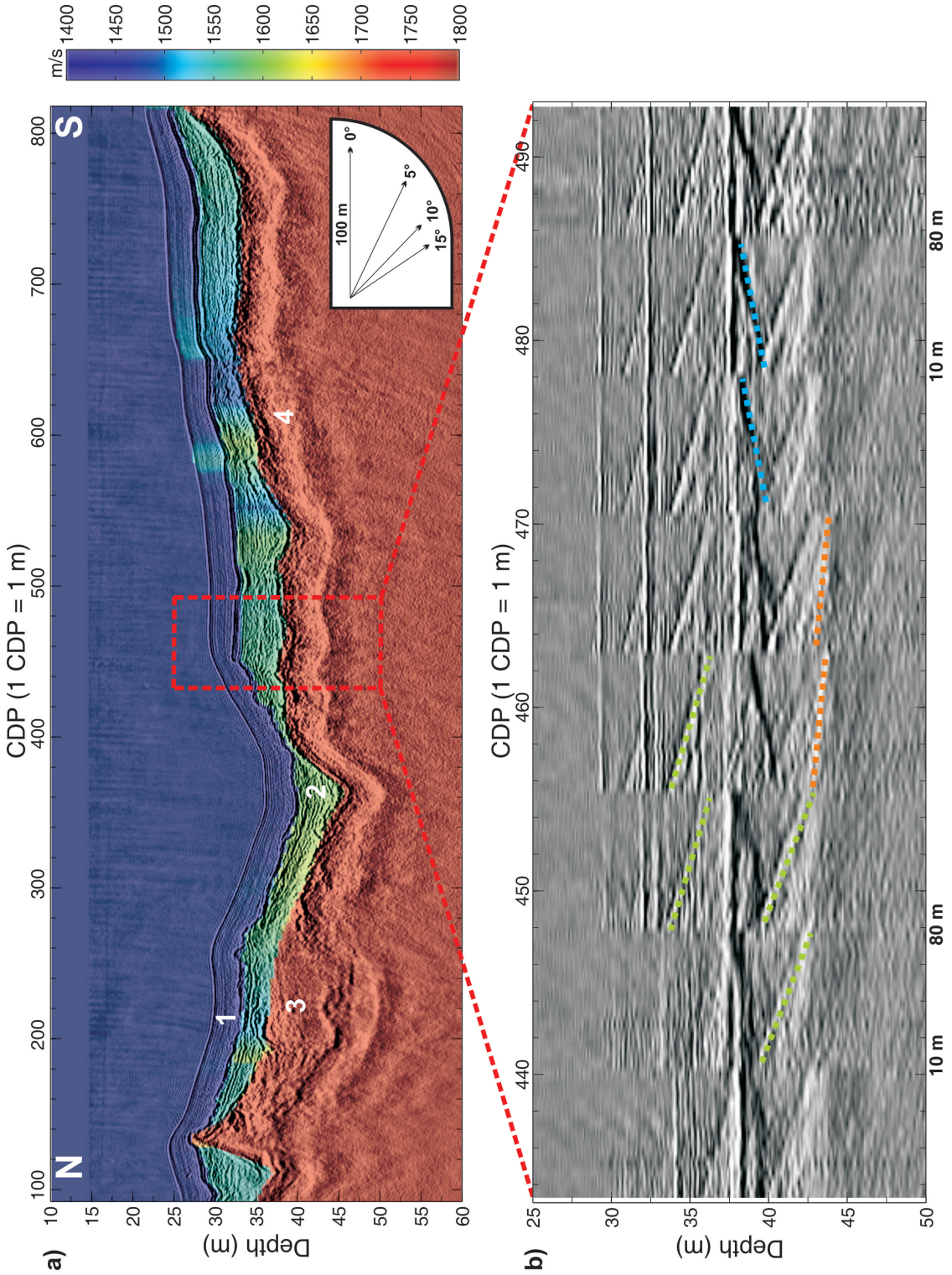

Figure 5.19: North Basin MCS line 2707-line13: a) Migrated data using the 2 package velocity model (the four target sediment/deposit packages are numbered) with 1800 m/s used beneath, applying Burg adaptive deconvolution; b) CRP super gathers combining every 9 CDPs between 430 and 490, highlighting examples of receiver ghosts of the focused reflections (green dots), interbed multiples (orange dots), and primary reflections from the unfocused deepest reflector (blue dots).

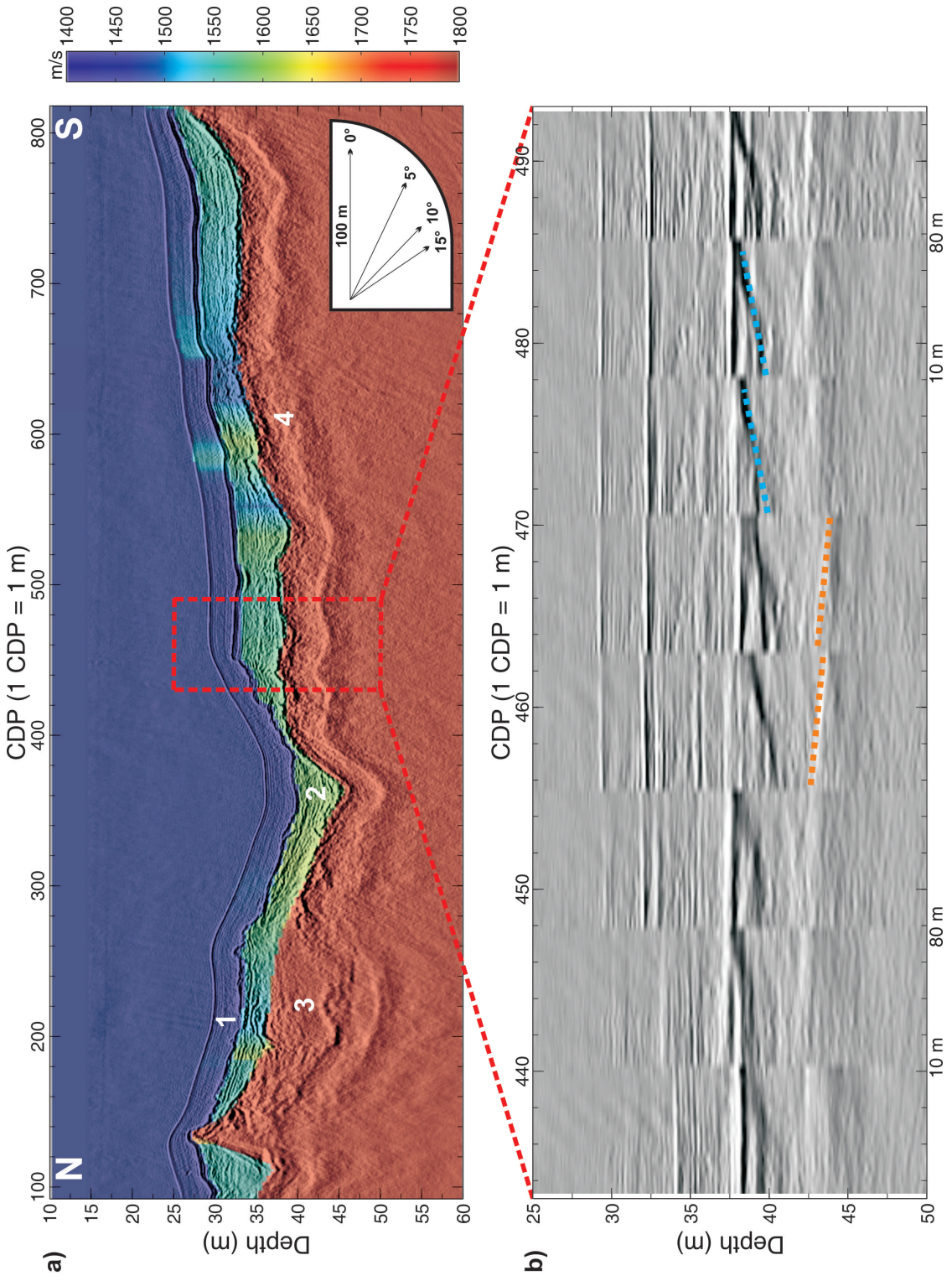

Figure 5.20: North Basin MCS line 2707-line13: a) Migrated data using the 2 package velocity model (the four target sediment/deposit packages are numbered) with 1800 m/s used beneath, applying Burg adaptive deconvolution, F-K filtering, and F-X deconvolution; b) CRP super gathers combining every 9 CDPs between 430 and 490, highlighting examples of interbed multiples (orange dots), and primary reflections from the unfocused deepest reflector (blue dots).

sharpens reflections. The Burg deconvolution algorithm has the best pulse compression over the narrow windows required by the data. Figures 5.19a and 5.19b show that this step enhances both the the bounding and internal reflections. In Figure 5.19a, package 3 on the North side is now more distinguishable from the overlying package 2, and definitely has no associated deposition elsewhere. The primary reflection from the base of package 4, still clearly visible in the CRP gathers (Figure 5.19b), can now just be distinguished from the bottom reflection of package 2 (e.g. CDPs 420–480 and 600–650). It is now clear that sediment package 1 contains several faint internal reflections, with the two c. 1 m apart in the centre being stronger, and that sediment package 2 is completely composed of internal layered reflections. The enhanced detail shows that the upper reflection of package 2 is strong and regular in the South, and rough and broken in the North. Where this strong upper reflection breaks, c. CDP 450, the internal reflections also appear cut-off.

Before attempting to design a new velocity model that removes the negative RMO from the remaining deeper primary reflections, an F-K filter is applied to the CRP gathers to remove all the delayed energy that has positive RMO and obscures the unfocused primary energy. Then, F-X deconvolution is applied using a Weiner filter (with an optimal amount of white noise to further suppress unwanted energy) to enhance the continuity of the remaining reflections. The F-X deconvolution can sometimes be detrimental to the resolution of closely spaced reflections (usually when dipping at different angles), and is only used where reflections are sparse and the continuity of reflections are notably enhanced. The final section is now less noisy (Figure 5.20a), and the reflections are more continuous; the CRPs are much easier to interpret with the removal of the unfocused receiver ghosts, suppression of noise, and the greater continuity of reflections (Figure 5.20b). These CRP gathers are used to remove the remaining RMO of the deeper primary reflections and a 4 package velocity model is produced. Figure 5.21a resolves the two packages beneath package 2. These packages are distinguished primarily by velocity:

3 Transparent deposit up to 15 m thick between CDPs 120 and 290 on the North side. The deposit lies within a relatively large trough and has an

average velocity c. 2300 m/s.

4 Transparent deposit up to 8 m thick, filling troughs up to the level of the crests in the underlying basement. The deposit extends from the middle to the southerly extent of the line and has an average velocity c. 3600 m/s.

Figure 5.21b shows that the RMO has been removed from the bottom reflection of the 4th package, but more noise is now present within the gathers and the section (Figure 5.21a). There has been no change in the trace scaling between Figures 5.20b and 5.21b; the introduction of the higher velocities has allowed the ray-tracing migration method to find times for steeply dipping, out-of-plane energy that increases noise in the layers above. This shortcoming with ray-tracing does not occur between CDPs 100 and 300 in the North above slower velocity package 3, where the reflections within package 1 and 2 remain well resolved, and there is little noise produced in the water column. Unfortunately, this shortcoming is unavoidable without compromising something else.

For all the previous migrations, maximum amplitude ray-tracing has been used with 1 m smoothing of the velocity model. Increasing the velocity smoothing from 1 m to 5 m reduces the noise in the image, but does not resolve the short depth scales of the data, and produces less accurate layer velocities. Figure 5.22a shows the migration produced by maximum amplitude ray-tracing with 1 m smoothing (same as Figure 5.21a but without the velocity model overlay), for comparison with the migration produced by the Eikonal equation (Figure 5.22b). The Eikonal equation calculation focuses the shallow packages and their internal reflections very well, but not the basement reflector, and fails in areas of high velocity contrast, e.g. CDPs 305 and 350. This is because the Eikonal method is a high-frequency approximation of the wave equation, and since the basement reflections at the bottom of the 3rd and 4th packages are dominated by lower frequencies, they are less well represented.

The clearest imaging of the deepest reflection is obtained if we ignore sediment package 2 (Figure 5.23). This reduces small scale velocity contrasts by blending the low velocities higher up the column with the high velocities beneath. Notice the relatively high velocities in the troughs and the lower velocities above the peaks; this is because above a peak lies only the slow sediment of package 2, but in a trough

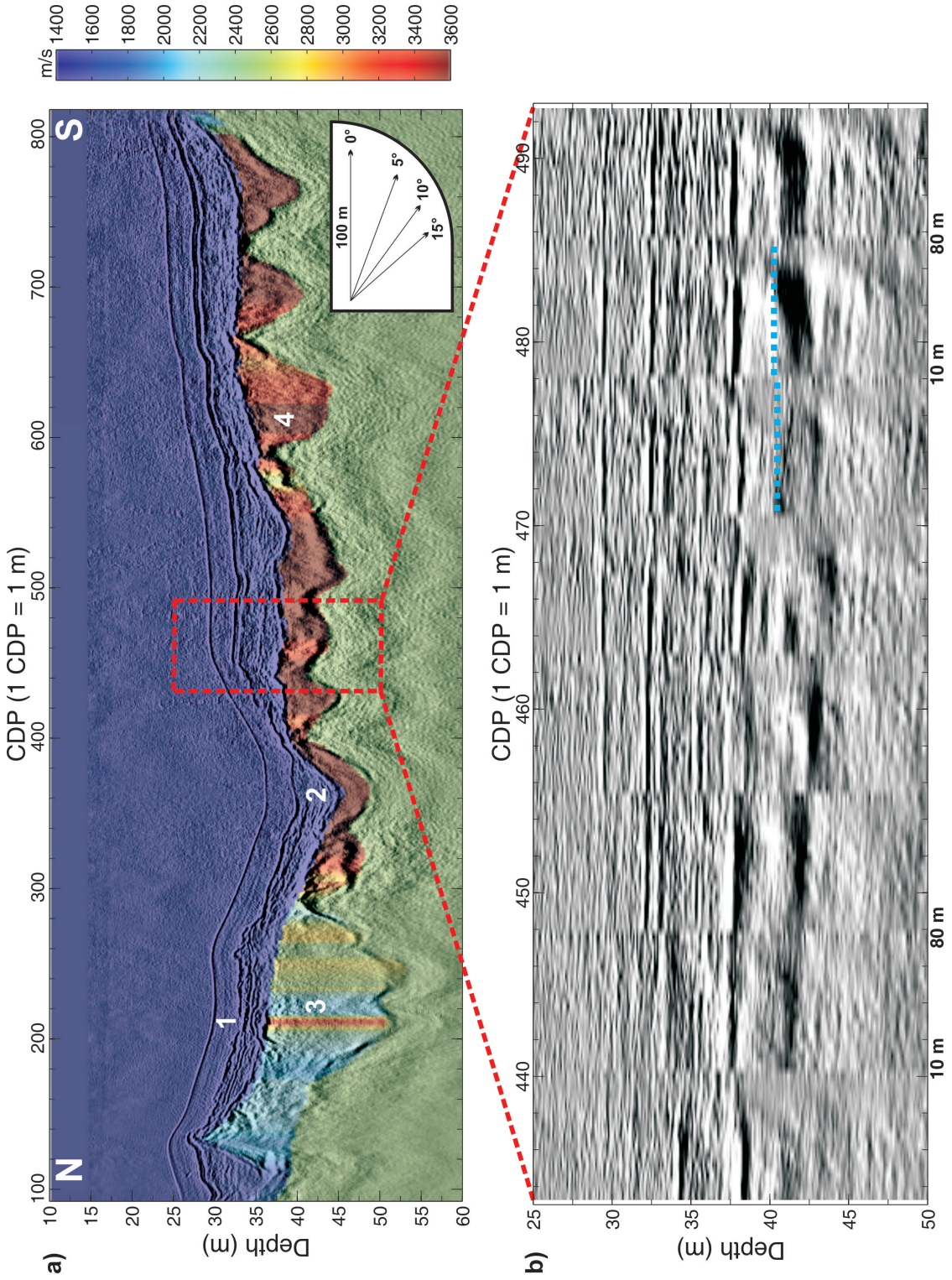

Figure 5.21: North Basin MCS line 2707-line13: a) Migrated data using the 4 package velocity model (the four target sediment/deposit packages are numbered) with 2500 m/s used beneath, applying Burg adaptive deconvolution, F-K filtering, and F-X deconvolution; b) CRP super gathers combining every 9 CDPs between 430 and 490, highlighting examples of the primary reflections from the deepest reflector (blue dots).

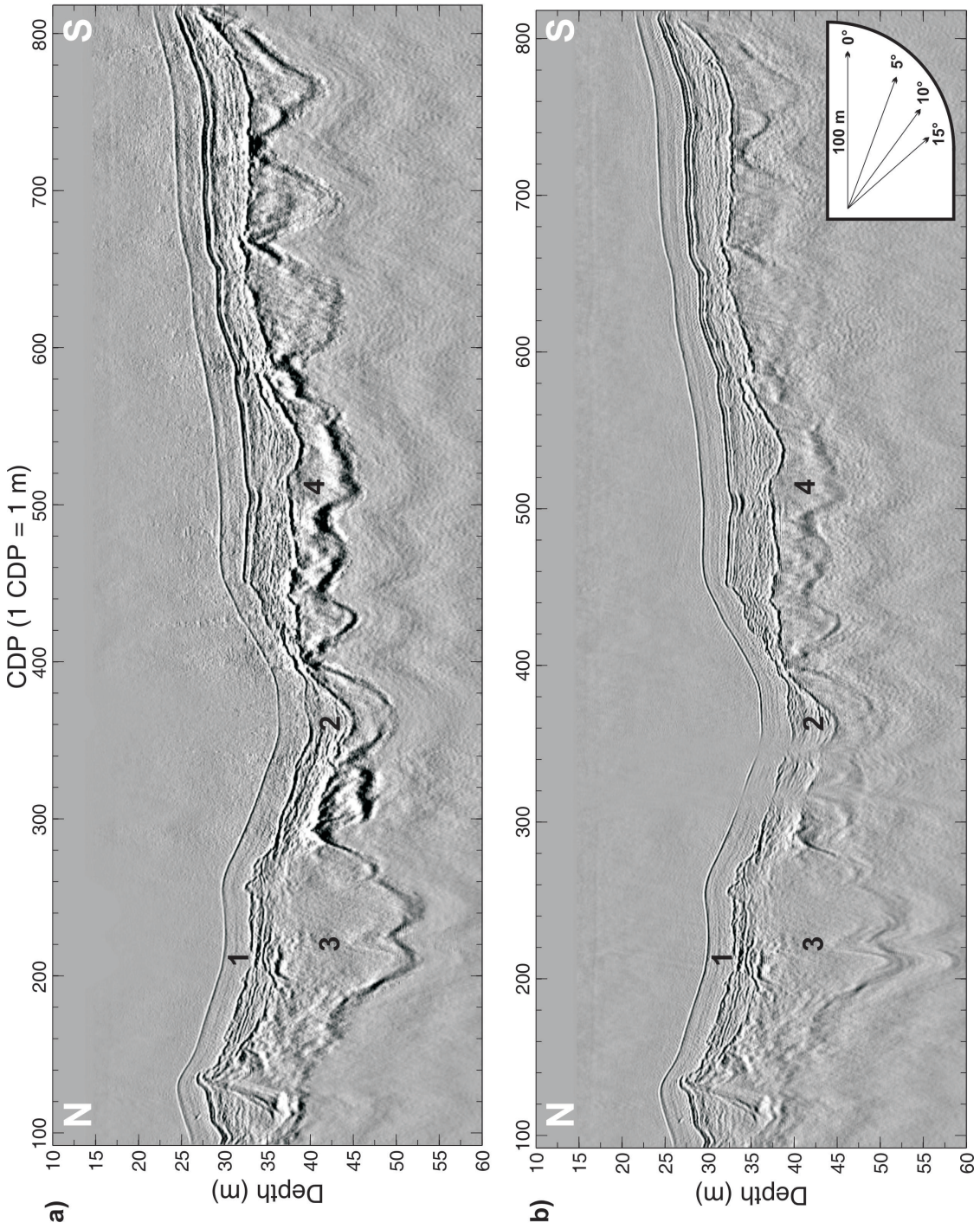

Figure 5.22: North Basin MCS line 2707-line13 (the four target sediment/deposit packages are numbered): a) Result from migrating with 1 m velocity smoothing using maximum amplitude ray-tracing with the 4 package velocity model, and 2500 m/s used beneath; b) Result from migrating with the Eikonal equation with the 4 package velocity model, and 2500 m/s used beneath.

there is a larger thickness of package 4 so the velocity required is higher rather than being an imaging artefact. The velocities shown in 5.23a are not related to an individual sediment/deposit package and are therefore of no use in determining sediment type.

The velocity within the basement also affects the imaging of the deepest reflection. A basement velocity of 2500 m/s has been used with the 4 package velocity model because this is close to the mean velocity found within adjacent package 3. A high velocity is useful because it moves any noise beneath the last reflection deeper down the section. Figure 5.24a shows that when a basement velocity of 1500 m/s is used, noise from reverberations and multiples gather up around the lower reflections of packages 3 and 4. However, if the velocity is too high, such as in Figure 5.24b where 3500 m/s is used, the lowest reflection of slower package 3 becomes unfocused, and where the basement moves close to the water column, the velocity contrast is too great and unwanted energy appears within the data and water column above (e.g. CDP 100 within the red dashed box). As no reflections within the basement are imaged, the basement velocity is unconstrained and is varied to optimise the imaging of the layers above.

Where possible (without detrimental effects to the migrated image) a uniform velocity, or uniform velocity gradient, has been applied to entire packages. This is usually achieved in the thicker sediment packages within other MCS lines that have simpler horizontal structures, as opposed to the more complex shapes of the underlying bedrock and till demonstrated here. Figure 5.25a shows a 4 package velocity model containing the averages for the sediment/deposit packages, and Figure 5.25b the migrated result without the velocity overlay. On comparison with Figure 5.22a, there is a slight loss of structure in all reflections, most significantly the basement reflection where there is the highest velocity variation, but generally the average velocities produce a similar image. Hence, we are justified in using the average velocity of the sediment/deposit in our interpretations; it is preferable that estimations of the average are made where the reflectors are sub-horizontal to avoid problems due to velocity gradients.

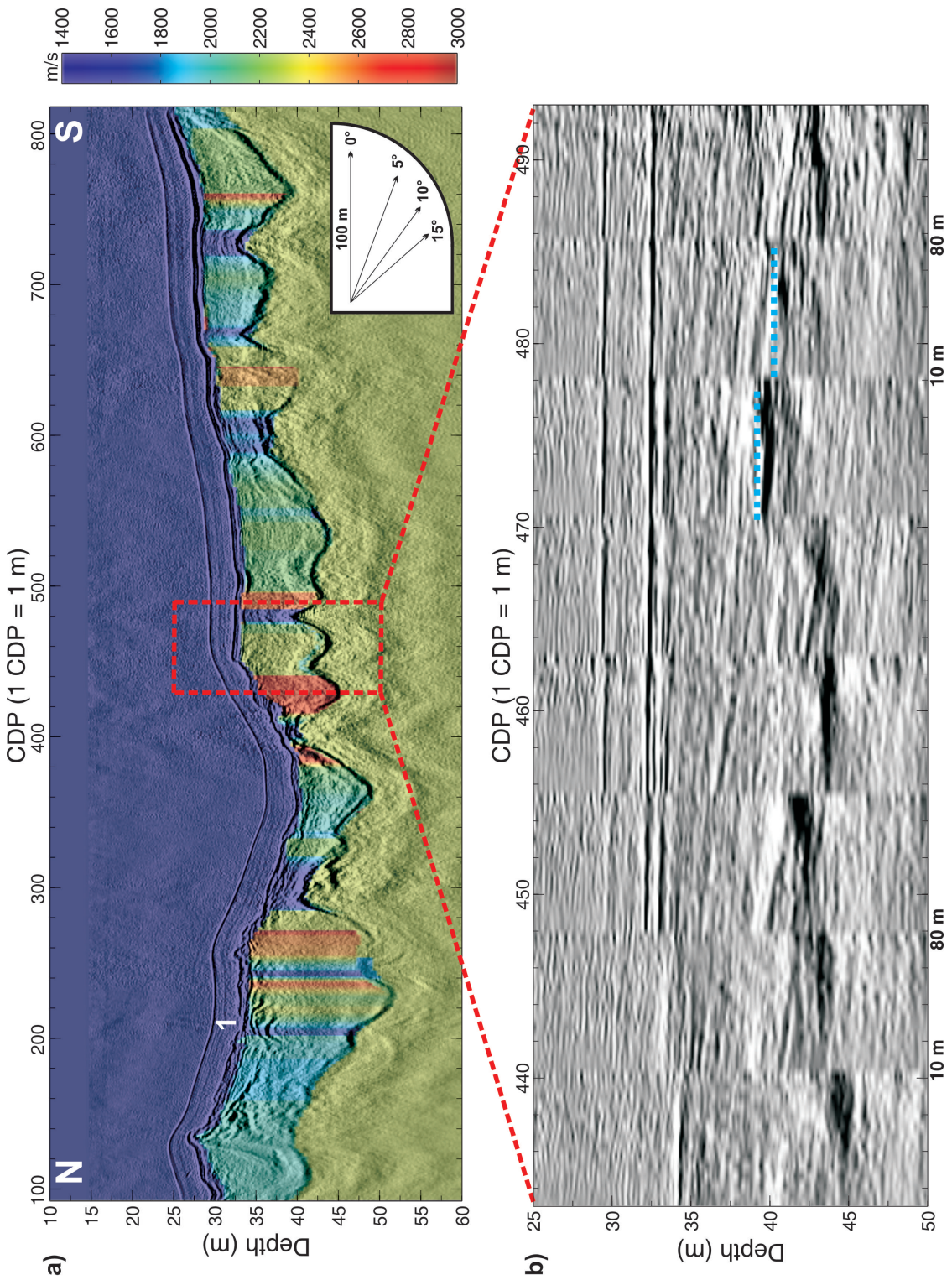

Figure 5.23: North Basin line MCS line 2707-line13: a) Migration using a 2 package velocity model (the four target sediment/deposit packages are numbered) that focuses the deepest reflection beneath package 1, with 2500 m/s used beneath; b) CRP super gathers combining every 9 CDPs between 430 and 490, highlighting examples of the primary reflections from the deepest reflector (blue dots).

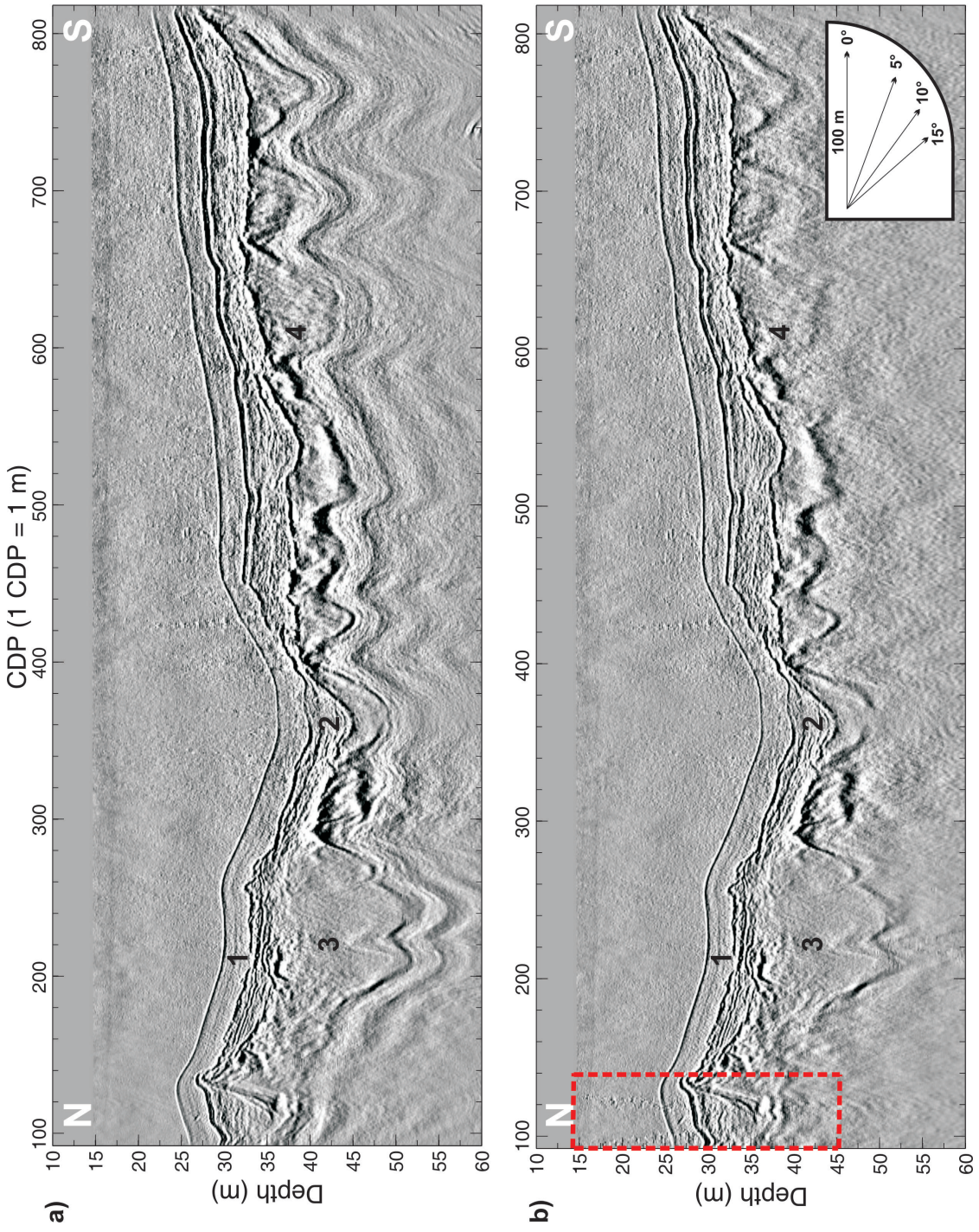

Figure 5.24: a) North Basin MCS line 2707-line13 (the four target sediment/deposit packages are numbered): a) Migration using the 4 package velocity model with 1500 m/s used beneath; b) Migration using the 4 package velocity model with 3500 m/s used beneath.

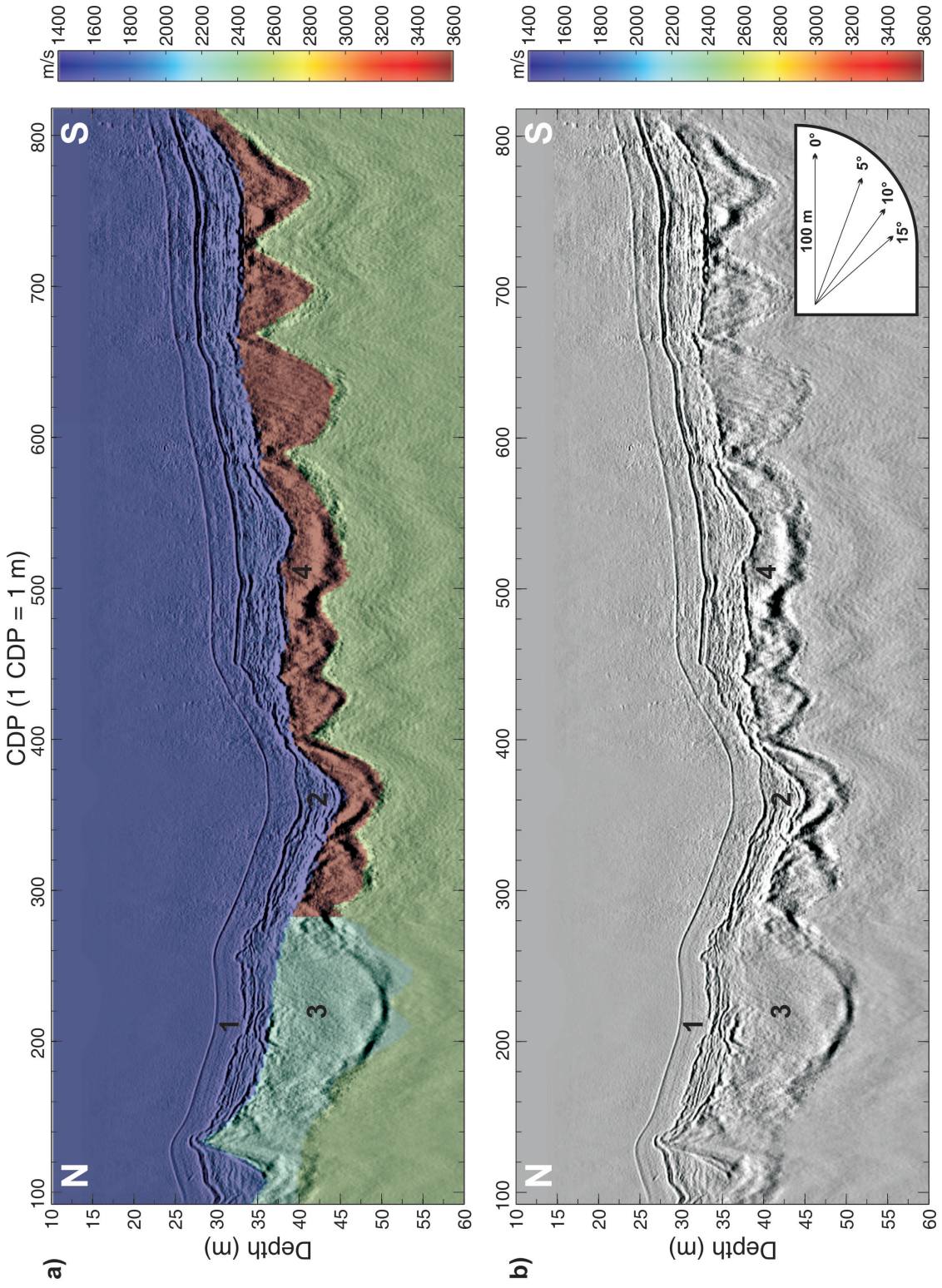

Figure 5.25: North Basin MCS line 2707-line13 (the four target sediment/deposit packages are numbered): a) Migration using the average velocities of the 4 package velocity model with 2500 m/s used beneath, applying Burg adaptive deconvolution, F-K filtering, and F-X deconvolution; b) As above, but without the velocity model overlay.

Once a coherent migration is achieved and a velocity model settled upon, true-amplitude recovery is used to suppress/mute noise within the water column and the basement, and strengthen the reflections of interest for the final image. To summarise, the processing method is as follows:

1. Migrate using the best available velocity model (use a 1450 m/s constant velocity model initially).
2. Apply Burg adaptive deconvolution to the migrated offset sections.
3. Apply a F-K filter to the subsequent CRP gathers to remove the receiver ghost reflections that have a large positive RMO.
4. If required, apply F-X deconvolution to these CRP gathers to suppress noise and improve continuity of reflections.
5. Stack with the filtered CRP gathers and evaluate the migrated image.
6. If the velocity model still needs improving, remove RMO from a chosen horizon and go back to step 1 and re-migrate with the edited velocity model. If image and associated velocity model are satisfactory continue to step 7.
7. Mute the water column and suppress unwanted noise beneath the packages.
8. Identify the average velocities in the sediment/deposit packages.

5.4.3 Surface Maps

Two surfaces and an isopachyte are constructed by picking sequence horizons within all the MCS and single channel two-way time data. The horizons are converted to depth using average sequence velocities determined from PSDM, and interpolated using the kriging functions in ArcGIS™ *Geostatistical Analyst*.

Kriging provides mean and RMS prediction errors like deterministic methods (e.g. inverse distance weighting), but also measures the uncertainty in the predictions. These serve as diagnostics when deciding which parameters for the kriging model produce the most accurate and valid predictions. Kriging also allows the production of prediction standard error maps for the prediction maps.

The K-Bessel model (otherwise known as Matern) was chosen because it has greater flexibility than the commonly used variogram models (e.g. spherical, exponential and Gaussian) when modelling a variety of spatial processes, especially local spatial behaviour that occurs near the origin (Minasny and McBratney, 2005). This is advantageous because local variation is of greatest interest here, and geology from glacial genesis is often locally and strongly variable, which can sometimes suffer more from the smoothing effects of Kriging (Marinoni, 2003; Lim and Teo, 2009). The *Geostatistical Analyst* calculates a nugget from the data that accounts for measurement error and variation at spatial scales too small to detect, and it calculates the anisotropy of the spatial correlations, which is accounted for by using an elliptical search neighbourhood. Here, anisotropy is produced by the geological structure of Windermere: the depth to the lakebed at a location is more likely to be of a similar level 500 m north or south given the lake stretches 17 km along this axis, rather than 500 m east or west, where the lakebed rises to form the shore. The ellipse produced in all cases had northwest–southeast orientation that generally follows the orientation of the lake.

The optimal models used to produce the surface maps and isopachyte in Chapter 6 were all valid and had a mean prediction error close to zero indicating the predictions are unbiased, and a small RMS prediction error indicating the predictions are close to the measured values. Valid models have an Average Standard Error equivalent to the RMS prediction error, meaning that the predictions generated by

the model have the same variability as the data (i.e., the model is not overestimating or underestimating the variability in the predictions), and that the prediction standard errors are accurate. All the datasets were augmented with lake boundary data where the associated depths are 0 m. This confines the interpolations to the area of the lake and constrains the basin structures, producing the most realistic outputs.

Figure 5.26 shows the prediction standard error as a function of location, for the basement/SSS I and lakebed/SSS V surfaces in Chapter 6. The true value shown on the prediction maps will be within ± two times the prediction standard error 95% of the time. Hence, when taking measurements from the prediction maps, locations close to data points are used. The root sum of squares of the standard errors in a location are used to produce the uncertainties in the reported thicknesses of the isopachyte.

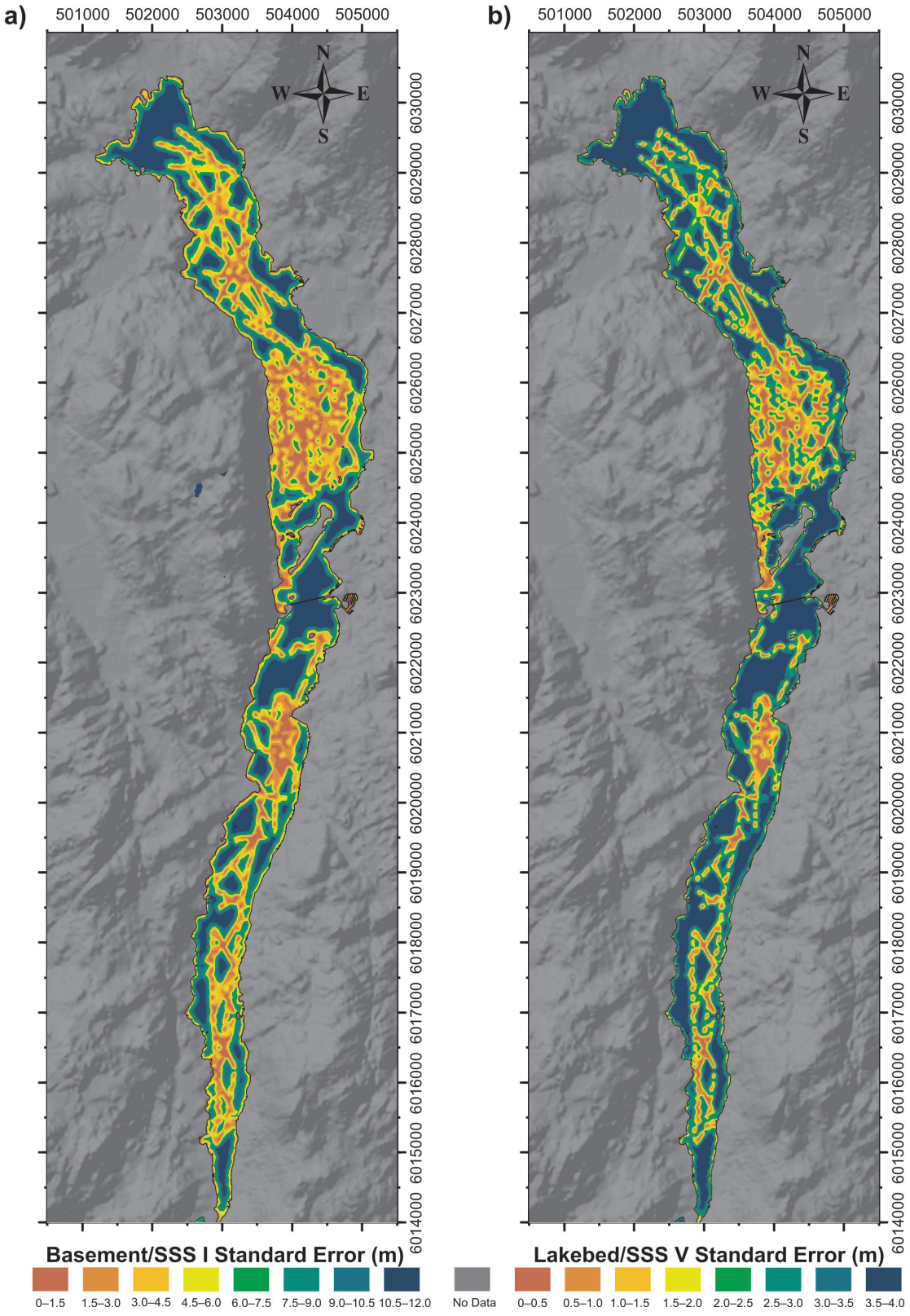

Figure 5.26: Prediction standard error maps: a) basement/SSS I; b) lakebed/SSS V. Co-ordinates are UTM zone 30.

5.5 Conclusions

Enough multi-channel and single channel Boomer data was acquired over Windermere to provide a reliable interpretation of the sub-surface. Chirp data was collected over specific core sites and features to improve the understanding of structural and acoustic properties of some deposits.

The multi-channel streamer sagged up to c. 3 m below the surface, which produced unacceptable migrations when a constant receiver depth was assumed. Ghost notch frequency analysis at each channel resolved the streamer depth profile beneath the lake surface and allowed for correct migration and determination of *in situ* velocities.

The relatively calm lake surface and deep streamer introduced significant lake surface ghost reflections that interfered with the primary reflections. These were successfully removed using F-K filtering of CRP gathers. Fortunately, the sagging of the streamer worked to further enhance the dip of the lake surface ghost reflections with offset, making their removal simpler. This fact should be considered before future surveys of fresh water lakes attempt to make the multi-channel streamer tow at a constant depth beneath the surface.

An optimum processing strategy was designed which includes PSDM with maximum amplitude ray-tracing to compute travel-times, Burg deconvolution of the migrated offset sections, and F-K filtering of the CRP gathers before stacking. It is shown that large velocity contrasts can increase noise in the data, hence, in some situations it may be preferential to migrate without the high-velocity layers, or perhaps blend two velocity layers together to improve the migration of target reflections.

Surface maps were made of selected horizons from the data using kriging. The K-Bessel variogram model provided the best results and anisotropy was determined from the data and accounted for in the surface predictions.

Chapter 6

Windermere Glacial History

6.1 Introduction

6.1.1 Episodes of Glaciation

During the Pleistocene glaciation, continual glacial epochs in Britain occur from the Middle Pleistocene onwards: Anglian, 300–250,000 BP; Wolstonian, 200–150,000 BP; and the Devensian, 120–10,000 BP (Eyles et al., 1983). The maximum southward extent of ice in Britain was reached during the Anglian glaciation, down to the River Avon and the River Thames, and the least in the Devensian (Eyles, 1983a,b). The degree of dissection in the overdeepened valleys of the Lake District reflects repeated valley glaciation (Boulton, 1977) and the three episodes of glaciation can be recognised on the western side of the Lake District, each marked with their own boulder clay, sands and gravel (Trotter et al., 1937).

Structural evidence left behind by the Anglian and Wolstonian glaciations in Windermere would have been erased during the Devensian glaciation, and so these glaciations are not discussed further. The Devensian glaciation consists of three stages of ice-advance (Figure 6.1): the "earlier Devensian ice maximum" which will not be discussed further; the advance of the British and Irish Ice Sheet (BIIS) during the Dimlington Stadial that produced the LGM at 21,400 ± 1,300 cal. BP (Bowen et al., 2002); and a less extensive ice-advance during the Younger Dryas (YD—locally known as the Loch Lomond Stadial), which occurred 12,800–11,550 ± 100 cal. BP after a short period of climate amelioration (see Section 6.4).

Corrie and valley glaciers developed in the central fells during the YD (Sissons, 1979), leaving behind geomorphological evidence such as frontal moraines (henceforth referred to as still-stand/retreat moraines). These have provided investigators

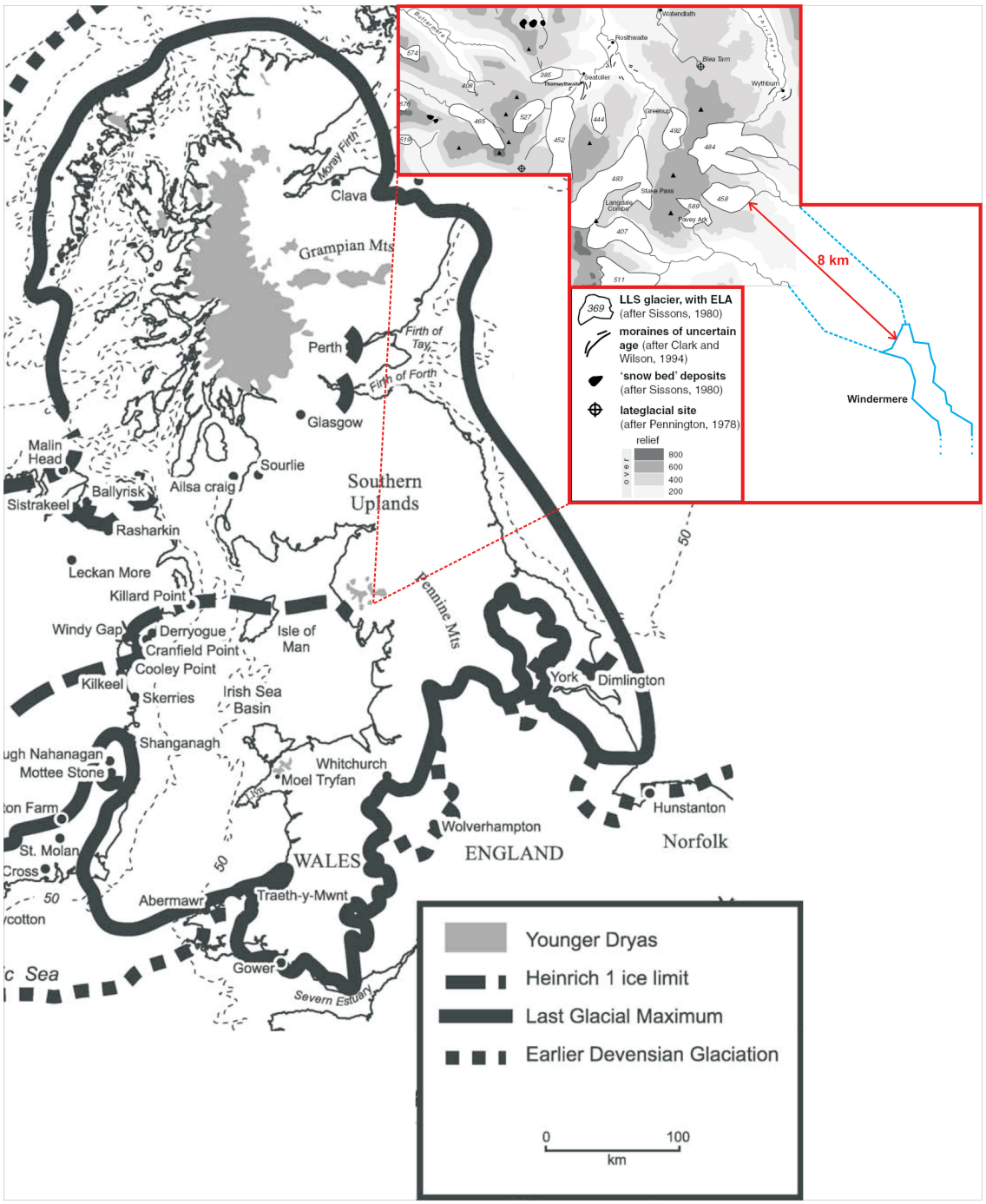

Figure 6.1: Devensian ice limits from Bowen et al. (2002). *Inset:* YD ice limits relative to Windermere, with water-way connections to Windermere indicated with blue dashed lines (adapted from Sissons, 1979; McDougall, 2001).

with information on the character of the YD glaciers and has allowed them to reconstruct the glacial advance and retreat of the ice margins (e.g., Evans and Cox, 1995; McDougall, 2001). However, similar detailed reconstructions have not been possible for the retreat of the BIIS after the LGM, because of a dearth of clearly identifiable or datable deglaciation structures within the Lake District related to ice-retreat during the Dimlington Stadial (e.g. Hollingworth, 1951; Sissons, 1979; Pennington, 1991; McDougall, 2001). Hollingworth (1951) believed this paucity of moraines was because of rapid climate amelioration at the end of the Dimlington Stadial, which caused the remnants of the BIIS in the Lake District to downwaste in-situ, with little increment through winter snowfall because it was out of equilibrium with the climatic environment. This view of rapid downwasting is shared by Pennington (1978).

However, Wilson (2004) has recently argued that valley moraines in upper Eskdale (between Sca Fell and Windermere) testify to a more complex retreat of the BIIS, and that BIIS still-stand/retreat moraines are *not* absent beyond the YD limits in the Lake District—they have simply been ignored by investigators perhaps because of complexity or poor preservation.

The removal of the BIIS is important to the history of the British Isles and presently the timing, extents, whether it confluenced with the Fennoscandian Ice Sheet in the North Sea, and the character of retreat are highly debated topics (e.g., Bowen et al., 2002; Bradwell et al., 2008). Windermere was surveyed because it is ideally situated beyond YD ice-margin limits (Figure 6.1), so that any geomorphological evidence of a retreating BIIS would be preserved beneath late-glacial and present day sedimentation. Windermere has also been a subject of numerous coring campaigns that date changes in sediments within the top 6 m of the lakebed to the YD event (e.g. Coope, 1977). Hence, it was also hoped that changes in the sedimentary record related to climatic events, such as the YD that affected the entire catchment of Windermere, would be seismically resolvable and provide a relative temporal scale to the seismic stratigraphy.

6.1.2 Windermere Geomorphology

Dome-like uplift about Sca Fell (c. 20 km northwest of Windermere) originated in the Tertiary, and formed a radial drainage pattern (Marr, 1906; Mitchell, 1956) where the former Windermere river valley formed the southern spoke (Mill, 1895). The subsequent glaciations excavated and overdeepened the pre-glacial river valleys. The present configuration of Windermere lake was last shaped by the BIIS during the Dimlington Stadial.

Windermere lies in a narrow, ice-gouged valley, dammed by a moraine covered rock bar at the southern end (Wilson, 1987), where the outflow drains westwards into the River Leven. The North Basin and the South Basin of Windermere are separated by a plateau forming shallow water, supporting numerous small islands off Bowness-on-Windermere and a relatively large island called Belle Isle (e.g. Figure 5.2). Belle Isle is protected on the northern side by irregularly placed large boulders, and the smaller islands are rock outcrops, with many showing signs of glacial erosion from the North (Mill, 1895). This island division presented difficulties to the pioneers of ice-erosion theory (Ward, 1875; Marr, 1896) because "the rocks in that location were not of any superior hardness". Ward (1875) argued that "because the valley widens in this location, the ice was able to spread laterally into the valleys in the East", and that the islands represent "degraded stumps of rocky hills that stood well above the valley bottom in pre-glacial times".

6.1.3 Windermere Bedrock Geology

The catchment of Windermere extends northwards towards the Cumbrian Mountains, through the Borrowdale Volcanics. These comprise: extremely fine-grained tuffs and flows dominated by andesites; interbedded agglomerates; vesicular lavas; and porphyritic lavas (Mitchell, 1956). The Borrowdale Volcanics influence the composition of the glacial drift and the lake sediments of Windermere, most significantly in the North Basin, where Troutbeck is sourced in volcanics and the rivers Rothay and Brathay cross volcanics only (Pennington, 1980); the short streams that flow into the South Basin cross Silurian rocks only (Holmes, 1964).

Windermere itself lies within mostly Silurian rocks of the Windermere Super-

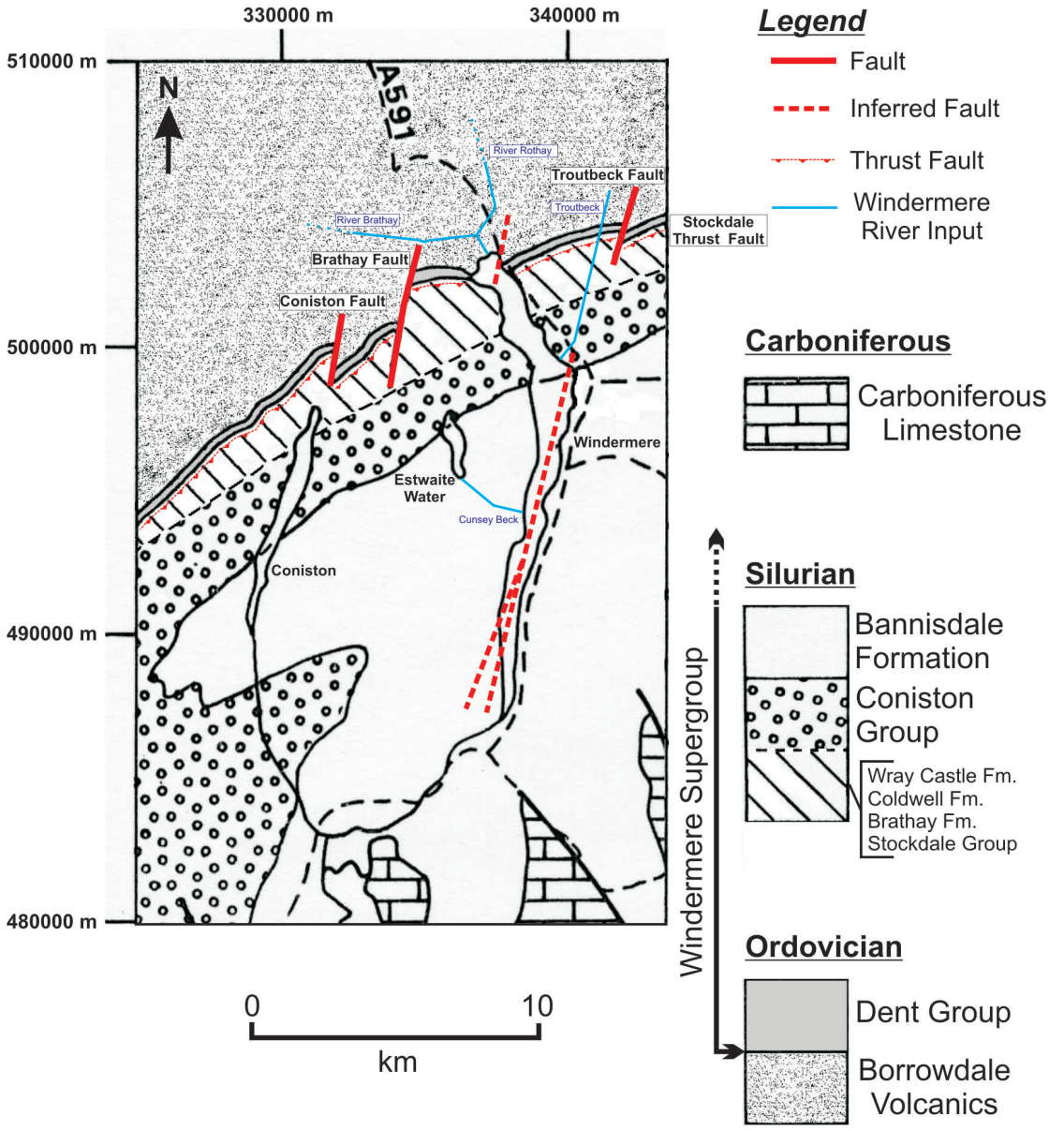

Figure 6.2: Map showing the solid geology around Windermere (adapted from Webb and Lawrence (1986), and based upon BGS (1996)). Co-ordinates are in OSGB.

group (Figure 6.2). The Stockdale Group (c. 150 m map extent adjacent to Windermere), Brathay Formation (c. 500 m map extent), Wray Castle Formation (c. 500 m map extent), and Bannisdale Formation (that encompasses the remainder of the lake and southerly catchment), are all dominantly composed of mudstone and siltstone facies. The Coniston Group, which lies between the Wray Castle and Bannisdale formations, spans 2.5 km from High Wray Bay to Hollow Beck and contains a dominant fraction of sandstone. Calcareous facies exist about the head

of the North Basin in the Coldwell Formation (c. 100 m map extent) and within the Ordovician Dent Group (c. 250 m map extent). However, calcarous sediment input is probably negligible because of the relatively insignificant sizes of the Coldwell Formation and the dominant calcareous facies within the Dent Group about Windermere (McNamara, 1979).

Figure 6.2 shows three bedrock faults that are inferred on the Ambleside solid geology map (BGS, 1996):

1. A North–South fault is inferred running into the top of the North Basin, similar to the visible Coniston, Brathay, and Troutbeck re-activated synvolcanic basement faults, which produce kilometre-scale map offsets within the oldest Silurian formations, and lose displacement southwards into the younger formations (Woodcock and Soper, 2006). Large offsets are not seen at the top of Windermere though, and the weakness that encouraged the initial river valley in this location could be due to a North–South ridge in the underlying Borrowdale Volcanics (McNamara, 1979).

2. Near the north end of the North Basin, the Stockdale Thrust Fault within the Stockdale Group is believed to be a rootless out-of-syncline thrust (Kneller and Bell, 1993; Woodcock and Soper, 2006) and should continue beneath Windermere (Figure 6.2).

3. There is an inferred fault running down the South Basin that bifurcates, suggesting that part of the South Basin lies within a half-graben structure.

The North Basin lies within the Westmorland Monocline. This terminates with the axial zone of the Bannisdale Syncline (Kneller and Bell, 1993) that passes through the location of Belle Isle. Figure 6.3 is a cross-section beginning at the south end of Windermere and running Northwest close to Windermere, and shows the dips of the formations in the Windermere Supergroup. A small anticline in the Coniston Group, produced by backthrusting in the Silurian units beneath (Kneller and Bell, 1993), occurs beneath the location of the plateau dividing the North and South basins of Windermere. This relative uplift here, already alluded to by Ward

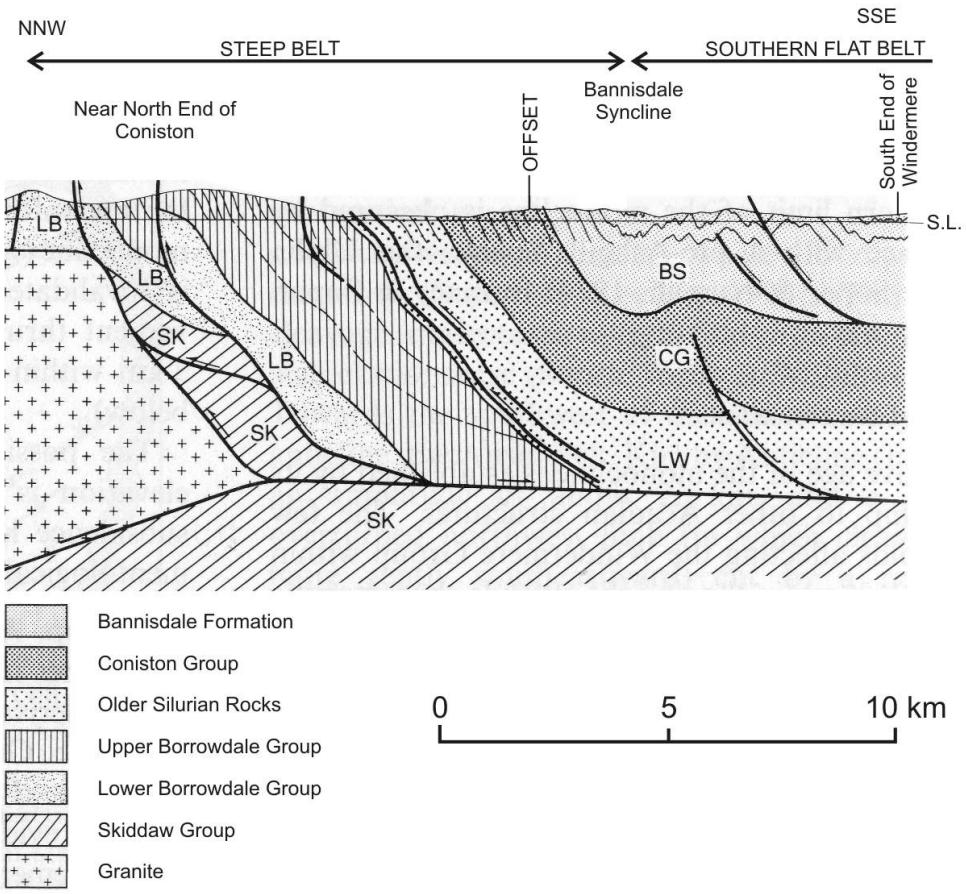

Figure 6.3: Cross-section through the Westmorland Monocline (Kneller and Bell, 1993). The south end of Windermere is located. The cross-section runs northwest generally towards the north of Coniston but steps southwest at "OFFSET", and passes through the southern part of Coniston.

(1875), is probably an important factor during the evolution of Windermere into a dual basin lake.

6.1.4 Windermere Valley Glacier

The valley glaciers of the Lake District during the Dimlington Stadial nucleated in the Cumbrian Mountains, and were less than 500 m thick, snow-blown, and wet-based (Sissons, 1979). The Windermere valley glacier would have been driven by snow accumulating on local topographic highs such as Sca Fell. The snow metamorphosed into ice at depth, and pressure melting at the base created "active ice" that moved down river valleys in response to gravitational spreading (Eyles, 1983b).

The valley containing Windermere and all the adjacent topography shown in the maps, was completely covered by ice (Ward, 1875). The dominant form of glacial erosion was by plucking in the massive volcanic rocks of the Borrowdale Volcanics, and abrasion by smoothing and rounding in the Silurian mudstones and siltstones (Hollingworth, 1951).

Valley glaciers from Great Langdale, the Rothay Valley, and Stock Ghyll entered the North end of Windermere, coalesced, and instigated glacial overdeepening, producing the deepest location of Windermere in the North Basin (Vincent, 1985). Valleys become "overdeepened" when they are eroded below normal fluvial erosion (i.e., below an asymptotic long-profile that reaches sea-level). This is most significant where powerful tributary ice streams coalesce at valley junctions (Eyles, 1983b). Two other significant valley glaciers would have joined the Windermere valley glacier: the Troutbeck glacier in the southern part of North Basin; and the Esthwaite Water glacier in the northern part of South Basin.

Overdeepening also occurs where valleys narrow; the volume of ice required to pass in a given time necessitates a greater speed. There are already known examples of this in the Lake District (e.g. within Ennerdale Water— Hollingworth, 1951). Windermere narrows towards the southern end of the South Basin, making this another candidate location for significant overdeepening by the valley glacier. The opposite is true where valleys widen. Windermere widens at the south end of the North Basin, where it is believed that ice spread eastwards into adjacent valleys before surmounting the plateau supporting Belle Isle.

At the end of the Dimlington Stadial, Hollingworth (1951) suggested that the valley glacier in the South Basin of Windermere downwasted in-situ, which was supported by the findings that indicate Windermere is *not* dammed at the southern end by a retreat moraine (Coster and Gerrard, 1947; Wilson, 1987).

6.2 Seismic Stratigraphy

6.2.1 Migration Results

Six MCS lines are migrated and compared: MCS lines 2607-line11, 2607-line15, and 2607-line17 from the South Basin (Figure 6.4); MCS lines 2707-line4pm, 2707-line10, and 2707-line13 from the North Basin (Figure 6.5). Figures 6.6–6.13 show the PSDMs with complete velocity models for each line. Figures 6.14–6.16 show the PSDMs scaled with other MCS lines in their basins, and have been migrated with velocity models restricted to 1800 m/s to enhance the detail in the sediment packages (and of the lower velocities) by neglecting the faster velocities required by sequences beneath, which sometimes generate noise in the sequences above (Section 5.4).

1. MCS line 2607-line11 surveys obliquely (Northwest–Southeast) across the lower half of South Basin, over one of the thickest deposits of sediment in Windermere (Figure 6.6 and Figure 6.14a).

2. MCS line 2607-line15 surveys South–North for 4.5 km along the central part of South Basin (e.g. Figure 6.15a–6.15c), and has been separated into three 1.5 km sections for interpretation: 2607-line15a (Figure 6.7), 2607-line15b (Figure 6.8), and 2607-line15c (Figure 6.9).

3. 2607-line17 surveys obliquely (East-Southeast–West-Northwest) across the north end of South Basin over shallower sediments and glaciogenic features, which affords good penetration by the Boomer (Figure 6.10 and Figure 6.14b).

4. 2707-line4pm surveys North–South, slightly west of centre, of the wider, southern part of North Basin (Figure 6.11 and Figure 6.16a).

5. 2707-line10 surveys obliquely (Northwest–Southeast) across one of the deepest locations in Windermere, close to the north end of North Basin (Figure 6.12 and Figure 6.16b).

6. 2707-line13 surveys North–South near to the east shore, in the wider, southern part of North Basin (Figure 6.13 and Figure 6.16c).

Water velocity in the South Basin varies between 1450 m/s to 1480 m/s, with the faster velocities found nearer the middle of the basin, where the most distinct thermocline has been resolved at 20 m depth on MCS line 2607-line11 (Figure 6.14a). The warmer water at the surface produces the higher velocities here (see Appendix A4). The thermoclines can be observed in Figures 6.14–6.16, but are not of interest here, and have been removed with the water column noise in the other figures. The average water velocity in the South Basin is 1460 m/s ± 10 m/s. All the lines in the North Basin have an average water velocity of 1440 ± 10 m/s.

The seismic stratigraphy sequence (SSS) within these MCS lines is delineated into five sequences (SSS I-V), with individual seismic facies denoted with appended letters (e.g. SSS I(a)). This is based on seismic velocity, seismic character, geomorphology, and stratigraphic location. Two surfaces and an isopachyte of the sequences are produced: depth to the basement/SSS I surface (which includes SSS II also, but this is relatively insignificant); depth to the lakebed/SSS V surface; and an isopachyte of SSS III–V. The horizons in the two-way time data were converted to depth using the average lake water velocity of 1450 m/s, and the harmonic mean velocity of the sediments, using 1490 m/s for the average 3 m of SSS V that forms most of the lakebed, and an average velocity gradient of 1500 m/s + 6 s^{-1} within SSS III–IV beneath.

6.2.2 Acoustic Basement

The upper reflection of the acoustic basement is usually a broad and strong undulating reflection, except where penetration through the sequences above is only just achieved (e.g. Figure 6.6). It is completely transparent ignoring any remnant multiple energy. The undulations on MCS line 2607-line15a and 2707-line4pm have a wavelength c. 100–125 m, and a trough–crest height of up to 10 m.

6.2.3 SSS I(a)

This is a seismically transparent deposit that fills troughs in the basement surface, generally up to the top of their crests. Good examples appear on MCS 2707-line10 and 2707-line13 (Figures 6.12 and 6.13 respectively). SSS I(a) can be up to 10 m

thick and it has a high and variable velocity of 3500 m/s ± 500 m/s. There is always a strong basal reflection. There is sometimes a strong upper reflection (e.g. Figure 6.13), but where there is not, the velocity package usually extends above the crests and banding occurs, with slower velocities above the crests and faster velocities in the troughs. This is due to lower velocities in the facies directly above the crests (e.g. from SSS I(c) or I(d)) being incorporated into the velocity package (e.g. MCS line 2707-line4pm in Figure 6.11). This is not ideal, but in some cases this was necessary to reduce complexity and produce a better migrated image.

6.2.4 SSS I(b)

SSS I(b) is only observed between CDPs 4300 and 4600 on MCS line 2607-line15c (Figure 6.9). This is a seismically transparent facies, except for a single internal reflection dipping c. 10° that appears to divide the deposit. It has strong and irregular basal and upper reflections, and is closely associated with deposits of SSS I(a). However, it has a lower velocity of 3000 m/s ± 200 m/s and is not constrained by a trough in the basement. Instead, SSS I(b) forms a structure c. 10 m thick and 200 m wide.

6.2.5 SSS I(c)

This facies forms distinctively asymmetrical structures larger than 10 m thick, with steeper slopes between 15–20°, and shallower slopes between 5–15°. The best example occurs between CDPs 1200 and 1700 on MCS line 2707-line4pm where the structure is measured to be 40 m thick and and c. 300 m in length (Figure 6.11). It is evident that the structures form on the upslopes of basement highs, with the steeper slope of the structure forming further up the basement high, e.g. CDP 2780 on MCS line 2607-line15b (Figure 6.8). The structures have strong upper reflections and are transparent.

Placing an upper restriction on the size of SSS III(c) structures is difficult, because on MCS lines 2607-line15a and 2607-line15b in the South Basin it appears that these structures have been nested together to form major structures, possibly reaching 80 m thick and 500 m wide (Figures 6.7a and 6.8a). The problem is that

there is insufficient penetration to locate the basal reflections of these structures, and subsequently determine a velocity. This was only possible on MCS line 2707-line4pm where the velocity of SSS I(c) was determined to be 2500 m/s ± 300 m/s.

6.2.6 SSS I(d)

SSS I(d) forms symmetrical sharp crested structures up to 10 m high and 100 m across, with slopes of c. 15°. They have strong, well defined upper reflections, weak internal reflections, and variable basal reflections depending on penetration and whether it is basement or SSS I(a/c) beneath.

The structures can occur: individually, e.g. CDPs 3500–3560 on MCS line 2607-line15b and CDPs 1000–1500 on MCS line 2707-line4pm (Figures 6.8 and 6.11 respectively); in complexes, e.g. CDPs 500–650 on MCS line 2607-line17 and CDPs 300–700 on MCS line 2707-line4pm (Figures 6.8 and 6.11 respectively); or joined together at the bases, e.g. CDPs 1100–1300 on MCS line 2707-line10 (Figure 6.12).

The seismic velocity of SSS I(d) appears to vary according to location. In the South Basin SSS I(d) has a uniform average velocity of 2150 m/s ± 200 m/s. In the North Basin SSS I(d) forming the individual structures and those joined at the base have lower seismic velocities of 1750 m/s ± 50 m/s, which are readily identified on Figures 6.16a and 6.16b. Where SSS I(d) forms complexes on MCS lines 2707-line4pm (CDPs 300–700) and 2707-line13 (CDPs 100–300) in the North Basin (Figures 6.11 and 6.13 respectively), a quite variable average seismic velocity of 2200 m/s ± 300 m/s is observed. This is closer to that found in the South Basin.

6.2.7 SSS I(e)

SSS I(e) forms deposits c. 10 m thick that thin down slope from higher structures. The example of SSS I(e) on MCS line 2607-line15b forms a deposit atop SSS I(c), and has a downslope extent of about 200 m (Figure 6.8). It has a strong, smooth–irregular upper reflection, a weak and irregular basal reflection, and contains weak internal reflections orientated similarly to the bounding reflections. SSS I(e) on average has a seismic velocity of 2100 ± 200 m/s.

6.2.8 SSS I(f)

SSS I(f) is only observed between CDPs 1400 and 1900 on MCS line 2607-line15a (Figure 6.7). SSS I(f) forms a deposit up to 30 m thick and 700 m long that is contained by basement structures to the South and North, and fills over troughs in the basement beneath. It has a weak and extremely irregular upper reflection and a strong (but quite noisy), undulating basal reflection. It is filled with chaotic internal reflections and has a seismic velocity of 2300 m/s ± 300 m/s.

6.2.9 SSS II(a)

SSS II(a) is only observed between CDPs 4000 and 4150 on MCS line 2607-line15c (Figure 6.9). It forms a distinctive structure, with fine discontinuous internal reflections beneath a relatively rounded upper reflector and above a strong and irregular basal reflector. The structure is c. 8 m high and 150 m wide with slopes to the North and South of c. 5°. It is readily observed on Figure 6.15c because it has a distinctive velocity of 1650 m/s ± 30 m/s.

6.2.10 SSS II(b)

SSS II(b) is only observed between CDPs 1200 and 1320 on MCS line 2607-line15a (Figure 6.7), and is perched above SSS I(f) before it appears to collapse towards it. SSS II(b) has a strong and regular upper reflector that appears almost horizontal, and a strong basal reflector forming an undulating basement beneath. It exhibits some strong, finely layered internal reflections near the top, and has a velocity of 1800 m/s ± 100 m/s. It is c. 10 m thick and 120 m wide.

6.2.11 SSS III(a)

SSS III(a) is up to 35 m thick (Figure 6.6), and is composed of strong, horizontally layered reflections that generally change from sub-metre spacing to 1-metre spacing deeper down. This facies tends to be thicker where the depth to the underlying surface is greater (e.g. MCS line 2707-line10, Figure 6.16b). SSS III(a) forms the bulk of material on all the MCS lines, and has a variable basal reflection because

it covers over the undulating surface beneath, formed by the previous sequences or the acoustic basement. It has a strong upper reflection against either SSS IV or V in the North Basin, unless SSS IV has replaced some of the sequence (e.g. CDPs 920–1440 in Figure 6.16a). It has no upper reflection when it grades into SSS III(b) in the South Basin.

There is a pair of doublets labelled "Marker Beds" at the top of SSS III(a) in the North Basin (Figure 6.16), which have similarly very strong reflections and weaker, closely spaced reflections directly beneath. They are also possibly within the top of SSS III(b) in the South Basin (Figure 6.15a). The Marker Beds are closer together on the shallower MCS line 2707-line13 (Figure 6.16c) and are spaced furthest apart on the deeper MCS line 2707-line10 (Figure 6.16b).

The migrations are improved when the velocity models use an increasing velocity to represent SSS III (the velocity packages incorporated both SSS III(a) and SSS III(b) where the latter was present). These varied from 1500 m/s and 4 s^{-1} on MCS line 2607-line15a (Figure 6.15a) to 1500 m/s and 10 s^{-1} on MCS line 2707-line10 (Figure 6.16b). The average velocity gradient for SSS III is 1500 m/s and 6 s^{-1}. The average velocity within SSS III(a) is c. 1565 m/s. The greatest velocity reached within SSS III(a) is c. 1750 m/s on MCS line 2607-line11 (Figure 6.14).

6.2.12 SSS III(b)

SSS III is thicker in the South Basin and has been separated into facies (a) and (b) (Figure 6.15). SSS III(b) consists of weak, horizontally layered reflections less than 1 m apart and is up to 12 m thick (e.g. Figure 6.6). It has a similarly strong upper reflection against SSS IV or V as SSS III(a) does in the North Basin, but has no basal reflection because it grades into SSS III(a) where the horizontally layered internal reflections become stronger. SSS III(b) has an average velocity c. 1535 m/s.

6.2.13 SSS IV

This sequence occurs in two different forms: a disturbed unit with a strong and irregular upper reflection, a weak and irregular basal reflection, and random internal

reflections—the largest example of which is up to 7 m thick and 500 m across, between CDPs 900 and 1400 on MCS line 2707-line4pm (Figure 6.16a); a discrete unit with strong and regular upper and basal reflections, and weak internal structure that is sometimes nested together with similar units—good examples up to 3 m thick and 250 m in length are between CDPs 300 and 540 on MCS line 2607-line11 (Figure 6.14a), and between CDPs 380 and 500 on MCS line 2607-line17 (Figure 6.14b).

Discrete units of SSS IV occur above the Marker Beds (e.g. on MCS line 2707-line10, Figure 6.16b), whereas the disturbed units tend to cut through them (e.g. c. CDP 900 on MCS line 2707-line4pm, Figure 6.16a). SSS IV never interferes with SSS V above. The average velocity used for SSS IV is 1500 m/s ± 10 m/s.

All the localised occurrences of SSS IV sequences beneath SSS V have been located on Figures 6.4 and 6.5, along with arrows emanating from the estimated direction of origin where possible. Additionally, possible erosion surfaces beneath SSS V are located.

6.2.14 SSS V

SSS V forms the lakebed over most of Windermere (Figures 6.15 and 6.16). It is 2–5 m thick, being thinner only on slopes greater than 5° (e.g. between CDPs 1520 and 1750 on MCS line 2707-line4pm, Figure 6.11). SSS V does not accumulate on slopes greater than 10° (e.g. between CDPs 185 and 205 on MCS line 2607-line11, and CDPs 220 and 260 on MCS line 2607-line17 in Figure 6.14).

SSS V has strong and regular upper and basal reflections, unless a disturbed unit of SSS IV, or perhaps what appears to be an erosional surface (e.g. CDPs 120–450 on MCS line 2707-line13, Figure 6.13), makes the basal reflection irregular. It is mainly transparent except for a few weak, horizontal internal reflections. There is no disturbance in SSS V except where gas is present (e.g. CDPs 3000–3140 on MCS line 2607-line15b, Figure 6.8).

The average velocity of SSS V in the South Basin is 1505 ± 15 m/s. The velocity for SSS V in the North Basin is much more variable and ranges between 1400 m/s and 1500 m/s. In the North Basin the modelled velocities for SSS V are required to vary laterally along MCS lines 2707-line4pm and 2707-line13, but are satisfied

with a uniform package velocity of 1490 m/s along MCS line 2707-line10 (Figure 6.16). MCS line 2707-line4pm is particularly interesting (Figure 6.16a): velocity decreases from an unusually high 1600 m/s to 1500 m/s, whilst descending the slope between CDPs 1450 and 1650; a more typical and homogeneous velocity of 1480 m/s to 1500 m/s exists between CDPs 730 and 1450, and CDPs 1700 and 2000 in the more southern hanging depo-centre; and velocity decreases from 1400 m/s to an abnormally low 1250 m/s north of CDP 350 where gas is present. Nevertheless, the average velocity for SSS V tends to be c. 1490 m/s.

The Q_{SR} of SSS V was easily determined using the Chirp data. Where an isolated basal reflection could be windowed, the spectral signatures of SSS V were very similar and an average robust Q_{SR} of 32.6 ($+6$; -4) was derived along the sequence. Unfortunately, Q_{SR} for the other sequences could not be determined. This was because the only other sequence penetrated by the Chirp data was SSS III, within which there are no isolated reflections.

6.2.15 Basement/SSS I Surface

Figures 6.17 and 6.18 show the depths to the basement/SSS I surface in the South and North basins respectively. The basement/SSS I surface has been divided into eight sub-basins that form along the axis of the lake: five of similar size in the South Basin (sb_1–sb_5); and three in the North Basin (sb_6–sb_8), where sb_6 is the smaller hanging basin observed at the south end of MCS line 2707-line4pm (Figure 6.11), and sb_7 and sb_8 are two large sub-basins separated by the neck of the North Basin.

The facies of SSS I (and SSS II) are indicated on the maps; the ridges produced by facies I(c)–I(e) are not always clear within the surface due to variation being smoothed by the colour palette (i.e., if there is a depth variation of 9 m within one of the 10 m colour contours it will not be visible). They have been identified in the seismic data though and interpreted as accurately as possible on the maps.

There appears to have been a similar amount of glacial overdeepening in both basins, however, there is c. 30 m of SSS I(f) in sb_2, making this the most overdeep-end location.

6.2.16 SSS III–V Isopachyte

Figures 6.19 and 6.20 show the thickness of SSS III–V in the South and North basins respectively. The five sub-basins in the South Basin correspond with five SSS III–V depo-centres; in sb_1, sb_2 and sb_3, SSS III–V is generally 25–40 m thick, and in sb_4 and sb_5 generally 15–25 m thick. The deepest parts within the three sub-basins in the North Basin also correlate with depo-centres; generally the sediments in the depo-centres in the North Basin are 10–25 m thick.

On Figure 6.19 location A marks a "hanging deposits" of thinner SSS III–V deposits (18 m ± 2 m) that stretch at least 1.5 km southwards along the west side of the thickest SSS III–V deposits in Windermere (50 ± 3 m), which are contained within the main depo-centres of sb_2 and sb_3.

On Figure 6.20 location B on the southwestern side of sb_7 marks an isolated location where SSS III–V thickens to 15 m ± 2 m. This area is known to contain slumps of sediment from the steep western flank (Vardy, 2009) and is probably caused by the presence of a thicker SSS IV sequence. Location C marks the location where the thicker SSS III–V deposit shifts across sb_7. This is because it has been focused into the deeper parts of the basement/SSS I surface.

6.2.17 Lakebed/SSS V Surface

Figures 6.21 and 6.22 show the depth to the lakebed/SSS V in the South and North basins respectively. The lakebed along the axis of the South Basin is generally between 30–40 m deep. The impressions of sb_2–sb_5 are visible, with sb_2–sb_3 deeper and more prominent despite containing the thicker sequences of SSS III–V; sb_1 has been completely filled by SSS III–V. The transitions between the three sub-basins in the North Basin are very smooth, with the deepest parts of the lakebed generally always down the centre of the sub-basins, and between 30–60 m deep (excluding the shallower sb_6 that is only 25–30 m deep).

Figure 6.21 shows that the deepest part of the South Basin is a small area of c. 40 m depth (just outside the next contour range) in sb_3. The shoreline slope to lakebed is very steep here: over 150 m the depth reduces from 0 to 40 m (± 2 m) with a slope of 15°. There is a lakebed high at location A of 20.5 m (± 1) on the

axial line of the basin. This is at least 10 m shallower than elsewhere along the axial line and is produced by the top of a SSS I(c) structure beneath. Location B marks a channel 10–15 m deep that runs from the ferry crossing down to the entrance of the South Basin. This was found by Mill (1895) who proposed that sediment had been eroded away by current waters travelling into the South Basin. This can now be attributed to a glacially deepened channel that contains a relatively thick deposit of SSS III–V, but, which is not quite thick enough to completely fill the channel.

Location C on Figure 6.22 shows that the wider part of the North Basin is flanked to the West by the steepest topography near Windermere. Over a distance of 700 m, the topographic height above sea-level changes from 215 m to 0 m (± 1 m) on the lakebed, representing a slope of c. 17°. This location has been shown to be a source of mass-transport events (Vardy, 2009).

Location D on Figure 6.22 marks the deepest part of the North Basin, which is 60–65 m deep. This is not the deepest location because the greatest amount of glacial overdeepening occurred here, but because there is not a thick deposit of SSS III here like there are in the sub-basins of the South Basin. Along the axis of sb_8 the lakebed shallows steadily from the deepest location in both directions. Southwards, over 1.3 km, towards the neck of the North Basin, the lakebed shallows from 62 m (± 2.5 m) to 47 m (± 1 m) with a slope of 1°. It is evident that the sedimentation has smoothed out most of the impressions of the underlying basement/SSS I surface over most of the North Basin.

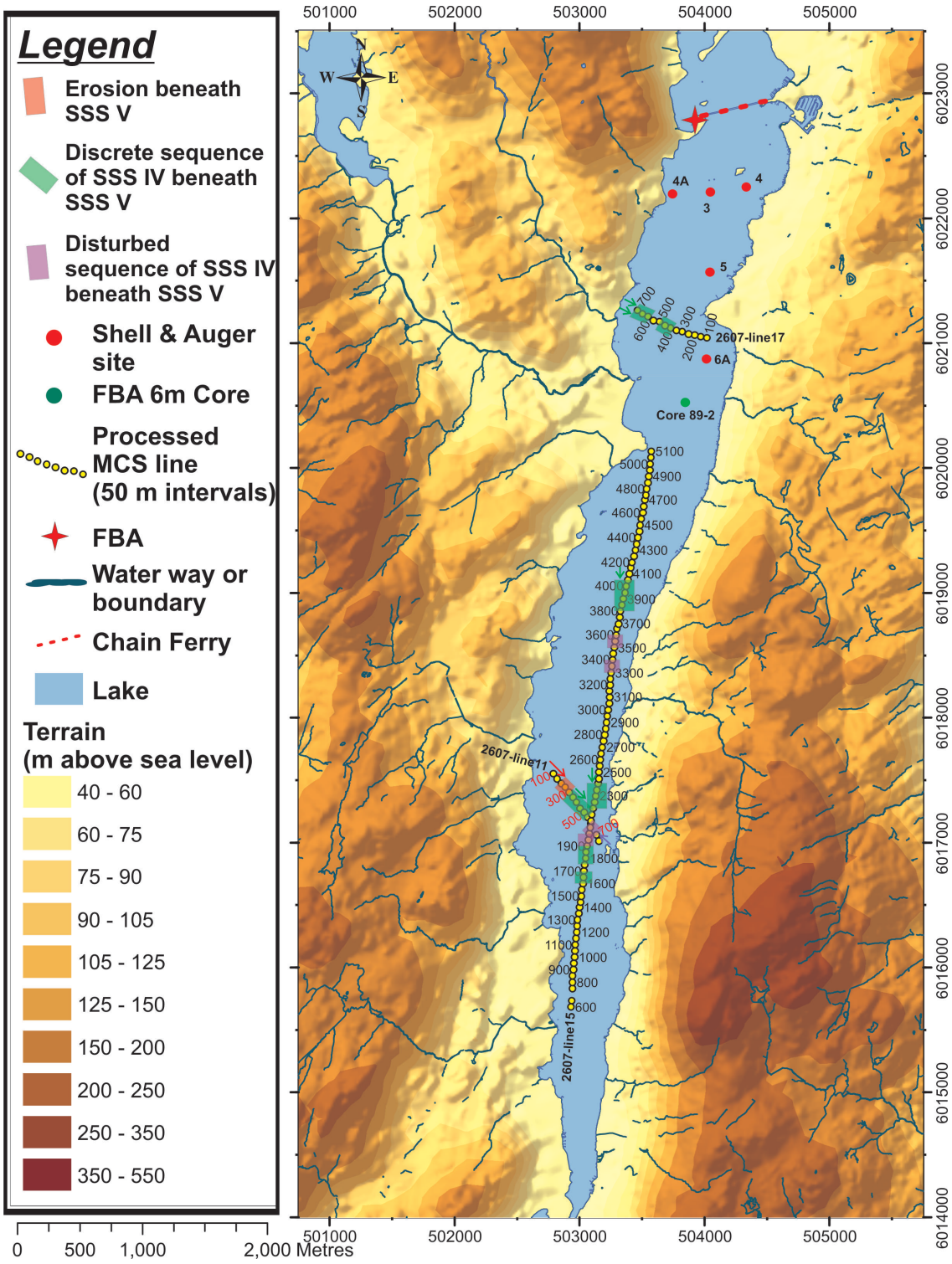

Figure 6.4: Location of the processed MCS lines in the South Basin, core sites, and mass transport features. Co-ordinates are UTM zone 30.

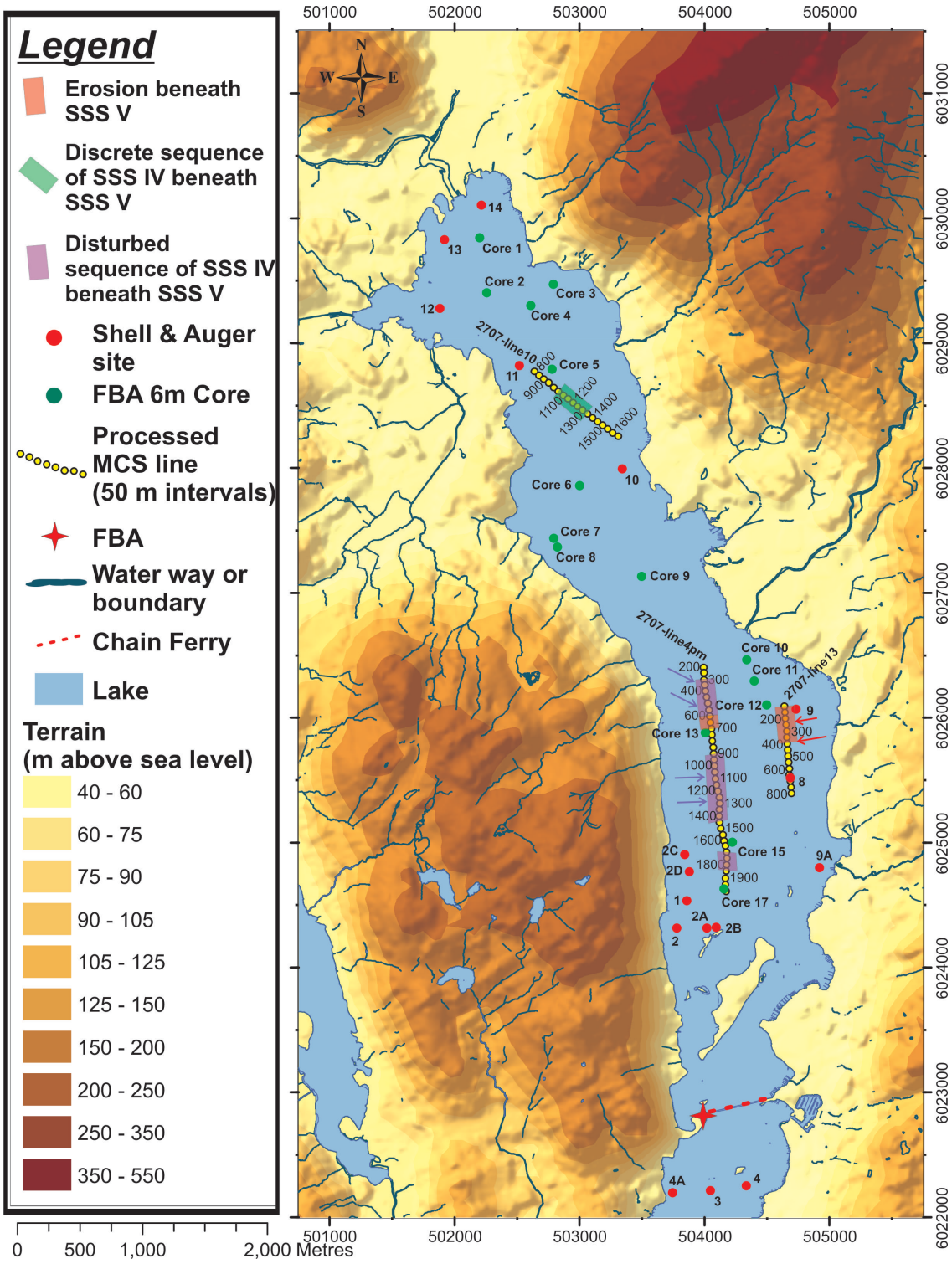

Figure 6.5: Location of the processed MCS lines in the North Basin, core sites, and mass transport features. Co-ordinates are UTM zone 30.

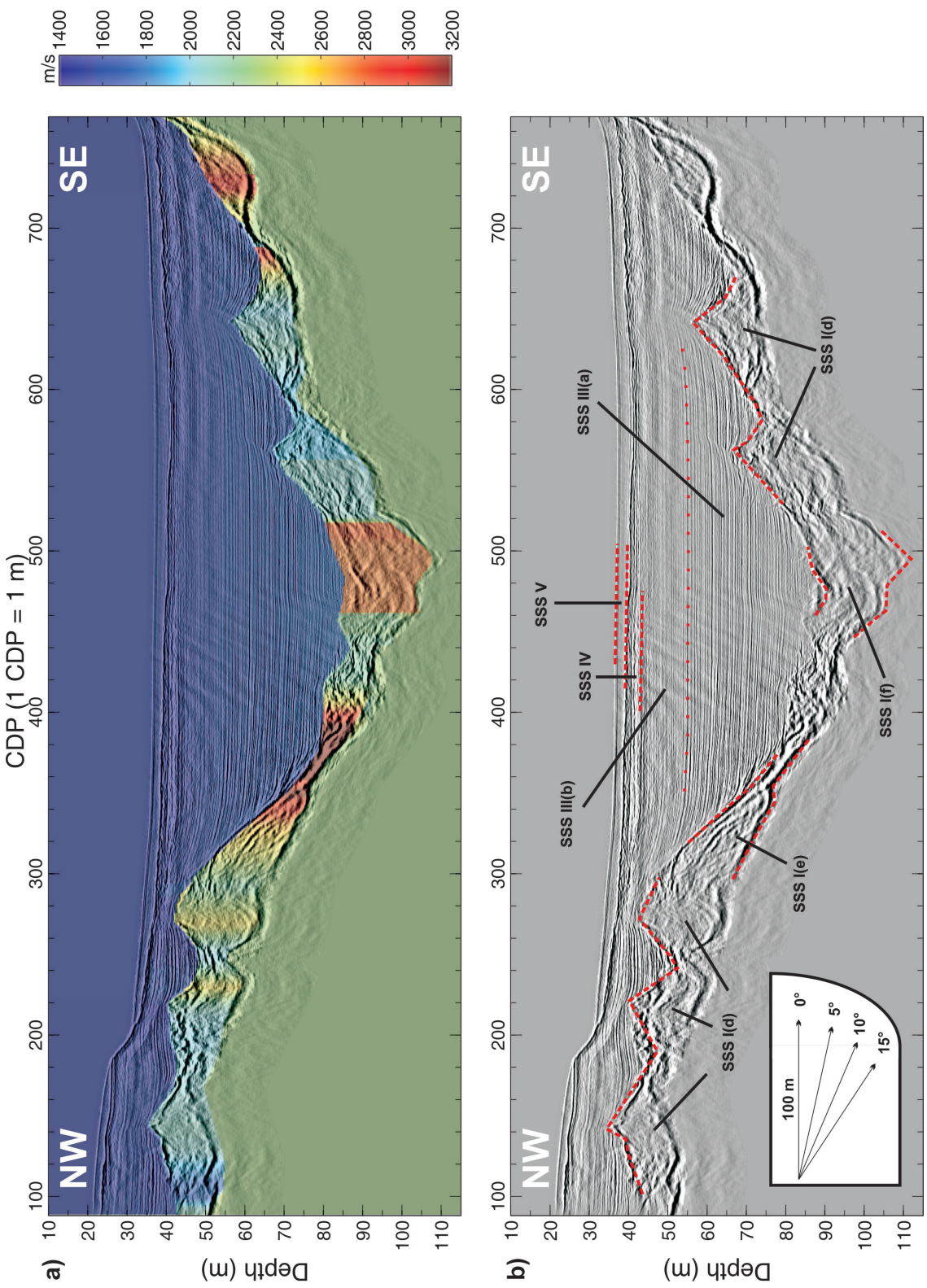

Figure 6.6: South Basin MCS line 2607-line11: a) Complete velocity model and migrated depth section, b) Interpreted migrated depth section.

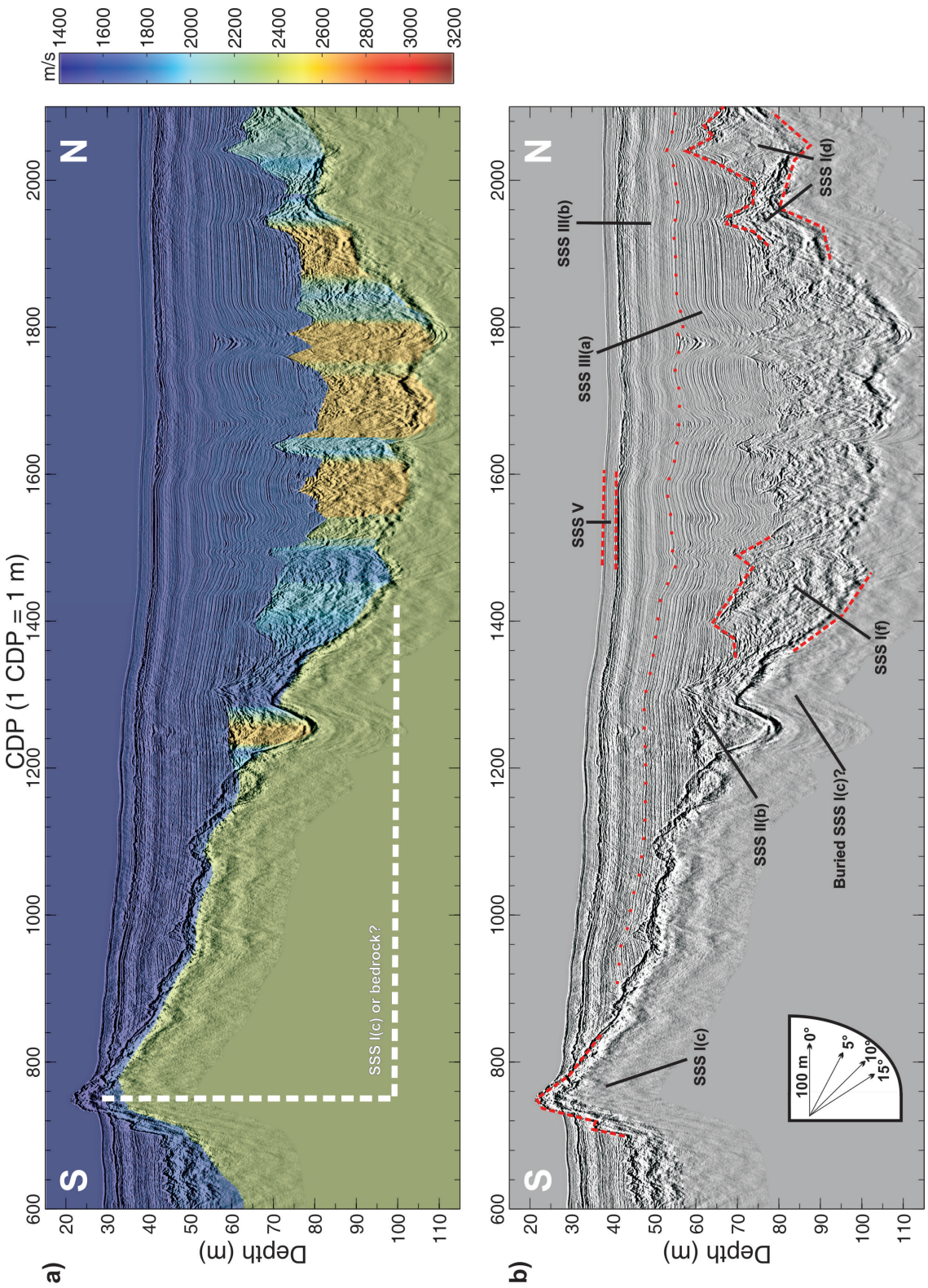

Figure 6.7: South Basin MCS line 2607-line15a: a) Complete velocity model and migrated depth section, b) Interpreted migrated depth section.

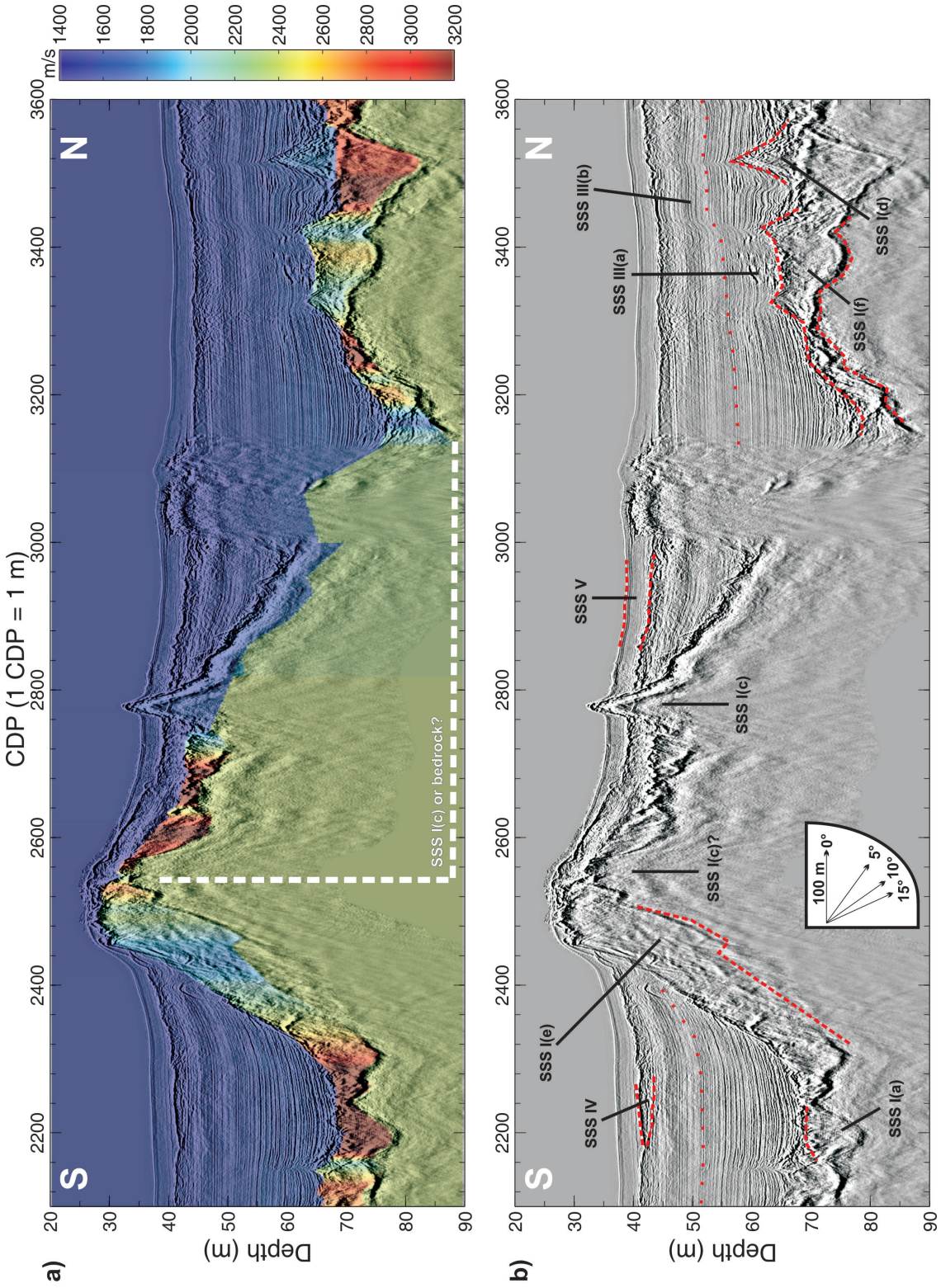

Figure 6.8: South Basin MCS line 2607-line15b: a) Complete velocity model and migrated depth section, b) Interpreted migrated depth section.

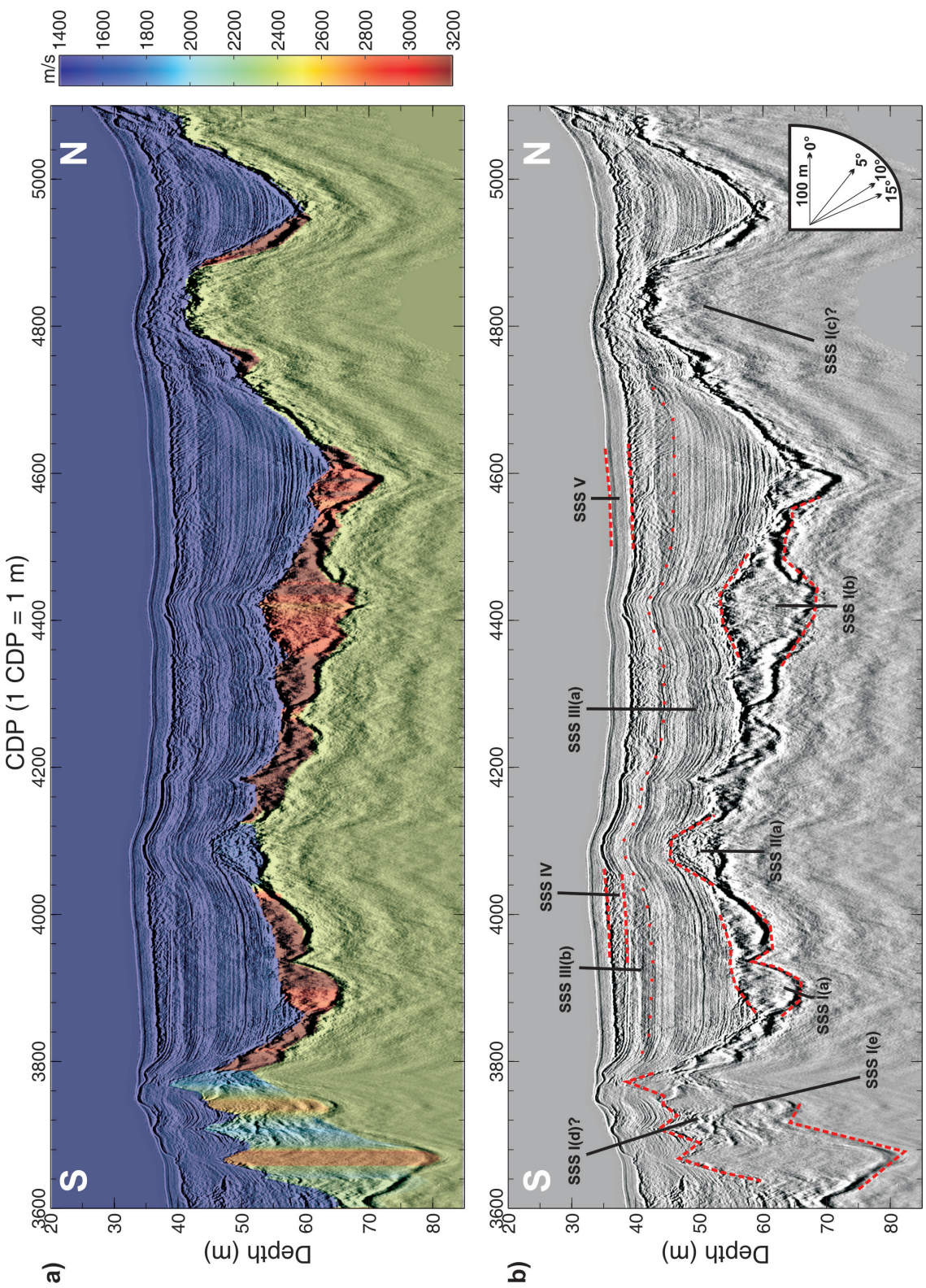

Figure 6.9: South Basin MCS line 2607-line15c: a) Complete velocity model and migrated depth section, b) Interpreted migrated depth section.

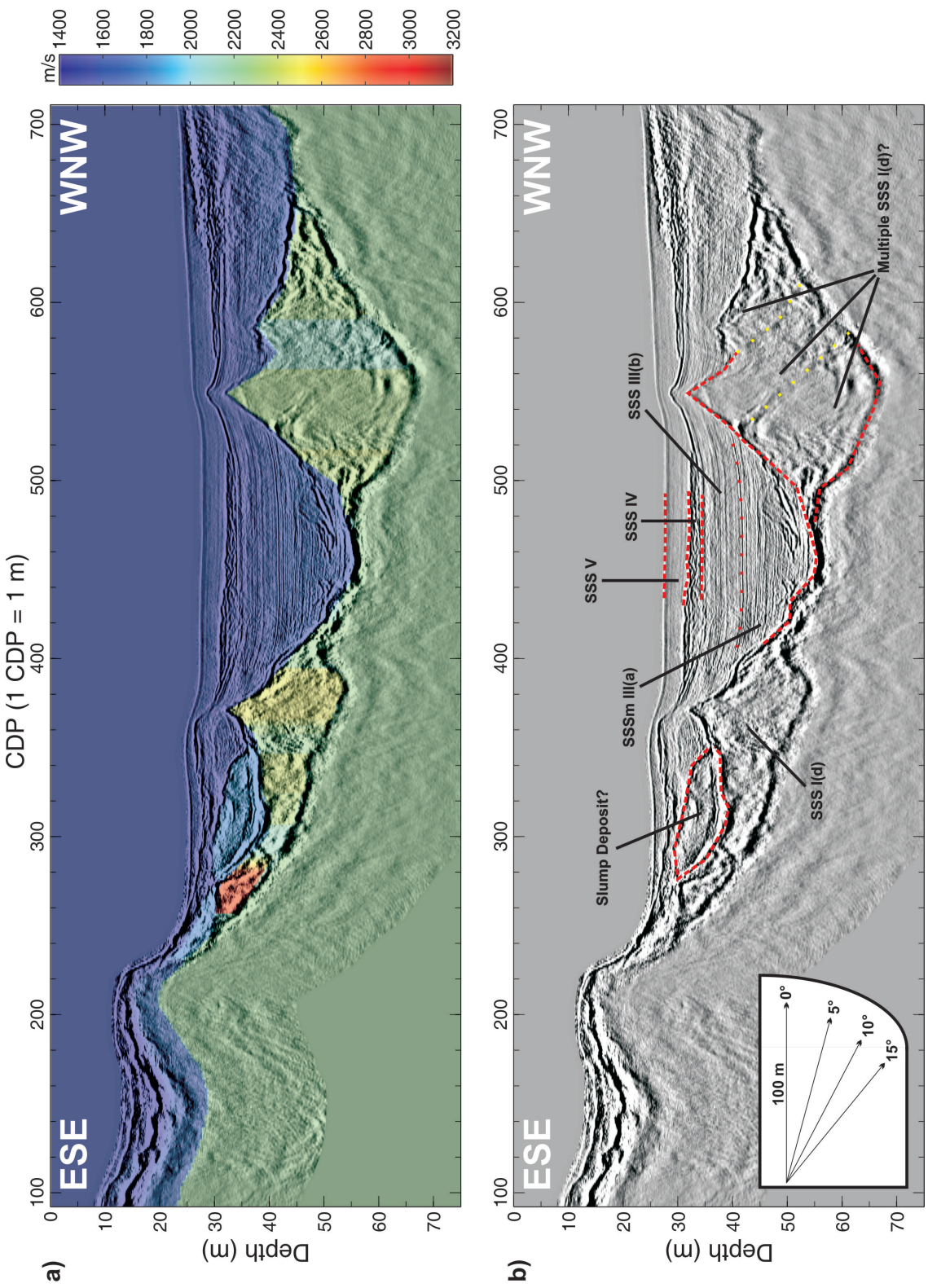

Figure 6.10: South Basin MCS line 2607-line17: a) Complete velocity model and migrated depth section, b) Interpreted migrated depth section.

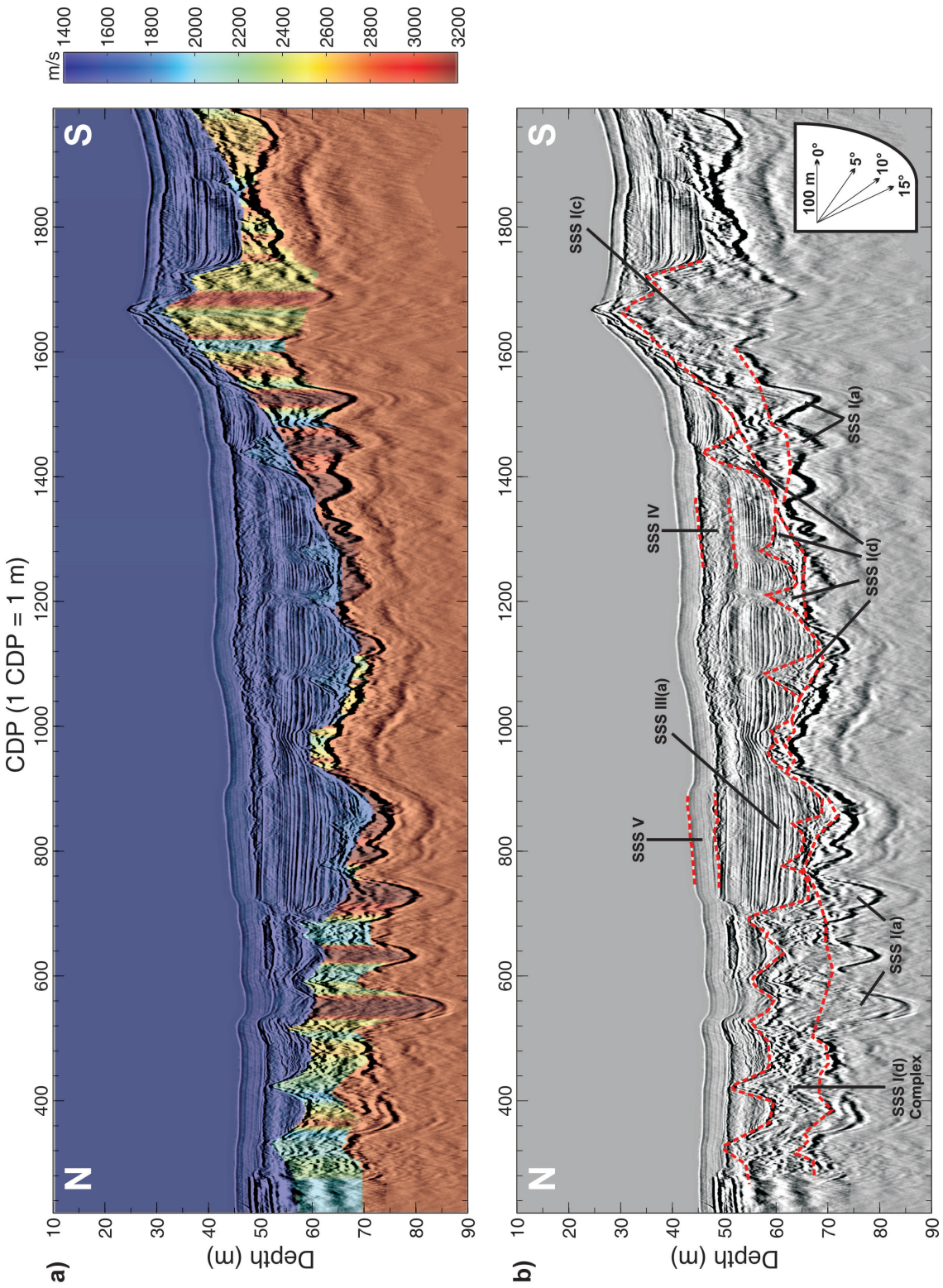

Figure 6.11: North Basin MCS line 2707-line4pm: a) Complete velocity model and migrated depth section, b) Interpreted migrated depth section.

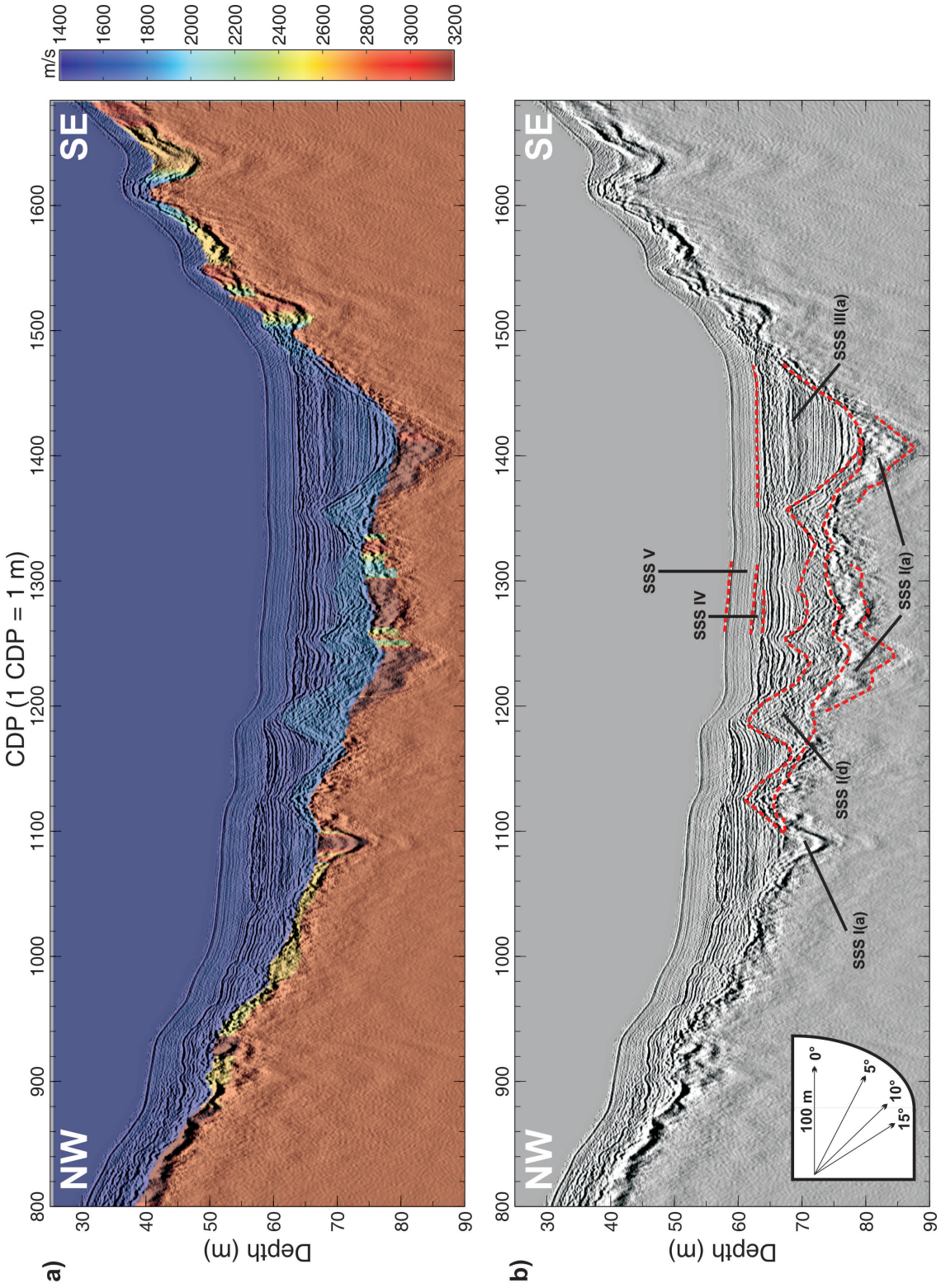

Figure 6.12: North Basin MCS line 2707-line10: a) Complete velocity model and migrated depth section, b) Interpreted migrated depth section.

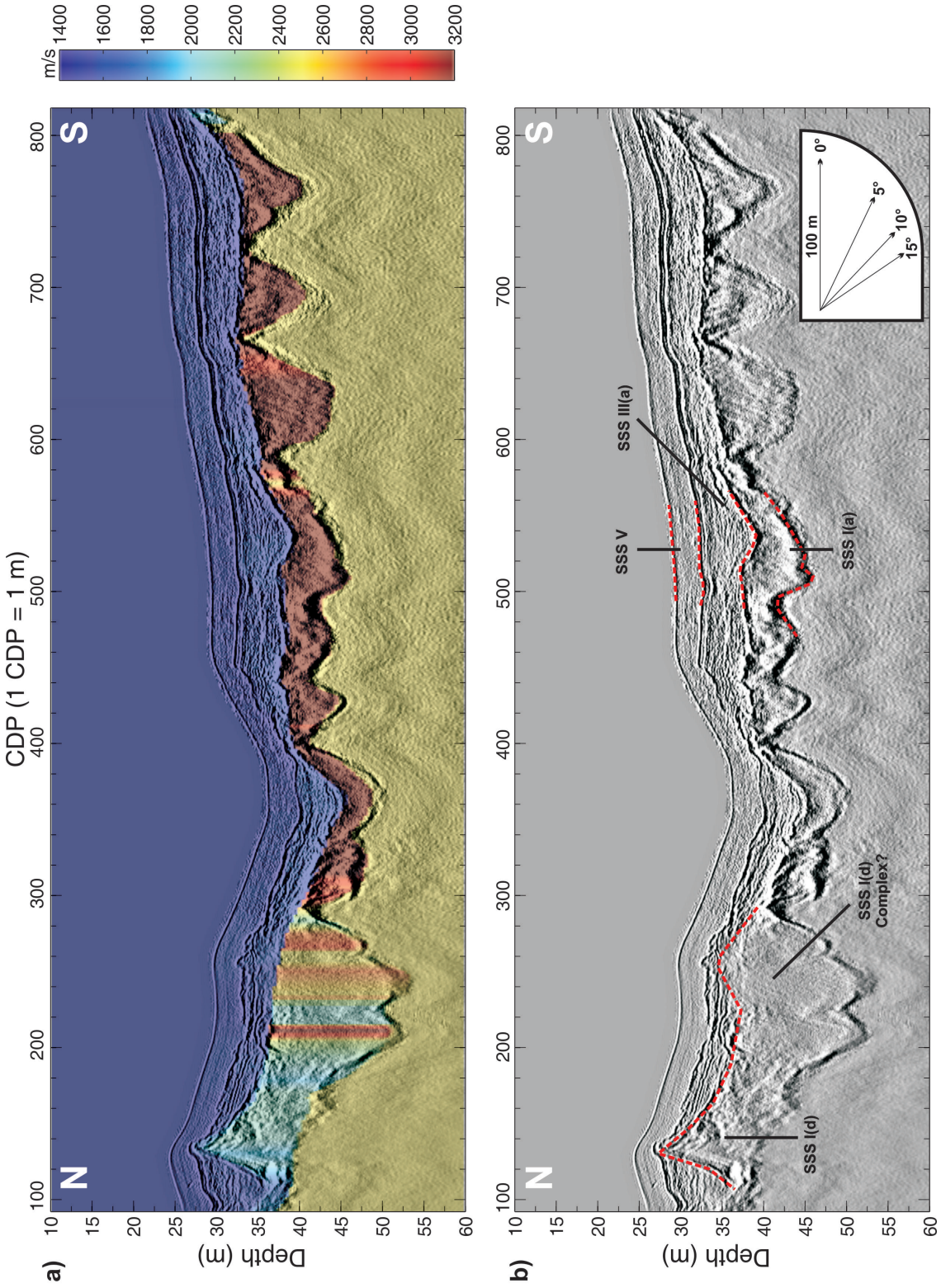

Figure 6.13: North Basin MCS line 2707-line13: a) Complete velocity model and migrated depth section, b) Interpreted migrated depth section.

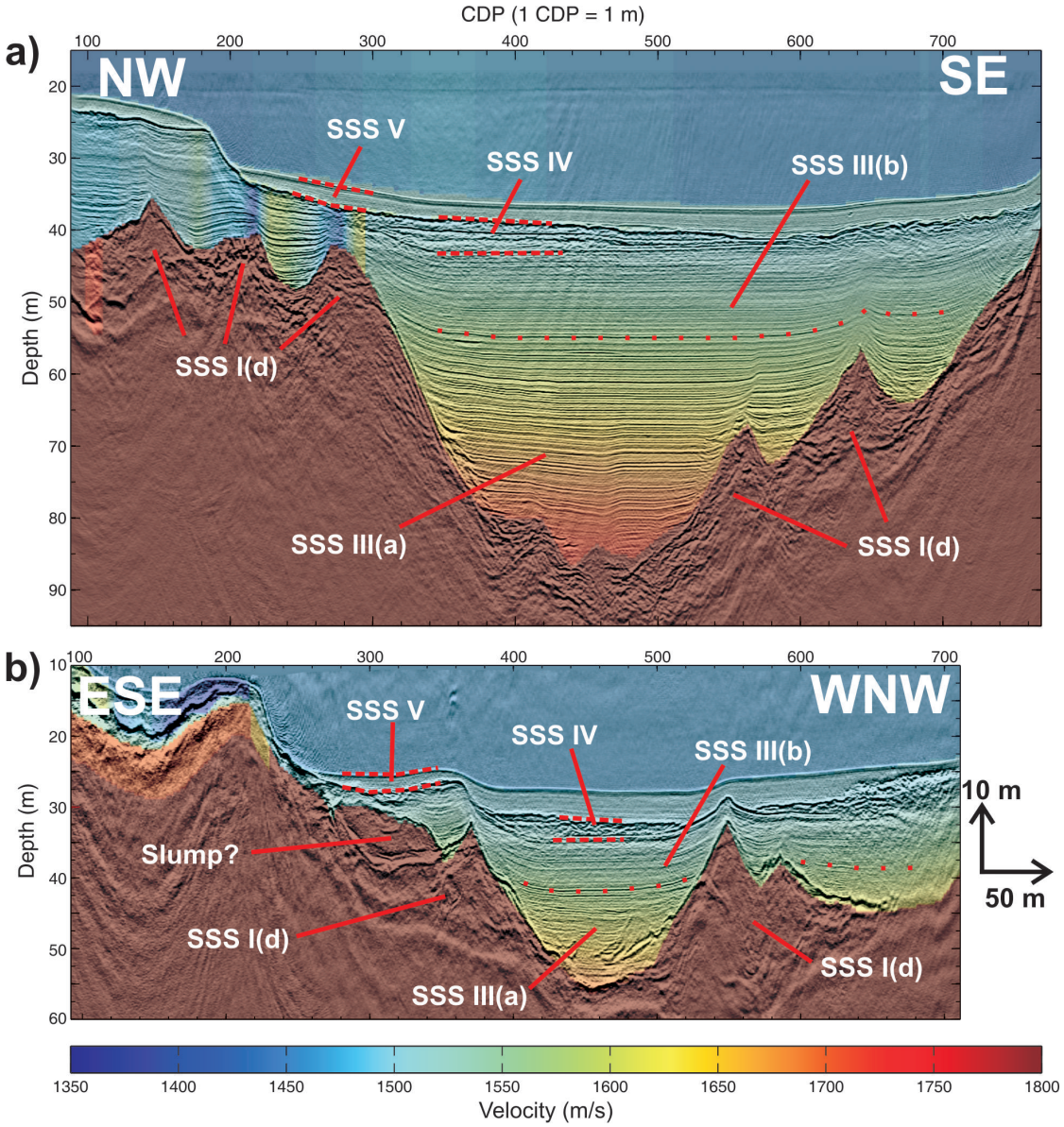

Figure 6.14: Sediment velocity models and migrated depth sections that show cross-sections of the South Basin: a) MCS line 2607-line11; b) MCS line 2607-line17.

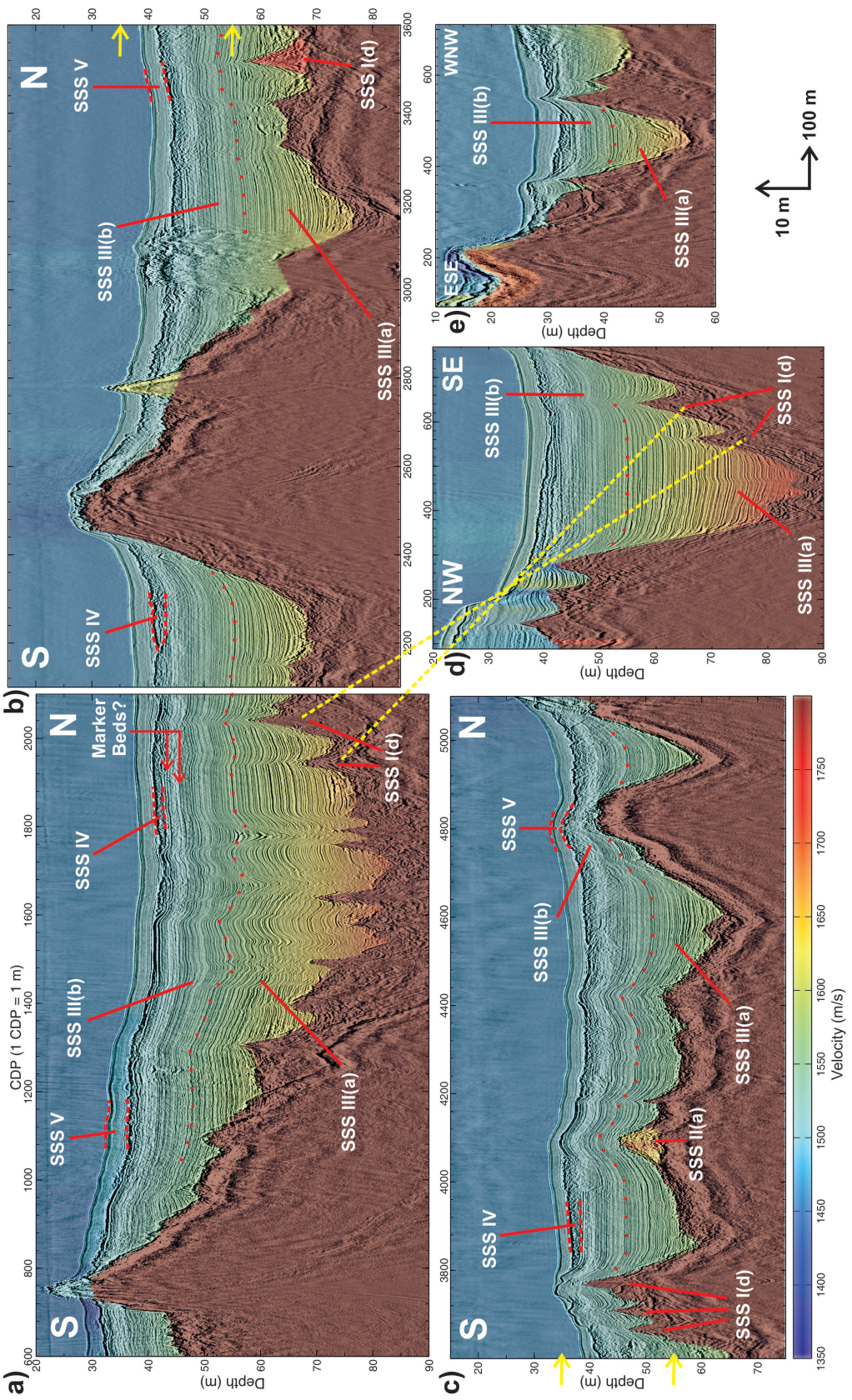

Figure 6.15: Sediment velocity models and migrated depth sections from the South Basin. Sections d and e are shown for cross-referencing and scale purposes only: a) MCS line 2607-line15a; b) MCS line 2607-line15b; c) MCS line 2607-line15c; d) MCS line 2607-line11; e) MCS line 2607-line17.

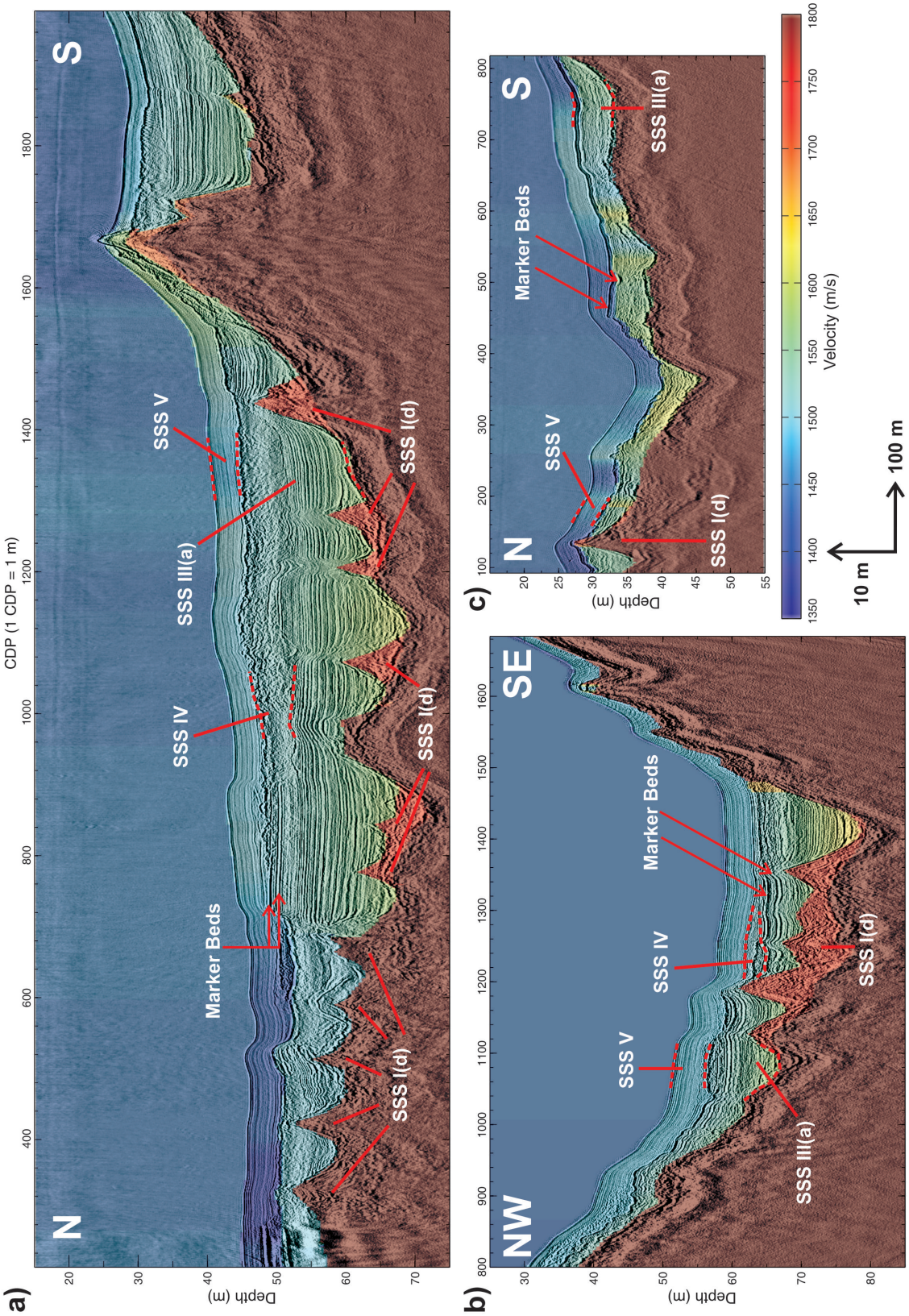

Figure 6.16: Sediment velocity models and migrated depth sections from the North Basin: a) MCS line 2707-line4pm; b) MCS line 2707-line10; c) MCS line 2707-line13.

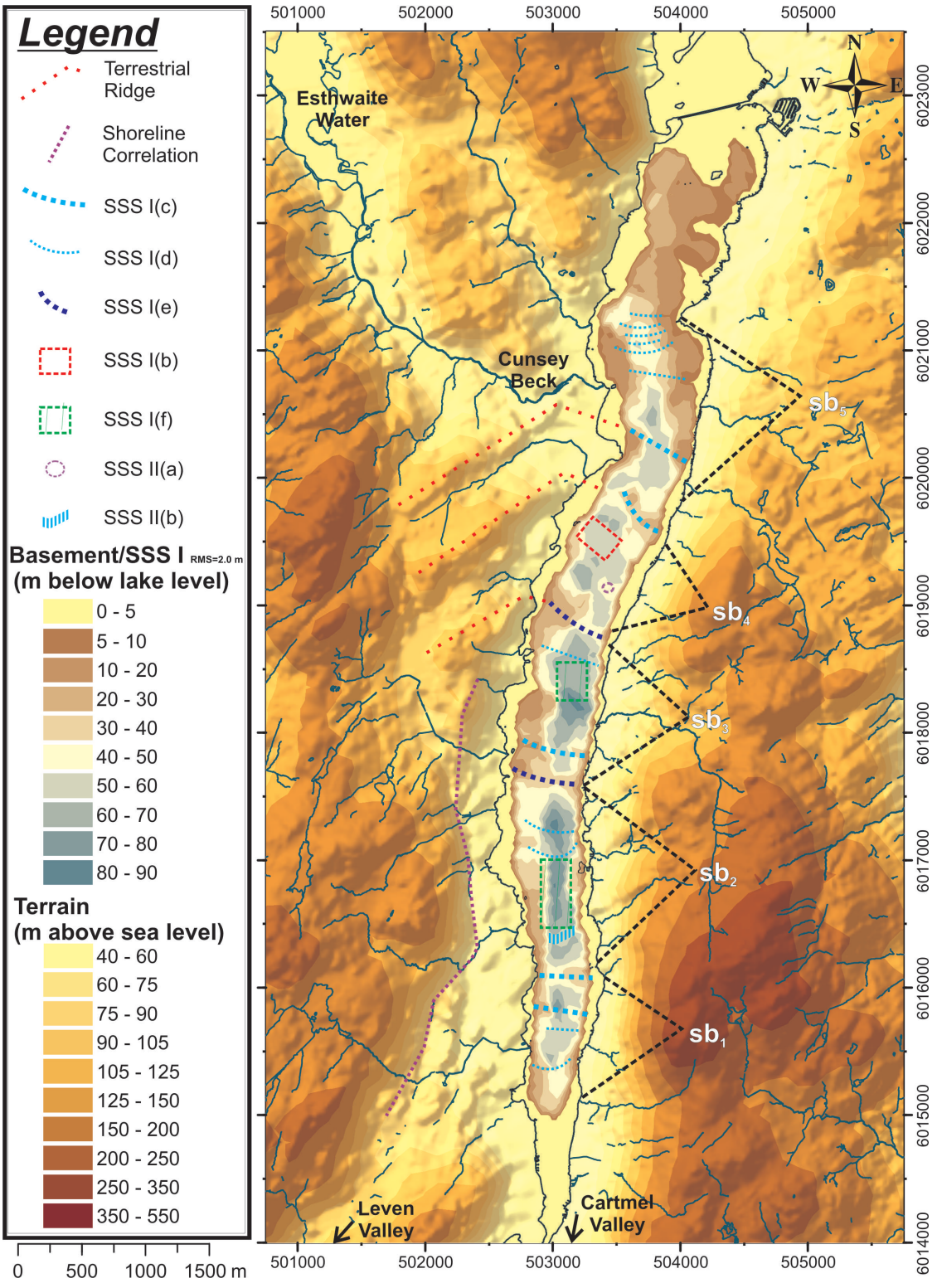

Figure 6.17: Basement/SSS I surface in the South Basin with ridges indicated. Lake boundary and waterways are shown. Co-ordinates are UTM zone 30.

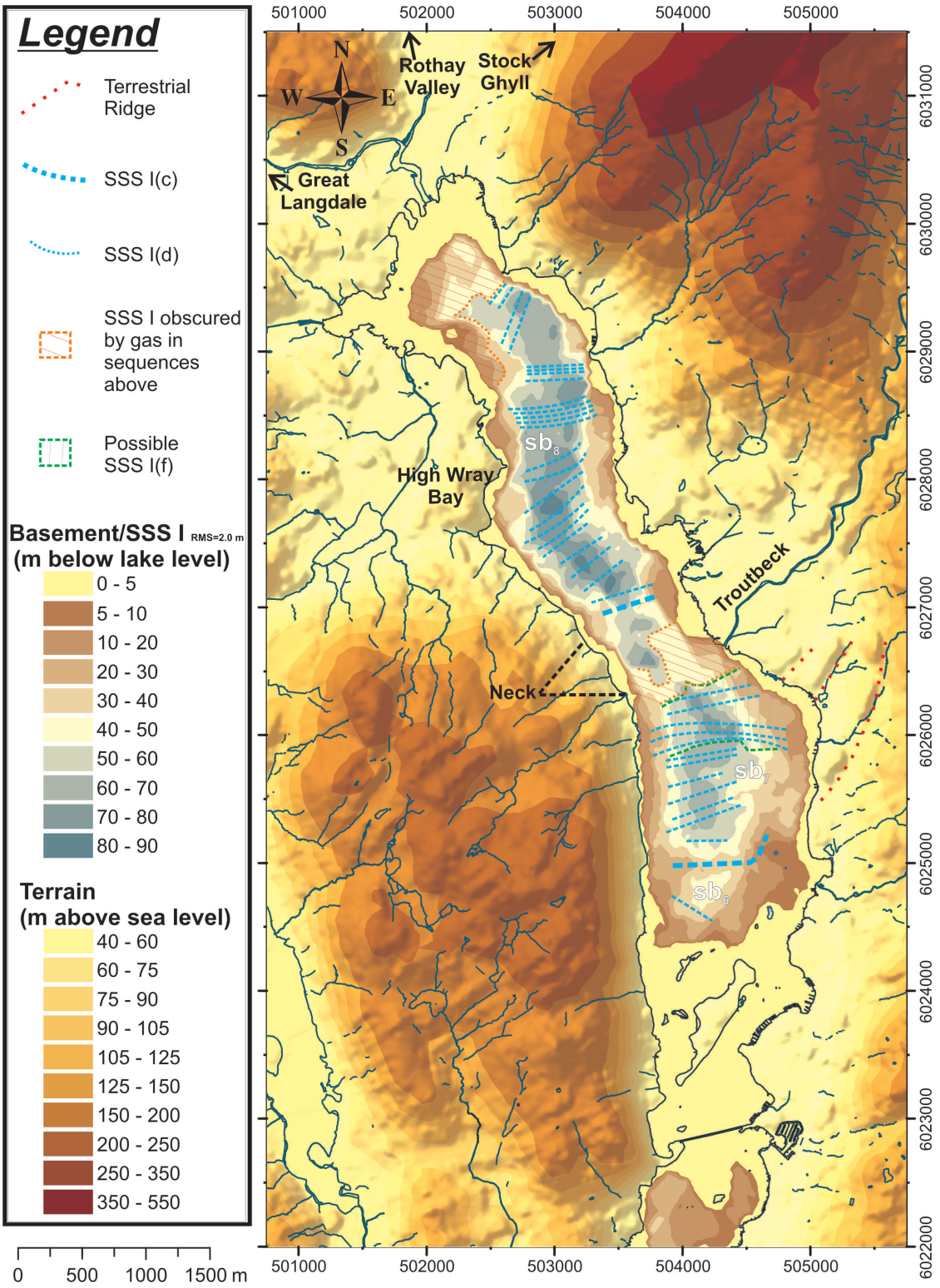

Figure 6.18: Basement/SSS I surface in the North Basin with ridges indicated. Lake boundary and waterways are shown. Co-ordinates are UTM zone 30.

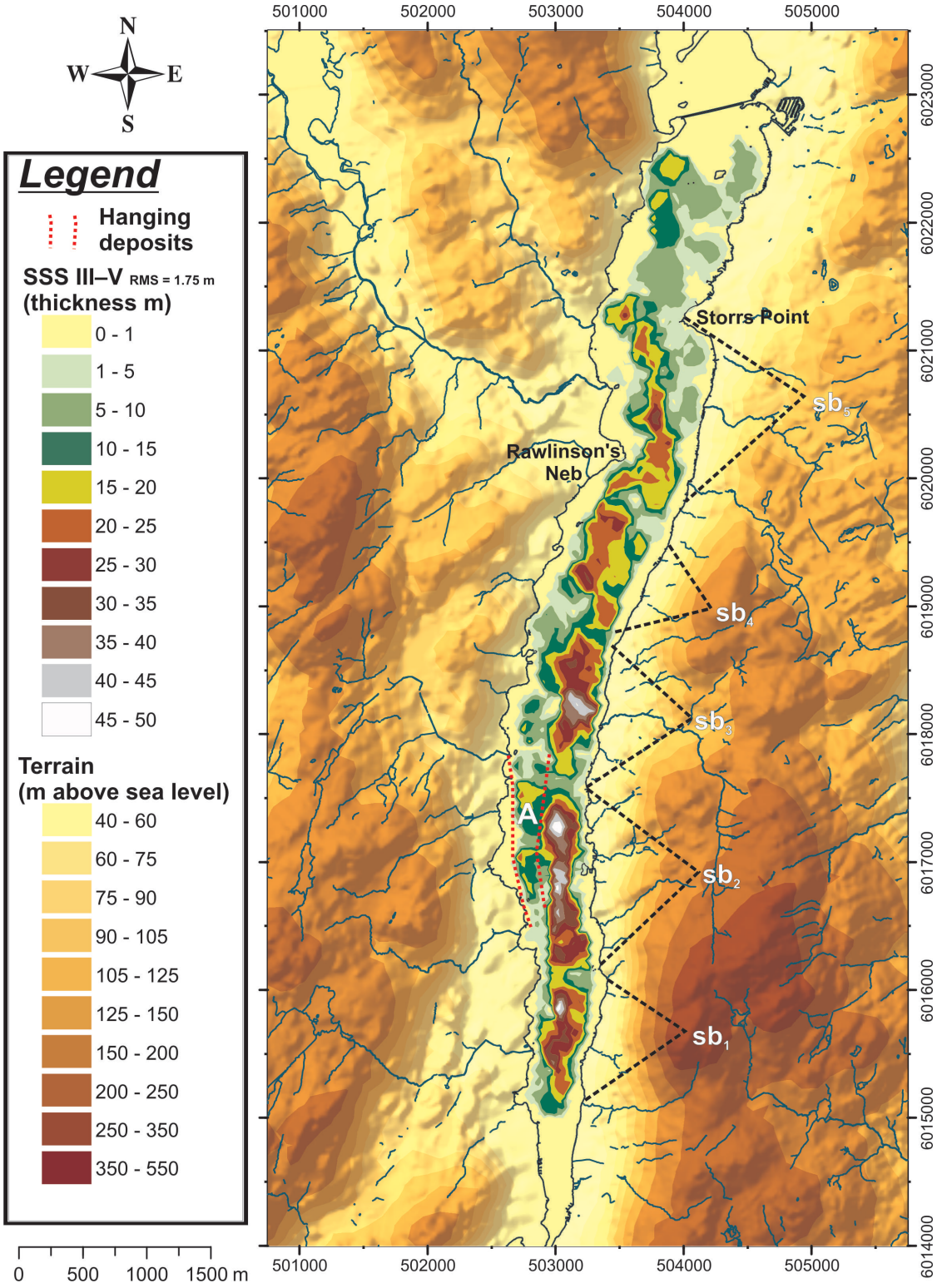

Figure 6.19: SSS III–V isopachyte in the South Basin. Lake boundary and waterways are shown. Co-ordinates are UTM zone 30.

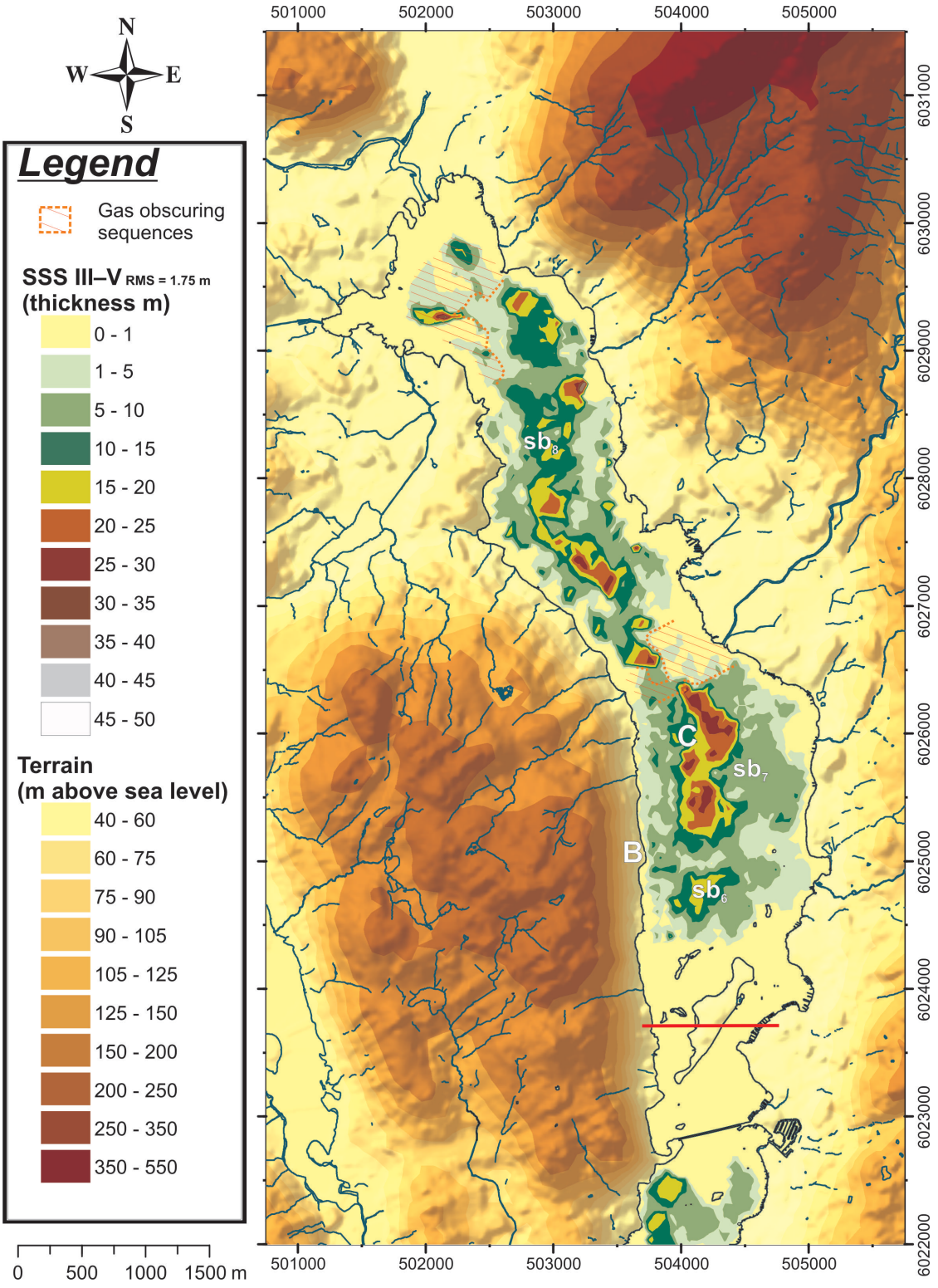

Figure 6.20: SSS III–V isopachyte in the North Basin. Lake boundary and waterways are shown. The red line is the divide between the North and South basins for the purposes of volume calculation. Co-ordinates are UTM zone 30.

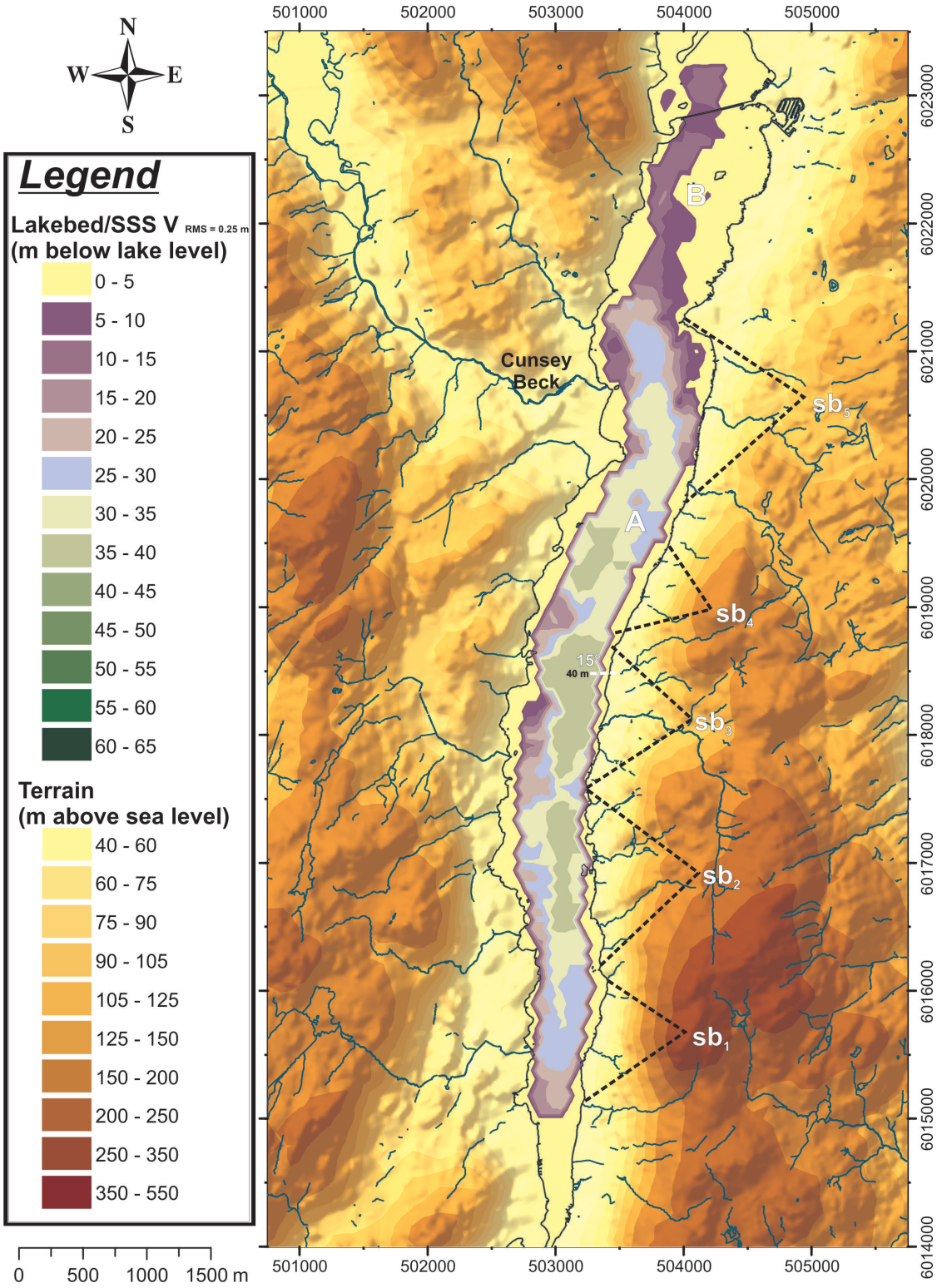

Figure 6.21: Lakebed/SSS V surface in the South Basin. Lake boundary and waterways are shown. The white dashed lines are where measurements of slope are made. Co-ordinates are UTM zone 30.

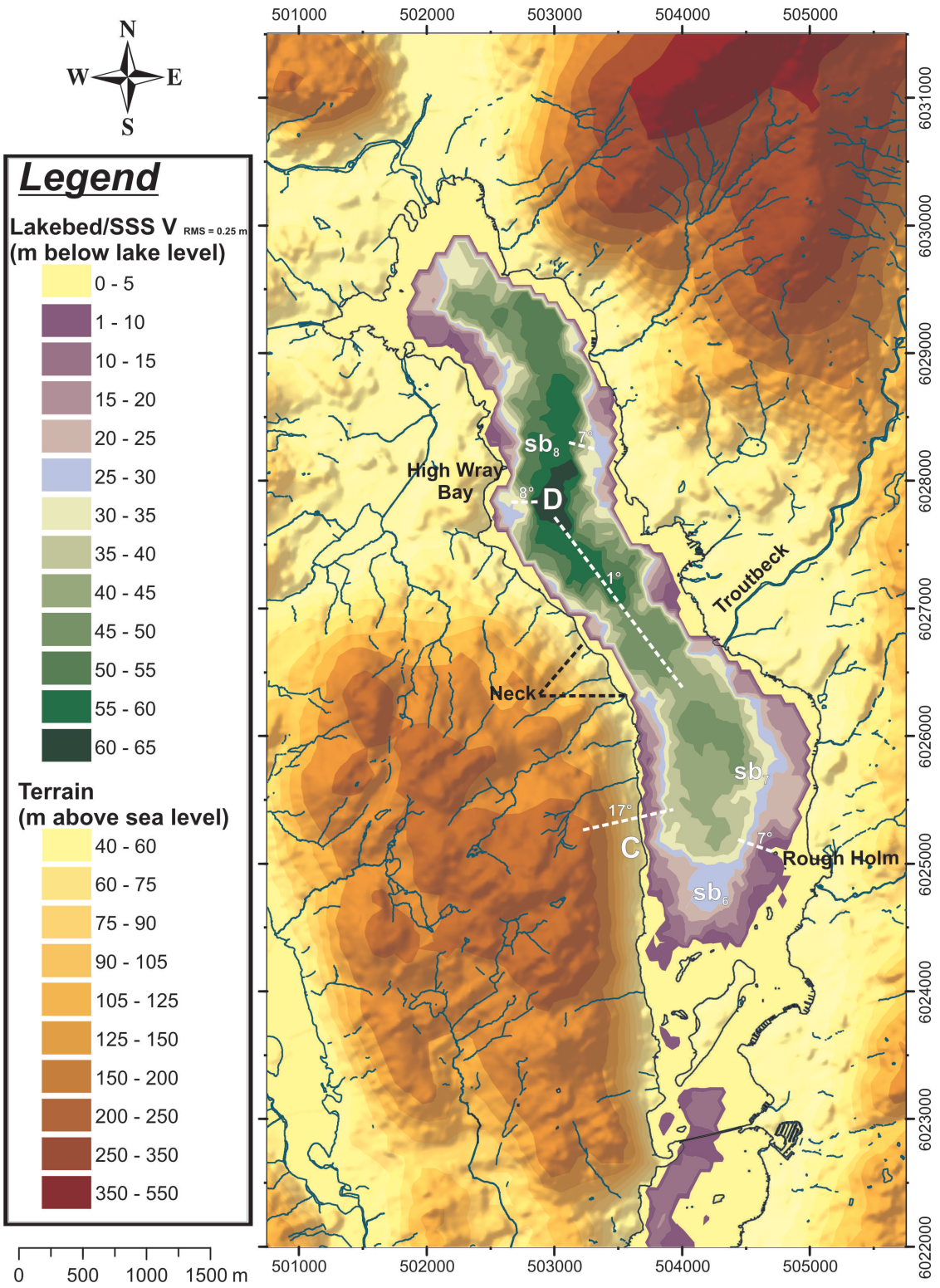

Figure 6.22: Lakebed/SSS V surface in the North Basin. Lake boundary and waterways are shown. The white dashed lines are where measurements of slope are made. Co-ordinates are UTM zone 30.

6.3 Stratigraphic Calibration

The seismic stratigraphy sequences can be associated to the following: till (I); glacio-fluvial (II); glacio-lacustrine/lacustrine (III); slumped/disturbed (IV); and lacustrine (V). Below, the seismic stratigraphic facies in each sequence are associated to a sediment/deposit type. The following facies are referred to as a till only if it is believed that they consist of material that conforms to this definition proposed by Boulton (1972):

"Till is an aggregate whose components have been brought together and deposited by the direct agency of glacier ice, which, though it may have undergone post-depositional deformation by flow, has not been significantly disaggregated and re-deposited."

6.3.1 Acoustic Basement—Bedrock/Till

Given the wet-based nature of Lake District glaciers, till deposited by previous glaciations is unlikely to have survived (personal communication—Dr. Geoff Corner, University of Tromsø), and bedrock was certainly reached beneath the lakebed at some of the shell and auger locations in the North Basin (Figure 6.5): 10 m depth at location 2b; 13 m depth at location 2d; 9 m depth at location 12; and 3 m depth at location 14. Hence, at least in the North Basin, the acoustic basement in the MCS data is probably bedrock.

However, the situation is the South Basin is less clear. The acoustic basement appears in some locations beneath the upper reflections of large, possibly nested SSS I(c) structures (Figures 6.7 and 6.8). In these locations thick SSS I facies possibly form the transparent acoustic basement.

No seismic velocities between 4.0–5.0 km/s were found, which is the seismic velocity for the Silurian bedrock beneath Windermere (Wilson, 1987; Taylor and Wilson, 1997).

6.3.2 SSS I Velocities

The velocities found within SSS I range from c. 1750–3500 m/s. Discounting the two end members (SSS I(a) and some of SSS I(d) in the North Basin), the velocity range for the other facies is a more concise 2100 m/s (SSS I(e)) to 3000 m/s (SSS (b)).

A seismic refraction survey of the buried floor and infill of the Gilpin-Kent Valley, south Cumbria, integrated with the adjoining Morecambe Bay Barrage feasibility survey (the areas are 15–20 km South of Windermere), found deposits ranging from 1900 m/s to 2800 m/s associated with till sequences (Knight, 1977; Taylor and Wilson, 1997).

Therefore, SSS I has the seismic velocity characteristics of till. The precise velocities for the individual seismic stratigraphic facies, along with their locations and geomorphology, will be used to refine their identification and genesis.

6.3.3 SSS I(a)—Lodgement Till

The locations of SSS I(a) and its relatively high and variable velocity (3500 m/s ± 500 m/s) associate favourably with deposits of lodgement till. Lodgement of englacial material occurs at the base of the glacier as a result of regelation (Eyles and Menzies, 1983). Glacial flour (generic term for fines that the glacier produces by abrasion, which are abundant if the bedrock is a fine-grained sedimentary rock—Eyles and Menzies, 1983) and perhaps coarser unlithified sediments become stiff (well drained and under variable high effective stresses) against the basement, and develop high bulk densities (Sladen and Wrigley, 1983). Hence, the troughs containing SSS I(a) provide ideal locations for lodgement till to form, and the observed high and variable seismic velocities are, at least in part, because of the varying degrees of over-consolidation that gives lodgement till a wide range of plasticity and strength (Money, 1983). The tills of glaciated valley terrain in the Lake District tend to be clast rich also (Sladen and Wrigley, 1983), and the lowest till deposits found in the FBA cores from Windermere (Pennington's Boulder Clay) are reported as poorly sorted cobble gravels in an 80% matrix (50% clay) (Pennington, 1943; Holmes, 1964; Pennington, 1975). Hence, local changes in clast content could be the other cause

of variations in seismic velocity within the sequence.

SSS I(a) is penetrated by the shell and auger investigation in Figures 6.23a and 6.24 in locations close to MCS lines 2707-line10 and 2707-line13 respectively (Figure 6.5). Both cores finish when they encounter 0.5 m of gravel and then cobbles, which correlate with the clast content of the lodgement till found beneath Windermere (recovery of the clay matrix with the shell and auger is sometimes difficult as it can be sucked out of the tube when withdrawn— Somerville, 1983).

SSS I(a) is not found in the troughs above the basement on the southern MCS lines 2607-line15a and 2607-line11 in the South Basin (Figures 6.7 and 6.6 respectively). This could be because it has been scoured out by the several re-advances in this location, apparent from the major nested push moraine structures (SSS I(c)).

However, the basal reflection of the trough on MCS 2607-line11 required a very precise velocity of 2700 m/s $\pm$ 100 m/s to focus coherently, which is too slow for SSS I(a) to be present; the geometry of the basal reflection also gives the impression of repeated downward carving into the basement with stepped incisions, which SSS I(f) has filled to produce a smoother U-shaped valley before sedimentation dominated. Hence, I believe the basement beneath SSS I(f) in the South Basin is formed by bedrock and contains very little SSS I(a). Note, this carving into the basement is not associated with one of the inferred faults in the South Basin (BGS, 1996), and therefore is not occupying a line of weakness.

6.3.4 SSS I(b)—Medial Moraine

SSS I(b) only exists on MCS line 2607-line15c centred on CDP 4450, and has lodgement till deposits adjacent to the South, with perhaps more of this deposit forming a mound in a trough at CDP 4590 further north (Figure 6.9). MCS line 2607-line15c is complex: there is no evidence of large push moraine structures (SSS I(c)) like those on MCS lines 2607-line15a and 2607-line15b further south, but there is a large still-stand moraine (SSS I(e)) at the south end. Hence, re-advances do not appear to have occurred here, which has preserved lodgement till in the troughs and this remnant SSS I(b) deposit.

In this location (see Figure 6.17) there would be confluence of lateral moraines

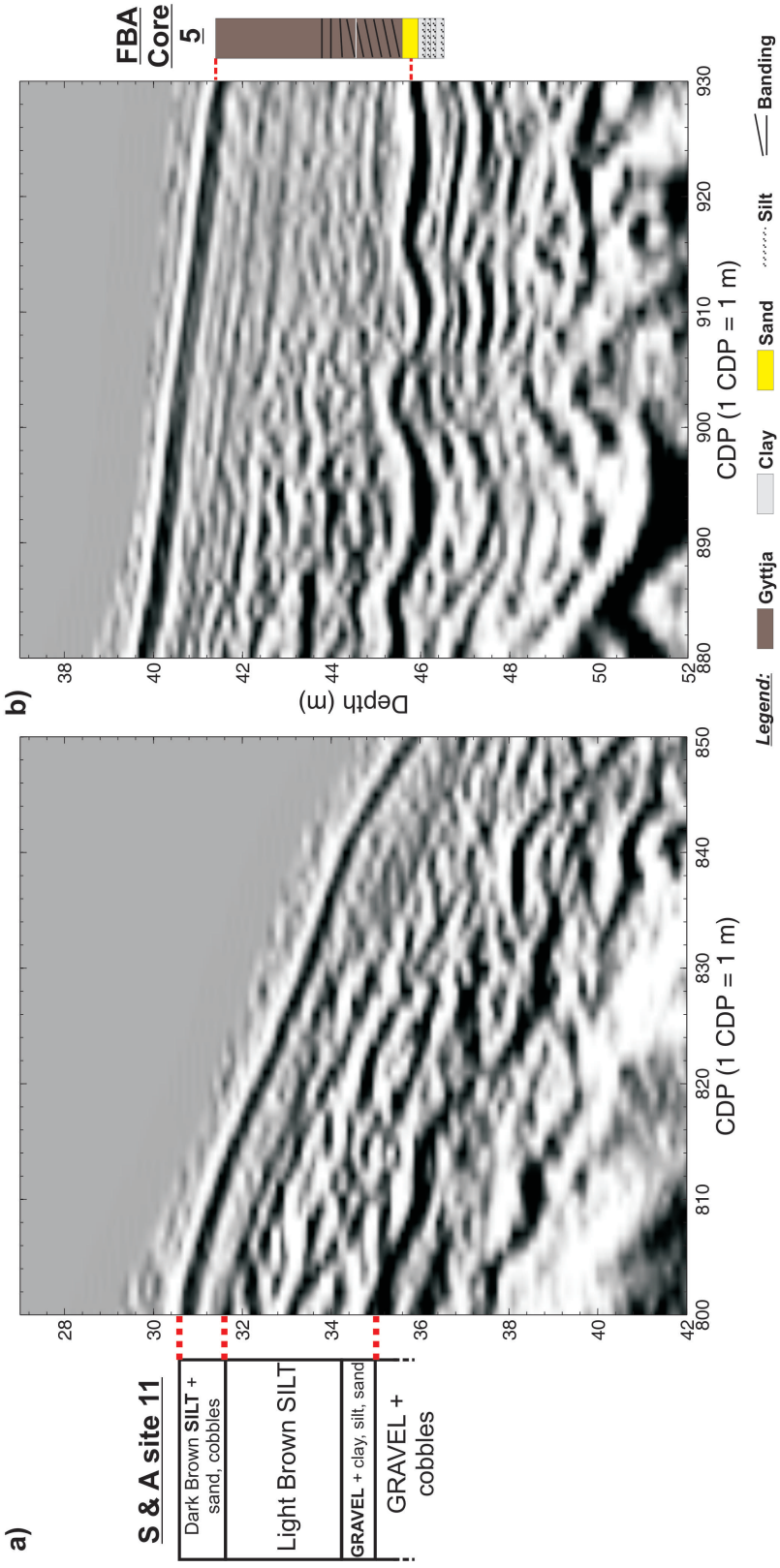

Figure 6.23: Enlarged images from MCS line 2707-line10. The FBA core and shell and auger results are vertically in scale with the image, but are not directly on the survey line. The red dots approximate the positions of the cores.

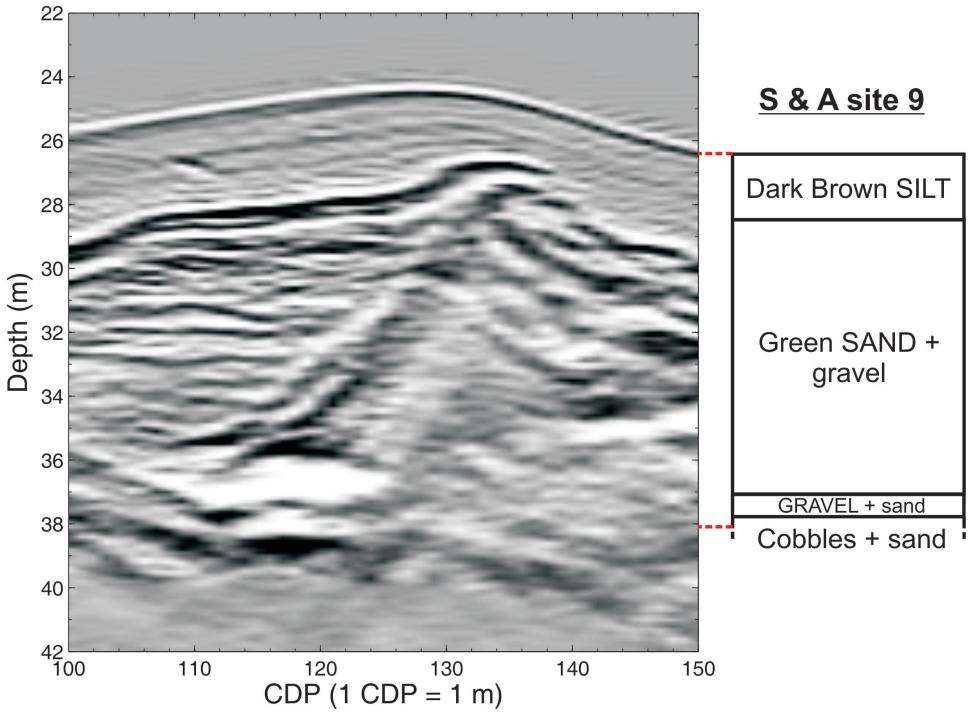

Figure 6.24: Enlarged image of the De Geer deposit from MCS line 2707-line13. The shell and auger result is vertically in scale with the image, but not directly on the survey line. The red dots approximate the position of the core.

between the North Basin and Esthwaite Water glaciers heading southwards. Hence, this is ideally situated to be a remnant of a medial moraine that formed from the two lateral moraines. Medial moraines comprise coarse grained supraglacial diamict mixed with englacial material and are frequently encountered along the valley floor at the contact of converging ice flows, within a composite valley glacier; the entire basal debris zone can be folded upwards by the intense transverse compressive strains (Eyles, 1983b). If this description is applied to SSS I(b), it explains the close association with lodgement till, the shape of the deposit, the dipping internal reflection that appears to divide the deposit in two, and the relatively high seismic velocity through over-consolidation. Therefore, the evidence suggests that SSS I(b) is a remnant of a medial moraine.

6.3.5 SSS I(c)—Large Push Moraine

SSS I(c) forms large asymmetrical push moraines with steeper distal slopes along Windermere. Tills, valley side debris, glacio-fluvial sediments, and glacio-lacustrine

sediments are easily bulldozed by the ice front during surge readvances into large, asymmetric, ice-cored, push moraine ridges, which often overlie bedrock slopes opposed to glacial flow (Eyles, 1983b).

Only the basement reflection beneath the 40 m high large push moraine at the south end of the North Basin on MCS line 2707-line4pm could be imaged (Figure 6.25), probably because this is almost certainly produced by a bedrock/till interface. Imaging this was difficult owing to the lack of penetration through the surface of the SSS I(c) deposit and the scattering of seismic energy within. This must have been produced by a significant re-advance of the valley glacier in the North Basin, and the material composing the structure would have undergone significant compression as it was pushed up-slope towards Belle Isle. The relatively high velocity of 2500 m/s ± 300 m/s for the structure testifies to this over-consolidation.

The steep valley sides in the South Basin (with a gradient of c. 15°—Figure 6.21) evidently contribute large amounts of valley side debris (e.g. SSS I(f)). When previous deposits were bulldozed in front of re-advancing ice, they would have made a significant contribution to the great thickness of the major nested push moraine structures on MCS lines 2607-line15a and 2607-line15b (c. CDP 750 on Figure 6.7a and c. 2500 on Figure 6.8a). They are clearly visible in Figure 6.17 as ridges containing sb_2. There is a large asymmetrical push moraine riding/forming the back of the major nested push moraine structure c. CDP 2780 on MCS line 2607-line15b (Figure 6.8). There is no indication of a basal reflection beneath this, supporting the conclusion that these are thick nested deposits (i.e., a coalition of multiple large push moraines pushed into each other) with no strong, consistent, impedance contrasts between.

6.3.6 SSS I(d)—De Geer Moraines

SSS I(d) structures differ to large push moraines (SSS I(c)) in the respect that they are only up to 10 m high and 100 m across, symmetrical, generally with lower velocities, much more frequent, and often with a locally regular spacing. These characteristics are more akin to De Geer moraines that form subaqueously at or near ice-margins, align transversely to ice flow, and are typically less than 10 m

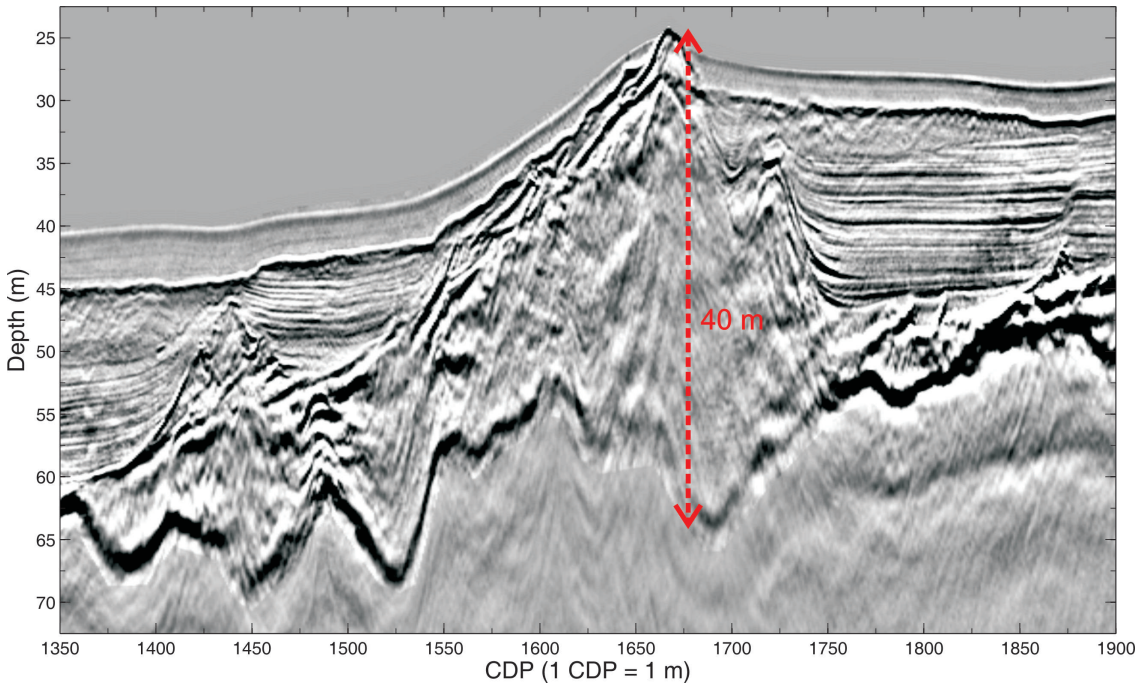

Figure 6.25: SSS I(c) from North Basin on MCS line 2707-line4pm.

high, and tens of metres in width (Golledge and Phillips, 2008).

Water-terminating ice-margins are at least partially floating, which reduces basal drag, and promotes the formation of two types of De Geer moraines. Grounding line De Geer moraines are constructed from till and sediment deposited in front of a retreating glacier at the summer ice-margin, and form during less extensive winter re-advances (e.g. Geer, 1889; Boulton, 1986; Dix and Duck, 2000). Alternatively, crevasse fill De Geer moraines are produced where there is a surge advance in the ice-margin. Basal crevasses are formed in the sole of the glacier through flexuring and stresses parallel to the ice front. These crevasses become filled with the till and sediments that had been deposited in the path of the advancing ice-margin, and their sharp crests are preserved if the ice-margin becomes buoyant, and is elevated by the pro-glacial water (Zilliacus, 1989; Golledge and Phillips, 2008).

Both terrestrial and marine grounding line De Geer moraines have been found in the British Isles: terrestrial grounding line moraines at Glen Chaorach are typically asymmetric with steeper distal slopes, less than 10 m high, c. 20–35 m wide, and have crests c. 30–400 m apart (Golledge and Phillips, 2008); terrestrial grounding line moraines at Tarbat Ness and Elgin, Scotland, are typically symmetrical to

slightly asymmetrical with steeper distal slopes, up to 7 m high, c. 50–60 m wide, and have crests c. 150–190 m apart (Finlayson et al., 2007); marine grounding line moraines in the vicinity of Orkney and Shetland exhibit sharp-crests and are less than 10 m high (Bradwell et al., 2008); marine grounding line moraines formed in Loch Ainort, Isle of Skye, have exposed heights of 0.2 m to 12 m, widths less than 30 m, crests less than 70 m apart, and are asymmetric with steeper proximal slopes of 18° (Dix and Duck, 2000).

The evidence in Windermere also supports the formation of grounding line De Geer moraines. For example, this type of De Geer moraine can coalesce where one winter's re-advance is slightly more extensive than the previous (Boulton, 1986). Besides the SSS I(d) complexes, good evidence of this is on MCS line 2607-line17, which surveys obliquely through at least two De Geer moraines (Figure 6.10). The De Geer moraine centred upon CDP 380 is a regular 10 m high, however, the one centred upon CDP 550 is nearing 20 m high. In fact, it appears to be three De Geer moraines nested together as there are steep, faint internal reflections dividing them (highlighted on Figure 6.10). It appears the most northern crest is pushing up the other two. Additionally, minor oscillations of the Dochart Glacier ice-margin (Scotland) formed grounding line moraines by pushing glacio-lacustrine sediments to high points on the valley floor, such as bedrock knolls, which acted as "pinning points" for the ice front (Golledge and Phillips, 2008). This process looks to have taken place on MCS line 2707-line4pm, where the seven individual De Geer moraines are mostly located on basement highs, or riding the back of the large push moraine (Figure 6.11).

Therefore, I believe SSS I(d) deposits are grounding line De Geer moraines formed by less extensive winter advances during the retreat of the Windermere valley glacier. However, given that accurate genetic interpretation of De Geer moraines is highly instructive about the character of glacial retreat, Section 6.3.13 briefly explores the viability of crevasse fill De Geer moraines in the North Basin.

The De Geer moraines in the South Basin are generally wider and have a higher velocity than those in the North Basin. The steeper valley sides in the South Basin would have deposited more coarse-grained material in the path of the re-advancing

ice-margin, which probably accounts for their larger size and faster medium. The higher velocity De Geer moraine complex in the North Basin also appears to be composed of a faster medium. Shell and auger results from a location c. 50 m due East of CDP 150 on MCS line 2707-line13 (Figure 6.5), suggest that the De Geer moraines that form the complex are sand dominated deposits containing some gravel (Figure 6.24).

The slower De Geer moraines in the North Basin probably comprise a larger proportion of fines (e.g. fine-silts and clay), which accounts for their relatively slow velocity. This can be attributed to their locations. SSS I(d) in the North Basin appears to occur in the wider parts, above and below the neck, where large amounts of glacio-lacustrine sediment (SSS III) have been focused (Figures 6.18 and 6.20). Pennington (1981) believes that deposition of glacio-lacustrine sediments occurred immediately after ice had left a location in Windermere, analogous to the immediate deposition of laminated clay-silts in a Norwegian pro-glacial lake that came into existence in 1937 (Østrem, 1975). Therefore, it can be assumed that as soon as the ice retreated from these locations in the basin, focused sedimentation initiated, and glacio-fluvial and glacio-lacustrine deposits began to settle along the path of the re-advancing ice-margin.

6.3.7 SSS I(e)—Still-Stand Moraine/Flowed Till

SSS I(e) forms still-stand moraines with flowed till deposits thinning away from the structure. They are produced during pauses in the ice front at actively retreating glacial margins, meaning that ice, englacial, and supraglacial material is still being transported to the ice front. These materials are not significantly disaggregated as they slide away from the moraine or the ice sheet, and re-deposit downslope of the ice-margin. Therefore, it is not surprising that SSS I(e) has a slightly lower velocity than the De Geer moraines (SSS I(d)) in the South Basin because they both should comprise similar material, except the flowed till would not be as consolidated. Such deposits would fit the description of the better sorted finer gravels in clay (80% matrix with a 50% clay fraction) found at the base of some of the FBA cores (Holmes, 1964; Pennington, 1975).

Both the SSS I(e) deposits on MCS lines 2607-line15b and 2607-line15c in the South Basin have an average velocity of 2100 ± 200 m/s (CDPs 2300–2500 on Figure 6.8 and CDPs 3600–3780 on Figure 6.9 respectively). The still-stand moraine and flowed till deposits on MCS line 2607-line15c though, also exhibit De Geer-like structures. A stationary ice-margin would be in a state of climatic equilibrium, hence, minor seasonal oscillations probably would occur and produce De Geer structures within the flowed till, especially when the glacier is on the verge of retreating.

Similarly, this scenario might explain the De Geer moraine complex with velocities of 2200 m/s ± 300 m/s on MCS lines 2707-line4pm and 2707-line13 in the North Basin (see Section 6.4).

6.3.8 SSS I(f)—Supraglacial and Melt-Out Till

SSS I(f) lies within sb_2 between the major nested push moraines in the South Basin (Figure 6.17). It is unlike any other deposit in Windermere: it comprises many random internal reflections and has a "hummocky" upper reflector that has slopes steeper than 20°, which exhibit no regularity.

Valley glaciers deposit large amounts of clast-rich coarse-grained supraglacial till (less than 15% clay/silt faction), which is principally derived by rockfall from the valley sides; as the ice sheet thins valley side instability increases, and rock debris accumulates forming an ever-thickening mantle atop the ice sheet (Eyles, 1983a; Paul, 1983). As the ice downwastes, a hummocky morainic topography consisting of steep sided bouldery mounds, ridges, and kettle holes is produced, through the melt of ice-cores and the inversion and upstanding of ice-surface trough fillings—this is a ubiquitous terrain type in upland and highland Britain (Paul, 1983; Eyles, 1983b).

Hollingworth (1951) found evidence for ice stagnation and downwasting in this location of the South Basin (Section 5.2.2), hence, SSS I(f) appears to be the supraglacial and melt-out tills that were left behind. Hollingworth (1951) assumed from this that stagnation and downwasting was the dominant form of ice removal in the Lake District. I would like to stress at this point that the dominance of SSS I(c) and I(d) deposits along Windermere testify to active ice retreat, and that this

is only a localised occurrence.

6.3.9 SSS II Velocities

The velocities found within SSS II range from c. 1620–1900 m/s. Assuming that they are relatively unconsolidated, the regression models from Richardson and Briggs (1993) predict a saturated bulk density (henceforth, bulk density) and porosity of 2.00–2.34 g/cm^3 and 17.5–38.5%, which both correspond to coarse-sand–gravel dominated deposits (Figure 6.26). Note, although the models in Figure 6.26 have been extrapolated beyond the data they were derived from, Chapter 4 demonstrated that the predictions are still reasonable.

From the Gilpin-Kent Valley study, a c. 30 m thick deposit of gravel beneath the clays filling the valley has a velocity c. 1800 m/s, and is associated with esker sedimentation by sub-glacial melt-waters (Taylor and Wilson, 1997).

The SSS II deposits are also beneath similar sediments (SSS III), therefore, they have velocities and stratigraphic positions associated with glacial-fluvial deposits. Their location and geomorphology will be used to refine their identification and genesis.

6.3.10 SSS II(a)—Sharp-Crested Esker

The geomorphology of SSS II(a) on MCS line 2607-line15c (CDPs 4000–4150, Figure 6.15c) resembles a cross-section through a "sharp-crested" esker with a layered internal structure (Shreve, 1985). This would have been fluvially deposited close to the ice-margin when the ice was not moving very fast and was relatively thin (Easterbrook, 1999). The large still-stand moraine c. 500 m south on MCS line 2607-line15c indicates that these conditions were present; flowing melt-waters heading towards the ice-margin would have carved upwards into the glacier, and deposited sands and gravels (Shreve, 1985). This suggested composition, as predicted by the velocity models, is supported by its higher velocity than the surrounding finer-grained sediment fill (SSS III) and its lower velocity than the till composing the De Geer moraines (SSS I(d)).

As this is a cross-section, the esker would have to be following a course close to

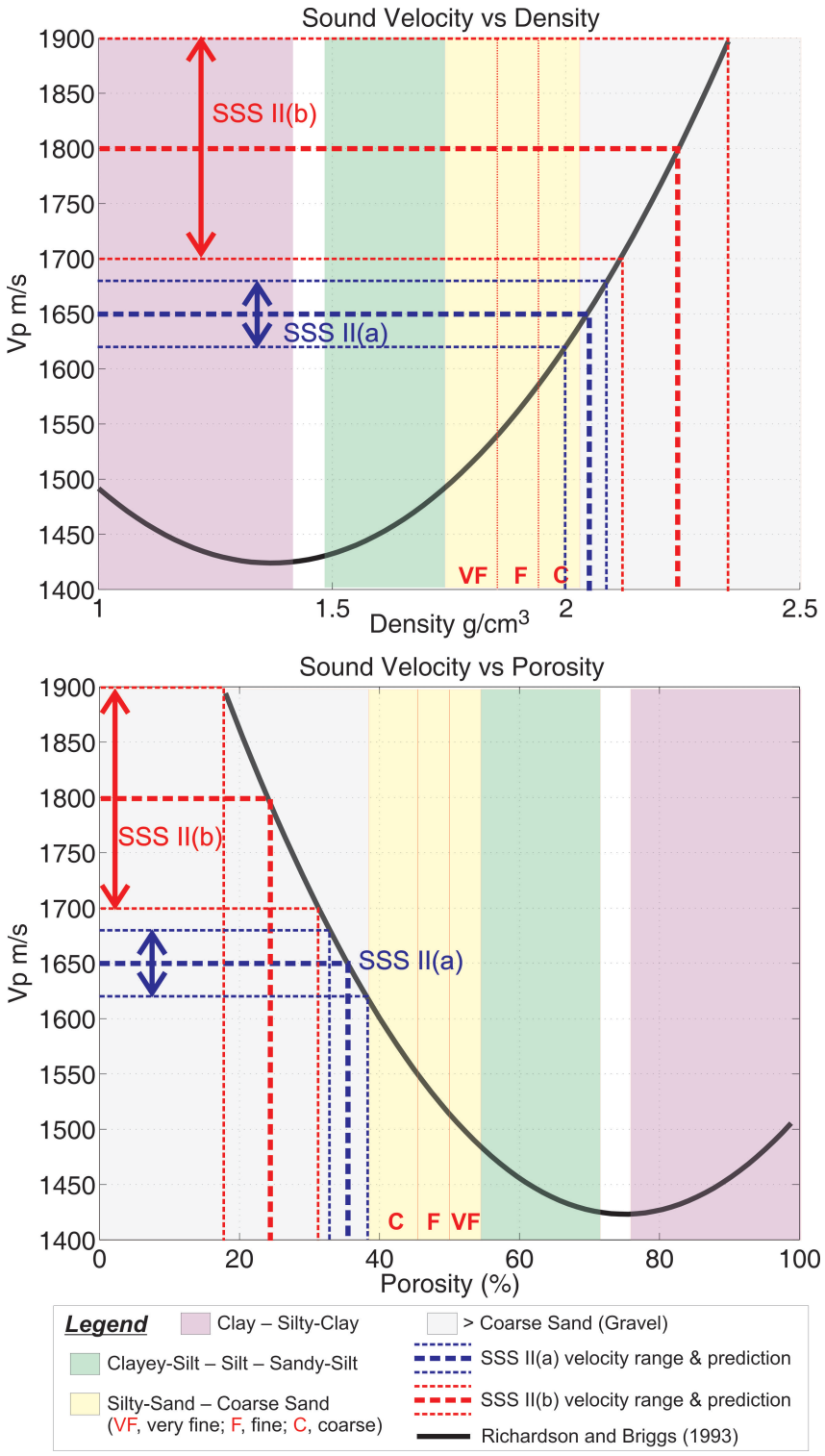

Figure 6.26: Empirical regression models relating velocity with bulk density and porosity from Richardson and Briggs (1993) using the local water velocity of 1450 m/s. Predictions of bulk densities and porosities for SSS II are marked with dashed lines (the fine dashed lines represent the velocity uncertainty). The graph is divided into sediment zones defined by the average bulk density and porosity values of sediment types from Hamilton (1980). The graphs have been extrapolated beyond the observations they were derived from (1.2–2.1 g/cm^3 and 32–90%).

the east side of the South Basin before it moves across to the west side at c. CDP 4100, in order for it to only appear once on MCS line 2607-line15c. Such a course is generally parallel to the east shore of the basin (Figure 6.17). Eskers comprising sand and gravel have formed in sub-glacial drainage channels close to ice-margins elsewhere in Cumbria (Pennington, 1975).

6.3.11 SSS II(b)—Kame Terrace

SSS II(b) is a good example of a kame terrace between CDPs 1200 and 1320 on MCS line 2607-line15a (Figure 6.7), which would have accumulated in the channel formed between the upper surface of the large push moraine to the South, and the front of a stagnating ice-margin that downwasted. This deposit appears to collapse into the large coarse-grained supraglacial and melt-out till deposit, which undoubtedly would have occurred when there was no ice left there to support it. Hence this ice-stagnation deposit is more evidence of localised ice-stagnation in this sub-basin, and supports the conclusion that SSS I(f) is hummocky supraglacial and melt-out till. This kame terrace even appears to have a small kettle hole, c. 50 m wide and 3 m deep on the surface. This would have formed after the sub-surface melt of a buried ice core.

SSS II(b) would comprise englacial debris that has been redistributed by melt-waters to form fluvial sand and gravel deposits, which could also contain some valley side debris. Some of the FBA cores encountered coarse-grain glacio-fluvial sediments and described them as better sorted, more rounded sands and gravel than those within the till deposits (Holmes, 1964). Sand and gravel kames are abundant where temporary glacial lakes existed in Cumbria (Pennington, 1975), and this kame terrace is in close proximity to the known terrestrial gravel kame terrace (with kettle holes also) on the west side of the lower reach of the South Basin (Hollingworth, 1951). Both these terraces would have formed at a similar time when ice was stagnating in this sb_2, and the size of the terrestrial kame (unfortunately no dimensions are given) suggests that the ice here downwasted rapidly (Hollingworth, 1951).

6.3.12 South Basin Ice Retreat Interpretation

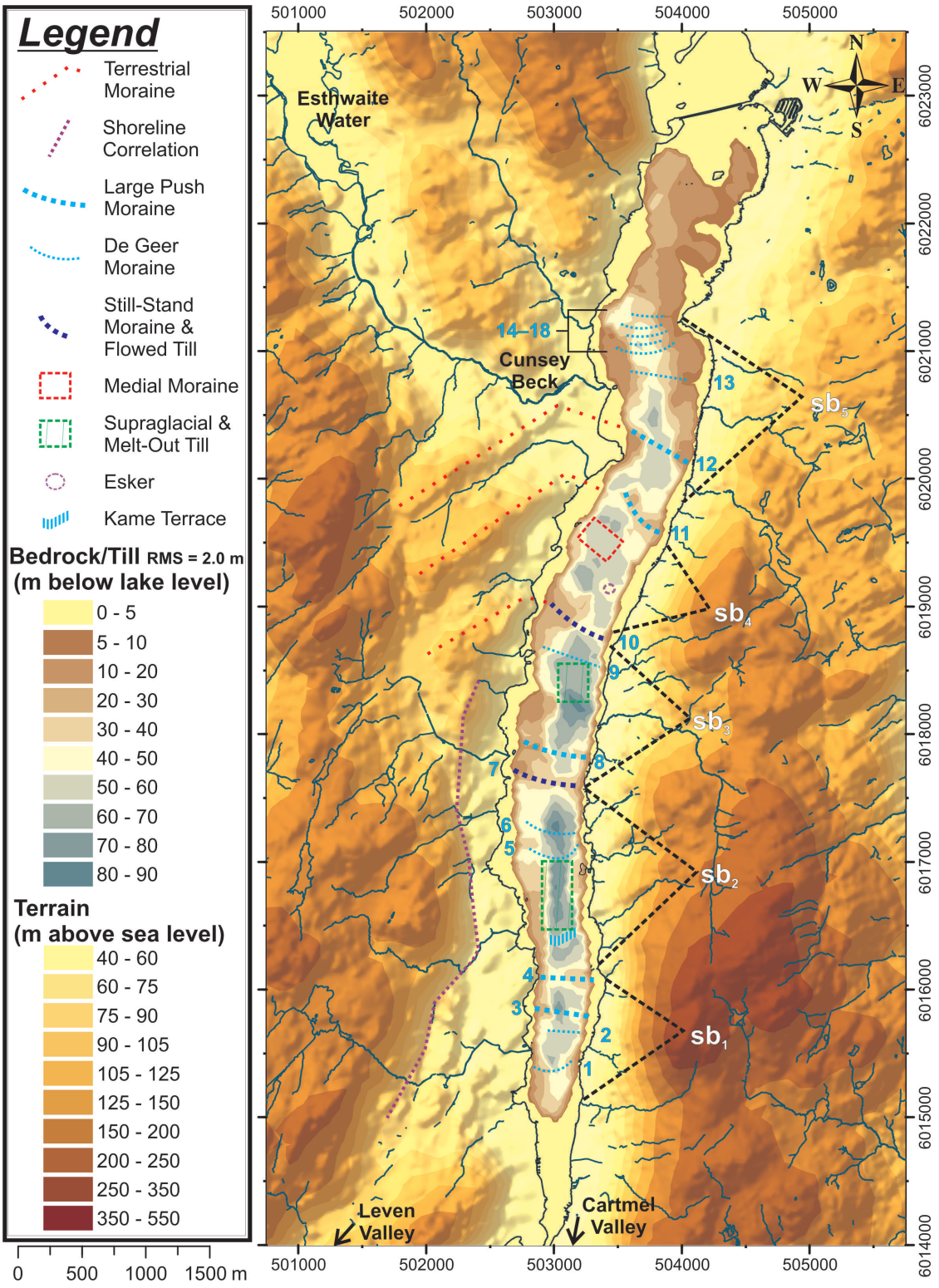

Figure 6.27: Bedrock/till surface in the South Basin with glacial deposits indicated. Lake boundary and waterways are shown. Co-ordinates are UTM zone 30.

Figure 6.27 shows the interpreted bedrock/till surface in the South Basin. The five sub-basins (sb_1–sb_5) are mostly bounded by large push or still-stand moraines. As the North Basin glacier advanced into the South Basin it was joined by the glacier advancing southwards from Esthwaite Water. The confluence of these two glaciers initiated the more significant overdeepening of the South Basin, which begins at sb_5 opposite Cunsey Beck, the inlet from Esthwaite Water. The greatest glacial overdeepening of c. 110 m beneath present lake level, which can be observed on MCS lines 2607-line11 (Figure 6.6) and 2607-line15a (Figure 6.7), occurs in sb_2 where the valley is narrowest (1280 m wide between the 90 m topographic contour either side). Generally, along the whole surface it appears that the deeper parts of the sub-basins, where the amount of glacial scour must have been greatest, occurs nearer to the side of the lake with the steeper topography (the deepest locations of sb_4 and sb_5 occur near the centre of the lake, but the topography either side is of similar height). This preference for the steeper side is more significant when the shoreline correlation (purple dots) west of sb_1–sb_3 are taken into account: they follow the base of steeper topography, which correlates with the shape of the *eastern* shoreline of the South Basin (c. 1 km away). When the valley glacier was present it would have snaked its way down the valley, between valley sides that were generally parallel to each other; the purple dots mark the western wall, which can be seen branching out towards the Leven Valley. This indicates that the ice bifurcated towards the Leven and Cartmel valleys before the end of the South Basin was reached. Therefore, the widening of the valley in this location, and separation of the valley glacier, is the reason why glacial overdeepening of the South Basin reduces south of sb_2.

During the retreat of the BIIS, when the ice-margin had retreated back to the south end of South Basin, the valley glacier did not immediately stagnate and downwaste as suggested by Hollingworth (1951). Two De Geer moraines (1 and 2) spaced 300 m apart indicate that the ice-margin began to retreat during the summers, and advance less extensively during the winters. More De Geer moraines are likely to have been deposited north of these before a surge advance bulldozed them, along with any sediments and valley side debris that had accumulated on

the basin floor, into the first large push moraine (3), that forms the front of the first major nested push moraine structure. Several surge re-advances terminated behind (3), building up the major nested push moraine structure; the last large push moraine (4) is the most clearly identifiable deposit atop the nested structure in the seismic data, and is very prominent across the map.

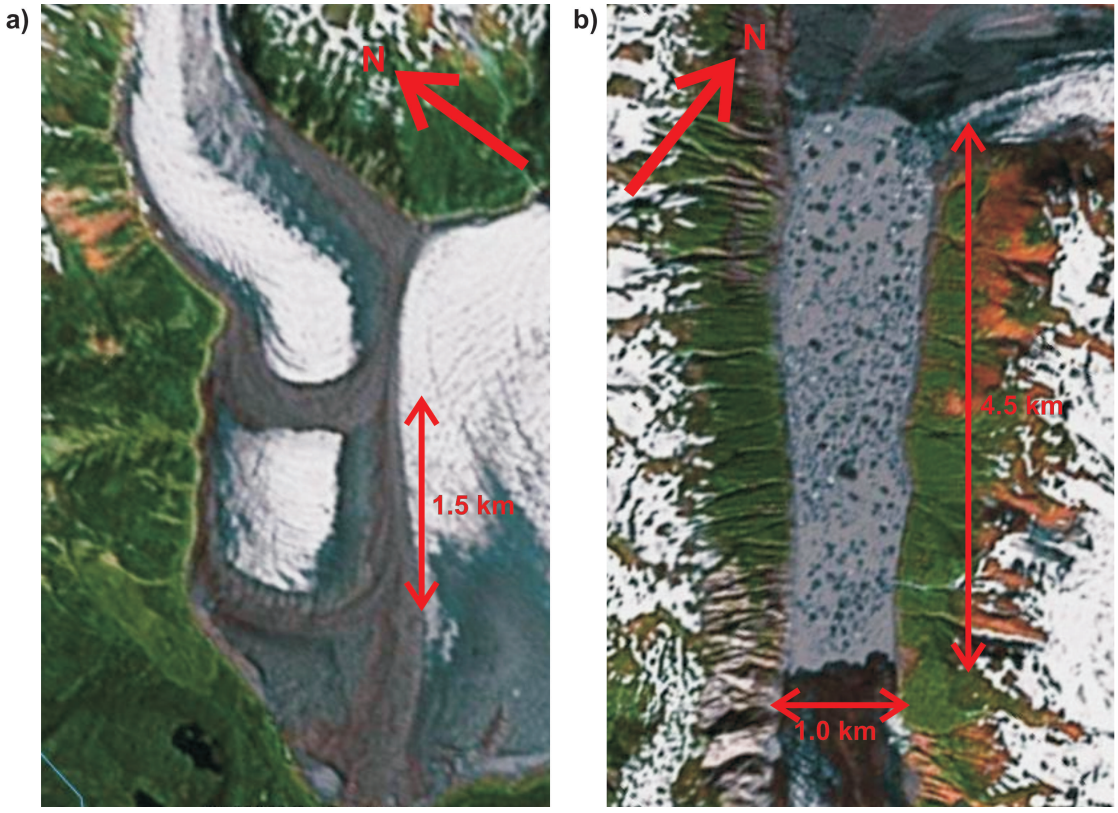

Figure 6.28: Images from Glacier Bay National Park and Preserve in Juneau, Alaska (Google Earth, 2009): a) stagnant ice-margin (365000 m E, 6491400 m N); b) stagnant ice buried beneath valley side debris (350000 m E, 6514300 m N). Coordinates are UTM zone 8.

After the last surge advance, the ice-margin was out of climatic equilibrium. Melt-down proceeded faster than melt-back from the ice-margin to a location at the north end of the supraglacial and melt-out till deposit, thinning the ice beyond the critical thickness necessary for flow, and causing the active ice to detach, leaving stagnant ice behind (e.g. Flint, 1971; Small, 1995). This was covered in valley side debris, and downwasted to become a hummocky supraglacial and melt-out till deposit. A kame terrace was deposited at the front, in the channel between the large push moraine and the thinning ice, from coarse-grain fluvial sediment deposited by

the melt-waters. Ice and melt waters also flowed away from the stagnating ice towards the Leven Valley forming terrestrial kame terraces (Hollingworth, 1951). Figure 6.28a shows an example of a stagnating ice-margin that broke off from a valley glacier after a surge advance, and is now sandwiched between two large push moraines—this is similar to the scenario proposed here. Figure 6.28b shows ice stagnating beneath steep valley sides, mantled with valley side debris; because it is not moving it does not ingest or transport away valley side debris, and will eventually form a hummocky supraglacial and melt-out till deposit, the same as that identified in sb_2 from the seismic data. This supraglacial and melt-out till deposit in Windermere spans 225 m in the valley-normal direction, and 550 m in the valley-parallel direction. This is of equivalent size to stagnant ice deposits produced by the Pleistocene valley glaciers in the San Juan Mountains, Colorado (Small, 1995).

The ice-margin continued again to retreat in the summers and advance less extensively during the winters, as indicated by two De Geer moraines 210 m apart (5 and 6), north of the stagnant ice deposits. Evidence of any further De Geer moraine deposits were erased by another series of surge advances that built up the second major nested push moraine structure, which has a large still-stand moraine formed off the front. The locations of the still-stand moraine and the last large push moraine are shown on the map (7 and 8 respectively). The retreat after the final surge was more complete on this occasion, although a thinner deposit of supraglacial/melt-out till is found between the foot of the major nested push moraine structure, and the front of the next De Geer moraine (9). It is probably thinner here because the valley sides are not as steep as those further south, hence, less valley side debris accumulated.

The valley widens now: south of the still-stand moraine atop the second major nested push moraine structure (7), there is c. 1450 m between the 90 m topographic contour either side of the basin; in the location of the next De Geer moraine further north (9) there is c. 2100 m between the 90 m topographic contour. At this point the retreating valley glacier would begin to divide, with the western part retreating towards Esthwaite Water, and the eastern part retreating towards the North Basin (e.g. Figure 6.29a). This wide area that generally extends 2250 m from De Geer

moraine (9) up to the next De Geer moraine (13), represents a relatively large snow accumulation area, which would have been part of the driving force behind the winter and surge advances that produced the De Geer moraines and large push moraines, along the narrower part of the valley further south. As a consequence, no individual De Geer moraines are produced through winter advances here, probably because too much accumulation area was being lost with the constant retreat of a more exposed ice-margin.

There are three De Geer structures though, formed within the crest of a large still-stand moraine (10) within this area (CDP 3700 on MCS line 2607-line15c (Figure 6.9)). However, this is a large deposit, and because the De Geer structures were probably produced through minor oscillations of the ice-margin when it was on the verge of retreat again, they are simply considered an inherent part of the still-stand moraine.

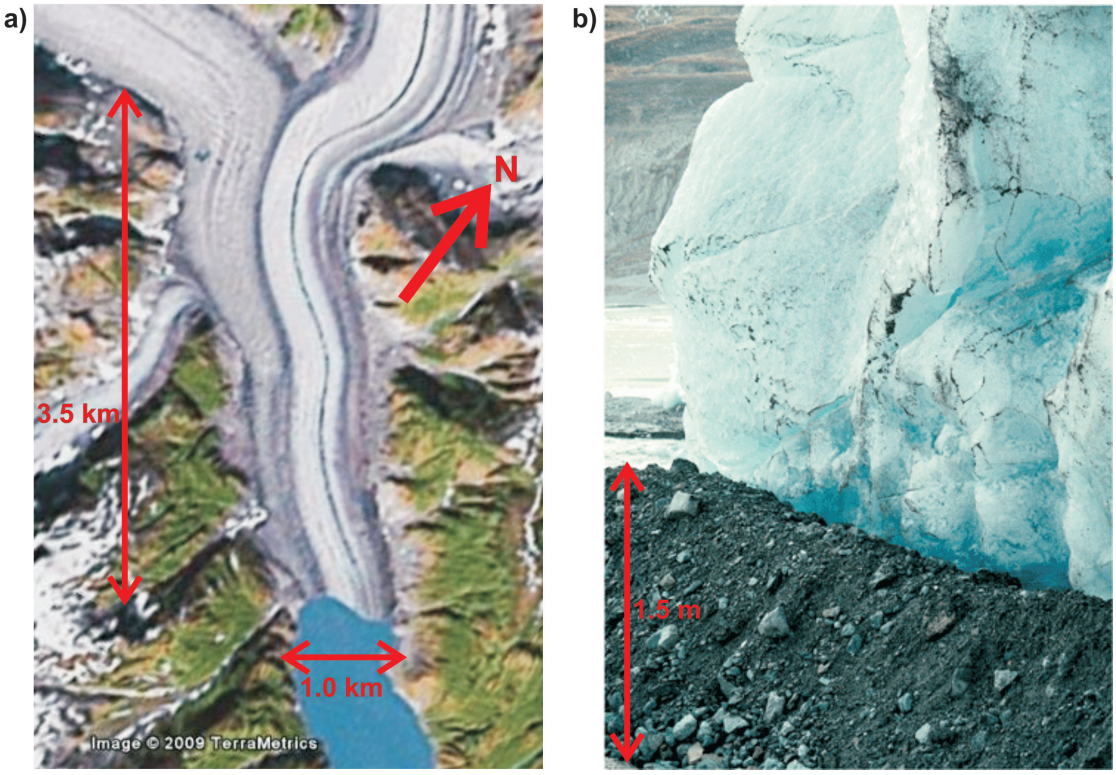

Figure 6.29: a) Image of two coalesced valley glaciers from Tongass National Forest, Juneau, Alaska (671500 m E, 6300700 m N: UTM zone 8); b) 1.5 m high push moraine forming at the base of an advancing ice-margin in Harriman Fiord, Chugach National Forest, Prince William Sound, Alaska (USGS, 2009).

After this pause the ice continued to retreat without winter advances, uncovering the esker and medial moraine deposits, before two surge advances (which were followed immediately by retreat) produced the last two large push moraines in the South Basin (11 and 12). There is a convincing correlation between the three large moraine structures (10, 11 and 12) that formed parallel to the ice-margin retreating up the South Basin, to three terrestrial topographic ridges (marked with red dots), which are orientated correctly to have been formed parallel to an ice-margin retreating towards Esthwaite Water. It is reasonable to assume that the climatic conditions required to produce a surge advance, or a still-stand moraine, would have affected both valley glaciers and their ice-margins at the same time. Therefore, it would be unsurprising if these large moraines *were* produced along the entire ice-margin, and that some residual till from these still exist in the terrestrial topography. However, if this is the case, it is surprising that these remnant terrestrial moraine ridges have not been discussed in the literature, hence, I am slightly hesitant in providing this explanation for their genesis, but their regular spacing, orientation, location, and correlation with the large moraines in the South Basin all support this hypothesis. Figure 6.29a shows two coalesced valley glaciers of a similar scale to those that would have been present along the South Basin; note the differences in composition and the irregular ice-margin at the front. This demonstrates how two joined ice-margins can still retain their own identity, and advance and retreat at slightly different rates and angles to each other, and ultimately form connected moraines that indicate different directions of stress during their formation.

After the surge advance that produced the last large push moraine (12) the two valley glaciers were separated by a topographic high, and became confined to retreating up narrower valleys once again. A De Geer moraine (13) was produced at the entrance to the Windermere valley; this represents a change back to the retreating regime with less extensive winter re-advances, probably encouraged by the sheltering of the ice-margin again, and the large snow accumulation area behind (the North Basin). Five more De Geer moraines (14–18) closely spaced over 300 m, begin 200 m further north, and mark the termination of the overdeepened sub-basins in the South Basin. All the De Geer moraines in the South Basin are believed

to be of the grounding line genre, and formed at the base of an advancing ice-margin (e.g. Figure 6.29b). The De Geer moraines in sb_1 and sb_2 have an average spacing of 250 m, and the De Geer moraines in sb_5 have an average spacing of 90 m. The large push and still-stand moraines (not including those nested together) are on average 1.1 km apart along the South Basin.

The literature suggests several causes of stagnant ice-margins (Small, 1995): surging, thick supraglacial debris, valley hypsometry, and rapid climate change—all factors which could be argued for the stagnation of ice along the South Basin. Certainly, the retreat of the ice-margin would have been encouraged by the rapid climate amelioration; there would have been a rapid rise in the equilibrium line altitude (ELA) of the valley glaciers (Clark, 1976; Shreve, 1988), forcing the rapid loss of accumulation areas, and increasing the likelihood of ice stagnation by stranding unnourished ice downstream (Small, 1995). The likelihood of ice stagnation would be increased in valleys with gentle axial slopes such as Windermere (if indeed any axial slope at all that can be determined from the bedrock/till surface), which have hypsometries susceptible to large amounts of accumulation area loss relative to ELA rise. These two factors have been shown to force the development of stagnant ice-margins by their selves, during the retreat of the Pleistocene valley glaciers that existed the San Juan Mountains, Colorado (Small, 1995). However, I believe surging in the South Basin of Windermere is the primary factor. Surging has been shown to periodically push valley glacier ice-margins beyond their normal climatically determined limits, forcing them to over-extend, thin beyond the critical thickness, and stagnate when they can no longer be supplied by active ice (e.g. Klutlan Glacier, Canada: Wright, 1980).

6.3.13 North Basin Ice Retreat Interpretation

The dominant character of glacial retreat changes from the South to North Basin. In the South Basin, several surge advances and rapid retreats, with the occasional still-stand, produces large push and still-stand moraines up the valley, with few De Geer moraines. In the North Basin however, glacial retreat was dominated by steady summer retreats and less extensive winter re-advances, which has produced

large groups of De Geer moraines forming a "washboard" like surface beneath SSS III.

Figure 6.30 shows the depths to the bedrock/till surface in the North Basin. Valley glaciers advanced into the North Basin from Great Langdale, the Rothay Valley and Stock Ghyll. As a result the greatest amount of overdeepening in the North Basin occurs in sb_8 (85 m ± 4 m below lake level to the bedrock/till surface) opposite High Wray Bay, which is at the centre of two topographic highs to the north-northeast and the south-southwest that channelled these valley glaciers together. The valley created by the topography widens slightly towards the neck of the North Basin, and the bedrock/till surface shallows, which is probably a result of reduced glacial scour. This occurs before the addition of the Troutbeck glacier, which resulted in increased overdeepening again in sb_7, next to the steep topographic high to the West. The preference for greater amounts of glacial scour adjacent to steep topography is observed again at the north end of sb_8.

As the Windermere valley glacier retreated over the bedrock plateau supporting Belle Isle and the other islands, the retreating regime that formed the De Geer moraines in the South Basin possibly continued along here, especially considering the large snow accumulation area that sb_6 and sb_7 represent to the North, which would forced winter advances. Unfortunately, the data over the plateau is sparse due to the water-way restrictions and the shallow depth, but the lakebed is certainly not a flat surface here (observed within the single channel Chirp data). The first distinct De Geer moraine (19) observed in the seismic data is located just north of the island plateau at the southern end of sb_6. The orientation suggests that at the time ice was attempting to re-advance around the west side of Belle Isle. The valley glacier continued to retreat a considerable distance up the North Basin, perhaps forming De Geer moraines as it did so, before a surge advanced bulldozed all the deposits along the basin floor into the 40 m thick (Figure 6.25), large push moraine (20) that separates sb_6 and sb_7. There are three terrestrial ridges that have the correct orientation and position to be linked with moraines in sb_7. Either of the most southern two could potentially have been produced at the same time as this large push moraine, and formed either the front or back boundaries of the small

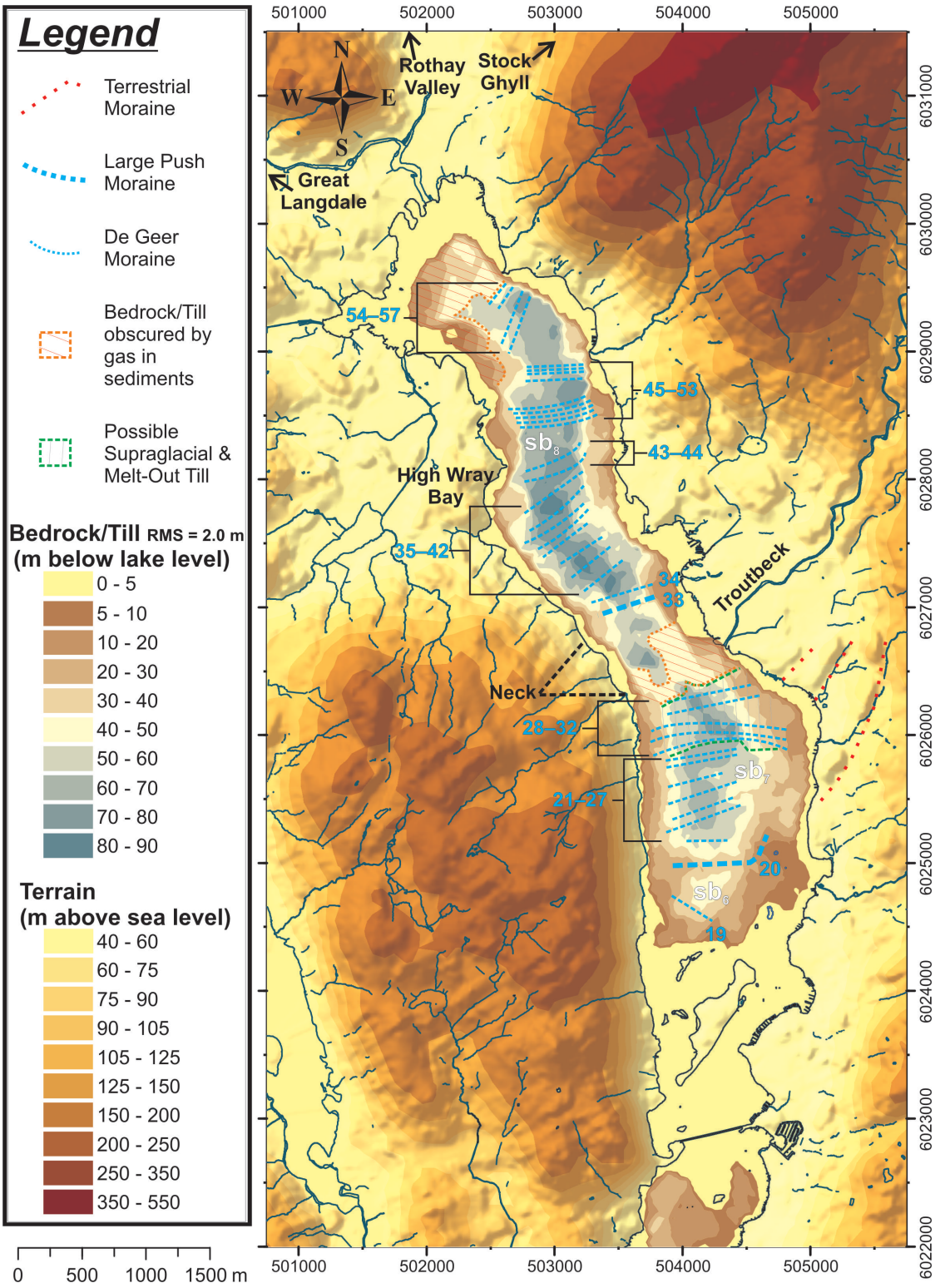

Figure 6.30: Bedrock/till surface in the North Basin with glacial deposits indicated. Lake boundary and waterways are shown. Co-ordinates are UTM zone 30.

hanging basin on the east flank of sb_7. Again, it is difficult to corroborate these correlations as terrestrial moraines in the Lake District, produced during the retreat of the BIIS, are not often mentioned in the literature.

After forming this large push moraine (20) the ice-margin must have retreated relatively rapidly as no significant amount of flowed till was deposited on the distal slope. Following a grounding line moraine ice retreat interpretation, the active ice-margin began to retreat in the summers and advance less extensively in the winters. The ice-margin pushed ground moraine and newly deposited glacio-lacustrine sediments into seven De Geer moraines (21–27), characterised by relatively lower velocities of 1750 m/s and spaced c. 100 m apart. These De Geer moraines appear to extend further south closer to the west side of the basin, where they would have been more sheltered by the adjacent steep valley side, and less influenced by the Troutbeck valley glacier. The Troutbeck valley glacier should have been retreating faster than the other confluenced glaciers, because it was sourced at a lower altitude, with less accumulation area above the ice-margin.

After these, five more De Geer moraines (28–32) form the De Geer moraine complex as described from MCS lines 2707-line4pm and 2707-line13 (Figures 6.11 and 6.13). These are characterised with higher velocities c. 2200 m/s and appear to be composed of sand dominated material. They extend completely across the basin and tend to be orientated perpendicular to the basin axis, and hence, probably perpendicular to the direction of valley glacier retreat. They are located just south of the neck of the North Basin, where there may have been a higher concentration of medial/lateral moraine deposits, which were uncovered and re-worked into these De Geer moraines. Alternatively, coarser sediments could have been derived from meltwaters issuing from the rapidly melting Troutbeck valley glacier, or from flowed till, depositing at the north end of sb_7, in front of the re-advancing ice-margin. It is difficult to reach a conclusion for the genesis of this complex: the 5-channel two-way-time brute stacks of the other MCS lines lack the penetration required, and the gas contained in the surface sediments to the north obscure the bedrock/till surface beyond the last De Geer moraine (32).

After the ice had retreated north of the neck of the North Basin, another surge

advance produced a large push moraine (33) across the top of the neck, which forms the beginning of sb_8. No more surge advances took place in the North Basin. The last was followed by immediate retreat and then a winter advance, which produced a De Geer moraine (34) on the back of the large push moraine. The valley glacier then continued to retreat quite regularly to the Northwest, producing eight more De Geer moraines (35–44) perpendicular to the basin axis, and spaced c. 110 m apart. The basin axis turned to the North and the retreat was more extensive, but then slowed up in two locations, producing closely spaced (c. 30 apart) De Geer moraines perpendicular to the basin axis (45–53). The basin axis turned towards the Northwest again, and a more regular retreat was resumed with 4 De Geer moraines (54–57) produced perpendicular to the basin axis, and spaced c. 100 m apart. Gas in the upper sediments obscures the bedrock/till surface further north.

The De Geer moraines give clues to the character of the ice retreat if they, and their genesis are correctly interpreted. Grounding line moraines have been shown to have chronological inferences during a steady ice-margin retreat (e.g. Boulton, 1986), but this is often difficult to prove as more extensive advances can erase previous annual cycles. Crevasse moraines are an indicator of periodically surging ice masses (Zilliacus, 1989). I believe the grounding line De Geer moraines are dominant within Windermere, and are certainly the only genre that exist in the narrower South Basin. However, the North Basin is more complex, and the ice-margin certainly did surge here. Hence, I use MCS line 2707-line4pm to demonstrate how a crevasse fill moraine interpretation could work just as well for the lower velocity De Geer moraines (21–27) in sb_7.

During the ice-margin surge that formed the large push moraine (20), crevasses formed on the surface and along the sole of the glacier snout through flexing upwards and faulting induced by stresses acting parallel with the ice front. Pre-existing glacial, glacio-fluvial, and glacio-lacustrine deposits were squeezed into the crevasses in the sole, forming the individual De Geer moraines (21–27) south of the location of the De Geer moraine complex (Figure 6.31a). As the ice-margin had to advance into the widest part of the North Basin, it is likely that the over-extended ice here would be thinner than that northwards, towards the neck. Thus, after the

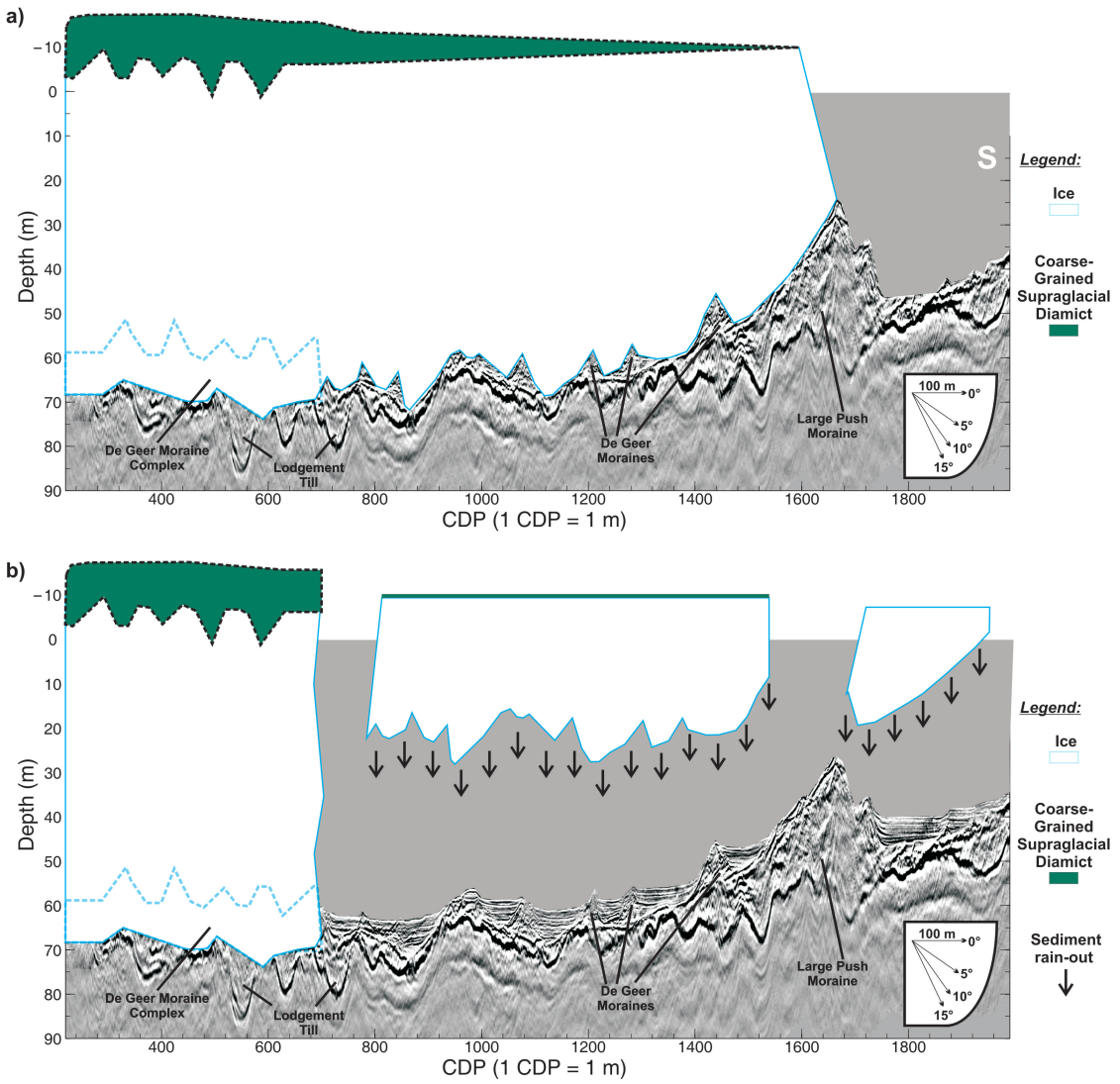

Figure 6.31: Crevasse fill moraine interpretation of the lower velocity De Geer moraines (21–27) formed on MCS line 2707-line4pm: a) Surge advance of the ice-margin forces sediment and ground moraine into crevasses along the sole; b) Buoyancy forces lift off the over-extended ice-margin, and rain-out sedimentation is focused into the gaps between the crevasse fill moraines.

surge, buoyancy forces induced by the lake water lifted the thinner ice-margin off the lakebed, rifting it from the valley glacier south of the location of the De Geer moraine complex (Figure 6.31b). As the floating ice melted, sediment rained out and was focused into the ice free depo-centres within sb_6 and sb_7. The ice-margin then might have continued to retreat producing De Geer moraines of the grounding line genre. This scenario explains the different velocities and different settings of the De Geer moraines, as a product of their different genesis. The same genesis

is also possible for all the 1750 m/s De Geer moraines north of the Neck of North Basin. This method of ice removal by buoyancy has been reported in Lake Zurich, where the velocities of "mud tills" formed beneath were found to be c. 1750–1900 m/s Heim and Finckh (1984).

6.3.14 SSS III Velocities

The velocities found within SSS III range from c. 1500–1750 m/s using an average velocity gradient of 1500 m/s and 6 s^{-1}. The velocity gradients required for SSS III implies that there is an increase in the elastic moduli of the unit with depth, either through increasing compaction, and/or through a greater proportion of coarse-grain sediments; qualitatively, the reflections are stronger and wider spaced with depth, which is most significantly observed on the North Basin lines MCS 2707-line4pm and 2707-line10 (Figure 6.16).

The infill of the Gilpin-Kent Valley is composed of silty-clay sediment, of which the fully saturated deposits have velocities ranging between c. 1500 m/s and 1900 m/s (Taylor and Wilson, 1997). Another investigation with very informative results is that of Heim and Finckh (1984), whom measured the compressional-wave velocities of glacio-lacustrine sediments within a 200 m bore hole drilled into the deepest basin of Lake Zurich in 1980. The topmost 30 m is composed of rhythmically banded fine-grained glacio-lacustrine mud formed from distal seasonal melt-waters with velocities ranging from 1530 m/s to 1650 m/s; between 30 m and 80 m is thinly bedded glacio-lacustrine muds, but with a larger component of sand and silt, and velocities steadily increase from 1660 m/s to 1800 m/s (Finckh et al., 1984). This rhythmically banded and thinly bedded two part structure, which is divided by an increase in coarse-grain content, would explain the different seismic characters of SSS III(a) and III(b) in the South Basin. The velocity gradient in the Lake Zurich sediments from 0 m to 80 m is c. 1530 m/s and 3 s^{-1}—this is close to that derived from MCS 2607-line15a in the South Basin, which has the thickest deposit of SSS III(b). The velocity gradient in the Lake Zurich sediments was produced by increasing compaction (Heim and Finckh, 1984).

Therefore, SSS III(a) has the seismic character and velocity of thinly bedded glacio-lacustrine sediment, and SSS III(b) rhythmically banded finer-grained glacio-lacustrine sediment formed from more distal melt-waters. Further interpretation will be based on their locations and actual sediment content where SSS III(a) was penetrated by the sediment investigations in the North Basin.

6.3.15 SSS III(a) and III(b)—Sediment Fill (a) and (b)

SSS III(a) shall be termed sediment fill (a) because it fills troughs within the undulating glacial retreat surface and is preferentially focused into the deeper troughs (e.g. MCS line 2707-line10 on Figure 6.16b). Figure 6.32 ties the top of the sediment fill (a) with a silty-sand layer 0.25–0.50 m thick, with clay and silty-clay varves beneath. A sand/sandy layer at the contact with the base of the gyttja is consistent with all the other FBA cores too (e.g. Figures 6.23a and 6.33). FBA cores 15 and 17 (Figure 6.32) show another sand layer beneath the first, and then encounter more clay and silty-clay varves. Hence, the Marker Beds are probably produced by these sand layers, which were deposited before the mass transport events (SSS IV) took place.

SSS III has been widely discussed in the literature and is dominated by fine minerogenic secondary clays that form water lain clay varves (e.g. Pennington, 1943, 1947; Smith, 1959; Holmes, 1964). Smith (1959) reported that underlying the clay varves in some of the FBA cores was stratified fine-sand and silt, with the sand alternating with the silts and clays during a gradual upward transition into the clay varves. This transition correlates with the seismic data, and is almost certainly due to the proximity of the ice-margin retreating further away from the lake basins, reducing the amount of coarse-grain sediment brought into the lake (Pennington, 1943, 1978).

This also justifies why SSS III is thickest in the sub-basins at the southern end of the South Basin: it was the first part of the lake to become ice-free and receive glacio-lacustrine sedimentation. SSS III(a) represents deposition when the ice-margin was in, or proximal to (without sediment traps between—i.e., another lake) the basins. Sediments carried into the lake by melt-water streams spread out as suspended, or bottom sweeping clouds (turbidity currents), into the relatively still water. These clouds are channelled by the contours of the lake floor, and denser clouds carrying coarser sediment will pass under clouds carrying finer sediment and deposit first (Smith, 1959). When the ice-margin left the South Basin and was retreating from Esthwaite Water and the North Basin, the denser, coarser sediment clouds were trapped and focused into the hollows in these basins. Only

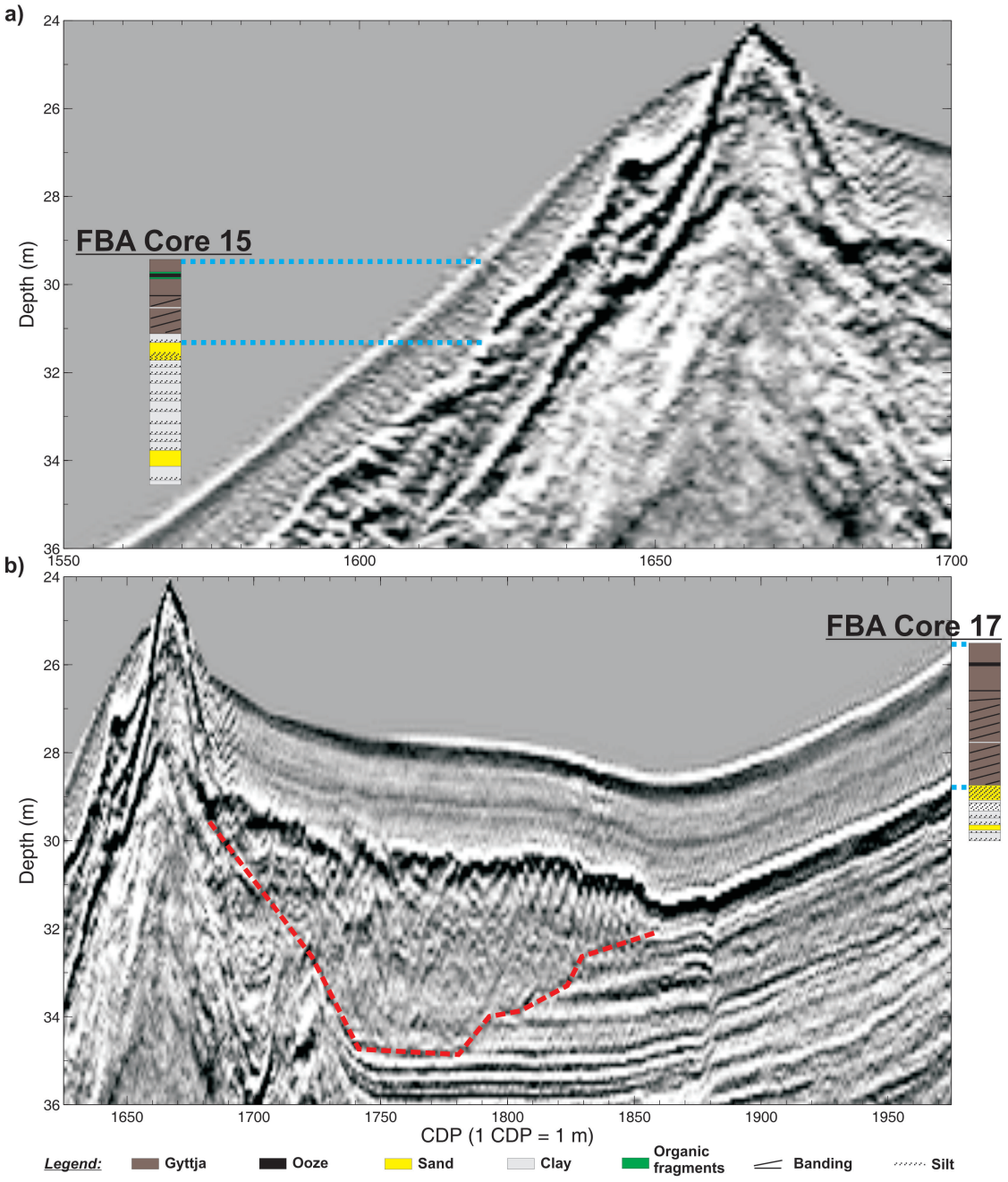

Figure 6.32: Enlarged images from MCS line 2707-line4pm. The cores are on line and vertically in scale with the image: a) FBA core 15; b) FBA core 17. The red dashed line marks the lower boundary of a disturbed sediment unit (SSS IV) beneath SSS V.

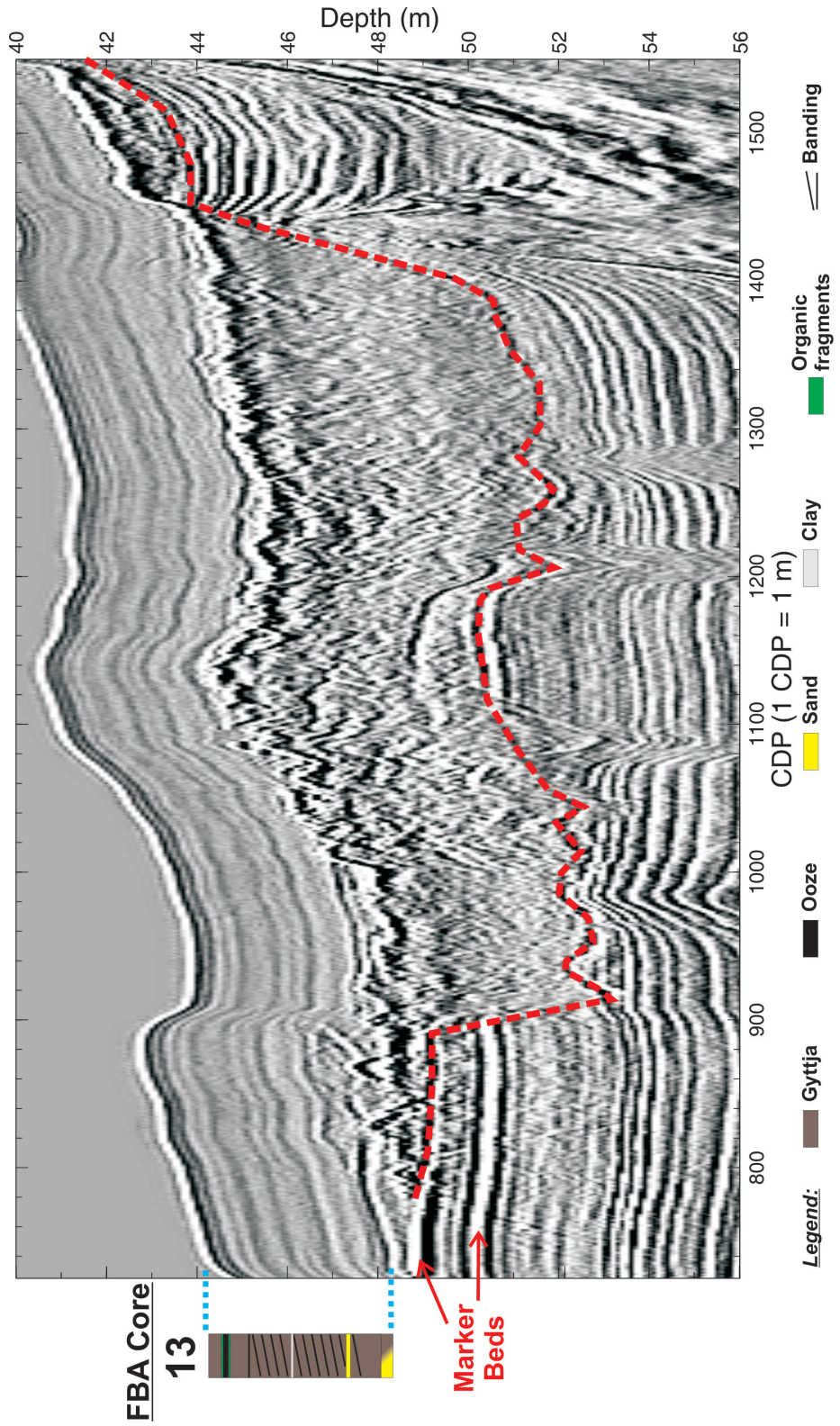

Figure 6.33: Enlarged image of the main depo-centre in MCS line 2707-line4pm. The FBA core is on the survey line and vertically in scale with the image. The red dashed line marks the lower boundary of a disturbed sediment unit (SSS IV) beneath SSS V.

the less dense, finer sediment clouds were transported into the South Basin. This produced sediment fill (b) above sediment fill (a) in the South Basin and because it is composed of more homogeneous finer sediments, it has a slightly slower average velocity and weaker impedance contrasts.

The layered impedance contrasts within SSS III are probably mostly produced by the varves: the winter deposit of fine clay that settles out of suspension under a frozen lake surface, is abruptly succeeded by the deposition of coarser fine-sands and silts (with some clay) washed into the lake by spring-summer melt-waters; the fine-sands, silts and clay then grade upwards into the fine winter clay as settling conditions improve and melt-water input reduces (Pennington, 1947; Smith, 1959). Hence, the most significant impedance contrast would exist at the winter-spring transition. However, there is an issue with resolution and in order to continue we need to divide SSS III up into its constituent units as identified by Pennington (1981) and shown in Figure 6.34: lower laminated clay; organic detritus silt; and upper laminated clay.

Varves within the lower laminated clay are reported to comprise fine-sand/silt layers up to 7.5 cm thick and clay layers up to 2.5 cm thick (Smith, 1959). Hence, the spacing between the winter-spring interface is c. 10 cm, which is the absolute limit of the vertical resolution in the migrations. These layers were not found in the centre of the lake though, because the FBA cores are not long enough to reach far into the lower laminated clay there. These layers were found at 30 m depth, on both sides of the lake, in the location of MCS line 2707-line10 in the North Basin (Figure 6.12). This depth is just visible in the migration, and it is evident that the fine layering observed on the flanks widens at greater depths where more sediment has been focused. Therefore, it is reasonable to assume that the varves within the lower laminated clay thicken to widths greater than 10 cm in the depo-centres of the sub-basins, and that they generate most of the regular layering observed within the seismic data.

However, the interfaces that generate reflections in the top couple of metres of SSS III are less clear. The varves at the top of the lower laminated clay become less than 5 mm thick due to reduced spring/summer melt-waters and grade into

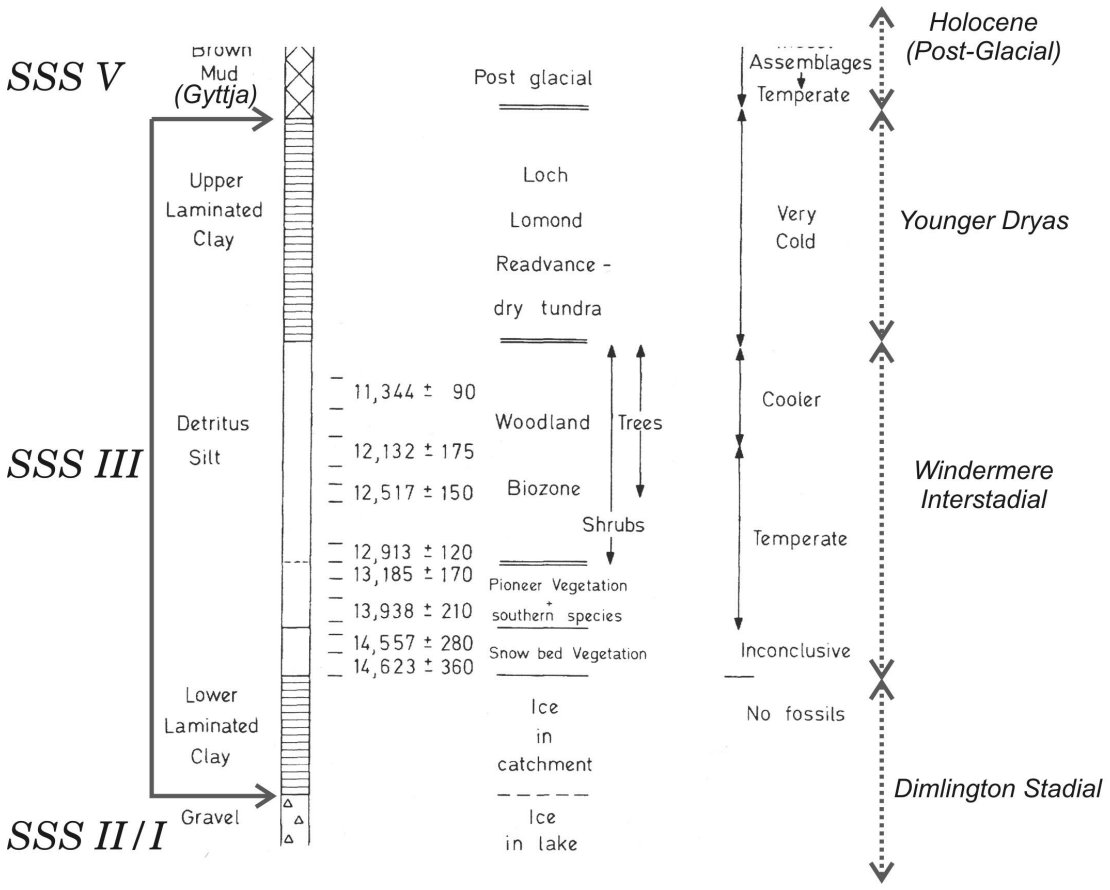

Figure 6.34: Constituent units of SSS III from Pennington (1981). Notes have been appended in italics. N.B. The lower laminated clay forms most of SSS III in deep water.

minerogenic unlaminated clay; this then grades into an organic detritus silt that is generally about 50 cm from the top of SSS III across the entire lake (Pennington, 1943; Smith, 1959).

In shallower water, the organic detritus silt reaches a significant thickness of up to 50 cm due to large accumulations of detritus being washed in at the lake margins and intense solifluction during the winter disturbing recent soils. However, this thins and disappears in waters greater than 25 m deep. In these waters there is instead a 1.5 m zone with narrow bands of unlaminated clay separated by narrow bands of silty-clay with low organic content, or sometimes a larger sandy layer (Pennington, 1947, 1953, 1962, 1991).

This unit is capped by a layer of grey unlaminated clay (2–5 cm) that grades upwards into the fine clay varves (less than 1 mm thick) of the upper laminated clay

(Pennington, 1947). The upper laminated clay is almost a uniform 50 cm thick in Windermere (Pennington, 1991) and occurs in all the lakes of the Lake District that receive drainage from high-corries, where glaciers re-established during the Younger Dryas (Pennington, 1981). The upper laminated clay forms the top of SSS III.

Therefore, varves within the top of the lower laminated clay and in the upper laminated clay are not responsible for the reflections within the top few metres of SSS III. The narrow bands of clay and silty-clays have more potential to generate reflections, but the most significant would be sandy layers, which are associated with flood deposits. Such deposits in this position of the stratigraphic column have already been used as the Marker Beds within the seismic data. These Marker Beds are possibly an indication of increased instability in the environment before the mass transport events (SSS IV) took place.

There can be no doubt that the lower and upper laminated clay are derived from glacio-lacustrine sedimentation: the laminated clays have a high degree of natural remanent magnetism that could only be achieved here by particles settling out of the water column unhindered (Mackereth, 1971); the absence of organic material, and the high calcium, sodium and potassium content (almost equivalent to unweathered Borrowdale Volcanics rocks) confirms deposition under pro-glacial conditions (Holmes, 1964; Mackereth, 1971).

6.3.16 SSS IV—Disturbed/Slumped Sediments

SSS IV forms localised disturbed sediments and sub-aqueous slumps between the sediment drape (SSS V) and the sediment fill (SSS III). These testify to major transport events that took place at a similar time in Windermere. It was not possible to find comparative velocities for this sequence in the literature.

Figure 6.33 demonstrates that the event which produced SSS IV occurred after the deposition of the Marker Beds in SSS III, but before the deposition of SSS V: at CDP 750 the top Marker Bed forms the boundary with SSS V; at CDPs 800–900 some disturbed sediment lies between; from CDPs 900–1400 the upper 5 m of the sediment fill (SSS III) has been replaced by a disturbed deposit (SSS IV). However, some remains of the Marker Beds can be seen between CDPs 1100 and

1200, indicating that there has been c. 4 m of additional sediment emplaced above in this location.

The southern end of MCS line 2707-line13 (Figure 6.16c) shows no disturbance between the Marker Beds and the sediment drape (SSS V), indicating that the west side of the basin (with the steeper topography) is more likely to have been the source of the process that produced the disturbed (SSS IV) deposit south of CDP 750 on MCS line 2707-line4pm. However, at the northern end of MCS 2707-line13 the Marker Beds have been removed between CDPs 140 and 450 and are replaced by an uneven erosional surface between SSS III and SSS V. This could be related to the disturbed sediment north of CDP 700 on MCS line 2707-line4pm, which exhibits tilted blocks of sediment fill (SSS III) and no Marker Beds (e.g. CDP 500, Figure 6.16a).

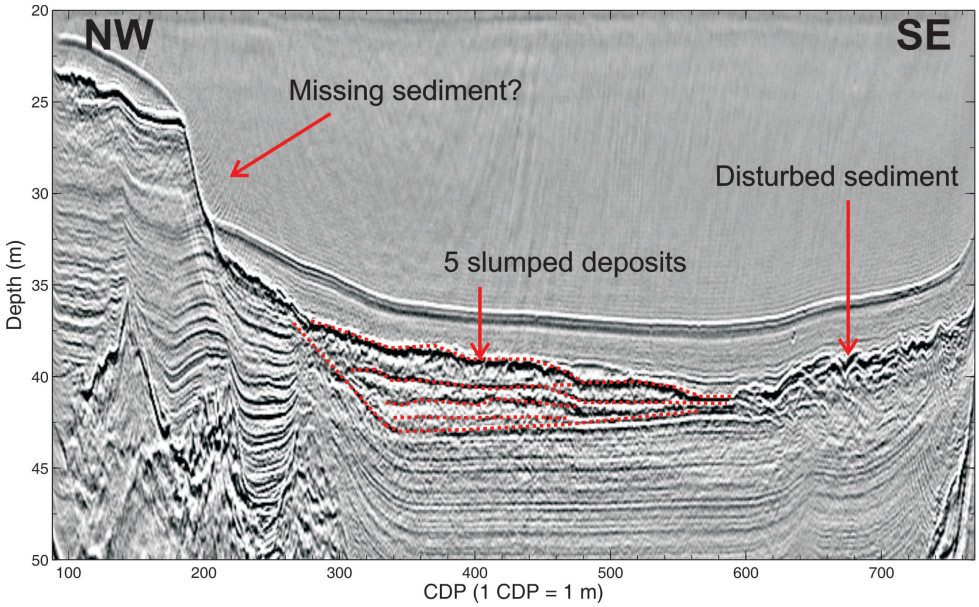

Figure 6.35: Nested slump deposits (SSS IV) outlined with red dashes from MCS line 2607-line11.

Figure 6.35 enlarges the best example of a nested slump deposits on MCS line 2607-line11. The sediment fill at a depth of 25–30 m between CDPs 100 and 200 become abruptly terminated. The slump deposits thin towards the Southeast, hence, they are probably sourced from the shallower, terminated sediment fill to the Northwest. Between CDPs 600 and 700 the sediment has a rough surface that is probably a result of the disturbance from the dissipation of energy from the adjacent slump-

ing.

Many of the FBA cores exhibit clay varves inclined at angles between 5° and 35° that flatten towards the top of the laminated clays (Pennington, 1947; Smith, 1959)—this led Pennington (1947) to correctly presume that the lower laminated clay was filling hollows in the basin floor, as observed in the seismic data. Smith (1959) presented a detailed analysis of the structures within SSS III caused by post-depositional movements down the slopes of the lake basins. The minor structures identified within angled single layers (crinkle marks, reverse and normal faults) are certainly unresolvable in the data; some of the major structures occurring on slopes, which cause a group of single layers to react as a single unit (oversteepening, overturning and collapse of original layering) may be indirectly observed in the seismic data by weakened reflections, or perhaps a transition of the reflections into transparency. In our sequencing, the above are considered part of the texture of SSS III. SSS IV has a seismic character associated with the largest of the major structures (Smith, 1959): slumped masses consisting of slump balls and contorted laminations, surrounded by a matrix of structureless clay. This description correlates well with the disturbed/slumped structure on MCS line 2707-line4pm (Figure 6.33). Slumps of up to a couple of metres thick were found in the FBA cores and were always beneath gyttja (SSS V) (Smith, 1959).

The instability that resulted in the slumping that produced the SSS IV deposits probably occurred when the lake level dropped slightly from the sudden reduction of melt-waters after the re-established ice in the corries had melted away. Slump events deposited directly above each other indicate that a single event did not cause the SSS IV deposits, but rather multiple events over a relatively short period of time.

6.3.17 SSS V Velocities

The lakebed sediments of Windermere comprise: a layer of ooze that forms the top 30 cm of SSS V in deepwater and has a bulk density of 1.05–1.17 g/cm^3 and a porosity of 90–95%; 1–5 m of gyttja that has a bulk density of 1.17–1.25 g/cm^3 and a porosity of 70–80%; then laminated clay with a bulk density of 1.7–1.9 g/cm^3 and porosity 24–35% (Pennington, 1943; Smith, 1959). Figure 6.36 shows these ranges

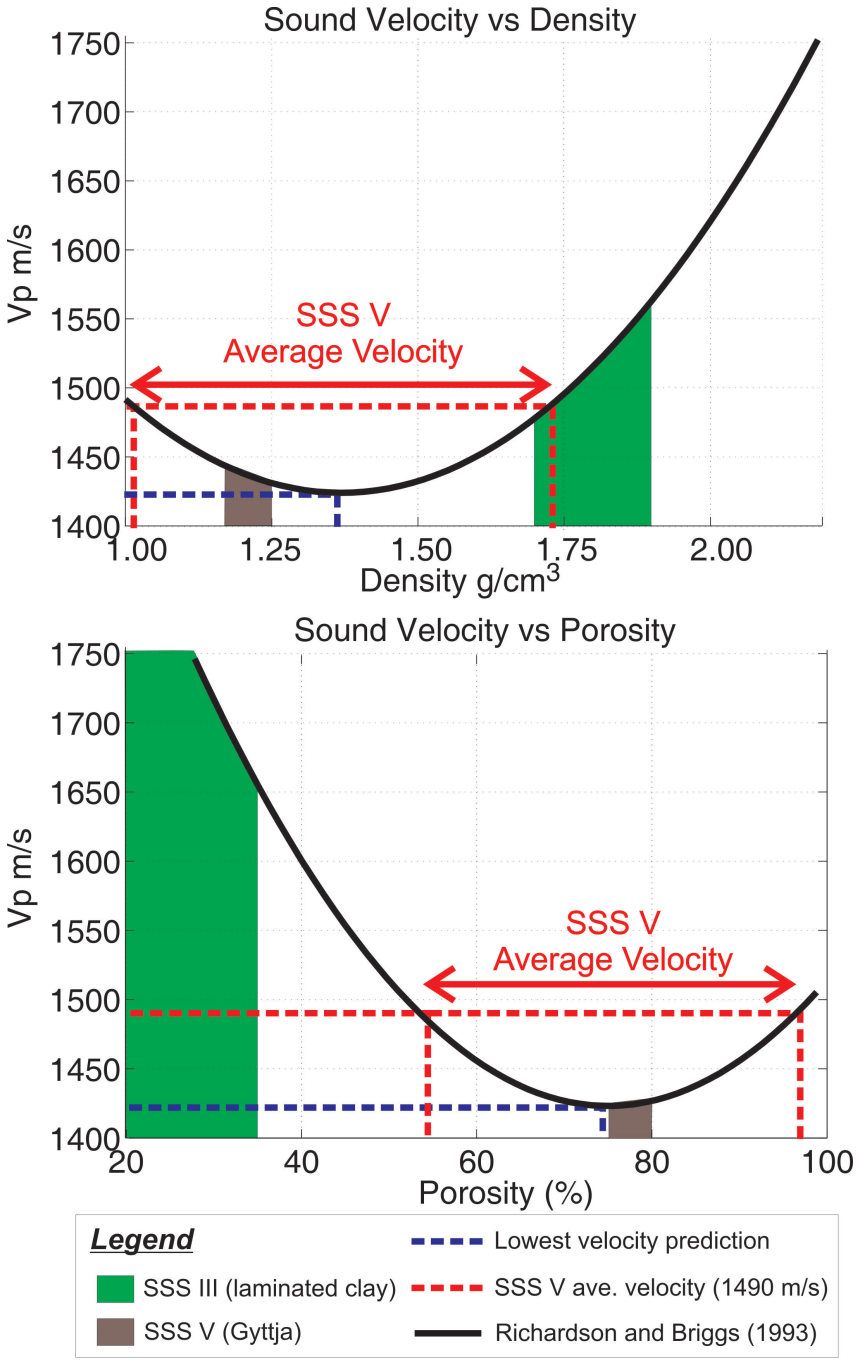

Figure 6.36: Empirical regression models relating velocity with bulk density and porosity from Richardson and Briggs (1993) using the local water velocity of 1450 m/s. The range of physical properties in the gyttja and laminated clay are shown (Pennington, 1943). The graphs have been extrapolated beyond the observations they were derived from (1.2–2.1 g/cm^3 and 32–90%).

for the gyttja and the laminated clay against the Richardson and Briggs (1993) regression models for bulk density and porosity, with the average velocity within SSS V shown. The lowest velocities predicted by the models are good predictions for the gyttja. However, it is unclear whether variations in velocity are through varying degrees of *in situ* compaction or varying amounts of ooze pooling at the surface in deep water. Nevertheless, this variability is a characteristic SSS V which incorporates both these units.

Additionally, Figure 6.36 shows that the velocity of 1500 m/s used for SSS IV and the top of SSS III would correlate well with the bulk density of the laminated clay beneath the gyttja; the porosity measurements appear doubtful though.

6.3.18 SSS V—Sediment Drape

SSS V forms the post-glacial sediment drape in Windermere and is dominantly composed of gyttja. This is entirely unconsolidated and comprises mainly silt size organic particles, with some larger organic fragments that produce a very complex internal structure. After the loss of melt-water impetus from glacier ice, sedimentation became dominated by terrestrial organic matter containing humic compounds, which flocculated the clay forming the mineral background and produces a visible change from clay texture (Holmes, 1964; Pennington, 1981). Figure 6.37 shows an example of some glacial clay that relatively quickly grades into gyttja when lacustrine sedimentation dominates (from Pikevatnet lake in Norway). This is similar to SSS V in Windermere, which is clayey at the base and more organic towards the top (Pennington, 1947). The complex, flocculated fabric is probably responsible for the low Q_{SR} within SSS V, creating an abundance of compliance heterogeneities that supports squirt flow attenuation.

Figure 6.37: Photo showing the transition of clay to gyttja in a core from a Pikevatnet lake in Norway.

SSS V contains a few thin horizons of clay and sand that are probably basin wide, representing the input from other erosional events (e.g. recent flooding of the catchment: Pennington, 1943). Smith (1959) reported SSS V as being on average 1 m thick in shallow waters and thickening to 5 m in deep water—this correlates accurately with the seismic data. However, Smith (1959) also reports that SSS V is an exceptional 8 m thick at the very northern end of the North Basin. This could not be confirmed due to the presence of gas found here. Gas originating from SSS V was also found to occur 2.5 m beneath the surface at the north end of MCS line 2707-line4pm in the North Basin, and 1.5 m beneath the surface at CDP 3100 along MCS line 2607-line15b in the South Basin (Figures 6.11 and 6.8 respectively). SSS V shows no significant change in thickness in these locations, but they are in closer proximity to some of the larger inflows into Windermere: Belle Grange Beck and Troutbeck in the North Basin; Burrow Beck in the South Basin. Pennington (1947) reports a layer of whitish clay containing abundant diatom skeletons with very little carbonaceous material forming at the mouths at inflow streams, hence, these might be associated with the more gaseous layers within SSS V.

6.3.19 Sedimentation Summary

The thickest sediment deposit in Windermere (including mass-transport deposits) is c. 53 m on MCS line 2607-line11 (Figures 6.6 and 6.19). This divides into 12 m for SSS III(b), 35 m for SSS III (a), 3 m of slump type SSS IV, and 3 m of SSS V.

The sediment volume within the North and South basins can be calculated from the isopachytes and confidently presented as minimum values, given that there would be a small shortfall in the shallow areas not covered by seismic data, which are strongly influenced by 0 m at the lake boundary. Using the divide through Belle Isle shown on Figure 6.20, the volume of sedimentation in Windermere is calculated and shown in Table 6.1.

There is at least 10^8 m^3 of sediment in Windermere. Even though the North Basin is wider and has a larger area, it contains 15% less sediment than the South Basin. However, the amount of sediment contained within the sediment drape (SSS V), which forms generally the top 3 m of lakebed across Windermere, is 14×10^6

Thickness (m)	Volume (10^6 m^3)		
	North Basin	South Basin	Total
0–Max	45.77	53.84	100.26
3–Max	31.64	42.78	74.47

Table 6.1: Volume of all sedimentation in basins (0–Max), and volume excluding SSS V (3–Max).

m^3 in the North Basin and 11 $\times$ 10^6 m^3 in the South Basin. Therefore, in post-glacial times the North Basin recieved the larger volume of sedimentation, but in late-glacial times it accumulated 25% less sediment than the South Basin. There is 10^7 m^3 more late-glacial sedimentation collected in the South Basin during the ice retreat; this is unsurpising considering the maximum thickness of sediment in the South Basin is 21 m greater than that in the North Basin.

If the ice had left both basins of Windermere at the same time, similar sedimentation, or perhaps more in the North Basin would be expected, given that today this has the more influential inlets and that it would have been closer to the retreating glaciers. Hence, this further justifies the classification of SSS III(b) as an additional facies to SSS III, and was clearly deposited while the South Basin was receiving sediment input from melting glaciers in the North Basin, and perhaps Esthwaite Water too.

6.4 Deposition Timeline

In order to temporally locate these glacial and lacustrine deposits/sediments, and obtain an idea of the time-scales involved in their formation, the time when glacial ice had been removed from the Lake District needs to be identified, and the association of SSS IV deposits directly beneath SSS V needs to be confirmed with the Younger Dryas (YD).

Sediments within FBA Cores from Low Wray Bay (North Basin, Windermere) and Blelham Bog (nature reserve c. 1 km West from the North Basin) have radiocarbon (^{14}C) dates published in Coope (1977) and Pennington (1975) respectively, for the sediments beneath SSS V. Sharing the same assumptions as the authors that the pollen/plant remains were from terrestrial organics, and omitting samples noted as having hard water errors, the ^{14}C dates have been calibrated here using *InterCal04* calibration curve (Reimer et al., 2004), with *Calib 5.0.1* (Stuiver and Reimer, 1993; Stuiver et al., 2005) ^{14}C calibration program (Table 6.2).

The earliest ^{14}C dates appear above the lower laminated clay, in the clay with slightly organic silt within SSS III. Cores from Blelham Bog and Low Wray Bay show good agreement with the earliest ^{14}C dates ranging from 16,800–18,140 cal BP (from Dock, grasses and moss stems). Therefore, we use an average of 17,600 $\pm$ 540 cal BP to mark the end of the glacio-lacustrine sediment input into Windermere that formed the lower laminated clay.

I adopt G. R. Coope's lithostratigraphy interpretation of an interstadial (as lithostratigraphy affects the acoustic architecture of our data rather than pollen), which implies that the change from laminated clay to clay with organic silt represents the termination of active glaciation in Northwest England, and the commencement of interstadial deposition. Hence, 17,600 $\pm$ 540 cal BP marks end of the Dimlington Stadial and the beginning of the Windermere Interstadial in England (Coope, 1977). N.B. Pennington (1981) reports the beginning of the Windermere Interstadial on palaeobotanical grounds where there is evidence of an environment that can support trees and shrubs. In this later publication she is quick to dismiss the presence of microfossils before 14,000 BP, since two dates from Low Wray Bay c. 14,000 BP (not included here) showed evidence of hardwater error. However, I

Sediment	^{14}C Date BP	Location	Age Cal BP	Plant Indicators
Gyttja	Post-Glacial			Juniper
	Note 3			
Upper Laminated Clay	10,490 ± 160	Blelham Bog	12,230–12,690	Rumex/Artemisia
	10,650 ± 170	Blelham Bog	12,840–12,400	Rumex/Artemisia
	11,344 ± 90	Low Wray Bay	13,140–13,290	Betula/ Juniperus
	Note 2			
upwardly decreasing organics	12000 ± 200	Blelham Bog	13640–14110	Betula
	12050 ± 180	Blelham Bog	13720–14130	Betula/Rumex
	12112 ± 125	Low Wray Bay	13820–14100	Betula
	12213 ± 150	Low Wray Bay	13840–14350	Betula/Rumex
Organic Detritus Silt	12441 ± 82	Low Wray Bay	14230–14680	Juniperus
	12460 ± 190	Blelham Bog	14200–14860	Betula
	12517 ± 150	Low Wray Bay	14310–14910	Betula
	12650 ± 170	Blelham Bog	14570–15160	Juniperus
	12500 ± 190	Blelham Bog	14240–14910	Juniperus
	12931 ± 120	Low Wray Bay	15080–15460	Juniperus
	Note 1			
Clay with upwardly increasing Organic Silt	13185 ± 170	Low Wray Bay	15320–15880	Rumex/Gramineae
	13450 ± 220	Blelham Bog	15620–16310	Rumex/Gramineae
	14330 ± 230	Blelham Bog	16800–17630	Rumex/Gramineae
	14557 ± 280	Low Wray Bay	17050–18020	moss stems
	14623 ± 360	Low Wray Bay	17060–18140	moss stems
Lower Laminated Clay	No organic remains			

Table 6.2: Calibrated ^{14}C dates from terrestrial plant remains in FBA cores from Windermere and Blelham Bog (Coope, 1977; Pennington, 1975).
Note 1: Below, Rumex (Dock), Gramineae (grass), and moss stems suggest alpine conditions becoming more temperate, between 17,600 ± 540 to 15,600 ± 280.
Note 2: Below, Juniperus (juniper), Betula (birch), imply the presence of temperate woodland. The return of Rumex indicates reduced woodland due to cooling.
Note 3: Below, Rumex and Artemisia (herbs and shrubs) in Blelham Bog, indicate the decline of woodland and cold conditions, where freeze-thaw cycles disturb open ground.

have complete confidence that the other dates from Blelham Bog and Low Wray Bay are, as the authors say, obtained from terrestrial plant remains and thus free from hardwater error. The basins are not surrounded by calcareous bedrock either (Section 6.1.3) so contamination from this form of older ^{14}C reservoir is also very unlikely.

The temporal location of the Windermere Interstadial has been located on Fig-

ure 6.38, which includes temperature curves derived from Atlantic sediments (Lea et al., 2003), central western European pollen (Davis et al., 2003), Greenland ice (Alley, 2000), and Antarctic ice (Jouzel et al., 2007). Figure 6.38 also dates the beginning of the BIIS deglaciation as 21.47 ± 1.3 cal ka BP, which is the average of all the initial BIIS deglaciation ages from cosmogenic radionuclides and calibrated ^{14}C data from Bowen et al. (2002); the dates for the duration of the YD (2,800–11,550 cal. BP ± 100) are derived from combining results from three investigations: McDougall (2001) derives a date for the YD from a collection of past investigations around the Lake District and other parts of the U.K.; Lea et al. (2003) and Alley (2000) use temperature indicators obtained from Atlantic sediment and Antarctic ice respectively.

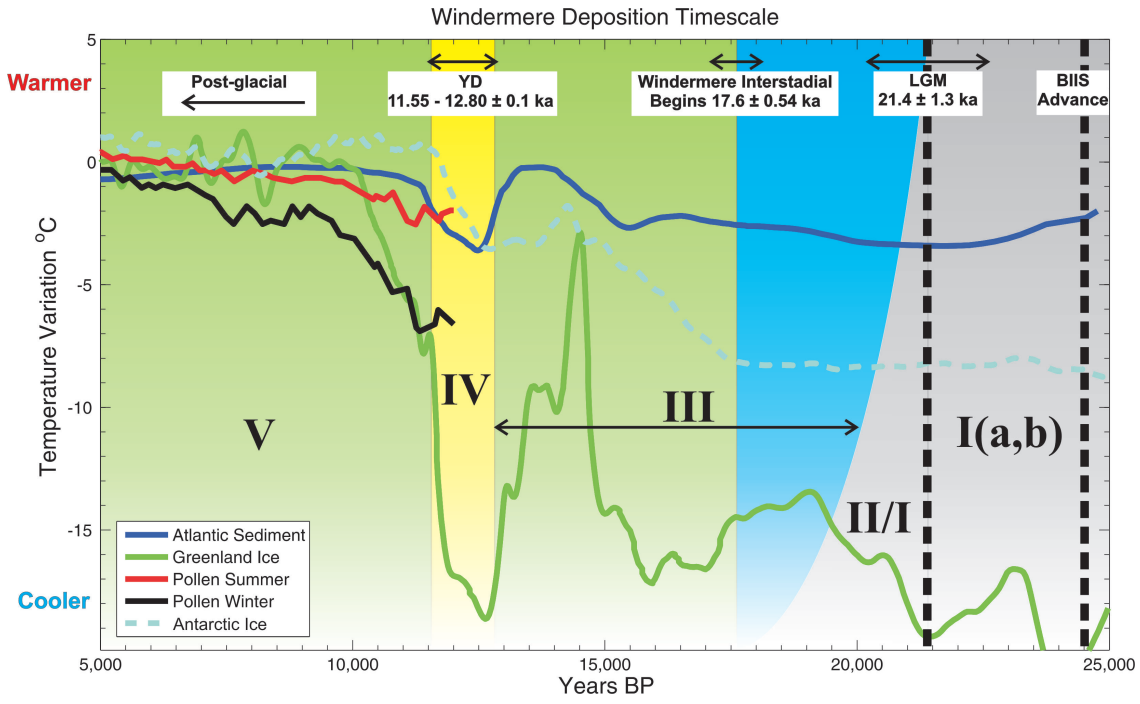

Figure 6.38: Temporal locations of SSS I–V with temperature curves (Lea et al., 2003; Alley, 2000; Davis et al., 2003; Jouzel et al., 2007). Grey represents the time glacier ice was present within Windermere; blue represents the time glacier ice was retreating from Windermere and its catchment; green represents no glacier ice present in the Lake District; yellow represents glacier ice advancing and retreating within the Windermere catchment.

The beginning of the Windermere Interstadial coincides with an increase in average Antarctic temperatures, which are often used to represent global climate

change. Sea surface temperature had on average increased a degree higher since the LGM, and reached the same temperature as before the onset of the BIIS advance, c. 24.5 ka BP, where before there had been an extensive marine transgression of British and Irish seaways (Bowen et al., 2002).

During the Windermere Interstadial temperatures warm and eventually fall away again towards the YD. The Older Dryas (OD) has little effect on the lithostratigraphy because climate change in western Britain at this time was small in amplitude: in Blelham Bog the OD is recognised as a zone of reduced annual deposition of pollen from theromphilous species (Pennington, 1975), and occurs at 13, 930 ± 210 cal BP; in Low Wray Bay, within the interstadial organic detritus silt, there is an increase in rock fragments and Rumex assemblages (Dock), dated 14,100 ± 260 cal BP. This indicates a relatively short period of increased soil erosion and reduced woodland because of the sudden cooling. These dates correlate with a sharp fall in the Greenland Ice temperature curve, but not in Atlantic SST, substantiating the small amplitude effect of the OD for more southerly, Atlantic adjacent, Western Britain.

The beginning of the YD correlates with the deposition of the upper laminated clay within SSS III, which is constrained by ^{14}C dates that range between 12,840 and 12,230 cal. BP in Blelham Bog. In Blelham Bog the upper laminated clay has c. 500 years of varves, and in Windermere there are 400-450. This implies that the upper laminated clays were produced by outwash produced from c. 500 years of active glaciation within the upper catchment (Pennington, 1947, 1991). From the core in Low Wray Bay, ^{14}C dates could not be obtained in the upper laminated clay due to organics being too sparse, however, c. 400 years before (13,210 ± 80 cal BP) there is declining organic content in the organic detritus silt, and a significant reduction in the amounts of pollen from theromphilous woodland species, indicating the onset of climatic cooling. In both locations pollen is sparse, but Artemisia (hardy herbs and shrubs) is present representing bare soil exposure through the destruction of continuous vegetation cover, and soil perturbation by frost (Pennington, 1947). This environment correlates with that required to produce the SSS IV deposits, hence they almost certainly formed during, or nearer the end of the YD.

In deep water the Windermere Interstadial and the YD deposits of SSS III form silty-clay, unlaminated clay, and fine clay varve units, which makes separation of stadial glacio-lacustrine sediment, and interstadial lacustrine sediment by seismic character impossible. Only sediment disturbances or slumps can truly be attributed as a stadial unit (SSS IV). Additionally, the lacustrine sedimentation during the Windermere Interstadial was relatively small over the c. 5000 years: Mackereth (1971) found that in the lower laminated clay (within which varves indicate a rapid rate of accumulation of 2 cm/yr), the direction of magnetic remanence varies little with depth, whereas in the partially organic interstadial deposits, there are bewildering changes in declination of the magnetic remanence between consecutive 1 cm thick sections. He concluded that the small depth of organic interstadial sediment must represent the accumulation of several thousands of years and that if this volume of material had retained the same solid-water content as the post-glacial gyttja (0.78 g/ml opposed to 0.19 g/ml respectively), the deposit would expand and be equivalent to 5000 years of post-glacial deposition. This agrees exactly with the duration of the Windermere Interstadial derived here from the earliest ^{14}C dates from the FBA cores, and the date of the onset of YD from the literature (Figure 6.38).

Tables 6.3–6.5 summarise the seismic attributes, spatial characteristics, predicted composition, and age of the seismic stratigraphy encountered in the migrated MCS lines from Windermere.

Strat. Seq. No.	Seismic Facies	Seismic Character	Composition	Dimensions	Average Velocity	Basin	Time-Line Position
V	Sediment Drape	Transparent with few weak, horizontal internal horizontal reflections	Gyttja	2–5 m thick, thinner on slopes $> 5°$	1490 m/s	N/S	Holocene (Post-Glacial)
IV	Disturbed and Slumped Deposits	Disturbed sediment has random internal reflections with rough boundary reflections; slumps are discrete units with strong bounding reflections and weak internal structure	Re-deposited sand-silt and clay varves, and interstadial organic detritus silt	Up to 7 m thick and 600 m across	1500 m/s	N/S	Younger Dryas
III(b)	Sediment Fill (b)	Weak horizontal layered reflections < 1 m apart	Silt-clay and clay varves; interstadial organic silt near surface	up to 12 m thick	1535 m/s	S	Dimlington Stadial (during ice retreat in North Basin) / Windermere Interstadial
III(a)	Sediment Fill (a)	Strong horizontal layered reflections up to 1 m apart	Sand-silt and clay varves, with coarser sand fractions deeper down and occasional sand layers; interstadial organic silt near surface in North Basin	up to 35 m thick	1565 m/s	N/S	Dimlington Stadial (during and after ice retreat from basin) / Windermere Interstadial

Table 6.3: Seismic attributes and description of sediment deposits in Windermere.

Strat. Seq. No.	Seismic Facies	Seismic Character	Composition	Dimensions	Average Velocity	Basin	Time-Line Position
II(b)	Glacio-Fluvial (Kame Terrace)	Sub-horizontal upper surface pitted with kettles and some strong, fine internal layered reflections	Sorted and rounded sand and gravel with some valley side debris	10 m thick and 150 m wide	1800 m/s	S	Dimlington stadial (still-stand during active retreat)
II(a)	Glacio-Fluvial (Sharp-Crested Esker)	Strong, fine discontinuous internal reflections beneath a relatively rounded crest	Sand and gravel	8 m high and 150 m wide, with slopes of 5°	1650 m/s	S	Dimlington stadial (during ice stagnation)

Table 6.4: Seismic attributes and description of glacio-fluvial deposits in Windermere.

Strat. Seq. No.	Seismic Facies	Seismic Character	Composition	Dimensions	Average Velocity	Basin	Time-Line Position
I(f)	Supraglacial and Melt-Out Till	Irregular upper surface with chaotic internal reflections	Valley side debris, gravel, sand, silt and clay	Up to 30 thick and c. 500 m across	2300 m/s	S	Dimlington stadial (during ice stagnation)
I(e)	Flowed Till and Large Still-Stand Moraines	The deposit thins as it progresses down slope, forming a distal slope of a still-stand moraine. Contains some layered internal reflections	Partially sorted fine gravels in clay (80% matrix (50% clay fraction)	c. 10 m thick and c. 200 m downslope extent	2100 m/s	S	Dimlington stadial (during active retreat)
I(d)	De Geer Moraines	Symmetrical, sharp crested structures, with some random internal reflections	Relative to location (see Section 2.3.6)	Up to 10 m high and 50 m across	1750 m/s (N) 2200 m/s (N) 2150 m/s (S)	N/S	Dimlington stadial (during active retreat)
I(c)	Large Push Moraines	Asymmetrical structures with steeper distal slopes forming on the up-slopes of basement highs	Valley side debris, gravel, sand, silt and clay	Up to 40 m thick, and up to 300 m length	2500 m/s	N/S	Dimlington stadial (during active retreat)
I(b)	Medial Moraine	Transparent with strong bounding reflections	Valley side debris, gravel, sand, silt and clay	c. 10 m thick and c. 200 m across	3000 m/s	S	Dimlington stadial (during advance)
I(a)	Lodgement Till	Transparent deposit that fills troughs in the basement generally up to the crests	Poorly sorted cobble gravels with 80% matrix (50% clay fraction)	up to 10 m thick	3500 m/s	N/S	Dimlington stadial (during advance)

Table 6.5: Seismic attributes and description of till deposits in Windermere.

6.5 Conclusions

Prestack depth migration using six of the multi-channel seismic lines from the Windermere survey has produced highly detailed sub-surface images of a preserved terrestrial glacial retreat landscape. Five distinct seismic stratigraphic units were identified based upon seismic velocity, geomorphology, seismic character and stratigraphic location. Seismic velocity proved to be an invaluable tool for differentiating more ambiguous till and glacial-fluvial units, and the additional late-glacial sedimentation that exists only in the South Basin. The data showed that Windermere was glacially scoured to a depth of c. 110 m below lake-level and has allowed for an interpretation of the glacial retreat characteristics in each basin: the South Basin was dominated by surge advances and still-stands of the ice-margin, and the North Basin by relatively steady retreat that produced numerous packages of De Geer moraines through less extensive winter advances of the grounding line.

Traditional interpretation of the removal of the British and Irish Ice Sheet in the Lake District after the last glacial maximum is that of ice stagnation and rapid downwasting. There is only one localised occurrence of this in the South Basin where the evidence indicates that the ice-margin over extended during a surge advance and detached because it was out of climatic equilibrium. This left behind ice-stagnation deposits such as kame terraces and hummocky supraglacial and melt-out tills along the valley floor.

Maps produced of the sequence surfaces calculated that in post-glacial times the wider North Basin has received more sedimentation. However, the South Basin contains more sediment because in late-glacial times the South Basin received an additional unit of fine sedimentation when the valley glaciers were still present in the North Basin and Esthwaite Water. The velocity gradient and character of this late-glacial sedimentation (SSS III) correlates exceptionally well with that of the sediments within Lake Zurich (Heim and Finckh, 1984; Finckh et al., 1984).

New calibrations of radio-carbon dates from the literature and comparisons with climate data has determined the end of glacio-lacustrine sedimentation in Windermere to be c. 17.6 $\pm$ 540 cal. BP, which represents and the beginning of the Windermere Interstadial. This lasted c. 5000 years before cirque and valley glaciers

re-appeared in the catchment of Windermere during the Younger Dryas. This climatic event manifests within the stratigraphic record as mass-transport deposits that clearly occur between the late-glacial (SSS III) and post-glacial (SSS V) sedimentation.

Empirical models from Richardson and Briggs (1993) performed well when used to help identify coarse-grained glacio-fluvial deposits and to describe the variation in velocities within the gyttja at the lakebed. Additionally, Q_{SR} was measured for the gyttja (a complex organic detritus-silt) and found it to have a coarse-grain dominated fabric. This is essentially correct because it is composed of clay flocs, silt and organic material.

Finally, this survey indicates that the lakes of the Lake District probably all contain well preserved terrestrial glacial retreat deposits and late-glacial sedimentary records that relate to the retreat of the British and Irish Ice sheet.

Chapter 7

Conclusion

This thesis has shown that high-resolution marine seismic reflection data acquired using Chirp and Boomer sources, can generate accurate, precise and repeatable estimations of the *in situ* seismic quality factor (Q) and velocity, within the uppermost 100 m of marine or lacustrine sediments and deposits. Empirical relationships between Q and mean grain size, and between velocity, saturated bulk density and porosity, have been tested against laboratory results. Introducing the quantitative information into seismic interpretations, especially of till deposits, has helped to produce a new deglacial history for Windermere. This chapter presents conclusions to the main themes in this thesis and a discussion of further work.

7.1 Estimating Quality Factor

The Chirp sonar was the most effective source for estimating Q using the spectral ratio technique (Q_{SR}). However, it was demonstrated that combining Boomer and Chirp data from the same location can examine attenuation over at least four octaves of frequency (e.g. 0.5–8.0 kHz), which produces an improved result. An ideal sonar for the purpose of measuring Q_{SR} within the uppermost 100 m of sediment would have this effective power spectrum spanning c. 0.5–8.0 kHz and slightly lower if possible. This is because data above 8 kHz, in *all* the estimates of Q_{SR} that I have made, have always been too noisy to use with the spectral ratio technique. Meaning that the higher frequencies of the Chirp sweep have been redundant. Alternatively, more power could be attributed to the higher frequencies of the Chirp sweep to improve signal-to-noise ratio above 8 kHz, but at a cost to overall penetration.

To estimate Q_{SR} a suitable sediment package must be selected. It requires a consistent sub-horizontal sub-bottom reflector and a consistent sub-horizontal seabed

reflection, both without any neighbouring reflections within 1 to 2 ms, to avoid tuning effects. Also, the target reflection must be shallower than the first seabed multiple, reducing the possibility of delayed energy affecting the spectra. Emphasis is placed on interpretation of spectral signatures before applying an iteratively reweighted robust least-squares regression to subdue the effects of noise and local heterogeneities.

Estimating Q_{SR} in the Solent was simpler than within Windermere because the strong reflections that reached above the noise floor in the Chirp data were fewer, and were more temporally spaced. The rhythmic nature to most of the Windermere sediments made it almost impossible to window an isolated sub-bottom reflection. Additionally, the question must be asked of whether the reflections observed within the Windermere data are time interfaces, or interference from many rhythmic sub-resolution interfaces. Nevertheless, enough locations existed within the gyttja (SSS V) where an isolated basal reflection could be used.

In the Solent, frequency-independent Q_{SR} values (with 95% confidence intervals) of 154(+14; −12), 135(+12; −10), 107(+6; −5) are obtained for silty clays, and a Q_{SR} of 63(+10; −7) for a fine-sand deposit. In lake Windermere, a frequency-independent Q_{SR} of 33(+6; −4) was obtained for gyttja (highly organic clayey-silt). The low Q_{SR} for the gyttja suggests that there are probably an abundance of compliance heterogeneities within (e.g. compliant clay flocs and plant remains, non-compliant mineral grains), which cause squirt flow to become a significant attenuation mechanism.

Hamilton (e.g. Hamilton, 1972) holds the view that attenuation can be considered to be linearly related to frequency, from hertz to megahertz, in unconsolidated marine sediments. Critically, the problem with his compilations of datasets and those of others, is that individual investigations generally use a narrow frequency range where a linear dependence of attenuation on frequency appears justified (Kibblewhite, 1989). The frequency range used here is relatively broad and the Q_{SR} observed still appears frequency-independent in a range of sediments. Even though the grain-sliding model predicts this type of attenuation, I believe that there are viscous intrinsic attenuation mechanisms in affect at the same time (e.g. Biot and

squirt flow), including some degree of inherent scattering, which will cause overall attenuation to vary in a complex manner from low-frequency seismic surveys to high-frequency laboratory studies. The important result here is that attenuation can be measured using a practical range of seismic frequencies in the field and that different sediment types exhibit different Q_{SR} values, which are inherent to the attenuation mechanisms that operate within them and the amount of scattering they produce at these frequencies.

7.2 Quality Factor and Mean Grain Size

Q values derived from the spectral ratio technique presented here have been denoted as Q_{SR} to represent the fact that estimations of Q are also a function of observation. Q estimated using seismic reflection data, where energy propagates more-or-less at normal incidence to bedding planes, could be expected to be different to Q measured using refraction seismics, where energy propagates along bedding planes and will encounter different forms of heterogeneities (e.g. irregular bedding surfaces). Hence, the Q_{SR} is not an isotropic Q for the medium, but if the criteria for the selection of sediment packages is upheld, the Q_{SR} values relative to each other should maintain a degree of consistency and anisotropy should be negligible.

Hence, comparing Q_{SR} to other Q values reported in the literature is not strictly ideal, but is necessary for the time being, until a larger catalogue of Q_{SR} and associated sediment physical properties are obtained. Therefore, it is advisable that datasets from the literature should be judiciously chosen, based on method of observation and the assumptions made on how attenuation scales with frequency.

Sediment Q is seldom used by industry for offshore site investigations because of practical difficulties with reflection seismology (e.g. restricted bandwidth), and because of uncertainties in rock-physics models. However, I have shown here that Q has the potential to characterise the dominant fabric of the sediment that is supporting wave-propagation. Generally, sediments with a clay dominated fabric (mean grain size 6–9+ ϕ) have a Q over 75, and sediments with a coarse-grain dominated fabric (mean grain size 0–6 ϕ, and larger grains) have a Q less than 75.

More observations of Q in sediments with a mean grain size of 6 ϕ will help confirm this transition.

7.3 Interval Velocity from Migration

Boomer multi-channel seismic (MCS) surveys were successfully acquired in the Solent over a 30 m core and a sampled sand deposit, and in lake Windermere, where more than 150 km of survey lines cover most of the lake. To reliably migrate high-resolution multi-channel seismic reflection data, accurate knowledge of the source-receiver geometry is crucial. The Windermere survey highlighted the problem of attempting to determine interval seismic velocities for migration when an inaccurate streamer depth profile was assumed. A method was developed to obtain the multi-channel streamer depth profile by utilising the destructive interference generated by the surface ghost recorded at each channel. It was found that the far channels of the multi-channel streamer were sagging c. 2 m below the nearest channel in the fresh water.

An optimal processing methodology for Boomer MCS data was developed using iterative Kirchhoff prestack depth migration, Burg deconvolution of the migrated offset sections, and F-K filtering of the common reflection point gathers. These processing steps successfully removed reverberation from each depth migrated offset section and any delayed energy with offset before stacking. Velocities were derived for sediment packages during the iterative process using horizon-based migration velocity analysis. The minimum vertical resolution for interval velocities is c. 1–2 m, which was achieved over the core site in the Solent.

The Solent investigation showed that Q_{SR} estimations can first determine whether a sediment is coarse-grain dominated or clay dominated. Migration velocities can then be used with empirical models from Richardson and Briggs (1993) to predict physical properties, and subsequent physical property correlations with sediment type can refine mean grain size or identify over-consolidated clays. The velocities found were 1610 $\pm$ 20 m/s for fine-sand, 1860 $\pm$ 30 m/s for sandy-gravel and 1630–1800 m/s in over-consolidated silty-clay from the core.

Within Windermere the depth migrations of six lines identified five seismic stratigraphic sequences with velocities correlating with examples from the literature: I—till (c. 2100–3000 m/s); II—glacio-fluvial (c. 1800 m/s); III—glacio-lacustrine/lacustrine (1500 m/s + 6^{-1}); IV—slumped/disturbed (c. 1500 m/s); V—lacustrine (c. 1490 m/s). Although there were some high-velocity contrasts in the velocity models, the Kirchhoff migration using maximum amplitude ray-tracing to calculate the travel times usually remained robust.

The frequency independent Q_{SR} values of +30 found in the Solent and Windermere, along with the observation that migration of the Boomer MCS data produced very high-resolution images, suggests that velocity dispersion is negligible within the sediments that form the uppermost 100 m of the lakebed/seabed encountered in this study. This is discussed further as future work below.

7.4 Empirical Velocity Models

This thesis is consistent with arguments made by Jackson and Richardson (2007), that the regressions from Hamilton and Bachman (1982) predict velocities that are too high. The Richardson and Briggs (1993) regressions are much more realistic, predicting reasonably accurate *in situ* bulk densities and porosities within unconsolidated fine-sand and gyttja, and even over-consolidated clays. The extrapolation into gravel sediments was also successful. Since these regressions have been based on measurements obtained from the upper 0.5 m of sediment, it is probable that increased over-burden, or better packing of the deeper sediment, leads to velocities that are slightly higher than those predicted by the models—this was possibly the case with the fine-sand deposit.

In Windermere, the "low velocity effect" occasionally caused the seismic velocity within the gyttja (SSS V) to be lower than the water velocity above. This was also predicted by Richardson and Briggs (1993) model very well.

7.5 Windermere Interpretation Summary

Seismic facies beneath Windermere have been interpreted by combining standard observations of seismic character and stratigraphic location with their geomorphology, and seismic velocity. The latter, provides a valuable insight to the relative compaction/composition of the facies, and can be used with empirical relationships of bulk density and porosity to predict sediment/deposit type. These facies interpretations have elucidated a new post-LGM deglacial history for Windermere (and the Lake District) that is dominated by active ice retreat from the lake rather than the traditional interpretation of ice-stagnation and downwasting.

Active ice retreat of the British and Irish Ice Sheet from Windermere after the LGM produced at least fifty-seven retreat moraines, which have been preserved beneath the glacio-lacustrine and lacustrine sediments. The style of retreat changed from being dominated by surge re-advances and still-stands in the South Basin, evidenced by large push and still-stand moraines, to more steady retreat in the North Basin that produced mostly De Geer moraines (quite regular, 10 m high and 50-100 m wide retreat moraines) through small winter re-advances of the ice-margin. Localised ice-stagnation and downwasting deposits do exist in a sub-basin at the south end of Windermere, but these are interpreted as forming after the ice-margin surged forward beyond its climatic equilibrium and detached from the retreating glacier.

The active deglacial features are buried beneath decametres of late-glacial sedimentation, which began depositing first in the South Basin of Windermere while ice remained in the North Basin. Hence, the thickest sediment sequence of up to c. 50 m exists in the South Basin and is the reason why the North Basin of Windermere is deeper. This sediment record could represent the thickest continuous sequence of late-glacial to present day sedimentation currently identified in the British Isles and should be the subject of intensive future research.

The area was not directly affected by Younger Dryas glacial activity but this period is recognised within the seismic stratigraphy as a series of slump and disturbed deposits. These active paraglacial features are buried beneath metres of post-glacial sedimentation.

Finally, it should be recognised that retreat moraines and the deglacial stratigraphy associated with the removal of the British and Irish Ice Sheet are rare, especially on land, and this has recently led to investigators going offshore to find such evidence (e.g. Bradwell et al., 2008). The Windermere survey has demonstrated that very good terrestrial deposits do exist and could be well preserved beneath many of the lakes in the Lake District.

7.6 Future Work

7.6.1 Remote Empirical Models

There is great uncertainty, due to the present lack of published data, concerning empirical relationships between Q_{SR} and mean grain size, and between high-resolution seismic velocity and saturated bulk density or porosity within the uppermost sediments. The results database needs to be expanded by surveying sites where the physical properties of sediments are known and the relationships need to be developed to different depths of burial, so that these remote measurement methods of Q and velocity would be widely used.

Additionally, more observations of Q_{SR} as a function of mean grain size and sorting, might unambiguously resolve well-sorted and poorly-sorted coarse-grain dominated sediments.

7.6.2 Velocity Dispersion

The comprehensive studies in sandy sediments from the Sediment Acoustics Experiment of 1999 Thorsos et al. (2001) and the crosshole tomography experiments of Turgut and Yamamoto (1990), both suggest that there is significant velocity dispersion (c. 100 m/s) in the frequency ranges of the seismic sources used here, within sandy sediments with low Q (10–30 at 4 kHz). This is larger than the precision achieved with the Boomer migration velocities and so could effectively be resolved by developing a method whereby different frequency bands of the Boomer MCS data are migrated using iterative prestack depth migrations. Afterwards, the velocity models could be compared, which would produce a direct interpretation of

velocity dispersion, which might possibly be related to specific sedimentary units. The same experiment using the Chirp sonar would provide an extended frequency range, however, a compromise between frequency content and penetration/range would have to be considered. If velocity dispersion could be obtained from Boomer MCS data, this could be compared to predictions of Q, which would be very beneficial towards understanding the attenuation mechanisms that occur within the many different sediments that have been surveyed over. For the moment, the ability of depth migration to correctly focus the energy across a broad range of frequencies suggests that velocity dispersion is minimal.

7.6.3 Windermere Sediment/Till Calibration

A core into the silty-clay varves of SSS III would allow for comparison of the layered seismic reflections with the interfaces that produce them. From this an absolute limit on vertical resolution could be derived and an investigation into the relationship between the spectral content of the reflections and spacing of the interfaces could be carried out. A core would also calibrate the seismic velocity measurements made in this thesis to sediment physical properties and grain size analysis of the gyttja (non-destructively in order to maintain the delicate flocs and plant fragments) would be useful to compare with the Q_{SR} estimates made for sediments.

Additionally, some of the large push moraines correlate with terrestrial ridges, of which there is no mention in the literature. A survey of these features would identify if they are till structures and determine whether they are related to the large push moraines in the seismic data.

Appendix A

Appendix

A.1 Appendix A: Robust Regression

Statistical packages often feature robust regression as part of their curve-fitting toolboxes. The following is the implementation used by Matlab® (The MathWorks, Inc., 2007):

The initial sum of the squared residuals (S) has the residuals (fitted response values $\hat{y}$ deducted from the observed response values y_i) weighted w_f according to the variance within their frequency bands σ_f^2:

$$S = \sum_{i=1}^{n} w_f \left(y_i - \hat{y}_i\right)^2; \tag{A.1}$$

$$w_f = \frac{1}{\sigma_f^2}. \tag{A.2}$$

Adjusted residuals r_{adj} are computed according to their leverages h_i, in which high-leverage data is downweighted to reduce their effect on the least-squares fit,

$$r_{adj} = \frac{y_i - \hat{y}_i}{\sqrt{1 - h_i}}. \tag{A.3}$$

The adjusted residuals are standardized (u) using the product of a tuning constant K (4.685) and the robust variance s, which is the median absolute residual (a robust measure of spread) divided by 0.6745. The values are picked to give reasonably high efficiency in the case of a normal error distribution and still offer protection against outliers when using a bisquare weight function (Fox, 1997).

$$u = \frac{r_{adj}}{K \cdot s}. \tag{A.4}$$

Bisquare weights are then calculated as a function of u. The weights decline as soon as the error departs from 0, and become 0 when the absolute error becomes larger than $K \cdot s$. The new weights (W_i) for the first robust regression are the product of w_f and w_i.

$$w_i = \begin{cases} (1 - (u_i)^2)^2 & |u_i| < 1 \\ 0 & |u_i| \geq 1 \end{cases} \tag{A.5}$$

$$W_i = w_f \cdot w_i \cdot w_{i+n} .... \tag{A.6}$$

After each iteration W_i is the product of the previous weights, and the recalculated w_i from repeating Equations (A.3) to (A.5). The process continues until the residuals converge.

A.2 Appendix B: Mean Grain Size

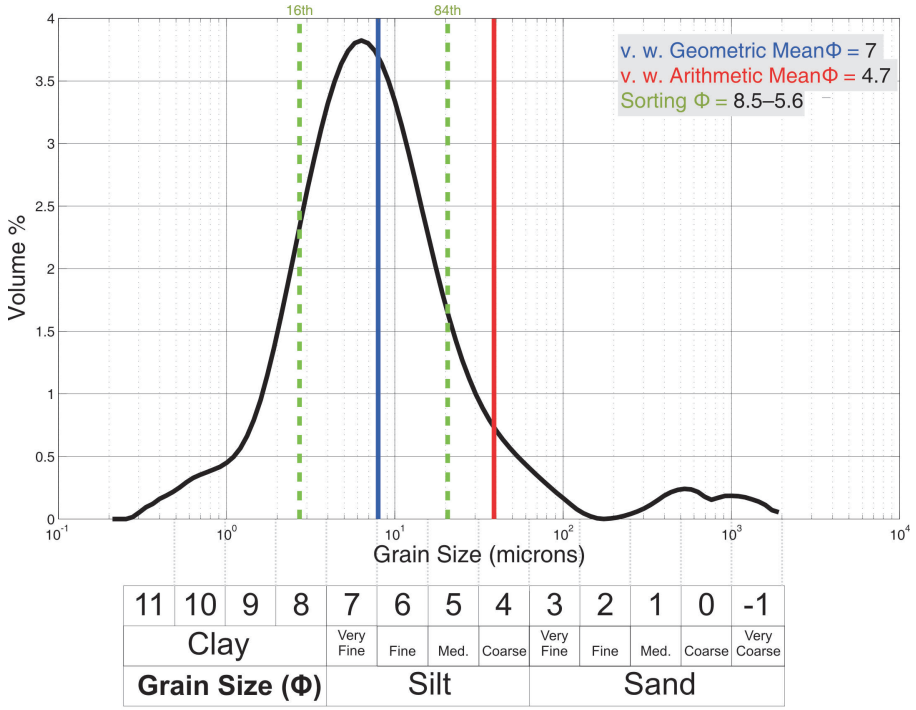

Figure A.1: Comparison of volume weighted arithmetic and geometric means for a clay–fine-grained sample from RC2.

The Mastersizer 2000 software defaults to the volume weighted arithmetic mean diameter, and this has been used in the literature for some recent geological investigations (e.g. Lario et al., 2002; Wang et al., 2009). This is the incorrect mean to use here though, because the mean grain *size* is the important measurement to the research, and not simply the diameter.

The results from the volume weighted arithmetic mean diameter and the volume weighted geometric mean diameter are shown for a clay dominated sample and a coarse-grain dominated sample from RC2 (Figures A.1 and A.2 respectively).

Figure A.1 shows that the volume weighted arithmetic mean is attributing much greater significance to the small fraction of sand grains that occur in this clay/silt dominated sediment—the mean result is one Phi category away from being classified as a sand. The volume weighted geometric mean better describes the fabric of the sediment classifying it as a fine–very fine silt, and falls within the 16th and 84th percentiles of the sample. In Figure A.2 the volume weighted arithmetic mean is

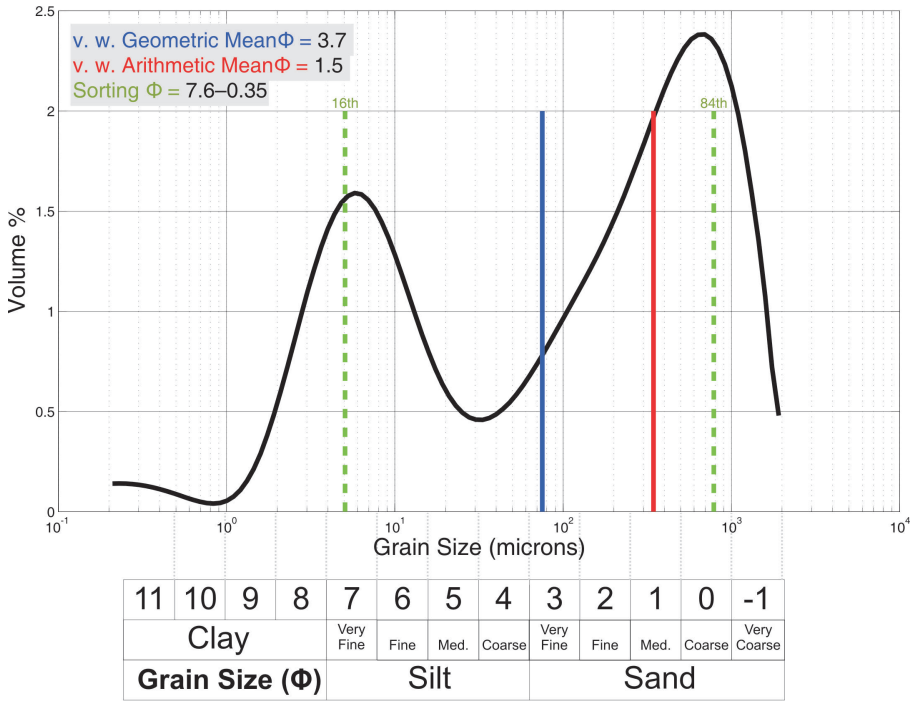

Figure A.2: Comparison of volume weighted arithmetic and geometric means for a coarse-grained sample from RC2.

hardly influenced by the relatively significant amount of sample that is very fine sand and finer. The mean of 1 Phi suggests that this particle size distribution is equivalent to a sediment with a monodisperse particle size distribution about a grain size of 1 Phi (pure medium grained sand). The volume weighted geometric mean classifies the sediment as fine sand, and when consideration is given to the range of the 16th and 84th percentiles that encompass the volume peaks of coarse sand and very fine silt, they together provide a more informative description of the particle size distribution within the sample. For log-normal grain size distributions the volume weighted arithmetic mean provides too much weight to the larger particles making it insensitive to changes in finer composition, and limits the range in mean grain size from sand to coarse silt, unless pure samples of clays or fine silts are provided.

Figure A.3 demonstrates that when the "mean grain size" between two grains is taken to simply represent the mean grain diameter, it *does* make sense to take the arithmetic mean. However, this grain diameter produces a 3D grain that is relatively much larger than the smaller grain. The geometric mean of the diameters produces

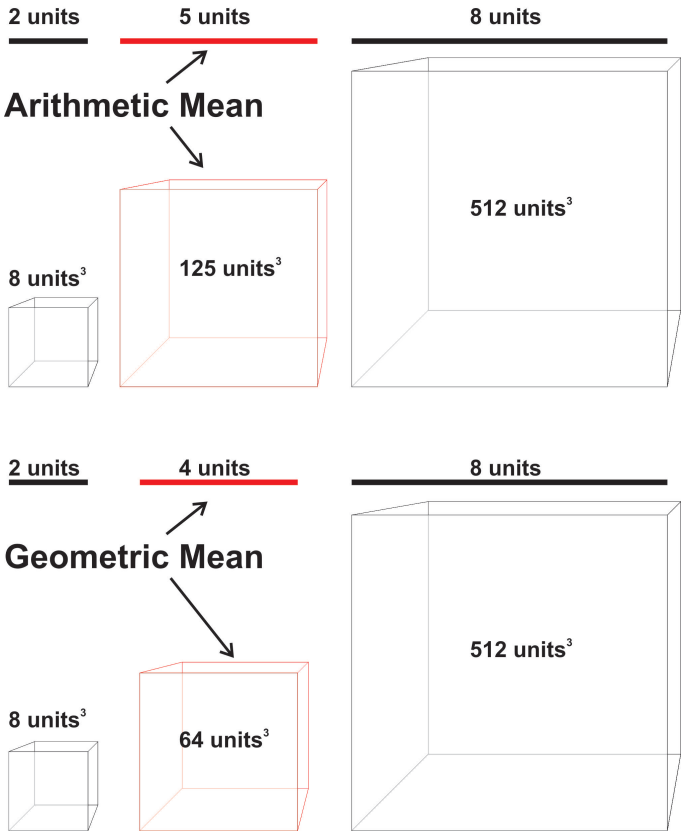

Figure A.3: Diagram showing how different mean volumes are produced by taking the arithmetic and geometric means of grain diameters.

a 3D grain that is better representative of the 3D "mean grain size" between the two grains, which is the definition of mean grain size that is important here. This shows the inherent differences of the two methods and why the volume weighted arithmetic means were always coarser than volume weighted geometric means in Figures A.1 and A.2.

Log-normal distributions are common for sediments (Krumbein and Pettijohn, 1938) and will be symmetrical around the geometric mean on a logarithmic size scale. Hence, geometric type means should be taken from logarithmically spaced classes in log-normal distributions, and arithmetic type means taken from more or less linearly spaced classes, from normal distributions Zhang and Zhang (1989); Merkus (2009). Although use of the volume weighted geometric mean grain size is rarely stated in geological literature, it is prevalent for particle size distributions in soil science (e.g. Pieri et al., 2006).

A.3 Appendix C: RC2 Grain Size Analysis

The core sections of RC2 are photographed and placed in order of depth. The grain size distributions shown next to each photograph come from samples taken at least every 25 cm along the cores. Sample locations are marked by adjacent colour squares that share the same colour as the associated grain size distribution. Where samples exhibited the same grain size distribution in a core section, the distributions were averaged together and the same colour squares are used at the sample locations. The electronic version of the thesis contains the entire length of the core. The printed version only contains the sections referred to in the text.

On the grain size distributions the weighted geometric means are indicated by the solid vertical lines, and the 16th and 84th percentiles by dashed vertical lines. The mean grain size and sorting are calculated for each core section where the grain size distributions are weighted by the length of core that they represent.

RC2 is 30.7 m long when the 3.2 m of seabed gravel and the missing core sections are included. The depth beneath the seabed, and the length of core beneath the seabed gravel, are shown alongside the cores in red and blue respectively. The lithology of each section is shown down the left hand side, and descriptions of the strata from the Fugro log and my own observations are noted. The lithology legend is as follows:

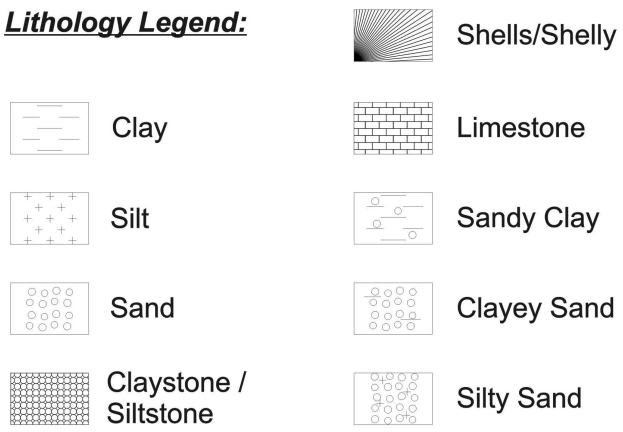

Figure A.4: Lithology legend for RC2 core section analysis.

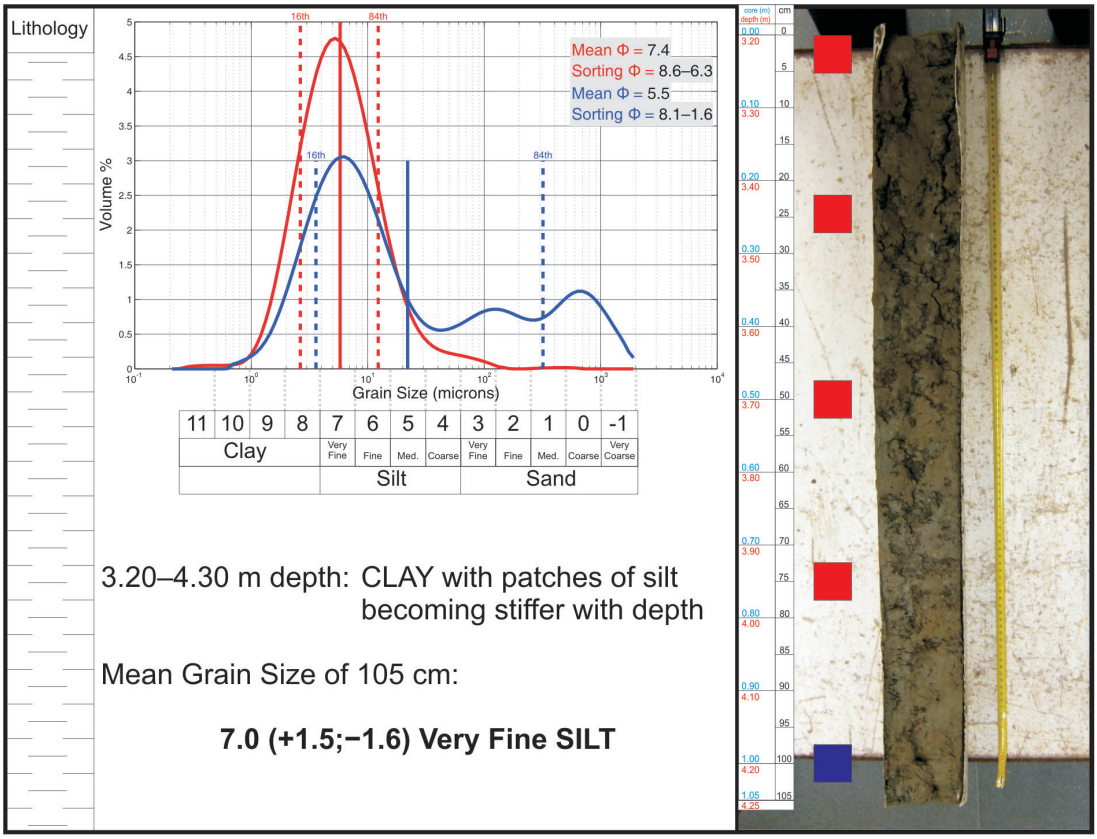

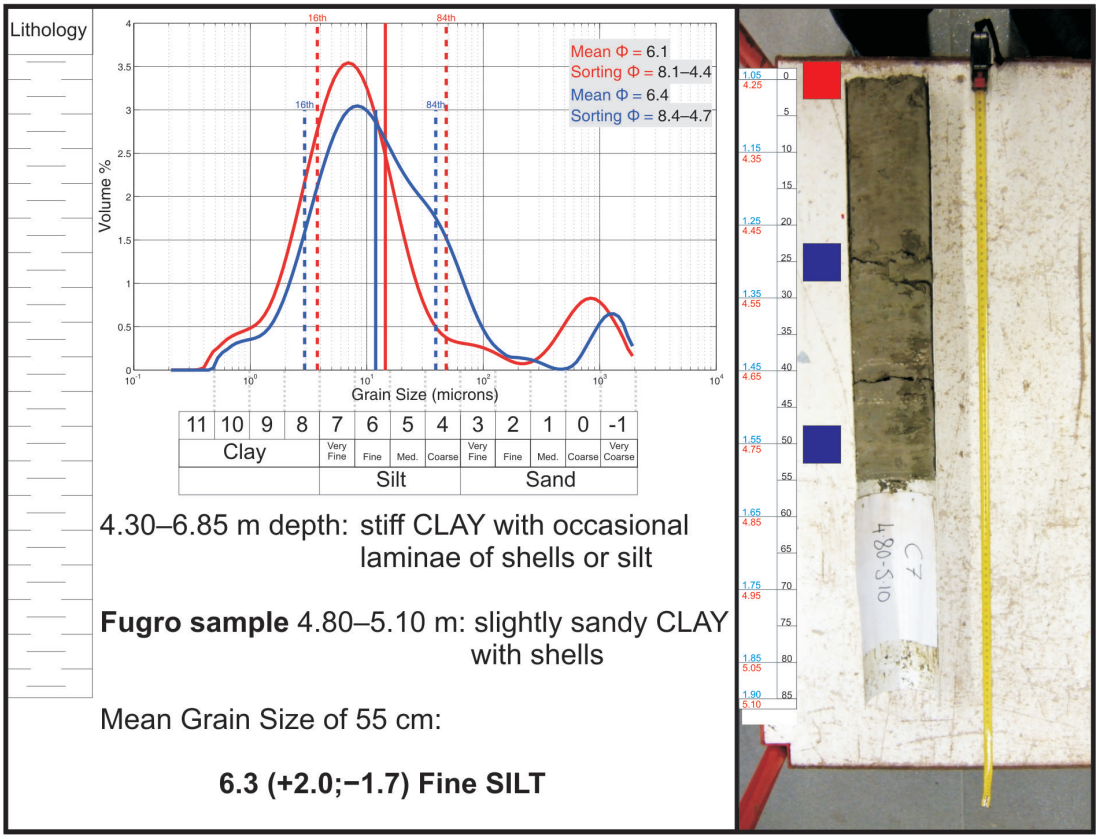

Figure A.5: RC2 0.00–1.90 m.

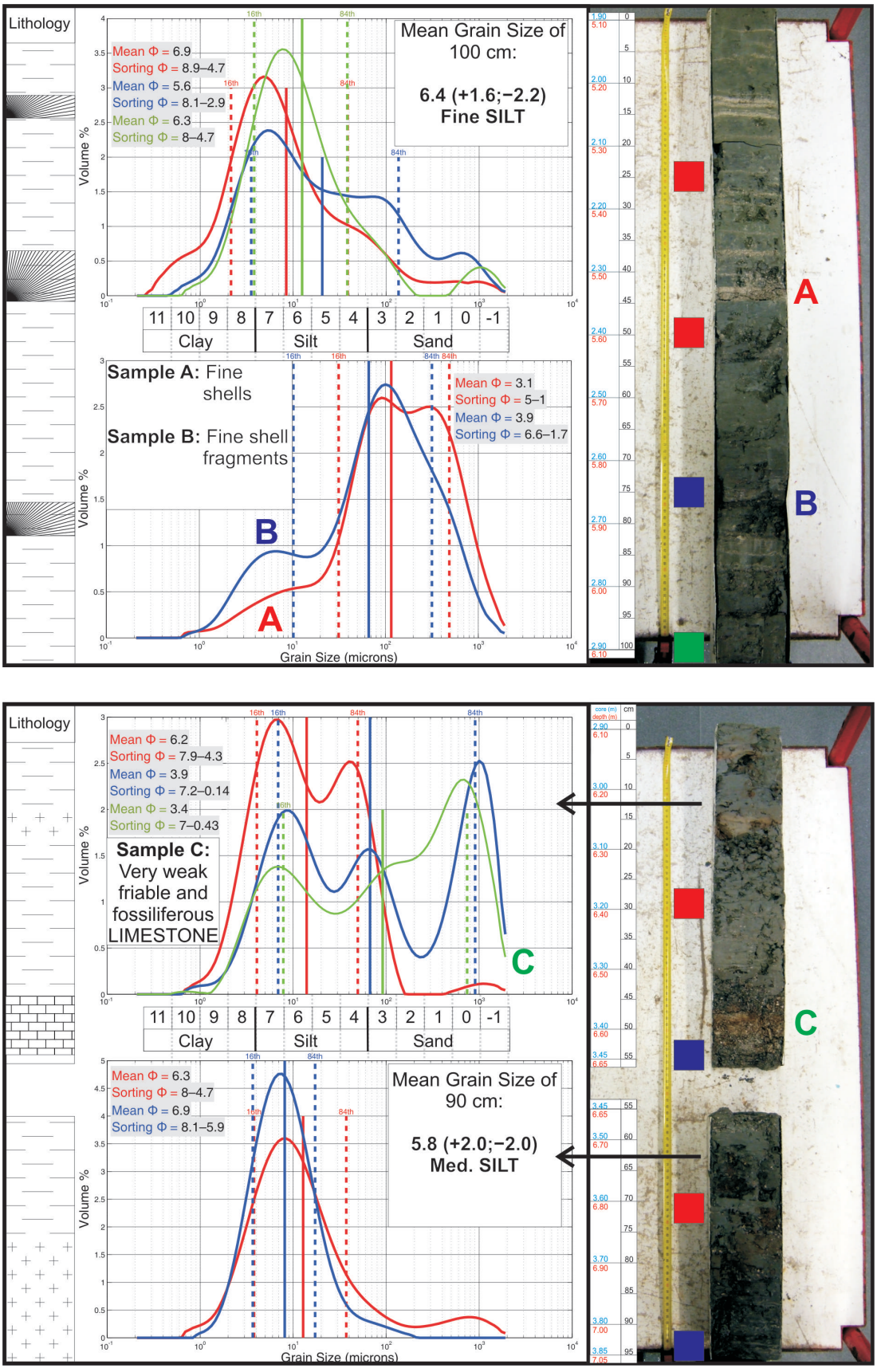

Figure A.6: RC2 1.90–3.85 m.

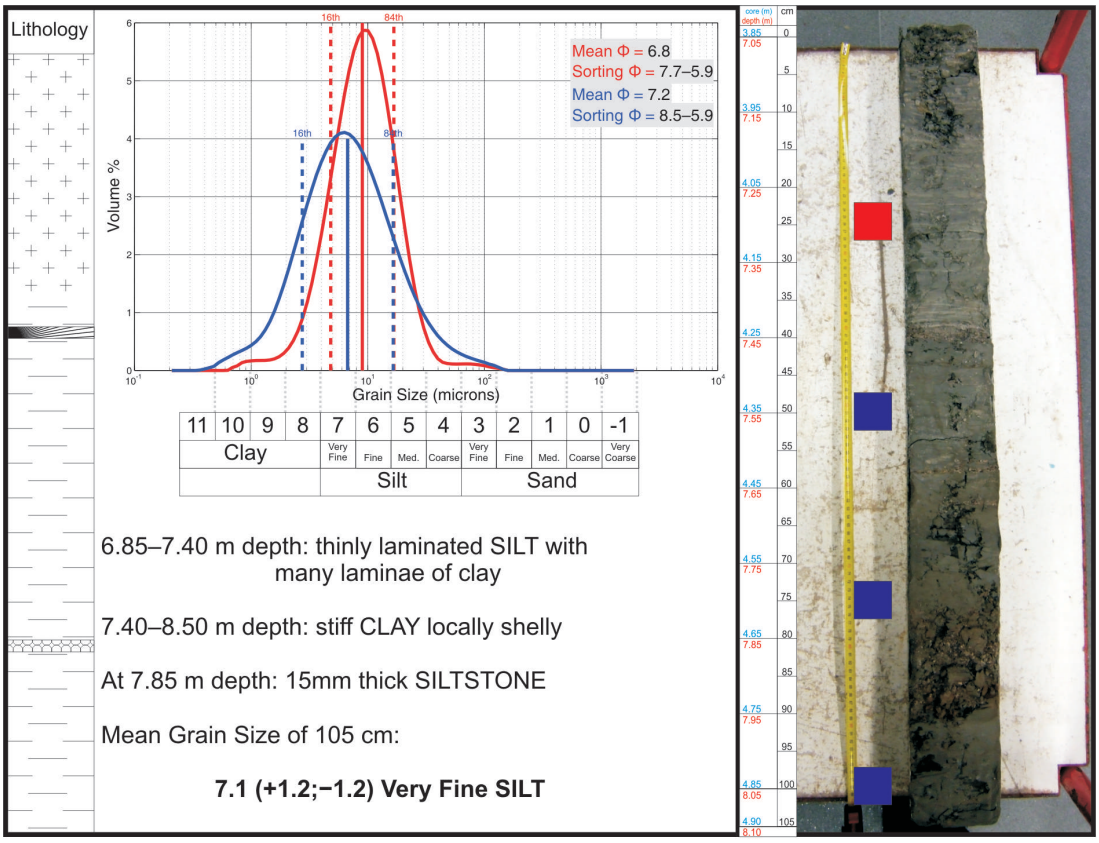

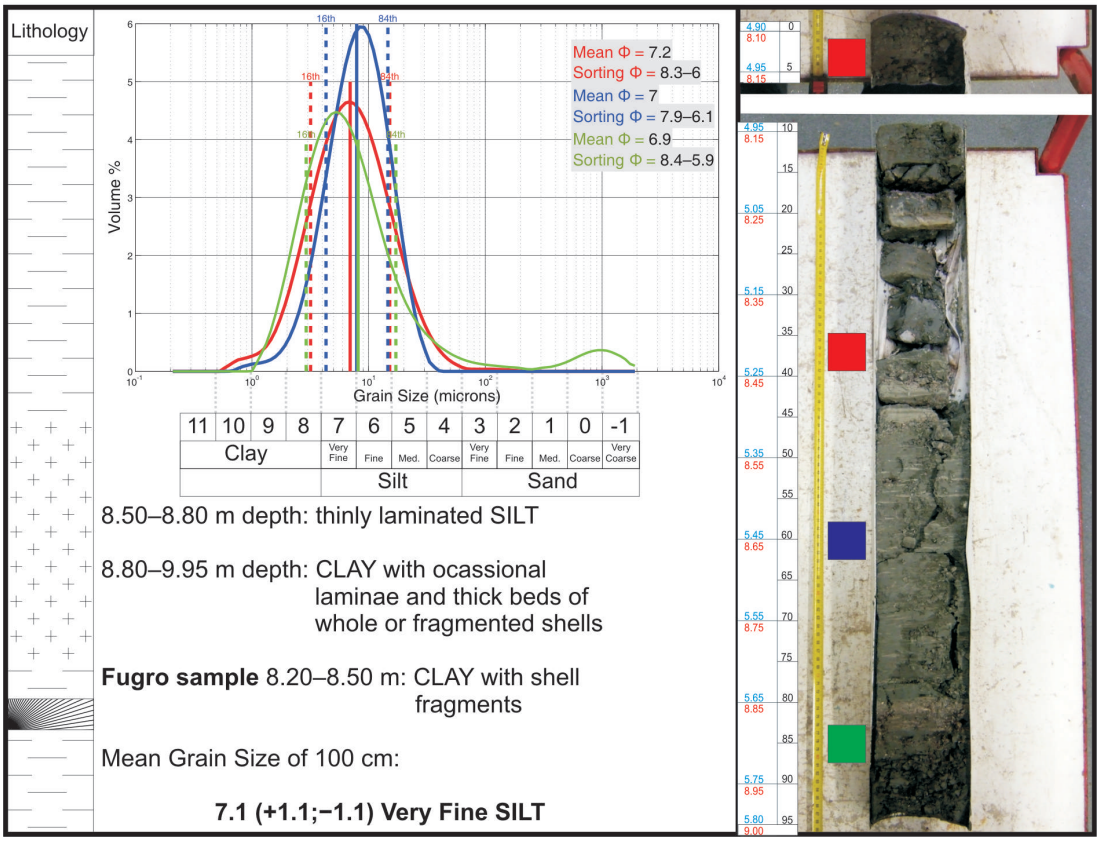

Figure A.7: RC2 3.85–5.80 m.

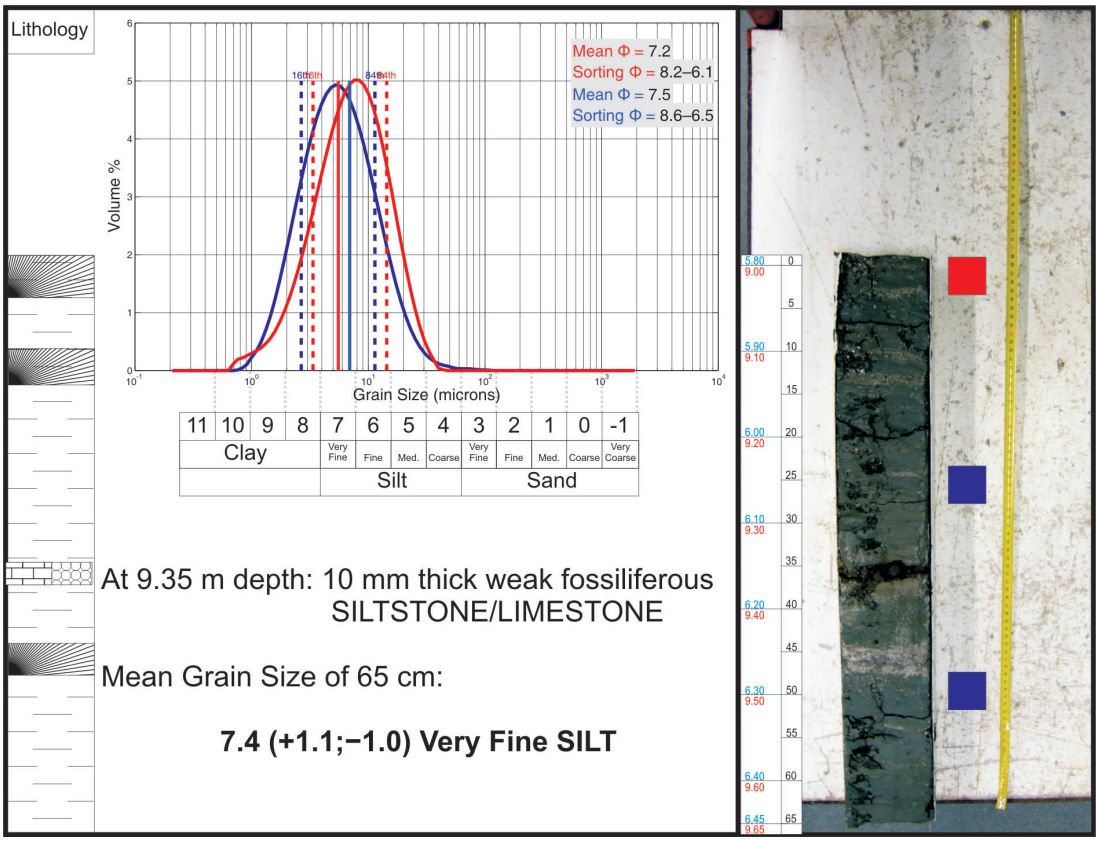

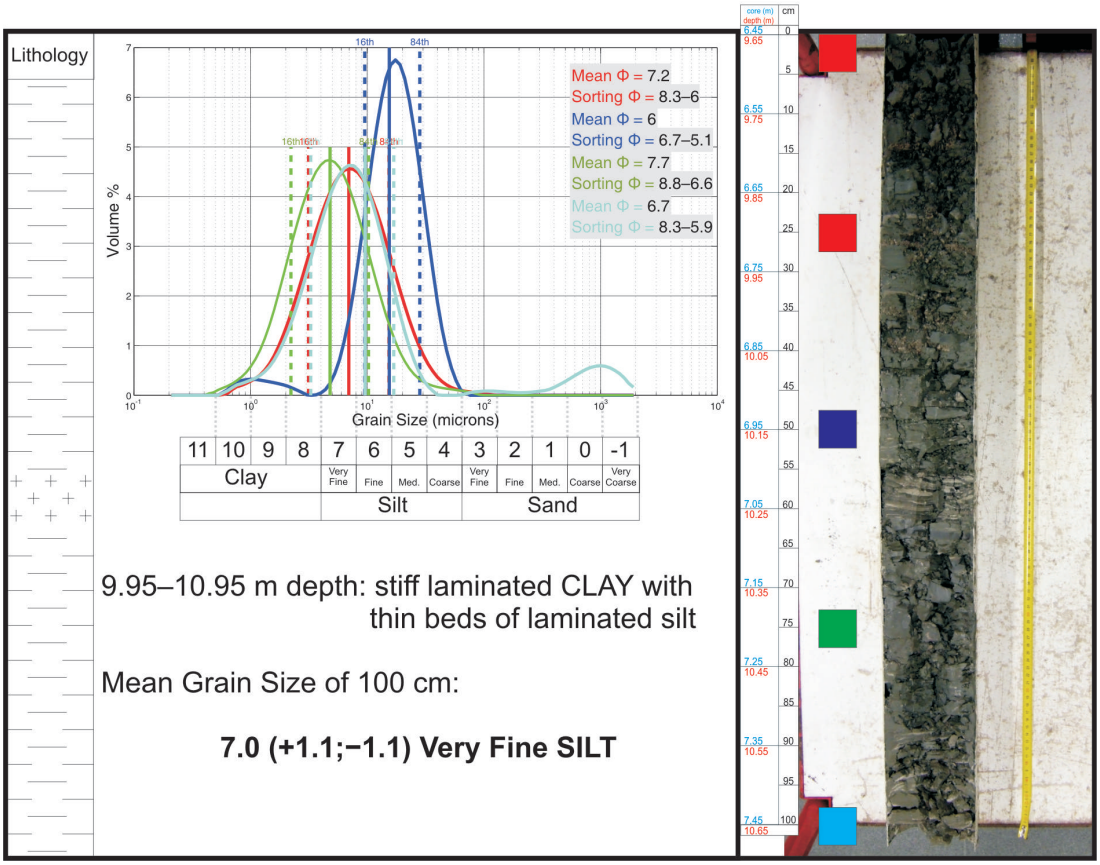

Figure A.8: RC2 5.80–7.45 m.

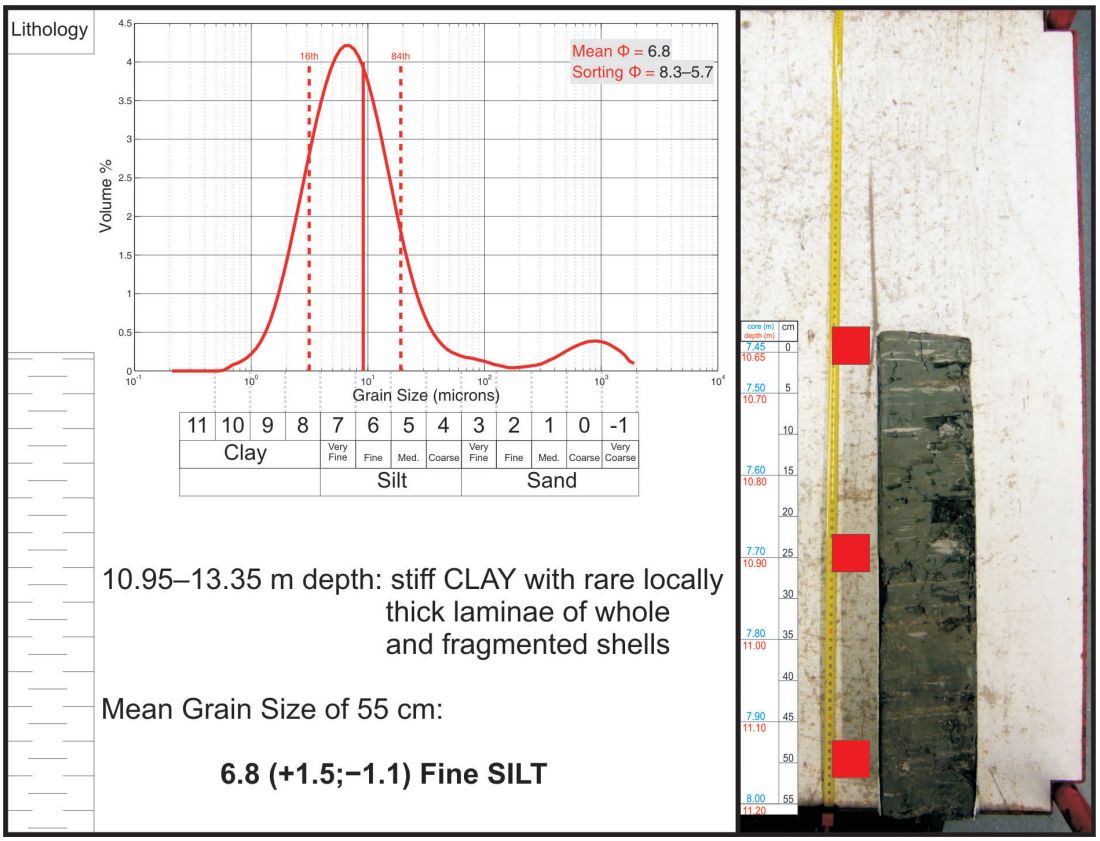

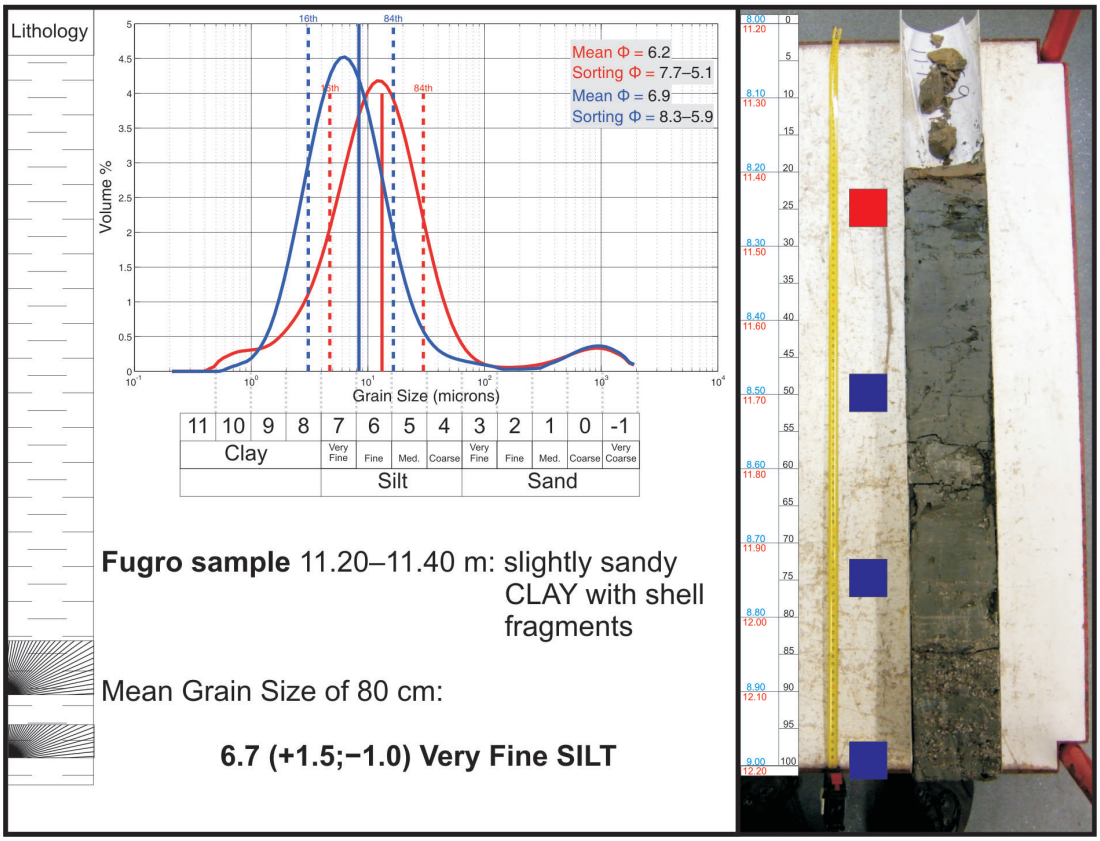

Figure A.9: RC2 7.45–9.00 m.

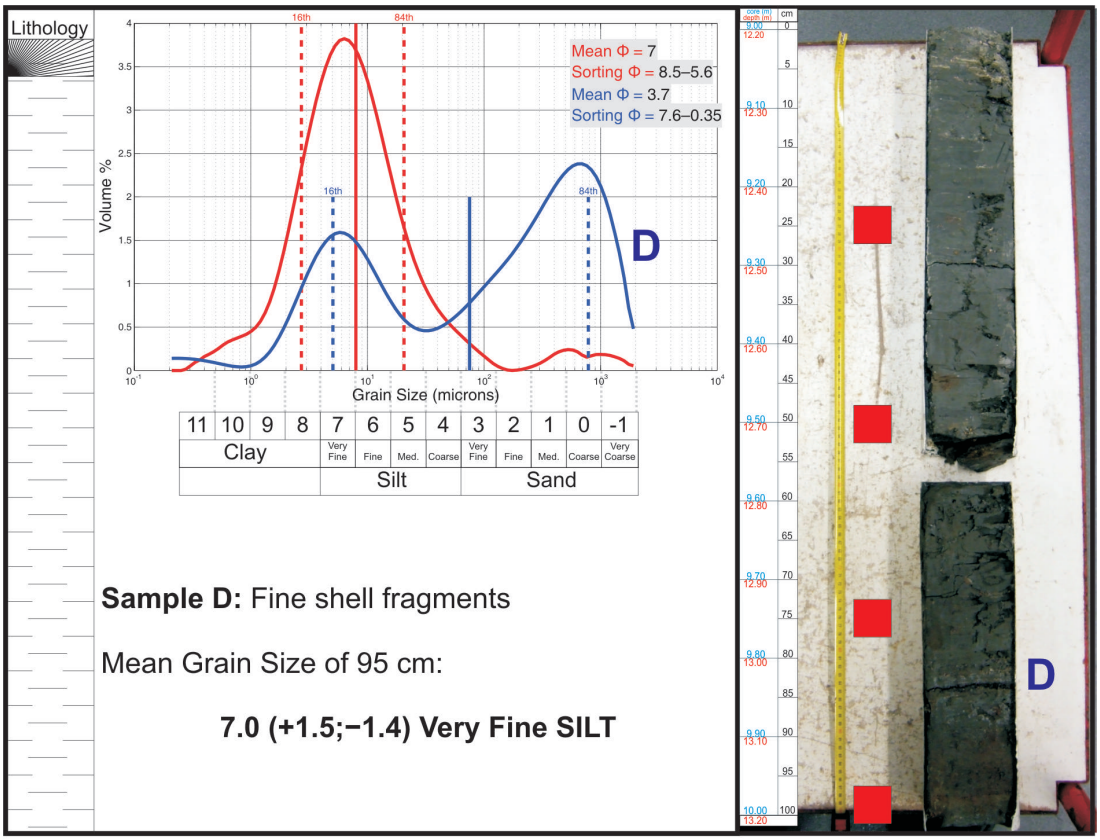

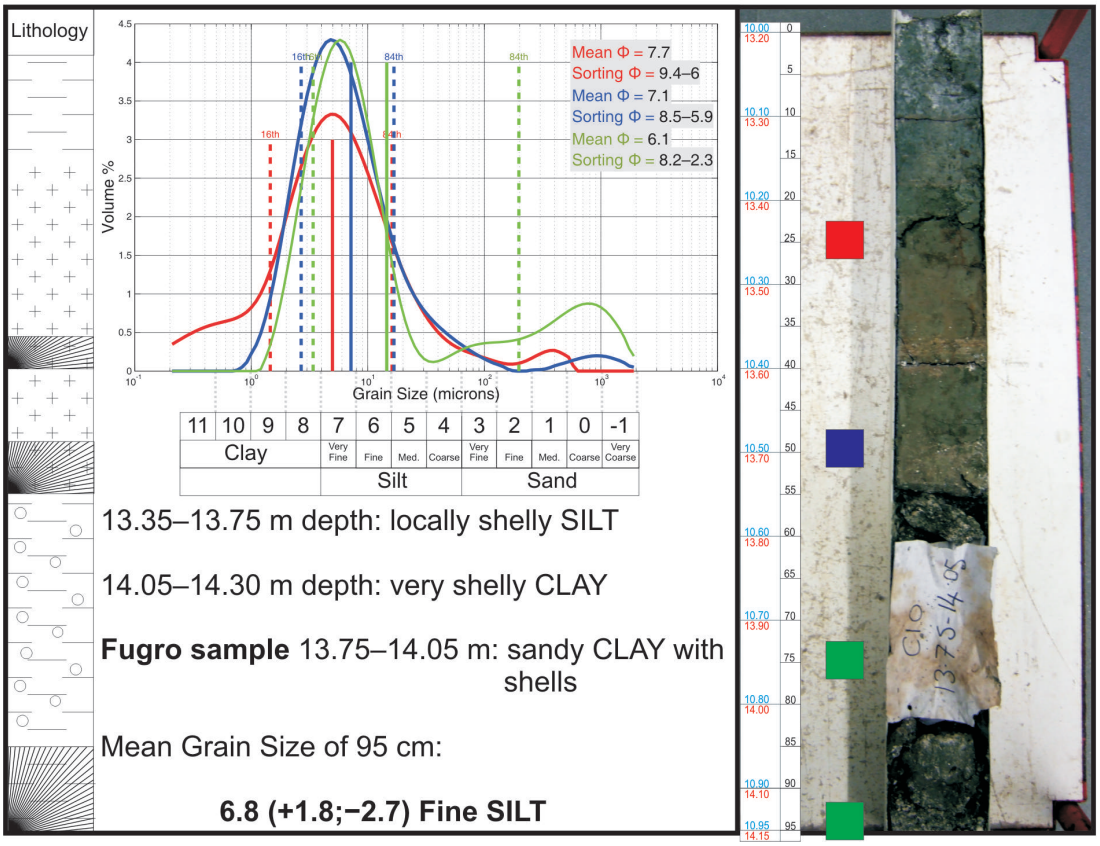

Figure A.10: RC2 9.00–10.95 m.

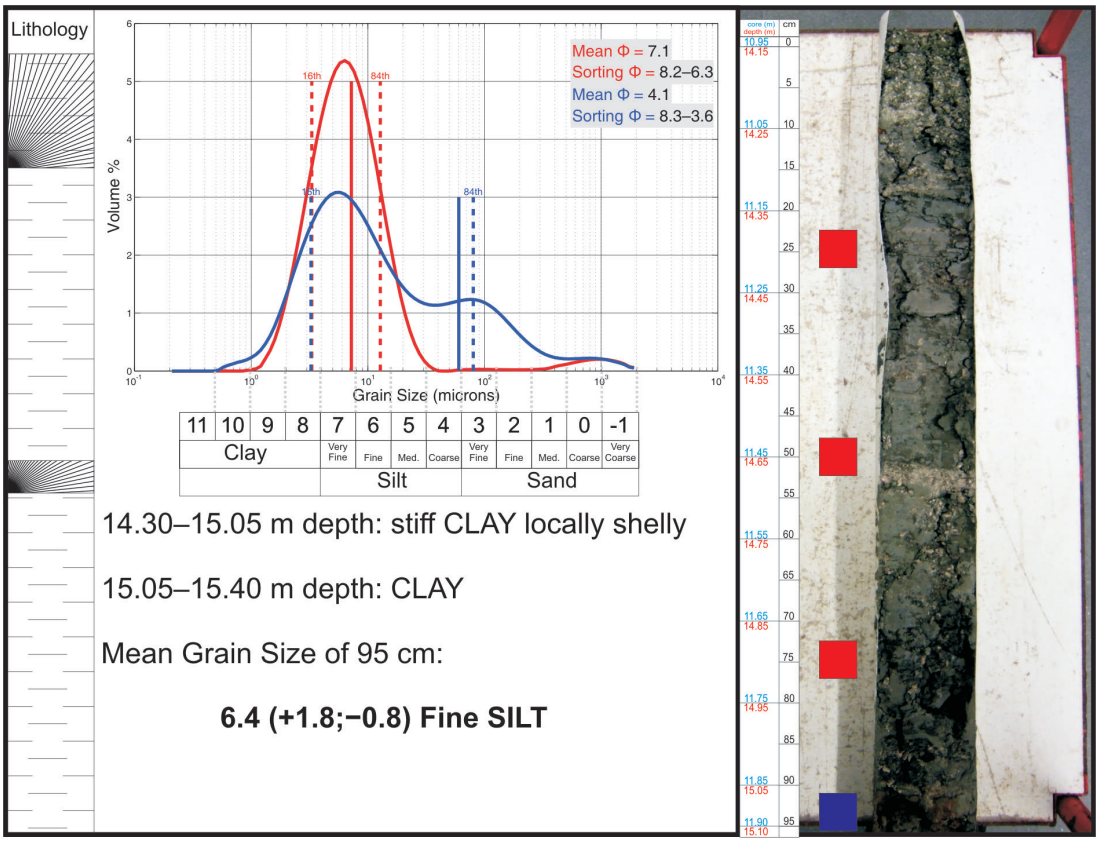

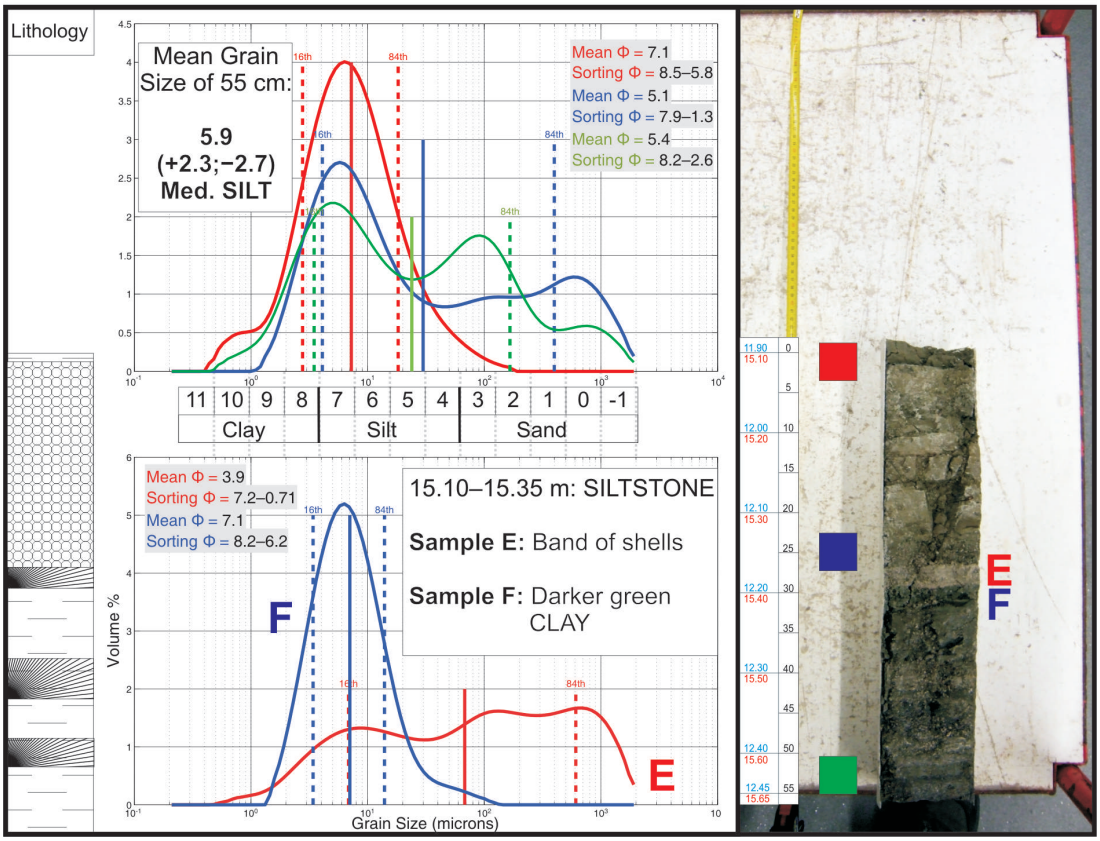

Figure A.11: RC2 10.95–12.45 m.

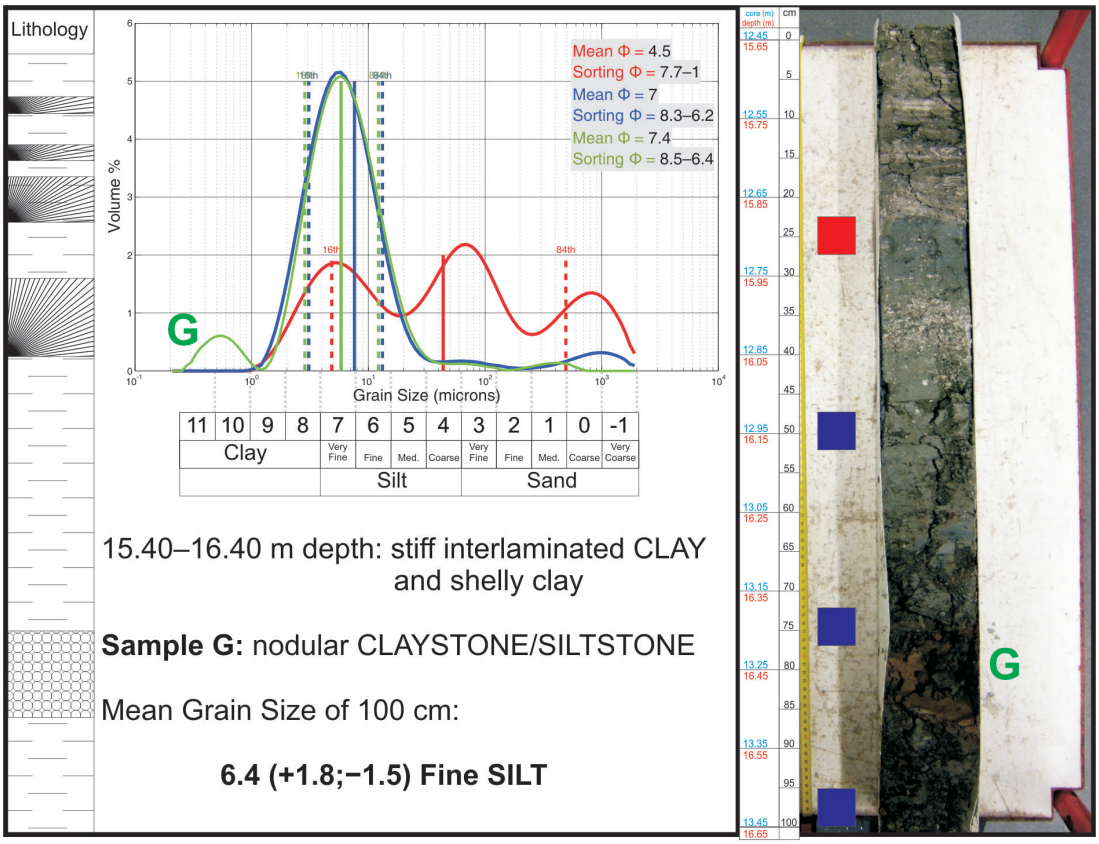

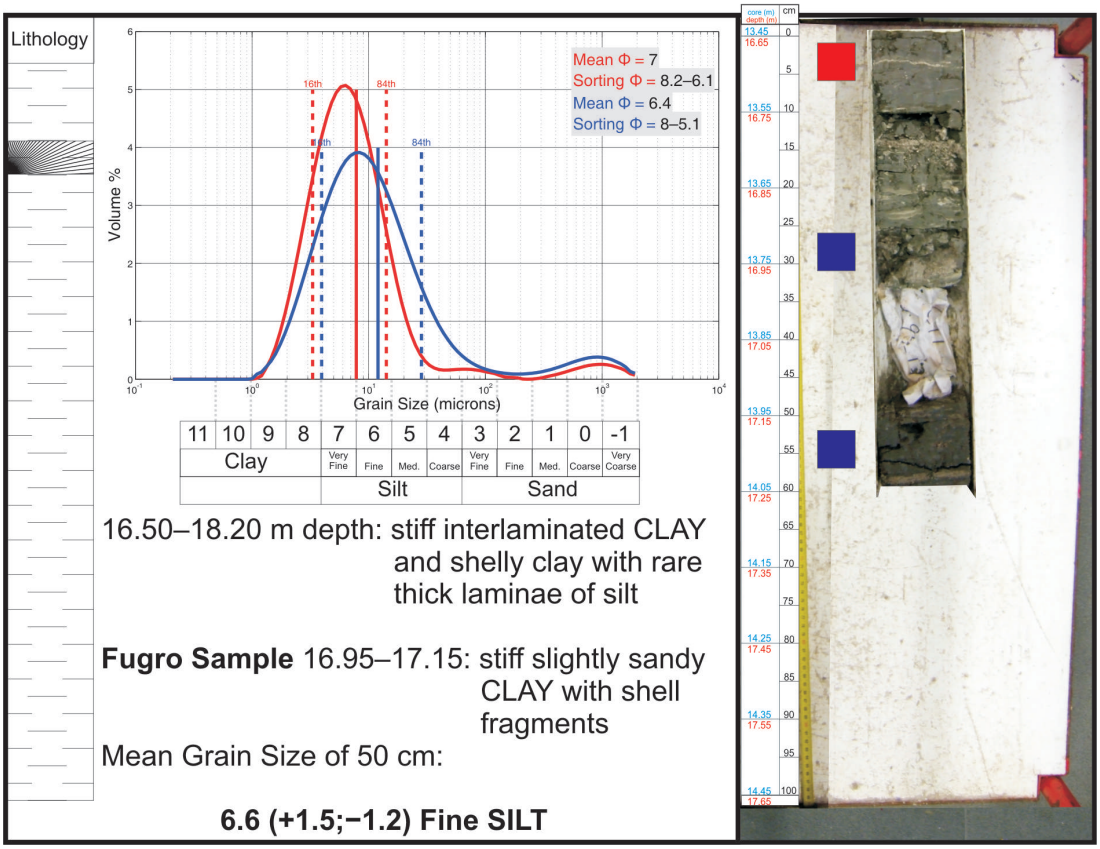

Figure A.12: RC2 12.45–14.45 m.

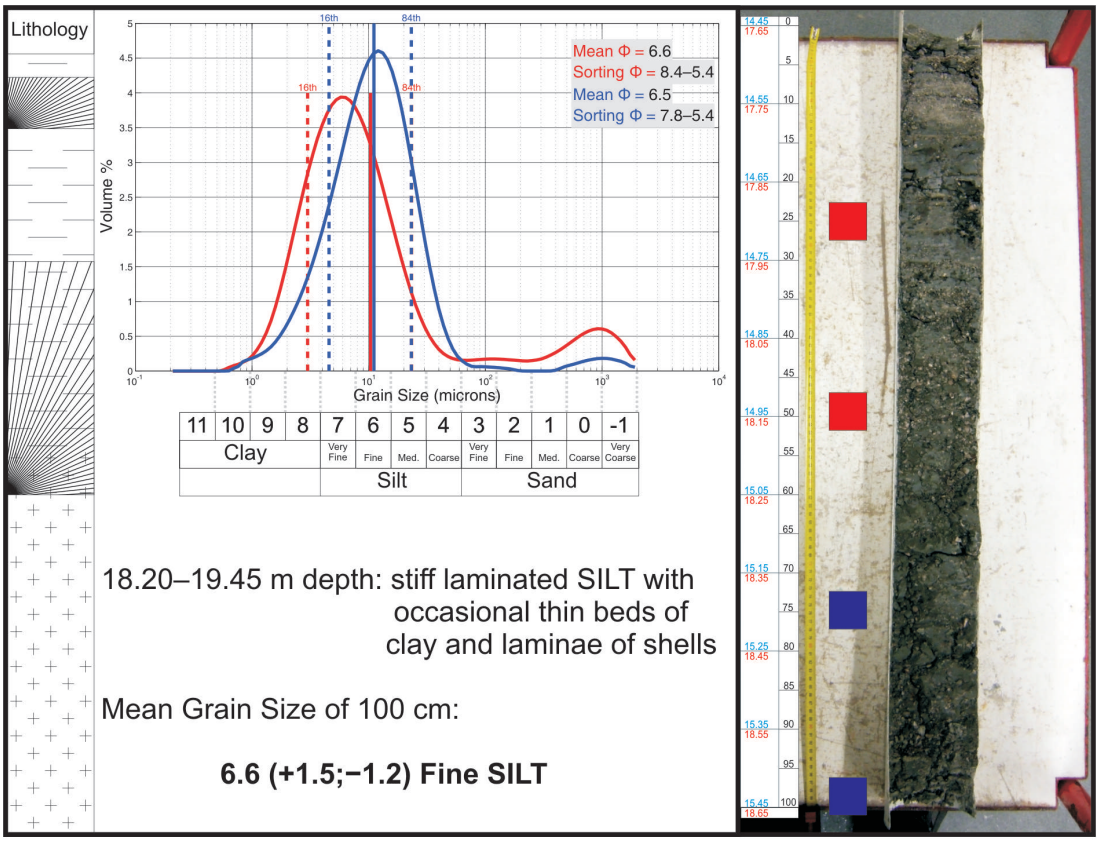

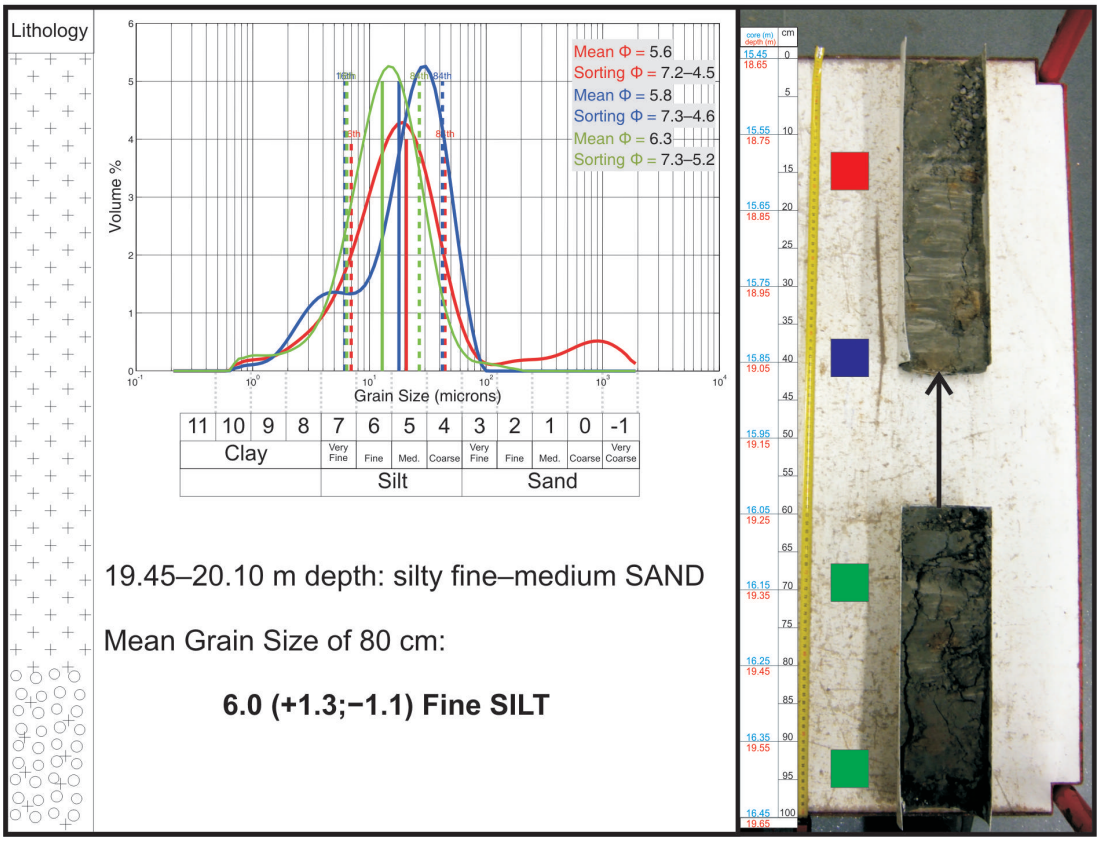

Figure A.13: RC2 14.45–16.45 m.

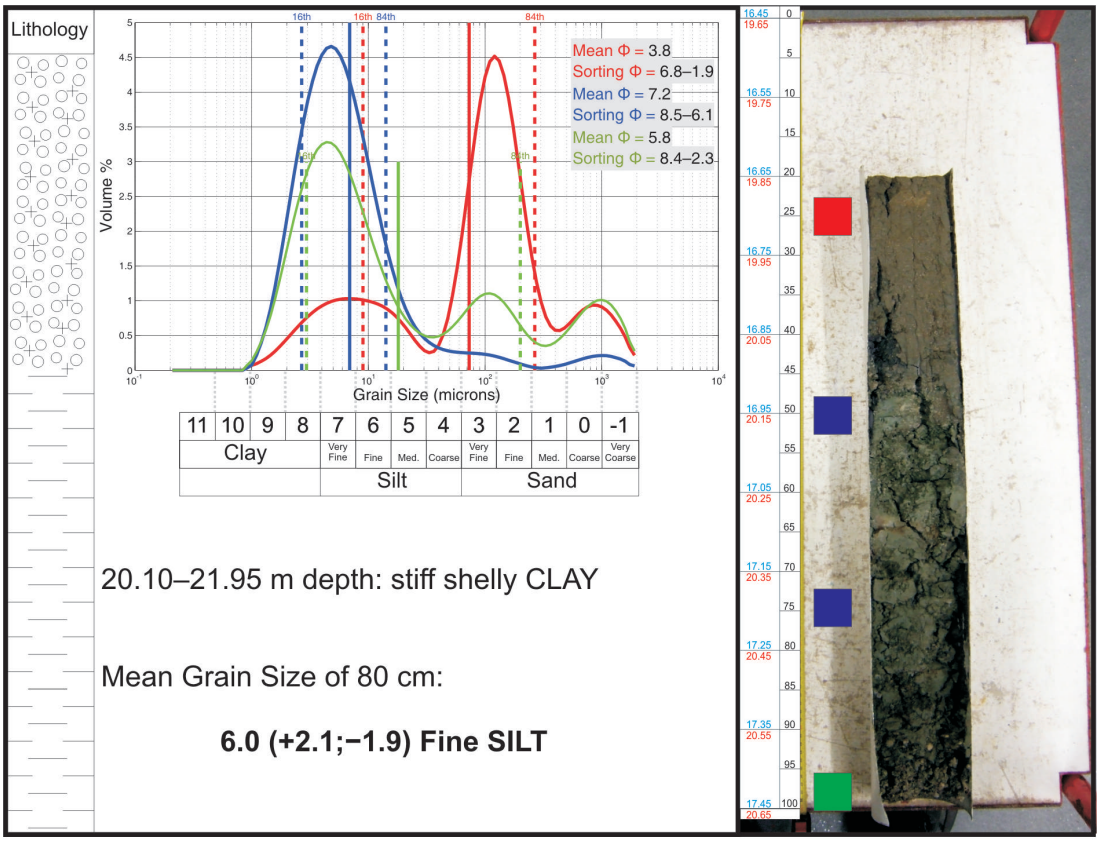

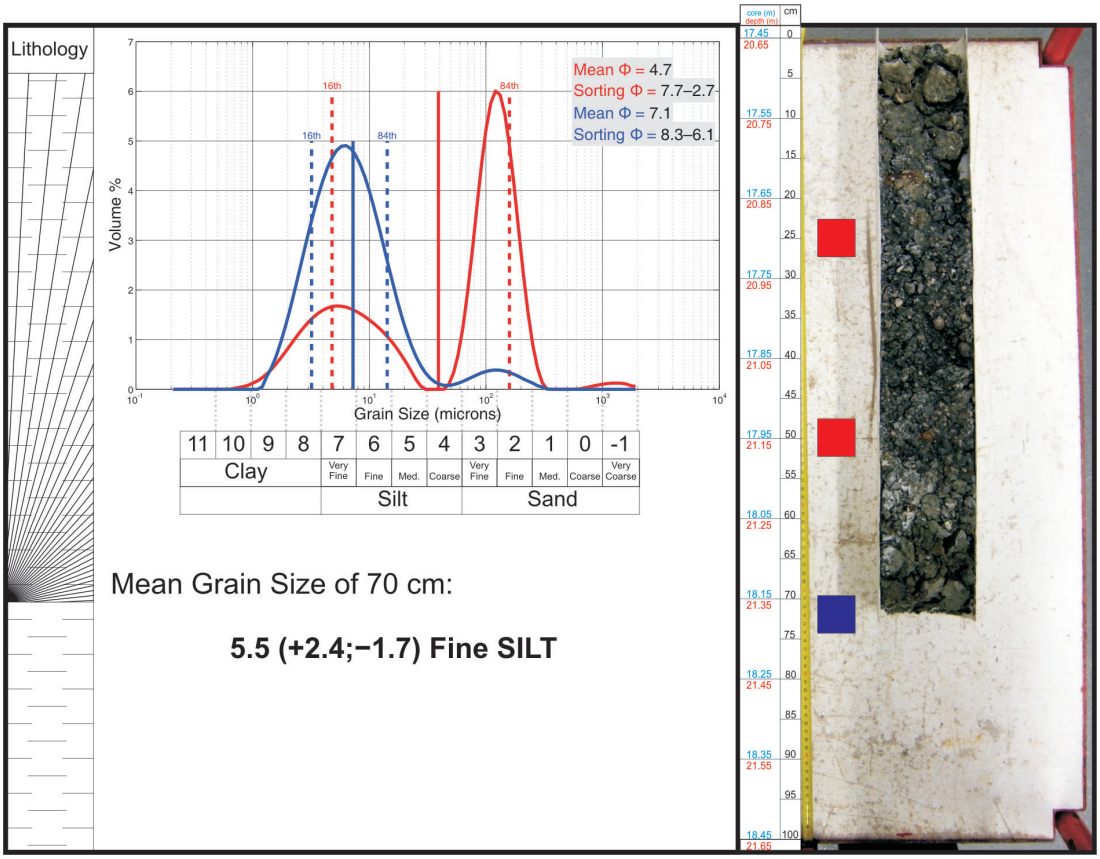

Figure A.14: RC2 16.45–18.45 m.

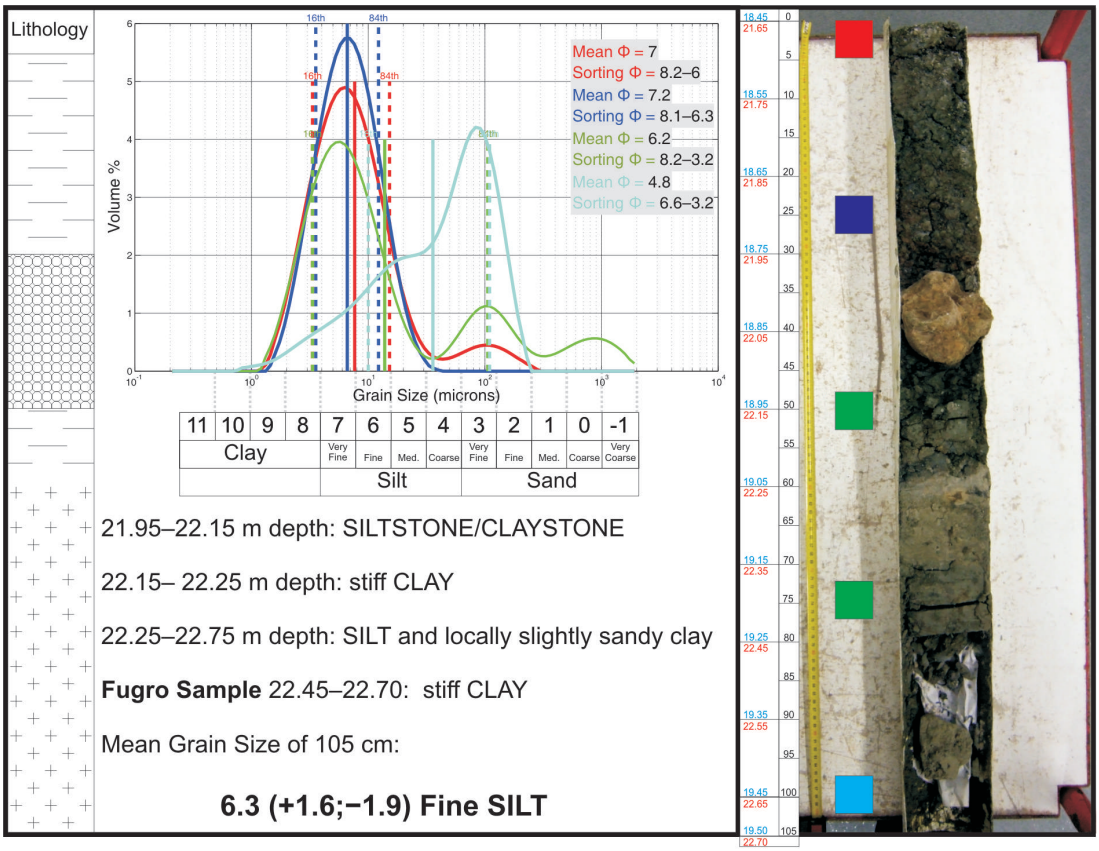

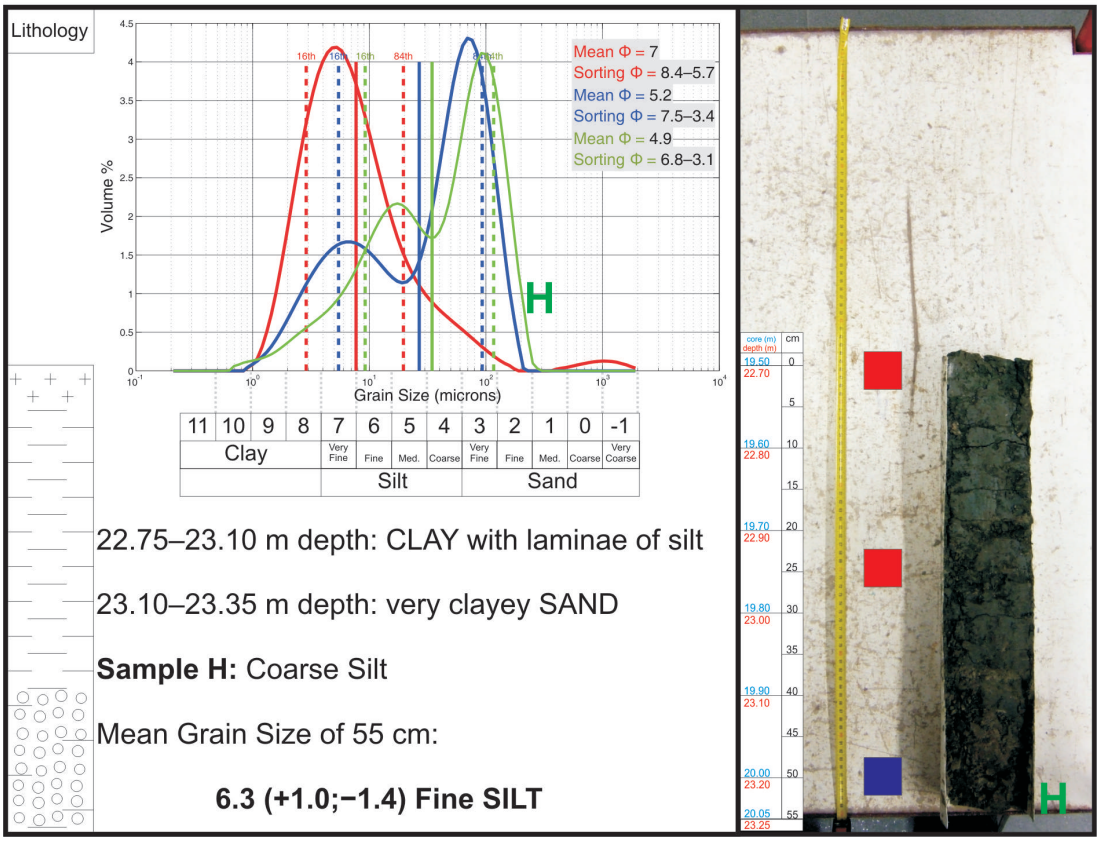

Figure A.15: RC2 18.45–20.05 m.

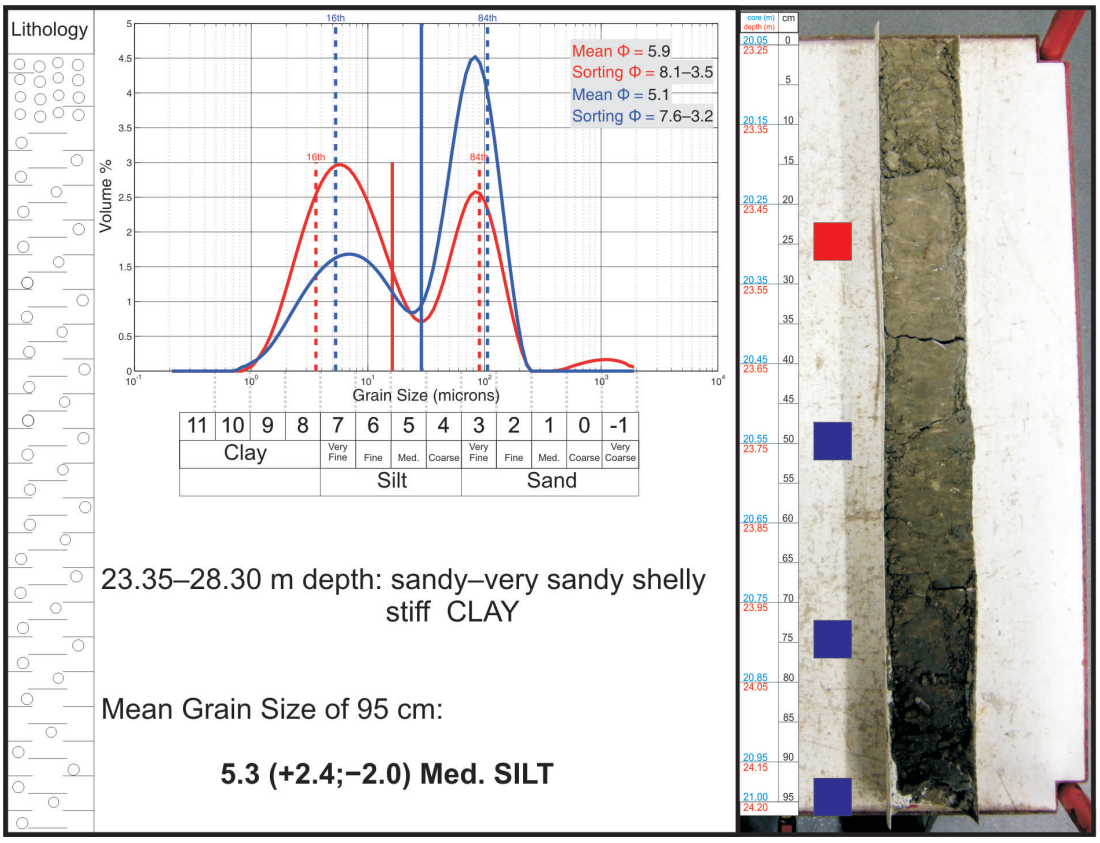

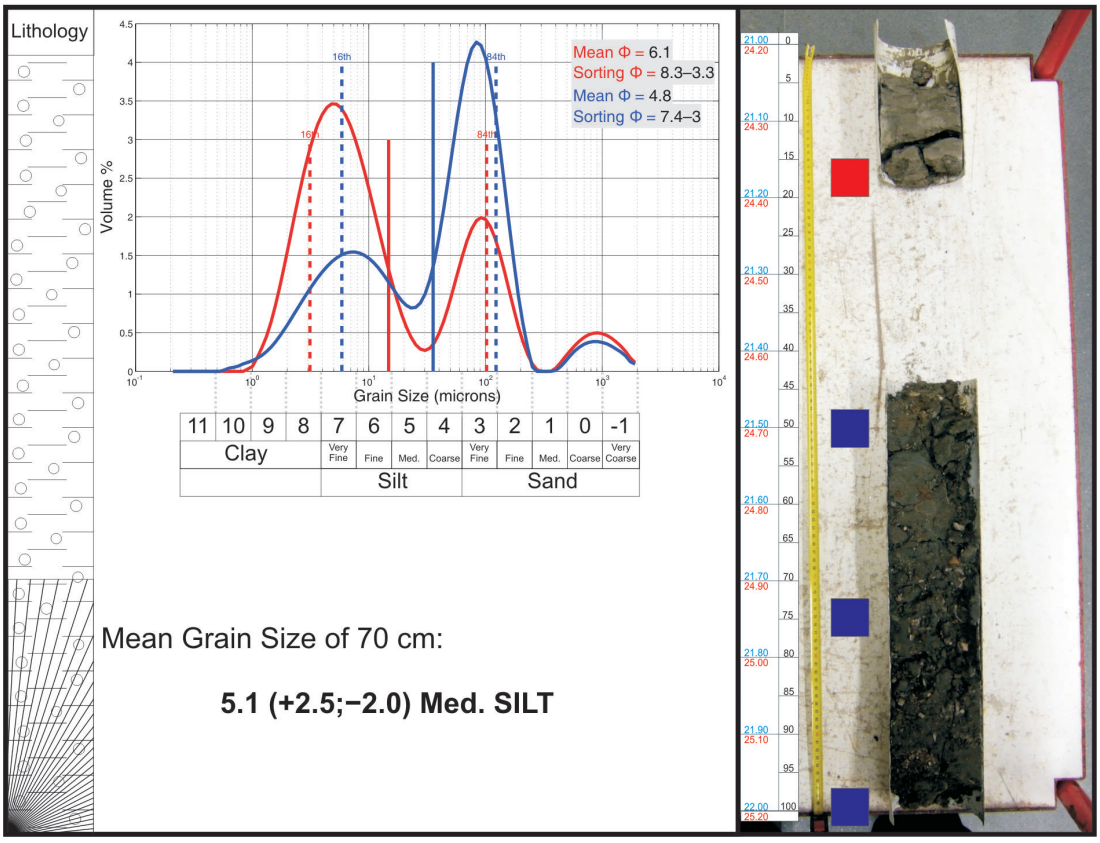

Figure A.16: RC2 20.05–22.00 m.

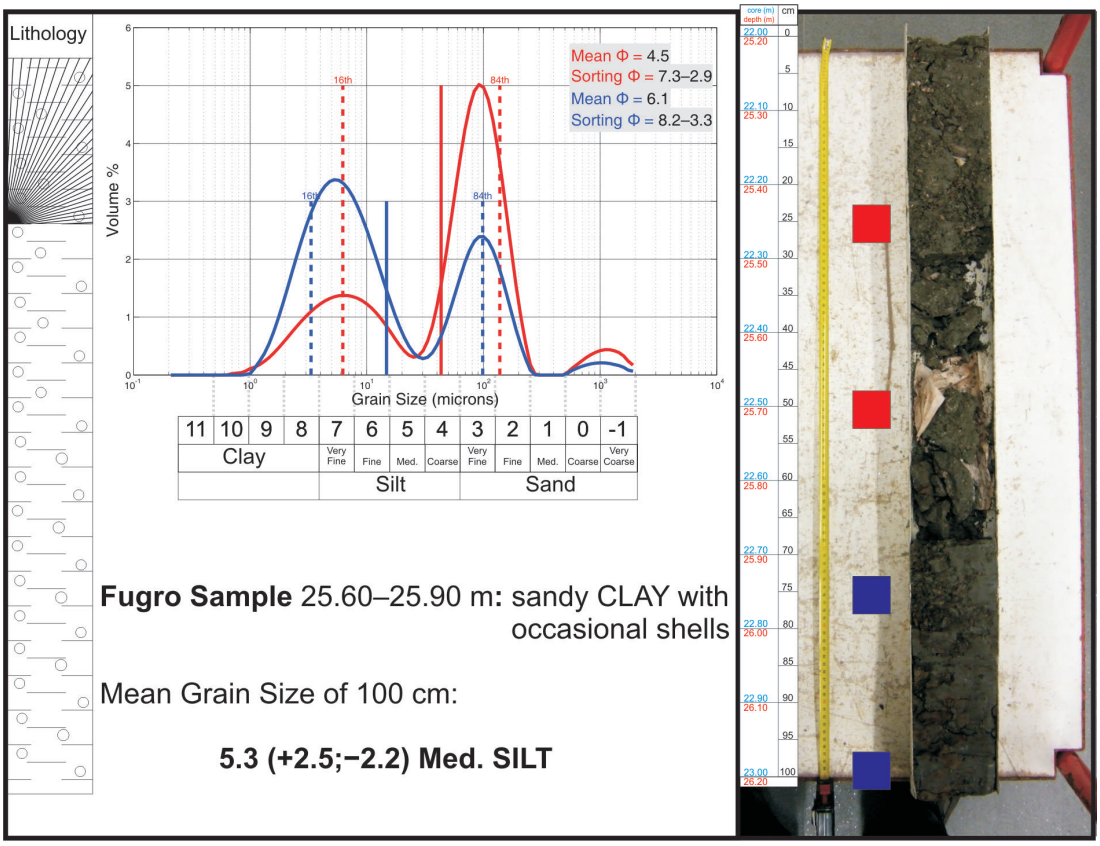

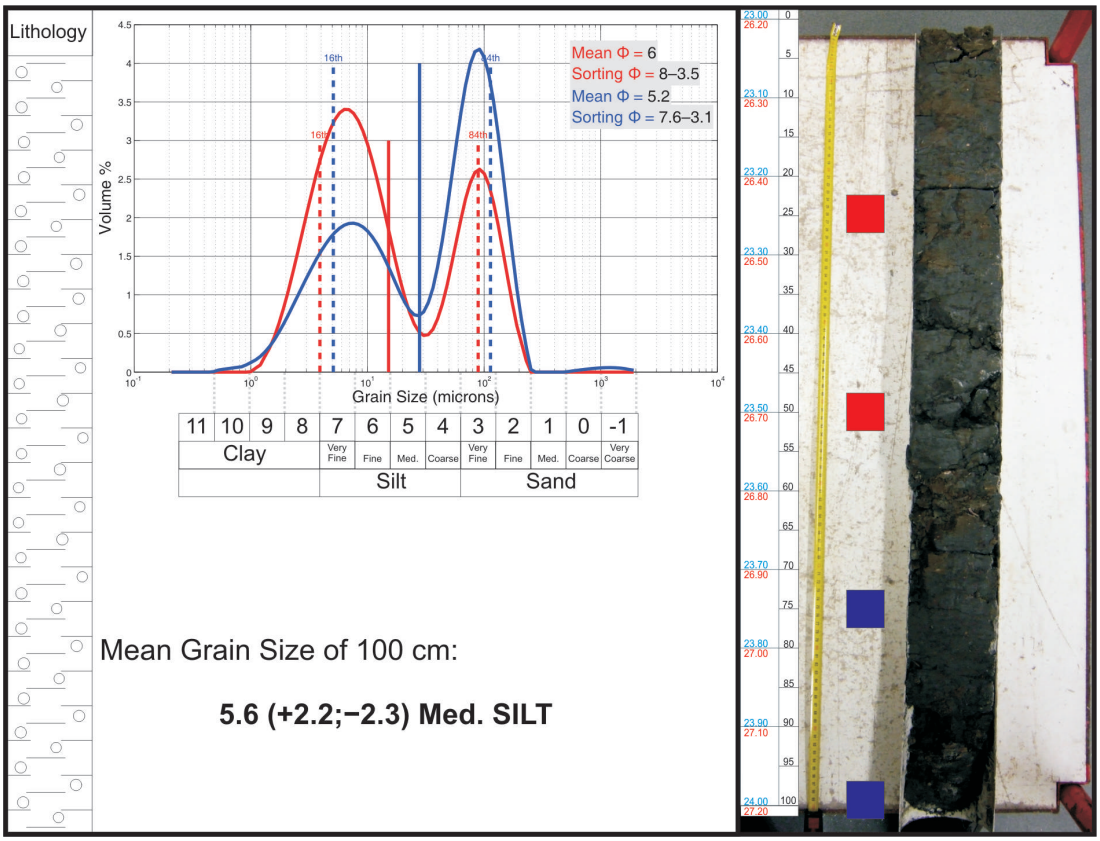

Figure A.17: RC2 22.00–24.00 m.

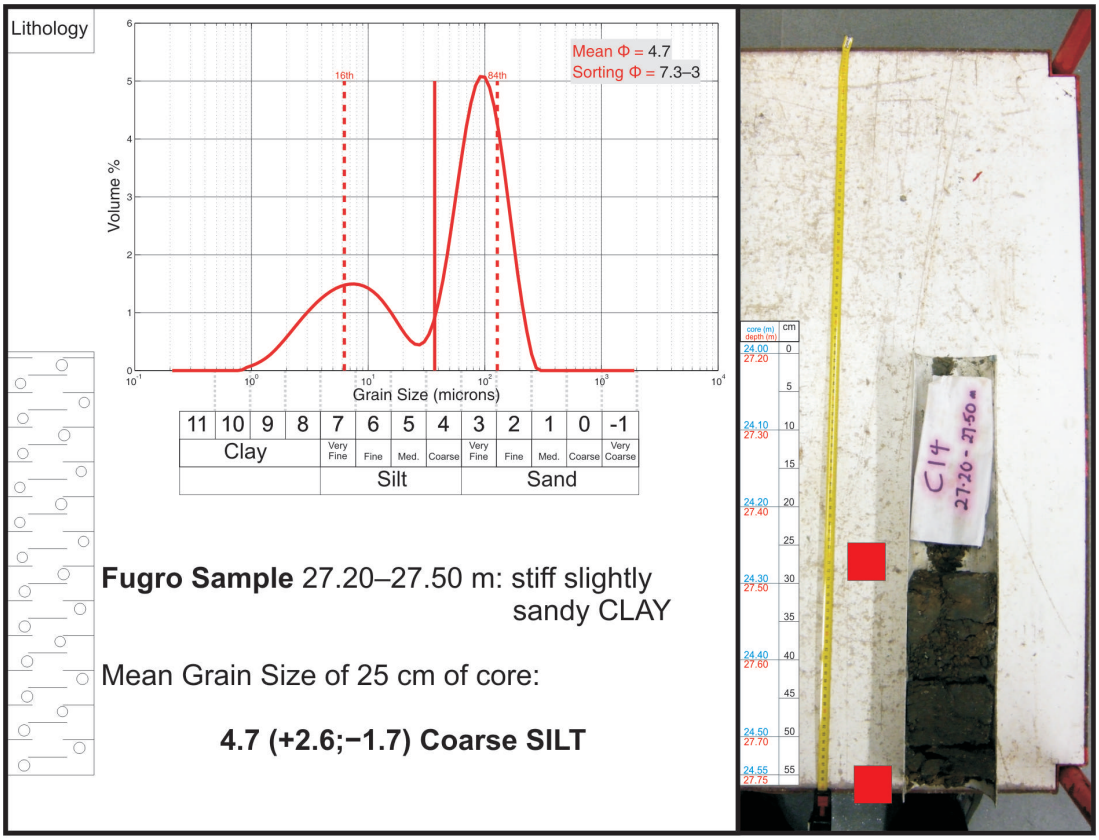

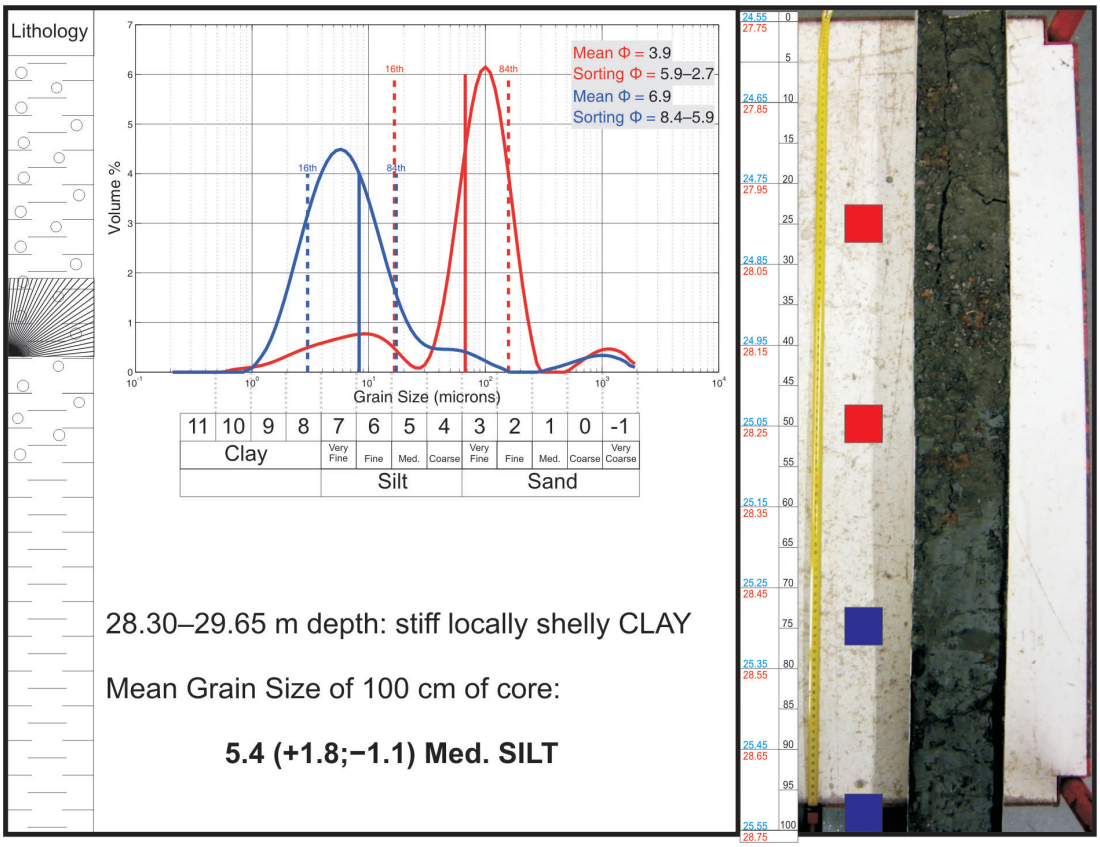

Figure A.18: RC2 24.00–25.55 m.

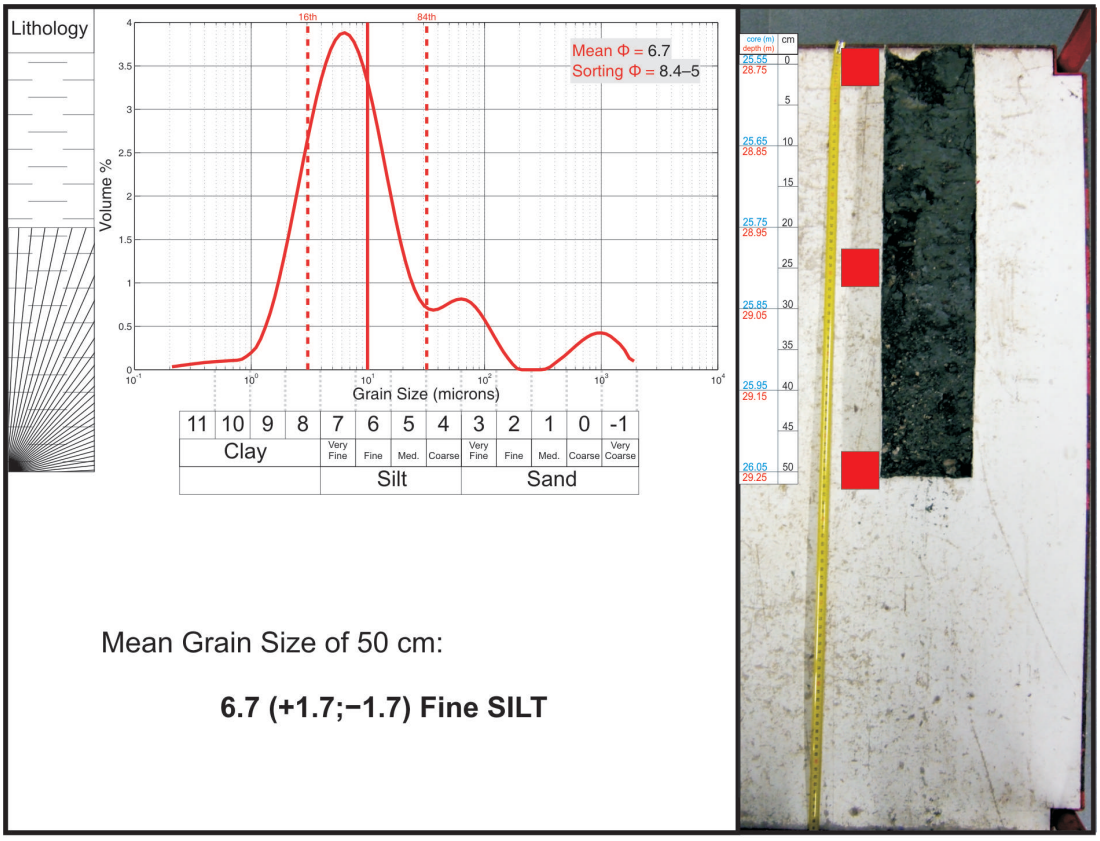

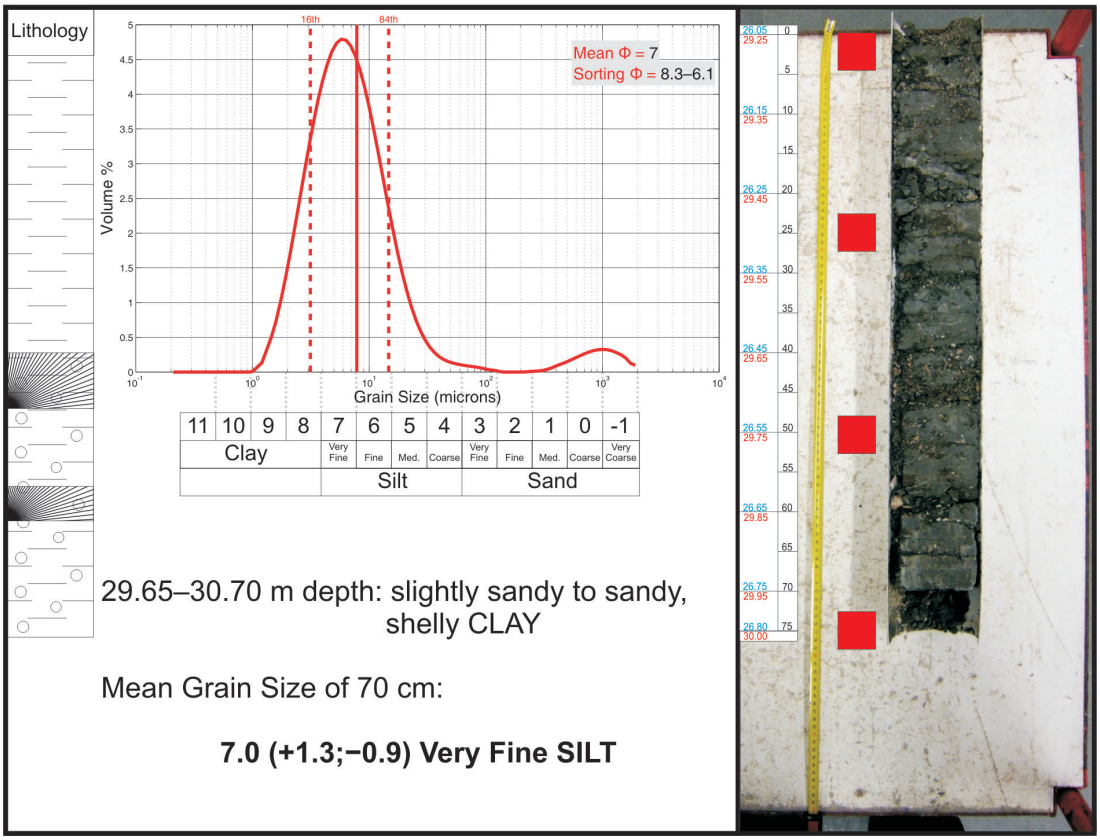

Figure A.19: RC2 25.55–26.80 m.

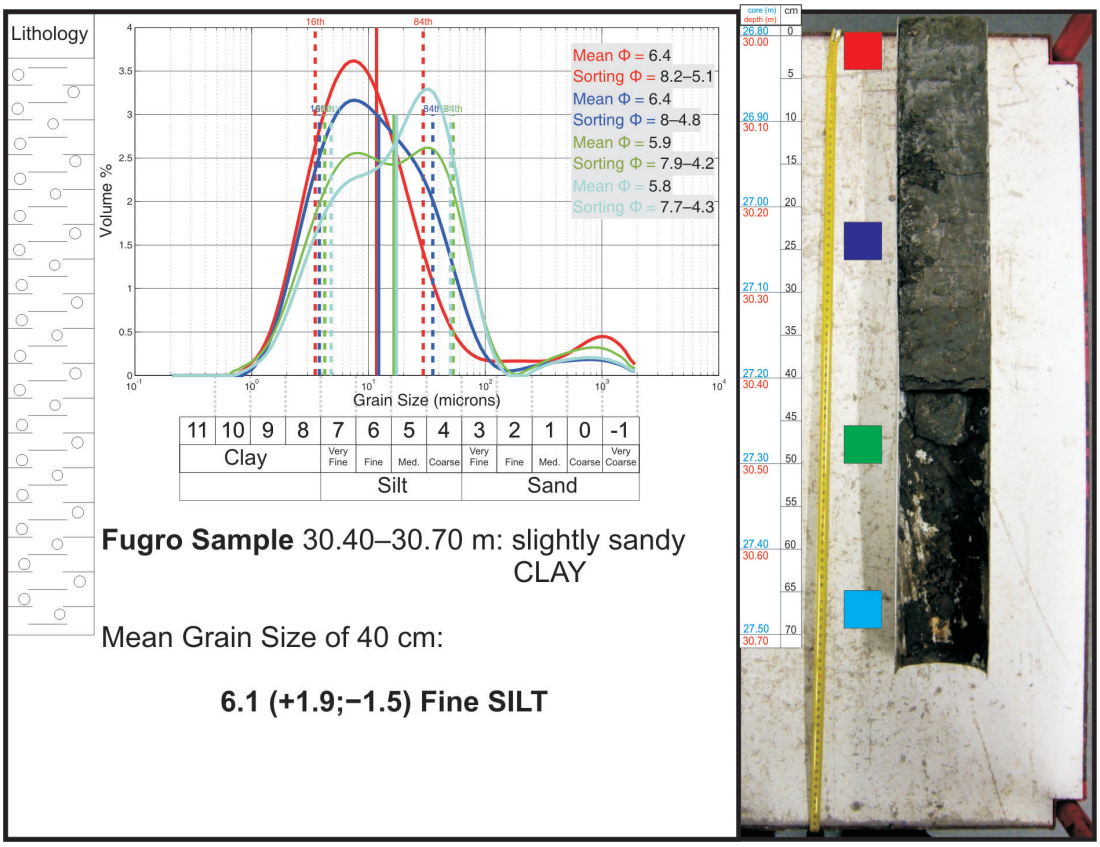

Figure A.20: RC2 26.80–27.50 m.

A.4 Appendix D: Windermere Water Velocity and Thermocline

Windermere undergoes isothermal cooling during the winter, and isothermal warming (surface warming with complete mixing) during April and May. Into the summer it becomes stratified with the development of a temperature gradient, which can occasionally become a sharp thermocline around September (Jenkin, 1942; Pugh, 1977). Diagrams from Jenkin (1942); Reynolds et al. (1982); Winfield and Sweeting (2007), have been reproduced in Figure A.21 for discussion on the fresh water velocity in Windermere during the MCS survey in September. The most recent data from 2002 (Figure A.21a) shows the temperature in the South Basin decreasing from 15–18° C at the surface, to 6–9° C below 25 m. The better resolved data from the South Basin in 1979–1980 (Figure A.21b) supports a temperature of 15–16° C at the surface and shows a more precise range of 7–8° C below 20 m. Finally, Figure A.21c shows a maximum surface temperature of 15–16° C in the North Basin, with also a bottom water of 7–8° C below 25 m. Overall, Figure A.21 shows that September has been, and still is, the last month where there is temperature stratification in Windermere.

September marks the beginning of the autumn overturn (Jenkin, 1942): calm weather during the summer produces a high surface temperature and an even gradient to the top of the hypolimnion, c. 25 m in the South Basin (Figure A.21a), and c. 20 m in the North Basin (Figure A.21c); wind mixing and surface cooling at night during September, with consequent convection, produces an isothermal epilimnion with a sharper discontinuity above the hypolimnion, possibly amounting to a thermocline c. 20 m in the South Basin (Figure A.21a and b), and c. 10 m in the North Basin (Figure A.21c). Jenkin (1942) explains that surface cooling and wind mixing forces the warm waters of the epilimnion downwards to c. 25 m (evident in Figure A.21b), which eventually brings Windermere back to an isothermal state by November.

The shallowness of the South Basin relative to the North Basin (mean depths 17.7 m and 26.0 m respectively: Mortimer and Worthington, 1942), allows stratification to establish sooner and become more marked, and through greater warming of the hypolimnion during the spring, the hypolimnion in the South Basin is warmer by at least 1° C (Jenkin, 1942). Figure A.22 supports this, and shows that during 1967–1968 the hypolimnion in the South Basin was 2° C warmer than in the North Basin; Figure A.22 also shows a fluctuation of 1° C in the hypolimnion in the same months, from year to year.

Thus, during September the water column is in a transitional state, with a potential thermocline. Ullyott and Holmes (1936) showed that the stratification of upper waters in Windermere change with a few days of wind from a calm-weather condition, with an even temperature gradient from 0–17 m, to an epilimnion of uniform temperature from 0–13 m, and a thermocline at 13–15 m. The topography around Windermere affords shelter to some locations, leaves others exposed, and possibly focuses wind action elsewhere too. Therefore, a single average water temperature (and seismic velocity) does not exist at this time of year, and will be dependent upon the depth to the lakebed, the wind conditions, the basin, and the conditions over night. A description of water column conditions with depth, on the 31st August 1932 from Jenkin (1942), illustrates this non-uniformity of the fresh water temperature structure across the lake, which the MCS survey may have encountered on a single day: In the South Basin there was an isothermal epilimnion at 17.3° C at 0–10 m, and a temperature gradient of 0.85° C/m between 10–20 m above the hypolimnion, which reached a few metres lower than that present in the North Basin at the time.

Using the evidence available, and assuming a fresh water density of 1000 kg/m^3 that does not vary with depth, expected water velocities are derived using the Belogol'skii et al. (1999) speed of sound as a function of temperature and pressure in distilled water:

From Table A.1 surface water velocities of 1466–1476 m/s are predicted. This is in agreement with the velocities determined from the direct arrival: 1465 m/s in

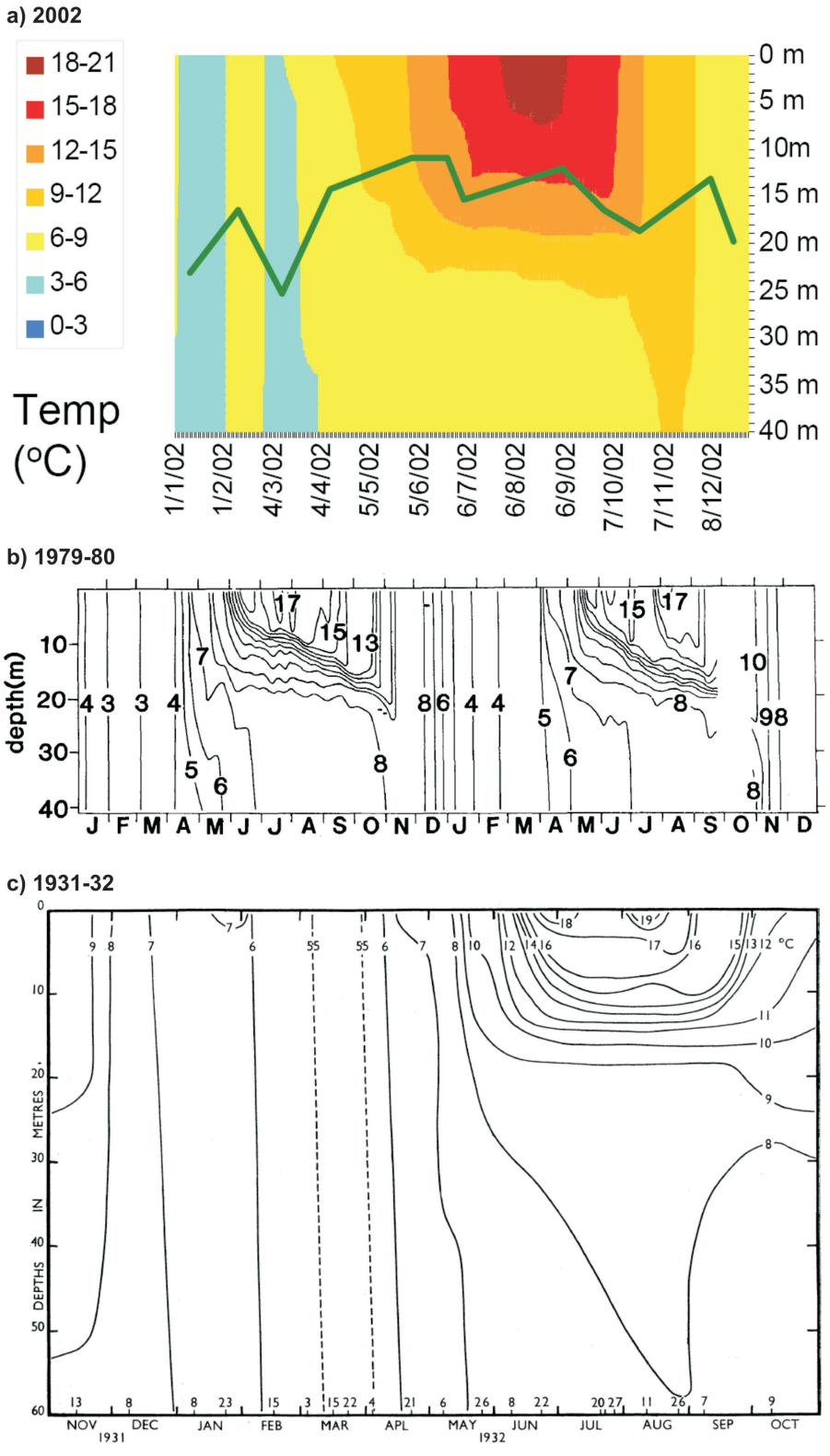

Figure A.21: Published temperature vs. depth profiles from Windermere: a) South Basin 2002 (ignore green line) (Winfield and Sweeting, 2007); b) South Basin 1979–1980 (Reynolds et al., 1982); c) North Basin 1931–1932 (Jenkin, 1942).

Basin	Temp. °C	Pressure MPa (Depth m)	Velocity (m/s)
South Basin	18	0.100 (0 m)	1476
	16	0.100 (0 m)	1469
	9	0.245 (25 m)	1443
	9	0.392 (40 m)	1443
	8	0.245 (25 m)	1439
	8	0.392 (40 m)	1440
	7	0.245 (25 m)	1435
	7	0.392 (40 m)	1435
North Basin	15	0.100 (0 m)	1466
	8	0.588 (60 m)	1440
	7	0.588 (60 m)	1436

Table A.1: Predicted fresh water sound velocities in Windermere for September.

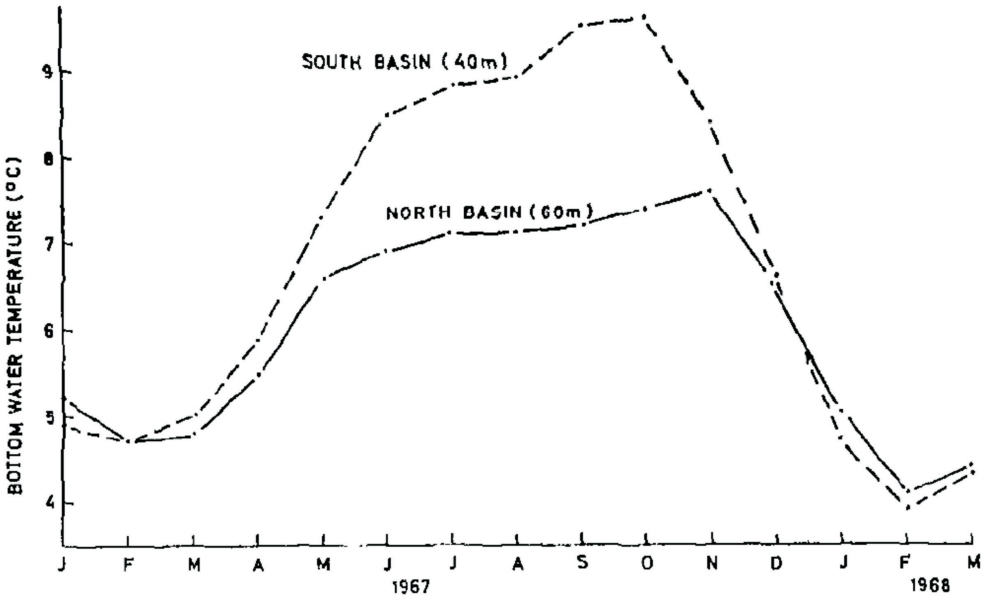

Figure A.22: Published temperature profile from Windermere: South and North Basin bottom water 1967–1968 (Pugh, 1977).

the North Basin and 1470 m/s in the South Basin. Below 25 m the velocities reduce and are between 1435–1443 m/s for temperatures 7–9° C. The additional pressure exerted at depths 40 m and 60 m has insignificant effects on the velocity; fluctuations in the sound velocity are dominated by changes in temperature with depth. Hence, in water depths greater than 25 m, average water velocities of around 1450 m/s are expected, and given the likelihood of a warmer epilimnion and hypolimnion in the South Basin, slightly faster average water velocities are expected here relative to the North Basin.

Bibliography

Red numerals and numbers after references link to pages in this thesis.

Akal, T., 1972, The relationship between the physical properties of underwater sediments that affect bottom reflection: Marine Geology, **17**, 251–266. 12, 61

Alley, R. B., 2000, The Younger Dryas cold interval as viewed from central Greenland: Quaternary Science Reviews, **19**, 213–226. 194

Belogol'skii, V. A., S. S. Sekoyan, L. M. Samorukova, S. R. Stefanov, and V. I. Levtsov, 1999, Pressure dependence of the sound velocity in distilled water: Measurement Techniques, **42**, 406–413. 233

Berryman, J. G., 1980, Confirmation of Biot's theory: Applied Physics Letters, **37**, 382–384. 16

Best, A. I., Q. J. Huggett, and A. J. K. Harris, 2001, Comparison of *in situ* and laboratory acoustic measurements on Lough Hyne marine sediments: Journal of the Acoustical Society of America, **110**, 695–708. 14, 15

BGS, 1996, England and Wales sheet 38, Ambleside, Solid Geology: 1:50 000 Series, **21**. 120, 121, 155

Biot, M. A., 1956a, Theory of propagation of elastic waves in a fluid-saturated porous solid. I. Low-frequency range: Journal of the Acoustical Society of America, **28**, 168–178. 8, 19

———, 1956b, Theory of propagation of elastic waves in a fluid-saturated porous solid. II. Higher frequency range: Journal of the Acoustical Society of America, **28**, 179–191. 8, 19

Boulton, G. S., 1972, Modern Arctic glaciers as depositional models for former ice sheets: Journal of the Geological Society, **128**, 361–339. 153

———, 1977, A multiple till sequence formed by a late Devensian Welsh ice cap: Glanllynnau, Gwynedd: Cambria, **4**, 10–31. 116

———, 1986, Push-moraines and glacier contact fans in marine and terrestrial environments: Sedimentology, **33**, 677–698. 159, 160, 176

Bowen, D. Q., F. M. Phillips, A. M. McCabe, P. C. Knutz, and G. A. Sykes, 2002, New data for the Last Glacial Maximum in Great Britain and Ireland:

Quaternary Science Reviews, **21**, 89–101. 116, 117, 118, 194, 195

Bowles, F. A., 1997, Observations on attenuation and shear-wave velocity in fine-grained, marine sediments: Journal of the Acoustical Society of America, **101**, 3385–3396. 9, 10, 39

Bradwell, T., M. S. Stoker, N. R. Golledge, C. K. Wilson, J. W. Merritt, D. Long, J. D. Everest, O. B. Hestvik, A. G. Stevenson, A. L. Hubbard, A. G. Finlayson, and H. E. Mathers, 2008, The northern sector of the last British Ice Sheet: Maximum extent and demise: Earth-Science Reviews, **88**, 207–226. 2, 118, 160, 208

Båth, M., 1974, Spectral analysis in geophysics: *In* Developments in Solid Earth Geophysics, Elsevier, Amsterdam, 415. 19, 21

Brodie, J., D. M. John, I. Tittley, M. J. Holmes, and D. B. Williamson, 2007, Important Plant Areas for algae: a provisional review of sites and areas of importance for algae in the United Kingdom: Plantlife International, Salisbury, UK. 69

Buchan, S., D. M. McCann, and D. T. Smith, 1972, Relations between the acoustic and geotechnical properties of marine sediments: Quarterly Journal of Engineering Geology and Hydrogeology, **5**, 265–284. 11, 12

Buchanan, J., 2006, A comparison of broadband models for sand sediments: Journal of the Acoustical Society of America, **120**, 3584–3598. 7, 8

Buckingham, M. J., 2000, Wave propagation, stress relaxation, and grain-to-grain shearing in saturated, unconsolidated marine sediments: Journal of the Acoustical Society of America, **108**, 2796–2815. 1, 9, 10, 16, 39

———, 2005, Compressional and shear wave properties of marine sediments: Comparisons between theory and data: Journal of the Acoustical Society of America, **117**, 137–152. 16

———, 2008, The Viscous-Grain-Shearing (VGS) theory of wave propagation in marine sediments: Journal of the Acoustical Society of America, **123**, 3440–3440. 9

Bull, J. M., R. Quinn, and J. K. Dix, 1998, Reflection coefficient calculation from marine high resolution seismic reflection (Chirp) data and application to an archaeological case study: Marine Geophysical Researches, **20**, 1–11. 24, 67

Burrascano, P. and P. Lucci, 1989, Efficient esitimation of the prediction distance

in high resolution seismic marine prospecting: Melecon'89: Proceedings of the Mediterranean Electrotechnical Conference, 157–169. 100

Chotiros, N. P. and M. J. Isakson, 2004, A broadband model of sandy ocean sediments: Biot-Stoll with contact squirt flow and shear drag: Journal of the Acoustical Society of America, **116**, 2011–2022. 8

———, 2008, High-frequency dispersion from viscous drag at the grain-grain contact in water-saturated sand: Journal of the Acoustical Society of America, **124**, EL296. 9

Clark, M., 1976, Evidence for rapid destruction of latest Pleistocene glaciers of the Sierra Nevada, California: Geological Society of America, Abstract Prog. 8, 361–362. 172

Coope, G. R., 1977, Fossil coleopteran assemblages as sensitive indicators of climate changes during the Devensian (Last) cold stage: Philosophical Transactions of the Royal Society of London B., **280**, 313–340. 118, 192, 193

Coster, H. P. and J. A. F. Gerrard, 1947, A seismic investigation on the outflow of Windermere: Geological Magazine, **84**, 224–228. 72, 123

Dann, R., M. Close, M. Flintoft, R. Hector, H. Barlow, S. Thomas, and G. Francis, 2009, Characterization and Estimation of Hydraulic Properties in an Alluvial Gravel Vadose Zone: Vadose Zone Journal, **8**, 651–663. 61

Davis, B. A. S., S. Brewer, A. C. Stevenson, and J. Guiot, 2003, The temperature of Europe during the Holocene reconstructed from pollen data: Quaternary Science Reviews, **22**, 1701–1716. 194

Dean, J. M., 1995, Holocene paleo-environmental reconstruction for the nearshore Newtown area, Isle of Wight: Third year honours Research Project, Southampton University. 26

Dix, J. K. and R. W. Duck, 2000, A high-resolution seismic stratigraphy from a Scottish sea 533 loch and its implications for Loch Lomond Stadial deglaciation: Journal of Quaternary Science, **15**, 645–656. 159, 160

Dvorkin, J. and A. Nur, 1993, Dynamic poroelasticity: A unified model with the squirt and the Biot mechanisms: Geophysics, **58**, 524–533. 8

Easterbrook, D. J., 1999, Surface Processes and Landforms: Prentice Hall Publish-

ing Company, 546. 163

Evans, I. S. and N. J. Cox, 1995, The form of glacial cirques in the English Lake District, Cumbria: Zeitschrift fur Geomorphologie, **39**, 175–202. 118

Eyles, N., 1983a, Glacial Geology: A Landsystems Approach: *In* Glacial Geology, An Introduction for Engineers and Earth Scientists, Ed. N. Eyles, Pergamon Press Ltd. 116, 162

———, 1983b, The Glaciated Valley Landsystem: *In* Glacial Geology, An Introduction for Engineers and Earth Scientists, Ed. N. Eyles, Pergamon Press Ltd. 116, 122, 123, 157, 158, 162

Eyles, N., W. R. Dearman, and T. D. Douglas, 1983, The Distribution of Glacial Landsystems in Britain and North America: *In* Glacial Geology, An Introduction for Engineers and Earth Scientists, Ed. N. Eyles, Pergamon Press Ltd. 116

Eyles, N. and B. K. J. I. Boyce, J. D. Halfman, 2000, Seismic stratigraphy of Waterton Lake, a sediment-starved glaciated basin in the Rocky Mountains of Alberta, Canada and Montana, USA: Sediment Geology, **130**, 283–311. 69

Eyles, N. and J. Menzies, 1983, The Subglacial Landsystem: *In* Glacial Geology, An Introduction for Engineers and Earth Scientists, Ed. N. Eyles, Pergamon Press Ltd. 154

Eyles, N. and H. T. Mullins, 1997, Seismic-stratigraphy of Shuswap Lake, British Columbia, Canada: Sediment Geology, **109**, 283–303. xix, 69

Finckh, P., K. Kelts, and A. Lambert, 1984, Seismic stratigraphy and bedrock forms in perialpine lakes: Geological Society of America Bulletin, **95**, 1118–1128. 179, 200

Finlayson, A., T. Bradwell, N. Golledge, and J. Merritt, 2007, Morphology and Significance of Transverse Ridges (De Geer Moraines) Adjacent to the Moray Firth, NE Scotland: Scottish Geographical Journal, **123**, 257–270. 160

Flint, R. F., 1971, Glacial and Quaternary Geology: Pub. John Wiley and Sons, New York. 168

Folk, R. L. and W. C. Ward, 1957, Brazos river bar: a study of significant of grain size parameters: Journal of Sedimentary Petrology, **27**, 3–26. 47

Fox, J., 1997, Applied Regression Analysis, Linear Models, and Related Methods:

Sage Publications. 30, 210

Geer, G. D., 1889, Andmoranerna i trakten mellan Spanga och Sundbyberg: Geologiska Foreningens i Stockholm Forhandlingar, **11**, 395–396. 159

Golledge, N. and E. Phillips, 2008, Sedimentology and architecture of De Geer moraines in the western Scottish Highlands, and implications for grounding-line glacier dynamics: Sedimentary Geology, **208**, 1–14. 159, 160

Google Earth, 2009, TerraMetrics image from Google Earth: Available at http://earth.google.com/. 168

Guigné, J. Y., N. G. Pace, and V. H. Chin, 1989, Dynamic extraction of sediment attenuation from subbottom acoustic data: Journal of Geophysical Research, **94**, 5745–5755. 23

Gutowski, M., J. Bull, T. Henstock, J. Dix, P. Hogarth, T. Leighton, and P. White, 2002, Chirp sub-bottom profiler source signature design and field testing: Marine Geophysical Researches, **23**, 481–492. 24, 44, 79

Hamilton, E., 1972, Compressional wave attenuation in marine sediments: Geophysics, **37**, 620–646. 6, 9, 13, 16, 23, 39, 40, 203

———, 1980, Geoacoustic modelling of the sea floor: Journal of the Acoustics Society of America, **68**, 1313–1340. 61, 62, 63, 164

Hamilton, E. and R. Bachman, 1982, Sound velocity and related properties of marine sediments: Journal of the Acoustical Society of America, **72**, 1891–1904. 1, 11, 12, 42, 61, 62, 63, 66, 206

Heim, C. and P. Finckh, 1984, Sonic velocity measurements on cores from Zubo: Contributions to Sedimentology, **13**, 125–134. 69, 178, 179, 200

Hollingworth, S. E., 1951, The influence of glaciation on the topography of the Lake District: Journal of the Institution of Water Engineers, **5**, 485–496. 73, 118, 123, 162, 165, 167, 169

Holmes, P. W., 1964, Sediment studies in the North Basin: PhD Thesis, University of London. 69, 72, 76, 119, 154, 161, 165, 180, 185, 189

Hosken, J. W. J., S. K. Mayo, and A. T. Walden, 1992, The influence of reflection coefficient statistics on the seismic method: scattering attenuation and transmission wavelets: *Proceedings:* Mathematical and Physical Sciences, **439**, 1–23.

19

Howell, F. T., 1971, A continuous seismic profile survey of Windermere: Geological Journal, **7**, 329–334. 69, 73

Jackson, D. R. and M. D. Richardson, 2007, High-frequency seafloor acoustics: *Pub.* Springer, 125–134. 11, 12, 206

Jannsen, D., J. Voss, and F. Theilen, 1985, Comparison to determine Q in shallow marine sediments from vertical reflection seismograms: Geophysical Prospecting, **33**, 479–497. 21

Jenkin, B. M., C. H. Mortimer, and W. Pennington, 1941, The Study of Lake Deposits: Nature, **147**, 496–500. 72

Jenkin, P. M., 1942, Seasonal Changes in the Temperature of Windermere (English Lake District): The Journal of Animal Ecology, **11**, 248–269. 69, 232, 233, 234

Jouzel, J., V. Masson-Delmotte, O. Cattani, G. Dreyfus, S. Falourd, G. Hoffmann, B. Minster, J. Nouet, J. M. Barnola, J. Chappellaz, H. Fischer, J. C. Gallet, S. Johnsen, M. Leuenberger, L. Loulergue, D. Luethi, H. Oerter, F. Parrenin, G. Raisbeck, D. Raynaud, A. Schilt, J. Schwander, E. Selmo, R. Souchez, R. Spahni, B. Stauffer, J. P. Steffensen, B. Stenni, T. F. Stocker, J. L. Tison, M. Werner, and E. W. Wolff, 2007, Orbital and Millennial Antarctic Climate Variability over the Past 800,000 Years: Science, **307**, 793–796. 194

Jurkevics, A. and R. Wiggins, 1984, A critique of seismic deconvolution methods: Geophysics, **49**, 2109–2116. 100

Kaye, G. W. C. and T. H. Laby, 1966, Tables of Physical and Chemical Constants. 13th Edition, Longman. 73

Kibblewhite, A. C., 1989, Attenuation of sound in marine sediments: A review with emphasis on new low-frequency data: Journal of the Acoustical Society of America, **86**, 716–738. 1, 203

Kim, G. Y., 2009, Physical and geoacoustic properties of surface sediments off eastern Geoje Island, South Sea of Korea: Quaternary International, **68**, 1313–1340. 61

Kneller, B. C. and A. M. Bell, 1993, An Acadian mountain front in the English Lake District: the Westmorland Monocline: Geological Magazine, **130**, 203–213.

121, 122

Knight, D. J., 1977, Morecambe Bay feasibility study—subsurface investigations: Quarterly Journal of Engineering Geology, **10**, 303–319. 154

Kragh, E. and L. Combee, 2000, Using a seismic reflector for resolving streamer depth and sea surface profiles: First Break, **18**, 463–467. 90

Krumbein, W. C. and F. J. Pettijohn, 1938, Manual of sedimentary petrography: Appleton Century Co., New York. 47, 214

Lario, J., C. Spencer, A. J. Plater, C. Zazo, J. L. Goy, and C. J. Dabrio, 2002, Particle size characterisation of Holocene back-barrier sequences from North Atlantic coasts (SW Spain and SE England): Geomorphology, **42**, 25–42. 212

Lea, D. W., D. K. Pak, L. C. Peterson, and K. A. Hughen, 2003, Synchronicity of Tropical and High-Latitude Atlantic Temperatures over the Last Glacial Termination: Science, **301**, 1361–1364. 194

LeBlanc, L. R., S. Panda, and S. G. Schock, 1992, Sonar attenuation modelling for classification of marine sediments: Journal of the Acoustical Society of America, **91**, 116–126. 18

Lim, S. C. and L. P. Teo, 2009, Generalized Whittle/Matern random field as a model of correlated fluctuations: Journal of Physics A: Mathematical and Theoretical, **42**, 1–21. 112

Long, A., 2004, What is Wave Equation Pre-stack Depth Migration? An Overview: PESA News, **72**, 32–33. 98

Mackereth, F. J. H., 1971, On the Variation in direction of the horizontal component of remanent magnetisation in lake sediments: Earth and Planetary Science Letters, **12**, 332–338. 185, 196

Marinoni, O., 2003, Improving geological models using a combined ordinary indicator kriging approach: Engineering Geology, **69**, 37–45. 112

Marr, J. E., 1896, On the lake basins of Lakeland: Proceedings of the Geologists' Association, **14**, 273–286. 72, 119

———, 1906, PRESIDENTIAL ADDRESS: Quarterly Journal of the Geological Society of London, **62**, 654–732. 119

———, 1916, The geology of the Lake District: Cambridge. University Press, Cam-

bridge. 72

Matheney, M. P. and R. L. Nowack, 1995, Seismic attenuation values obtained from instantaneous-frequency matching and spectral ratios: Geophysical Journal International, **123**, 1–15. 39

McCann, C. and D. McCann, 1969, The attenuation of compressional waves in marine sediments: Geophysics, **34**, 882–891. 13, 41

———, 1990, The Acoustic properties of marine sediments: Underwater Technology, **16**, 23–27. 12

McCarthy, J., 2007, TS7F – Hydrographic Surveying in Practice: A day is never long enough, one hydrographic surveyors quest: Strategic Integration of Surveying Services, FIG Working Week 2007, Hong Kong SAR, China, 1–9. 74

McDougall, D. A., 2001, The geomorphological impact of Loch Lomond (Younger Dryas) Stadial plateau ice fields in the central Lake District, northwest England: Journal of Quaternary Science, **16**, 531–543. 117, 118, 194

McNamara, K. J., 1979, Using a seismic reflector for resolving streamer depth and sea surface profiles: Geological Journal, **14**, 41–68. 121

Merkus, H. G., 2009, Particle size measurements: Fundamentals, practice, quality: *Springer Publishing*, **62**. 46, 214

Mill, H. R., 1895, Bathymetrical survey of the English Lakes: The Geographical Journal, **6**, 46–73,135–166. 68, 69, 119, 133

Minasny, B. and A. B. McBratney, 2005, The Matern function as a general model for soil variograms: Geoderma, **128**, 192–207. 112

Mitchell, G. H., 1956, The geological history of the Lake District: Proceedings of the Yorkshire Geological Society, **30**, 407–463. 119

Money, M. S., 1983, Dam and Reservoir Construction in Glaciated Valleys: *In* Glacial Geology, An Introduction for Engineers and Earth Scientists, Ed. N. Eyles, Pergamon Press Ltd. 154

Mortimer, C. H. and E. B. Worthington, 1942, Morphometric data for Windermere: Journal of Animal Ecology, **11**, 245–247. 69, 233

Muller, T. M. and S. A. Shapiro, 2004, Scattering attenuation in randomly layered structures with finite lateral extent: A hybrid Q model: Geophysics, **69**, 1530–

1534. 19

O'Doherty, R. F. and N. A. Anstey, 1971, Reflections on amplitudes: Geophysical Prospecting, **19**, 430–458. 19

Østrem, G., 1975, Lower Palaeozoic lithostratigraphical classification in the English Lake District: Glaciofluvial and Glaciolacustrine Sedimentation, Ed. A. V. Jopling and B. C. McDonald: Society of Economic Paleontologists and Mineralogists special publication No. 23, 101–122. 161

Paul, M. A., 1983, The Supraglacial Landsystem: *In* Glacial Geology, An Introduction for Engineers and Earth Scientists, Ed. N. Eyles, Pergamon Press Ltd. 162

Pennington, W., 1943, Lake sediments: The bottom deposits of the North Basin of Windermere, with special reference to the diatom succession: New Phytologist, **42**, 1–27. 76, 154, 180, 184, 187, 188, 190

———, 1947, Studies of the Post-Glacial history of British Vegetation. VII. Lake Sediments: Pollen Diagrams from the Bottom Deposits of the North Basin of Windermere: Philosophical Transactions of the Royal Society of London. Series B, Biological Sciences, **233**, 137–175. 180, 183, 184, 185, 187, 189, 190, 195

———, 1953, The lake sediments of Windermere: 1–4. 184

———, 1962, Late-glacial moss records from the English Lake District. Data for the study of Post-glacial history: New Phytologist, **61**, 28–31. 184

———, 1975, A chronostratigraphic comparison of Late-Weichselian and Late-Devensian subdivisions, illustrated by two radiocarbon-dated profiles from western Britain: Boreas, **4**, 111–117. 154, 161, 165, 192, 193, 195

———, 1978, Quaternary Geology: The Geology of The Lake District, Ed. F. Moseley, Yorkshire Geological Society Occasional Publication No. 3, 207–225. 118, 180

———, 1980, Excursion A7, Quaternary vegetational history of the Lake District: 5th International Palynological Conference, Cambridge, 1–4. 119

———, 1981, Records of a lake's life in time: the sediments: Hydrobiologia, **79**, 197–219. 161, 183, 184, 185, 189, 192

———, 1991, Palaeolimnology in the English Lakes — some questions and answers

over fifty years: Hydrobiologia, **214**, 9–24. 69, 118, 184, 185, 195

Pierce, J. W. and R. R. Graus, 1981, Use and misuses of the phi-scale: Discussion: Journal of Sedimentary Petrology, **51**, 1348–1350. 47

Pieri, L., M. Bittelli, and P. R. Pisa, 2006, Laser diffraction, transmission electron microscopy and image analysis to evaluate a bimodal Gaussian model for particle size distribution in soils: Geoderma, **135**, 118–132. 214

Pugh, D. T., 1977, Geothermal gradients in British lake sediments: Limnology and Oceanography, **22**, 581–596. 232, 235

Reimer, P. J., M. G. L. Baillie, E. Bard, A. Bayliss, J. W. Beck, C. J. H. Bertrand, P. G. Blackwell, C. E. Buck, G. S. Burr, K. B. Cutler, P. E. Damon, R. L. Edwards, R. G. Fairbanks, M. Friedrich, T. P. Guilderson, A. G. Hogg, K. A. Hughen, B. Kromer, G. McCormac, S. Manning, C. B. Ramsey, R. W. Reimer, S. Remmele, J. R. Southon, M. Stuiver, S. Talamo, F. W. Taylor, J. van der Plicht, and C. E. Weyhenmeyer, 2004, IntCal04 terrestrial radiocarbon age calibration, 0 to 26 cal Kyr BP: Radiocarbon, **46**, 1029–1058. 192

Reynolds, C. S., H. R. Morison, and C. Butterwick, 1982, The sedimentary flux of phytoplankton in the south basin of Windermere: Limnology and Oceanography, **27**, 1162–1175. 232, 234

Richardson, M. and K. Briggs, 1993, On the use of acoustic impedance values to determine sediment properties. *In* Acoustic classification and mapping of the seabed: *Proceedings:* Institute of Acoustics, **15**, 15–23. xviii, 11, 42, 61, 62, 63, 64, 66, 163, 164, 188, 189, 201, 205, 206

Rothwell, R. G. and F. R. Rack, 2006, New techniques in sediment core analysis: an introduction: *In* New techniques in sediment core analysis, ed. R. G. Rothwell, Geological Society, London, Special Publications, **267**, 1–29. 46

Schock, G. S., 2004a, A method for estimating the physical and acoustic properties of the sea bed using chirp sonar data: IEEE Journal of Oceanic Engineering, **29**, 1200–1217. 18, 19, 23

———, 2004b, Remote estimates of physical and acoustic sediment properties in the south china sea using chirp sonar data and the Biot model: IEEE Journal of Oceanic Engineering, **29**, 1218–1230. 18

Schock, S. G. and L. R. LeBlanc, 1990, Chirp sonar: New technology for sub-bottom profiling: Sea Technology, **31**, 35–43. 24

Shapiro, S. A. and P. Hubral, 1999, Elastic waves in random media: *Springer Publishing*. 19

Shreve, R. L., 1985, Esker characteristics in terms of glacier physics, Katahdin esker system, Maine: GSA Bulletin, 639–646. 163

———, 1988, Living Ice: Understanding Glaciers and Glaciation: Cambridge University Press, Cambridge, 225pp. 172

Shumway, G., 1960, Sound speed and absorption studies of marine sediments by a resonance method: Geophysics, **25**, 451–467. 13, 14, 40

Simpkin, P. G. and A. Davis, 1993, For seismic profiling in very shallow water: A novel receiver: Sea Technology, **34**, 21–28. 24

Simpson, H. J. and B. H. Houston, 2000, Synthetic array measurements of acoustical waves propagating into a water-saturated sandy bottom for a smoothed and a roughened interface: Journal of the Acoustical Society of America, **107**, 2329–2337. 9

Simpson, H. J., B. H. Houston, S. W. Liskey, P. A. Frank, A. R. Bedroz, L. R. Kraus, C. K. Frederickson, and S. Stanic, 2003, At-sea measurements of sound penetration into sediments using a buried vertical synthetic array: Journal of the Acoustical Society of America, **114**, 1281–1290. 9

Sissons, J. B., 1979, Palaeoclimatic inferences from former glaciers in Scotland and the Lake District: Nature, **278**, 518–521. 116, 117, 118, 122

Sladen, J. A. and W. Wrigley, 1983, Geotechnical Properties of Lodgement Till – A Review: *In* Glacial Geology, An Introduction for Engineers and Earth Scientists, Ed. N. Eyles, Pergamon Press Ltd. 154

Small, E. E., 1995, Hypsometric forcing of stagnant ice margins: Pleistocene valley glaciers, San Juan Mountains, Colorado: Geomorphology, **14**, 109–121. 168, 169, 172

Smith, A. J., 1959, Structures in the stratified late-glacial clays of Windermere, England: Journal of Sedimentary Petrology, **29**, 447–453. 180, 183, 184, 187, 190

Somerville, S., 1983, Site Investigation Procedures and Engineering Testing of

Glacial Sediments: *In* Glacial Geology, An Introduction for Engineers and Earth Scientists, Ed. N. Eyles, Pergamon Press Ltd. 72, 155

Stevenson, I. R., C. McCann, and P. Runciman, 2002, An attenuation-based sediment classification technique using Chirp sub-bottom profiler data and laboratory acoustic analysis: Marine Geophysical Researches, **23**, 277–298. 12, 18, 23, 24, 46

Stoll, R. D., 1974, Acoustic waves in saturated sediments: *In* Physics of Sound in Marine Sediments, edited by L. Hampton Plenum, New York, 19–39. 8

———, 2002, Velocity dispersion in water-saturated granular sediment: Journal of the Acoustical Society of America, **111**, 785–793. 8

Stuiver, M. and P. J. Reimer, 1993, Extended ^{14}C database and revised CALIB radiocarbon program: Radiocarbon, **35**, 215–230. 192

Stuiver, M., P. J. Reimer, and R. Reimer, 2005, CALIB ^{14}C calibration program: Version 5.0.1 Available at http://calib.qub.ac.uk/calib/. 192

Taylor, W. P. and C. D. V. Wilson, 1997, Tectonically influenced glacial erosion, and ensuing valley infill: a geophysical survey: Quarterly Journal of Engineering Geology and Hydrogeology, **30**, 97–113. 153, 154, 163, 179

The MathWorks, Inc., 2007, Robust Regression: Curve Fitting Toolbox, www.mathworks.com/access/helpdesk_r13/help/toolbox/curvefit/ch_fitt5.html, accessed 26th January, 2008. 210

Thorsos, E., K. Williams, N. Chotiros, J. Christoff, K. Commander, C. Greenlaw, D. Holliday, D. Jackson, J. Lopes, D. Maghee, J. Piper, M. Richardson, and D. Tang, 2001, An overview of SAX99: Acoustic measurements: IEEE Journal of Oceanic Engineering, **26**, 4–25. xix, 6, 208

Trotter, F. M., S. E. Hollingworth, T. Eastwood, and W. C. C. Rose, 1937, Gosforth district: explanation of Map 37: Memoir of the geological survey of Great Britain, HMSO, London. 116

Turgut, A. and T. Yamamoto, 1990, Measurements of acoustic wave velocities and attenuation in marine sediments: Journal of the Acoustical Society of America, **87**, 2376–2383. xix, 5, 6, 208

Ullyott, P. and P. Holmes, 1936, Thermal stratification in lakes: Nature, **138**, 971.

233

USGS, 2009, Push Moraine: USGS Glossary of Glacier Terminology: Available at http://pubs.usgs.gov/of/2004/1216/m/m.html. 170

Vardy, M. E., 2009, Real-time imaging of decimetre-resolution 3D seismic volumes: PhD Thesis, University of Southampton. 81, 82, 132, 133

Vardy, M. E., L. J. W. Pinson, J. M. Bull, T. J. Henstock, J. W. Davis, and M. Gutowski, 2010, 3D seismic imaging of buried Younger Dryas mass movement Flows: Lake Windermere: Geomorphology, **in press**. 81, 82

Velegrakis, A., 2000, Geology, Geomorphology and Sediments of the Solent System: *In* Proceedings in marine science 1, Solent Science—A Review, *Elsevier*, 2000, 21–39. 26

Vincent, P., 1985, Quaternary geomorphology of the southern Lake District and Morecambe Bay area: *In* The geomorphology of North-west England, Ed. R. H. Johnson, Manchester University Press, 159–177. 123

Wang, J., L. Zhu, M. Nishimura, T. Nakamura, J. Ju, M. Xie, W. Takahiro, and M. Testsuya, 2009, Spatial variability and correlation of environmental proxies during the past 18,000 years among multiple cores from Lake Pumoyum Co, Tibet, China: Journal of Paleolimnology, **42**, 303–315. 212

Ward, J. C., 1875, The glaciation of the southern part of the Lake District and the glacial origin of the lake-basins of Cumberland and Westmoreland: Quarterly Journal of the Geological Society, **31**, 135–166. 119, 121, 123

Webb, B. C. and D. J. D. Lawrence, 1986, Conical fold terminations in the Bannisdale Slates of the English Lake District: Journal of structural geology, **8**, 79–86. 120

Wentworth, C. K., 1922, A scale of grade and class terms for clastic sediments: Journal of Geology, **30**, 377–392. xviii

West, I. M., 1980, Geology of the Solent estuarine system: N.E.R.C. Publication, Series C, **22**, 6–12. 26

White, R. E., 1992, The accuracy of estimating Q from seismic data: Geophysics, **57**, 1508–1512. 38

Williams, K., D. Jackson, E. Thorsos, D. Tang, and S. Schock, 2002, Comparison of

sound speed and attenuation measured in a sandy sediment to predictions based on the Biot theory of porous media: IEEE Journal of Oceanic Engineering, **27**, 413–428. 9, 18, 19, 39

Wilson, C. D. V., 1987, The outflow of Windermere, Cumbria: a re-appraisal: Geological Journal, **22**, 219–224. 72, 119, 123, 153

Wilson, P., 2004, Description and implications of valley moraines in upper Eskdale, Lake District: Proceedings of the Geologists' Association, **155**, 55–61. 118

Winfield, I. J. and R. Sweeting, 2007, Climate Change and some of its effects in Windermere: Lake District Still Waters Partnership, Fifth Annual Liaison Meeting: Climate Change and the Lake District. 232, 234

Woodcock, N. H. and N. J. Soper, 2006, The Acadian Orogeny: the mid-Devonian phase of deformation that formed slate belts in England and Wales: The Geology of England and Wales, 2nd Edition, Ed. P. J. Benchley and F. Rawson, Pub. The Geological Society, 131–146. 121

Wright, H. E., 1980, Surge moraines of the Klutlan Glacier, Yukon Territory, Canada: Origin, wastage, vegetation succession, lake development and application to the late-glacial of Minnesota: Quaternary Research, **14**, 2–18. 172

Zhang, C. and S. Zhang, 1989, A robust-symmetric mean: A new way of mean calculation for environmental data: GeoJournal, **40**, 209–212. 46, 214

Zilliacus, H., 1989, Genesis of De Geer moraines in Finland: Sediment Geology, **62**, 309–317. 159, 176